SPECTROSCOPIC AND THEORETICAL CONSTRAINTS ON THE DIFFERENTIATION OF PLANETESIMALS

A DISSERTATION SUBMITTED TO THE GRADUATE DIVISION OF THE UNIVERSITY OF HAWAIʻI IN PARTIAL FULFILLMENT OF THE REQUIREMENTS FOR THE DEGREE OF

DOCTOR OF PHILOSOPHY

IN

ASTRONOMY

AUGUST 2009

By
Nicholas A. Moskovitz

Dissertation Committee:

E. Gaidos, Chairperson
R. Jedicke
N. Haghighipour
D. Jewitt
S. Krot

We certify that we have read this dissertation and that, in our opinion, it is satisfactory in scope and quality as a dissertation for the degree of Doctor of Philosophy in Astronomy.

DISSERTATION

COMMITTEE

_____

Chairperson

_____

_____

_____

_____

Gěi wǒ de jiārén.

Acknowledgements

Whatever weaknesses may be present in the following pages, they undoubtedly would have been far greater without support, insight and inspiration from numerous individuals. First and foremost, I am deeply grateful to my advisor Eric Gaidos whose intelligence, patience and deep curiosity have helped to guide me through the intellectual rigors of completing this dissertation. I want to extend a special thanks to Robert Jedicke who, through his enthusiasm and thoughtful insight, has been an invaluable contributor to this work. Thanks are due to the rest of my committee members (David Jewitt, Nader Haghighipour and Sasha Krot) for their helpful perspectives and for tactfully listening to my sometimes outlandish ideas.

Many of my peers have been instrumental (in small ways and large) to the completion of this dissertation. To those who fall into the ubiquitous category of "too many to mention", I thank you for your support. Others have been absolutely essential in their contributions to this work and I would be remiss if I did not recognize them individually. Mahalo nui loa to Mark Willman for the multitude of conversations that have helped me to navigate around a host of scientific road blocks, and whose excellent stories and good humor have made many a night on Keck and the 88" vastly more entertaining. I am also indebted to Bin Yang, an always dependable source of incisive opinions and measured criticism.

This dissertation has been significantly enriched thanks to a number of conversations with Ed Scott, Jeff Taylor, Gary Huss, Paul Lucey, Sam Lawrence and David Nesvorny. My thanks to Bobby Bus for being an excellent resource for observing

knowledge and who, along with Richard Binzel, has been exceedingly generous with the sharing of data. I also want to thank several other “experts on the mountain” who have helped me to become a competent observer: John Dvorak, Dan Birchall, John Rayner, Jana Pittichova, Greg Wirth and Greg Aldering. I am very appreciative of the help I have received from the staff and faculty at the IfA, but I would particularly like to thank Karen Meech for starting me down a path that has led to the realization that the smallest bodies in the universe are indeed the most interesting, and Narayan Raja whose genius has saved me from countless hours of frustration that otherwise may have resulted in the destruction of more than one desktop computer. I would also like to thanks the good folks at NASA who deemed my research sufficiently interesting to provide three years of funding.

Both at work and away, Lisa Chien has shared with me her brilliance, humor and irrepressible spirit. I can not imagine having tried to complete this thesis without her; I am so lucky that she has been a part of this adventure. Lastly I must send thanks to my family: to my parents for always providing their love and encouragement, and impressing upon me at an early age a deep fascination for the natural world. I am so very grateful for their support and the opportunities that they have provided me. And to my sister whose joie de vivre and audacious pursuit of her dreams have been an inspiration to me.

Abstract

The differentiation of small proto-planetary bodies into metallic cores, silicate mantles and basaltic crusts was a common occurrence in the first few million years of Solar System history. In this thesis, observational and theoretical methods are employed to investigate this process. Particular focus is given to the basaltic, crustal remnants of those differentiated parent bodies.

A visible-wavelength spectroscopic survey was designed and performed to constrain the population of basaltic asteroids in the Main Belt. The results of this survey were used to provide statistical constraints on the orbital and size-frequency distributions of these objects. These distributions imply that basaltic material is rare in the Main Belt (particularly beyond the 3:1 mean motion resonance at 2.5 AU), however relic fragments of crust from multiple differentiated parent bodies are likely present.

To provide insight on the mineralogical diversity of basaltic asteroids in the Main Belt, we performed a series of near-infrared spectroscopic observations. We find that V-type asteroids in the inner belt have spectroscopic properties consistent with an origin from a single parent body, most likely the asteroid Vesta. Spectroscopic differences (namely band area ratio) between these asteroids and basaltic meteorites here on Earth are best explained by space weathering of the asteroid surfaces. We also report the discovery of unusual spectral properties for asteroid 10537 (1991 RY16), a V-type asteroid in the outer Main Belt that has an ambiguous mineralogical interpretation.

We conclude this thesis with a theoretical investigation of the relevant stages in the process of differentiation. We show that if partial silicate melting occurs within the

interior of a planetesimal then both core and crust formation could have happened on sub-million year (Myr) time scales. However, it is shown that the high temperatures necessary to facilitate these processes may have been affected by the migration of molten silicates within these planetesimals and by chemical interactions between liquid water and silicate rock. Finally, a 1-dimensional model of heat conduction is used to explore whether differentiation would have occurred for planetesimals across a range of sizes (4 - 250 km) and times of accretion (0 - 3 Myr).

Table of Contents

List of Tables

List of Figures

Chapter 1

Introduction

1.1 Introduction to Asteroids and Meteorites

In the standard paradigm of planet formation (e.g. Wetherill 1980) km-size planetesimals formed by the gradual accumulation of smaller particles. Most planetesimals were incorporated into the terrestrial planets and cores of the gas and ice giants, however some of this material exists in the present-day Solar System as a vestige of the planet formation process. These relics make up a variety of populations including the asteroids, comets, irregular satellites, the Kuiper Belt, the Oort Cloud and meteorites. The asteroids, which serve as the focus of this dissertation, include objects that are disrupted remnants of larger parent bodies, aggregates of these collisional fragments, and intact planetesimals that have survived since the epoch of planet formation.

The asteroids are typically categorized into three dynamical classes (Fig. 1.1). The Trojan asteroids are in a 1:1 mean motion resonance with Jupiter, populating the L_4 and L_5 Lagrangian points 60° ahead of and behind Jupiter's orbit. The Main Belt asteroids reside between the orbits of Jupiter and Mars in a band that extends from approximately 2.0 to 3.5 Astronomical Units (AU). The near-Earth objects (NEOs) are a dynamically short-lived population of bodies that have been ejected from the Main

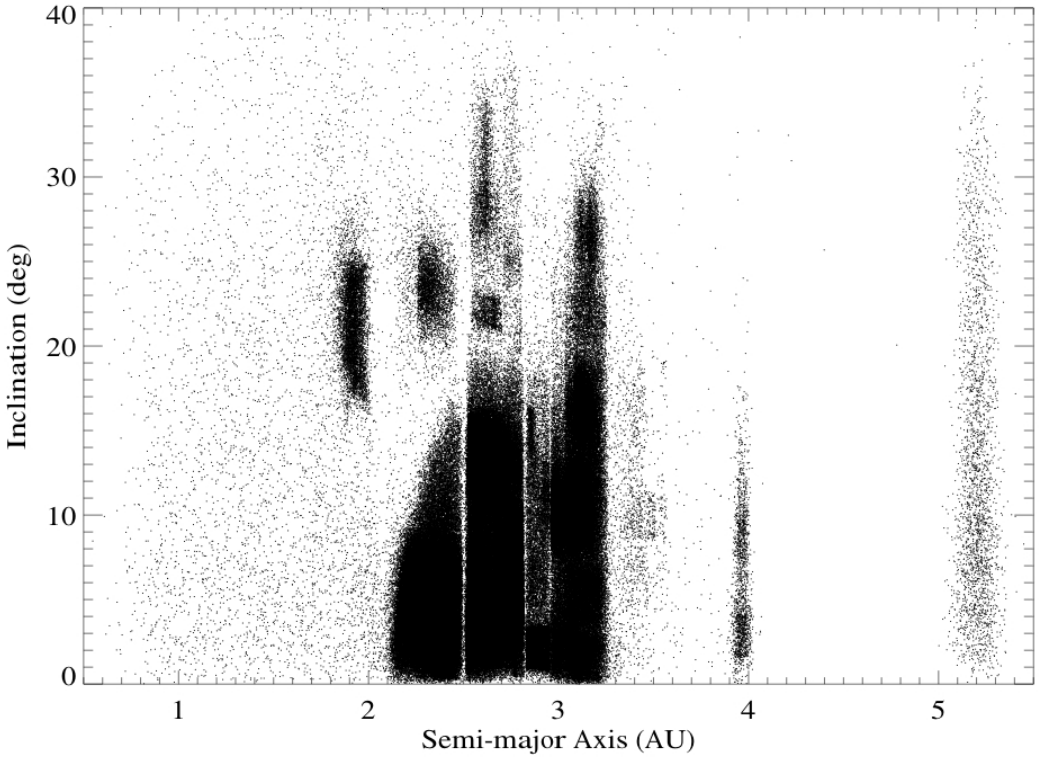

Figure 1.1 Inclination versus semi-major axis in osculating element space for all known asteroids. Data are from Bowell (2007). NEOs are the diffuse collection of points inside of approximately 2.0 AU. The Trojan clouds span the full range of inclinations with mean semi-major axes of 5.2 AU. The dense swarm of Main Belt asteroids represents over 95% of all known asteroids. The Kirkwood gaps are apparent at 2.06, 2.5, 2.82, 2.95 and 3.27 AU.

Belt into planet crossing orbits with perihelia typically less than 1.3 AU (Morbidelli et al. 2002).

In the Main Belt, asteroids cluster into dynamical associations characterized by similar orbital properties (Fig. 1.1). These clusters were first noted and interpreted by Hirayama (1918) as collisional families. More recently, the identification of many 10's of asteroid families (Bendjoya & Zappalà 2002) has been facilitated by analytical tools such as the hierarchical clustering method (HCM, Zappala et al. 1990) and a steadily increasing number of discovered asteroids (Bowell 2007). These families

range in size from many thousands of members (Nesvorný et al. 2008) to individual asteroid pairs (Vokrouhlický & Nesvorný 2008). The collisions that formed these families are thought to have occurred sometime after the late heavy bombardment (LHB), an event approximately 3.8 - 4.1 billion years (Gyr) ago that may have been triggered by the migration of Jupiter and Saturn through their mutual 2:1 mean motion resonance (Gomes et al. 2005). Perturbations from these migrating gas giants would have dynamically scattered asteroids in the Main Belt, effectively erasing any orbital clustering of pre-LHB asteroid families (Gomes 1997).

Asteroids within the same family typically share photometric and spectroscopic properties (Cellino et al. 2002), thus supporting a scenario of common origin from collisionally disrupted parent bodies. Taxonomic classification into photometric (Tholen 1984) and spectroscopic (Bus & Binzel 2002a; DeMeo et al. 2008) classes across visible and near-infrared wavelengths has resulted in the identification of approximately 15-25 distinct types of asteroids (depending upon the specific classification scheme). Although the visible and near-infrared ($\sim\ 0.5 - 2.5\ \mu m$) photometric and spectroscopic properties of asteroids can be degenerate for different mineralogies (e.g. Rivkin et al. 2000), the half-dozen most common taxonomic types have generally well accepted mineralogical interpretations (Gaffey et al. 1993a). In the Bus taxonomic system (Bus & Binzel 2002a), the C-, D- and X-type asteroids are considered to be primitive bodies that have undergone minimal thermal processing and are analogous to carbonaceous chondrite meteorites. However, the X-complex includes what Tholen (1984) referred to as the M-type asteroids, which have a very different mineralogical interpretation (see §1.5.1). The Q- and S-type asteroids are commonly interpreted as bodies that have experienced moderate thermal alteration (possibly including partial silicate melting) and are typically associated with the ordinary chondrites (Vernazza et al. 2008; Nesvorný et al. 2009). Lastly, the V-types are representative of high degrees of silicate melting and are commonly linked to the HED meteorites (Drake 1979). Other less common asteroid types such as the R- and

T-types have ambiguous mineralogical interpretations (Gaffey et al. 1993a) without any known meteoritic analogs.

The link between Main Belt asteroids and meteorites here on Earth has strengthened over time due to progressive improvement in our understanding of orbital dynamics. It has long been known that the dynamical structure of the Main Belt includes prominent mean motion resonances with Jupiter (Fig. 1.1, Kirkwood 1876). More recent works have shown that secular resonances are also important to the dynamics of Main Belt asteroids (e.g. Wisdom 1985). Asteroids that migrate into these resonances experience an amplification of their eccentricities and can eventually achieve planet crossing orbits (Gladman et al. 1997). It is believed that this scenario describes the origin of NEOs and meteorites here on Earth. Investigations of dynamically important processes such as the Yarkovsky effect (Bottke et al. 2000) and resonant interactions (Carruba et al. 2005) suggest that small fragments throughout the Main Belt can migrate into resonances and be delivered as meteorites to Earth (Vernazza et al. 2008).

1.2 Physical Processes Relevant to Planet Formation and the Evolution of Small Bodies

The study of asteroids has contributed greatly to our understanding of processes that have governed the evolution of planetary bodies in the Solar System. For instance, their location between the terrestrial and gas giant planets provides clues about how planet formation differed in these two regions. The distribution of asteroid spectral types (and by extension composition) as a function of semi-major axis (Gradie & Tedesco 1982) provides supporting evidence for the former presence of a heliocentric temperature gradient in the solar nebula. Such a gradient would have resulted in a "snow line" (Hayashi 1981) somewhere interior to Jupiter's orbit (Ciesla & Cuzzi 2006) beyond which water ice would have condensed out of the nebula. The increased surface

density of solids beyond the snow line resulted in larger planetesimals that grew faster than in the inner nebula. The presence of large planetesimals instigated a period of rapid, runaway growth that resulted in the formation of massive ($\sim 10 - 15\ M_{\oplus}$) cores (Chambers 2006). These cores ultimately accreted gaseous envelopes to become the gas giant planets. Thus, the location of the asteroids between the gas giants and terrestrial planets suggests that they represent the boundary between two distinct reservoirs of planet-forming material: relatively anhydrous bodies from within the snow line (represented by S- and V-type asteroids in the inner Main Belt) and more water-rich bodies from outside of the snow line (represented by C- and D-type asteroids in the outer Main Belt). However, radial scattering of planetesimals in the solar nebula (Raymond et al. 2004) likely mixed these two populations so that the location of the snow line may not be precisely represented by the present-day heliocentric distribution of asteroidal spectral types.

A further consequence of the Main Belt's location between Mars and Jupiter is that it may have acted as a repository for planetesimals that were scattered from the inner Solar System ($a < 2.0$ AU, Bottke et al. 2006) and perhaps even the Kuiper Belt (Levison et al. 2008; McKinnon 2008). Thus, asteroids in the present-day Main Belt may include material that originated from a wide range of heliocentric distances, providing a potentially accessible natural laboratory for studying various formation environments. Unfortunately, remote observations have yet to distinguish the place of origin for putative Main Belt interlopers.

The physical properties of asteroids provide insight on evolutionary processes that have otherwise been obscured on larger planetary-size bodies by the accretion process, fluvial, aeolian and/or tectonic activity. For example, the preservation of craters and the morphology of asteroids offers insight on collisional processes (e.g. Bottke et al. 2005a; Ostro et al. 2000). The size-frequency distribution of collisional families suggests details about the ages of families and sizes of their parent bodies (Parker et al. 2008). Due to their small sizes and lack of atmospheres, asteroids provide

the opportunity for studying the weathering of chondritic material by particle and/or radiation bombardment (i.e. space weathering, Clark et al. 2002; Willman et al. 2008), dynamical migration due to the Yarkovsky force (Chesley et al. 2003), and rotational variation due to the YORP effect (Lowry & 10 co-authors 2007).

Isotopic, petrologic and chemical analyses of meteorites have also provided a wealth of information regarding very specific physical processes that altered their asteroidal parent bodies. For example, CB chondrites likely formed in a vapor-melt plume produced by the collision of two Moon-sized proto-planets 4.562 Gyr ago (Krot et al. 2005a). CI and CM carbonaceous chondrites exhibit evidence for significant aqueous alteration on their respective parent bodies (Krot et al. 2005b). The unique composition of pallastites (cm-size olivine grains embedded within a matrix of Fe-Ni metal) suggests that these samples originated at the core mantle boundary of a parent body that melted and differentiated (Scott 1977). These examples are a small sampling of the detailed information that can be gleaned from meteorites regarding the evolution of their asteroidal parent bodies.

Asteroids (e.g. Grimm & McSween 1993) and meteorites (Krot et al. 2005b) also provide insight on the post-accretional thermal processing of their respective parent bodies. A full spectrum of thermal alteration states are represented by these objects; from primitive C-type asteroids (Gaffey et al. 1993a) to fully melted iron meteorites (Chabot & Haack 2006). This variety can be attributed to a complicated interplay of the time of accretion, initial composition, size, and location of the parent body in the solar nebula (Hevey & Sanders 2006; McSween et al. 2002).

1.3 The Process of Differentiation

Numerous groups of meteorites and asteroids (§1.5) are thought to have derived from planetesimals whose interior temperatures were high enough to facilitate the process of metal-silicate differentiation. Here we present a broad, qualitative outline

of the differentiation process and postpone a more detailed theoretical discussion until Chapter 4.

The first planetesimals to accrete out of the solar nebula were undifferentiated and presumably had a chemical composition similar to CI chondrites (Lodders 2003). The primary mineralogical components of these planetesimals were silicates (pyroxenes and olivine) and iron-nickel-sulfeur (Fe-Ni-S) metal. These bodies were likely to have accreted "cold" (i.e. in thermal equilibrium with the nebular environment, Grimm & McSween 1989), however, it is possible that the small ($\sim$cm-size) aggregates that formed the building blocks of these planetesimals experienced significant thermal alteration from the release of chemical energy (Clayton 1980).

The internal temperatures of bodies that accreted early (within a few million years, Myr) would have increased due to the availability of various heat sources (§1.4). If temperatures reached the Fe-S eutectic (~ 1200 K), then Fe-S melt would have quickly segregated from the surrounding silicate matrix on a time scale much faster than a few million years (Taylor 1992) . This Fe-S melt would have gravitationally sunk to the center of the body or, if the abundance of dissolved volatiles in the melt were sufficiently high, then it could have been carried to the surface and ejected from the body (Keil & Wilson 1993). Further heating to the solidus temperature of the silicates (~ 1400 K) would have initiated silicate melting. Buoyancy and compaction forces (Taylor et al. 1993) would have driven the initial partial melts to the upper layers or surface of the planetesimal. Again depending on volatile content, these initial silicate melts may have been ejected from the planetesimal (Wilson & Keil 1991).

The difference between the solidus and liquidus temperatures of chondritic silicates is typically about $400 - 500$ K (e.g. Agee et al. 1995), thus by ~ 1900 K silicate material would have been completely molten. Such liquidus temperatures are comparable to the Fe-Ni eutectic (Taylor et al. 1993). Thus, planetesimals that reached these high temperatures would have completely melted and could have differentiated into an "onion layer" structure with an Fe-Ni-S core, an olivine-rich

mantle and a plagioclase/pyroxene-rich basaltic crust (Ruzicka et al. 1997). The subsequent solidification of the silicate crust and mantle would follow a crystallization sequence with olivine condensing first, followed by low-calcium pyroxene, then high-calcium pyroxene and finally plagioclase (Taylor 1992; Sunshine et al. 2004). Fully differentiated bodies were the most altered planetesimals, other bodies experienced less extreme thermal histories.

1.4 Heat Sources in the Early Solar System

A number of processes likely contributed to the thermal evolution of planetesimals. The decay of short-lived radioactive isotopes (SLRs) such as ^{26}Al and ^{60}Fe (Urey 1955; Goswami et al. 2005) was a significant source of heat in the early Solar System (the half lives of these isotopes are 0.74 and 1.5 Myr respectively). Isotopic analyses of meteorite samples (e.g. Lee et al. 1976) suggest that initial ^{26}Al abundances were high enough to melt planetesimals that accreted within a few half lives of the parent isotope or, equivalently, within a few million years after the formation of CAIs (Grimm & McSween 1989). The formation of calcium-aluminum inclusions (CAIs) is an effective "time zero" for the history of the Solar System and is often assumed to be the time at which ^{26}Al and other SLRs were introduced. Although ^{60}Fe has a comparable decay energy per atom to that of ^{26}Al (3 MeV versus 4 MeV), its abundance in the solar nebula was lower by a factor of 2.5-5 (Ghosh & McSween 1998; Tachibana & Huss 2003; Tachibana et al. 2006) and thus is typically ignored as a heat source in calculations of the thermal evolution of planetesimals (e.g Hevey & Sanders 2006). This is reasonable due to large uncertainties in other thermally relevant quantities such as time of accretion and composition.

Electrical induction from the highly charged solar wind and intense magnetic field of the young Sun may have been another important source of thermal energy for planetesimals (Sonett & Colburn 1968). However, this mechanism is poorly

constrained (McSween et al. 2002) and may be incompatible with observations of T Tauri winds (Wood & Pellas 1991). Inductive heating would have been active over a time scale comparable to SLR decay times (several hundred thousand years during which the Sun was in its T Tauri phase), thus it is not possible to disentangle the thermal consequences of these two heating mechanisms through studies of asteroids and meteorites. For these reasons, discussions on the thermal evolution of proto-planetary bodies typically consider SLR decay as the exclusive heating mechanism in the early Solar System. In line with convention, we adopt this assumption throughout this work.

Impact heating was also common on planetesimals (Mittlefehldt 1979), however, for small bodies, its thermal effects would have been localized with negligible global consequences (Keil et al. 1997). Gravitational potential energy released during accretion would have provided an additional heat source primarily through frictional and collisional dissipation. The energy per unit mass released by gravitational accretion of a spherical body with constant density is:

$$\epsilon = \frac{4\pi}{5} G\rho R^2, \tag{1.1}$$

where G is the gravitational constant, ρ is the density (assumed to be 3300 kg/m^3, a value typical for chondritic silicates), and R is the radius of the accreting body. Figure 1.2 compares the energy per unit mass that is available to a planetesimal from the decay of ^{26}Al versus the amount from gravitational binding. The energy from ^{26}Al was calculated for 4 different times of instantaneous accretion relative to the onset of decay and by assuming a planetesimal with an overall aluminum mass fraction of 0.009 (Anders & Grevesse 1989), an ^{26}Al/^{27}Al ratio of 5×10^{-5} (Goswami et al. 2005), and an ^{26}Al decay energy of 4.0042 MeV (Lide 2002). This figure shows that the energy from gravitational binding was an important heat source for bodies that grew to very large sizes ($\gtrsim 2000$ km). It is unlikely that this describes the conditions of formation

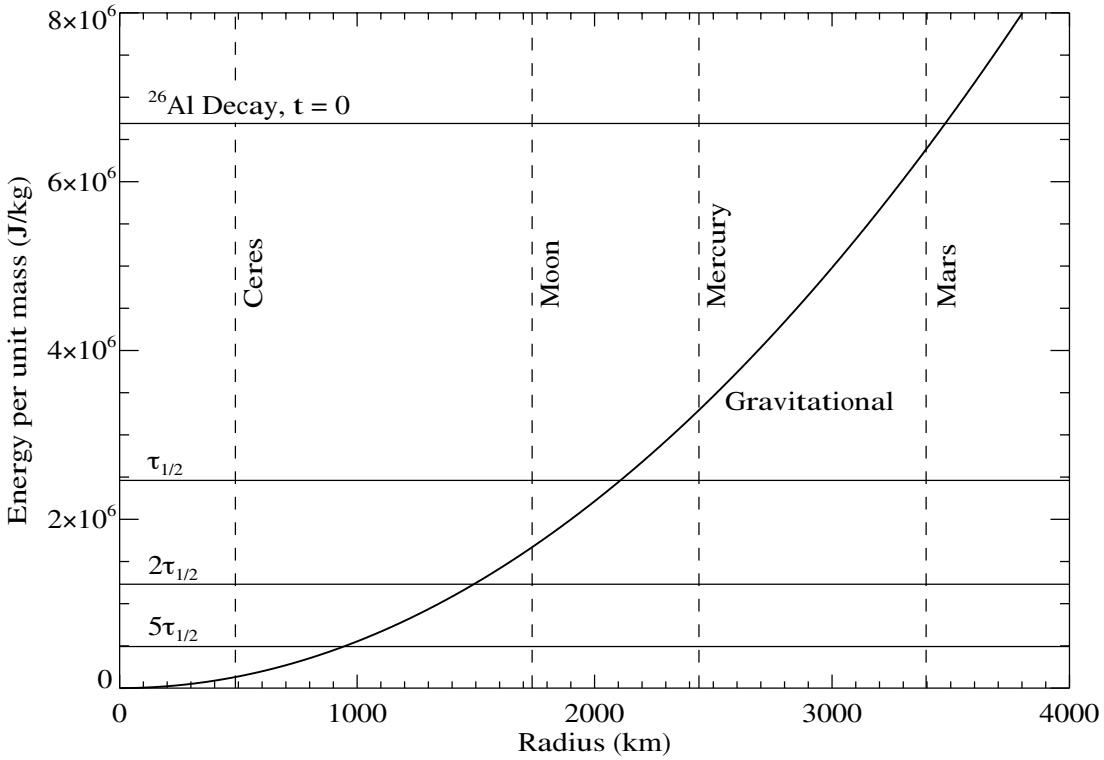

Figure 1.2 Energy per unit mass of planetesimal as a function of radius. The energy available to a planetesimal from the decay of ^{26}Al would depend on its time of accretion relative to the onset of isotopic decay. For an accretion time simultaneous with the onset of decay (t = 0), ^{26}Al would have produced $\sim 6.7 \times 10^6$ J/kg. The energy available for bodies with times of accretion corresponding to 1, 2 and 5 half lives ($\tau_{1/2} = 0.74$ Myr) after the onset of decay are plotted. The gravitational binding energy that is released during accretion (Eqn. 1.1) becomes significant relative to ^{26}Al heating when a body achieves a radius of ~ 1000 km within a few Myr of the onset of SLR decay. The radii of Ceres, the Moon, Mercury and Mars are indicated by the vertical dashed lines.

for the asteroids and planetesimals considered in this work. For this reason we ignore the consequences of energy released by gravitational binding for the remainder of this discourse.

If we assume that ^{26}Al was the dominant heat source for small bodies in the early Solar System, then the time of accretion becomes the most important variable in determining the thermal evolution for a given body. The well-established

proportionality between accretion time and heliocentric distance (Safronov 1969) implies that planetesimals from the inner Solar System incorporated a high abundance of live radionuclides and may have reached temperatures high enough to have melted and differentiated (Hevey & Sanders 2006). Planetesimals that formed at greater heliocentric distances presumably accreted too slowly to reach such large temperatures. It is uncertain where the boundary between these two regions lay (Bottke et al. 2006), however the inferred compositional gradient across the asteroid belt could be related to heliocentric zoning by ^{26}Al heating (Grimm & McSween 1993). This remains an open problem that is complicated by the superposition of compositional effects from the heliocentric temperature gradient in the solar nebula.

1.5 Relics of Differentiated Bodies

Collisional disruption of a fully differentiated body would produce a suite of fragments representing its various compositional layers. Such fragments have been observed amongst the asteroids and meteorites, though these objects may be aggregates that re-accreted following disruption. Here we outline the observational evidence that extreme thermal processing of proto-planetary material did occur in the early Solar System. Particular attention is paid to the basaltic fragments of differentiated parent bodies, because these objects are the focus of the observational (Chapters 2 and 3) and theoretical (Chapter 4) portions of this work.

1.5.1 Core and Mantle Fragments

Metal-rich cores of differentiated planetesimals are thought to be represented by M-type asteroids (Belskaya & Lagerkvist 1996). However, M-type asteroids do not have unique spectral properties and are often grouped with enstatite-chondritic asteroids (highly reduced primitive bodies that never melted) into the X-complex of modern taxonomic systems (e.g. Bus & Binzel 2002a). Rivkin et al. (2000) showed that

approximately 1/3 of spectroscopically classified M-types (based on visible wavelength data) display a $3\ \mu m$ absorption feature diagnostic of hydrated minerals. This feature is inconsistent with the geothermal histories expected for the metallic cores of differentiated bodies. Thus, these authors proposed to divide the M-class into two groups: the metallic M-type asteroids which tend to be smaller (< 65 km) with faster rotation periods (mean = 5.7 hr) and do not display a hydration feature, and the hydrated W-types which tend to be larger (> 65 km) with slower rotation periods (mean = 8.2 hr) and do display a $3\ \mu m$ absorption band. This cutoff of 65 km for a metallic core is consistent with calculated upper limits to the size of parent bodies that could have been catastrophically disrupted over the age of the Solar System (Davis et al. 1999) and with the estimated sizes of iron meteorite parent bodies based on metallographic cooling rates (Haack et al. 1990; Chabot & Haack 2006). The relatively fast average rotation periods for M-types agrees with theoretical relations between rotation rate and density (Harris 1979). These small sizes and fast rotation periods are consistent with, but not diagnostic of a metal-rich composition.

Distinguishing metallic M-type asteroids from other asteroids with similar spectral features requires a combination of spectroscopic data across a wide range of wavelengths, albedo measurements, and information about the polarization properties of their surfaces (Belskaya & Lagerkvist 1996). Metal-rich M-types are characterized by a relatively featureless and moderately red-sloped visible through near-infrared (NIR) spectrum (DeMeo et al. 2008), lack of a $3\ \mu m$ absorption feature (Rivkin et al. 2000), a high radar albedo (Magri et al. 2007), and polarization properties consistent with metallic powders (Dollfus et al. 1979). Approximately 100 metallic M-type asteroids larger than 30 km are thought to reside in the Main Belt (Belskaya & Lagerkvist 1996). The canonical example of an M-type asteroid that meets all of these criteria is 16 Psyche (Lupishko 2006).

The magmatic iron meteorites, which comprise a large majority of the iron meteorites, are also thought to represent the cores of differentiated bodies (Taylor

1992). These meteorites are primarily composed of Fe-Ni metal and can be divided into distinct groups based on their trace element and Ni abundances (Scott & Wasson 1975), a process which identifies 13 groups of 5 members or more (Krot et al. 2005b). Oxygen isotope analyses have shown that these groups do have distinct isotopic signatures (Chabot & Haack 2006). Approximately 15% of iron meteorites do not fall into these chemical groups, these samples are referred to as "ungrouped irons" and are thought to represent at least 50 distinct parent bodies (Chabot & Haack 2006). In total it is estimated that as many as 90 differentiated parent bodies are represented by the iron meteorites (Keil 2000).

The slow cooling of iron meteorites within their parent bodies allowed the formation of Widmanstatten patterns, configurations of large, interleaved crystals. The specific structure of this pattern is dependent on the composition and cooling rate of the Fe-Ni metal (Chabot & Haack 2006). Metallographic cooling rates inferred from Widmanstatten patterns provide constraints on the sizes of the asteroidal cores and surrounding silicate mantles from which the iron meteorites came. Most irons likely came from parent bodies of 10s to 100s of kilometers in diameter (Chabot & Haack 2006), however the determination of a large dispersion in cooling rates for the iron IVA group suggests that their parent body was $\sim 10^3$ km in size (Yang et al. 2007). Other iron meteorite groups with reportedly large cooling rates may also represent the cores of large planetesimals (e.g. Yang & Goldstein 2006).

Other achonditic meteorites, such as the mesosiderites, pallasites, aubrites and ureilites, have textures and/or compositions that are indicative of formation on heavily metamorphosed parent bodies, many of which are consistent with melt residues from partially differentiated planetesimals (see table 6 in Krot et al. 2005b). These meteorites are rare, making up only a few percent of all meteorite falls (Harvey & Cassidy 1989). In total there are approximately 20 parent bodies represented by the non-basaltic, differentiated achondrites (Keil 2000).

Differentiated achondritic asteroids are also rare. The A-type asteroids are interpreted as olivine-rich mantle fragments from differentiated parent bodies (Burbine et al. 1996). R-type asteroids may represent the cumulate mantle from a differentiated parent body (Feierberg et al. 1980), but could also be heavily weathered ordinary chondrite-like material (Hiroi & Sasaki 2001). Why there is not more mantle material amongst Main Belt asteroids remains an open question with answers possibly related to collisional grinding and/or space weathering (see §1.7).

Mineralogical analyses based on telescopic observations suggest that some collisional families of asteroids may represent differentiated bodies. Nathues et al. (2005) suggest that the observed color variation across the surface of 15 Eunomia is due to an enhancement of pyroxene on one hemisphere and an enhancement of olivine on the other. These authors conclude that such heterogeneity is consistent with a compositional gradient across the mantle of a differentiated body. Mothé-Diniz et al. (2008) performed three different methods of mineralogical analysis on a set of 30 NIR spectra to conclude that members of the Eos family tend to have olivine and minor amounts of orthopyroxene on their surfaces, compositions that are compatible with an origin on a partially differentiated parent body. Sunshine et al. (2004) performed analyses on NIR spectra of several S-type asteroids and found that the derived silicate mineralogies for the Thetis, Agnia and Merxia families contained relatively large quantities of high-calcium pyroxene. The presence of significant amounts of high-calcium pyroxene requires that the parent bodies of these asteroids experienced igneous differentiation. We note that none of these families have members with reflectance spectra that are typically associated with asteroidal or meteoritic basalts (§1.5.3)

1.5.2 Basaltic Crust: Meteorites

Amongst differentiated achondrites, there are only two groups of purely basaltic meteorites. The angrites are basaltic in composition, however they are unlike any

other basalt in the Solar System in that they have the lowest known content of alkali metals (Mittlefehldt et al. 1999). The origin of the angrites is uncertain due to their unusual nature and paucity of members (< 20). However, Pb-Pb dating suggests that the angrite parent body was one of the earliest objects to form in the Solar System (Baker et al. 2005), a scenario which is consistent with the formation of basaltic melt fueled by the decay of SLRs.

The HEDs (howardites, eucrites and diogenites) are the second group of basaltic achondrites and are far more numerous than the angrites (> 500 samples). The HEDs are unique in that they are the only group of meteorites (other than those from the Moon and Mars) that have been convincingly linked to a specific parent body: the large Main Belt asteroid Vesta is their putative source (§1.5.3). The occurrence of polymict breccias (e.g. howardites that contain pieces of eucrites and diogenites) argue for a common origin on a single HED parent body (Keil 2002). The three subgroups of HEDs are thought to derive from different depths within their parent body (Krot et al. 2005b). Howardites have brecciated textures that include both diogenites and eucrites and are thought to be analogous in composition to Vesta's surface regolith (Pieters et al. 2006). The eucrites are plagioclase-pyroxene basalts derived from the differentiated crust. The diogenites are rich in orthopyroxene and likely originated in the upper mantle of the HED parent body at depths of greater than 10's of kilometers (Burbine et al. 2001). There is open debate about whether the HEDs (particularly the eucrites) formed from partial melts or through fractional crystallization of a totally molten body (Mittlefehldt et al. 1999). However, due to their low abundances of Fe and other siderophile elements such as W, the HEDs almost certainly are derived from a parent body that differentiated into a metallic core with a silicate mantle and crust (Dreibus & Wänke 1980; Lee & Halliday 1997).

Most HEDs share a common signature of oxygen isotope ratios, indicating that they originated from a single parent body (Greenwood et al. 2005). However, recent studies (Yamaguchi et al. 2001; Scott et al. 2009) have shown that some eucrites have

anomalous oxygen isotope compositions and thus could represent other differentiated parent bodies. To date, 6 aberrant eucrites have been identified (Scott et al. 2009). These unusual meteorites suggest that basaltic asteroids other than Vesta must be present in the Main Belt, a presumption that is supported by the recent discovery of several non-Vestoid basaltic asteroids (§1.5.4).

1.5.3 Basaltic Crust: Vesta and the Vestoids

Traditionally, the HEDs have been linked to the large Main Belt asteroid 4 Vesta. Vesta, discovered on March 29, 1807 by Heinrich Wilhelm Olbers (Lynn 1907), is the second most massive asteroid in the Main Belt and due to its high albedo (~ 0.4) is the only Main Belt asteroid visible to the naked eye. Based on images of Vesta from the Hubble Space Telescope, Thomas et al. (1997) determined that its shape is ellipsoidal with a mean radius of 266 km. Viateau & Rapaport (2001) determined the mass of Vesta based on perturbations to the orbit of the small Main Belt asteroid 197 Arete. Their calculated mass of (1.306±0.016)$\times 10^{-10} M_{\odot}$ yields a mean density of (3.3±0.5) g/cm^3. These relatively large uncertainties make it impossible to infer the presence of a core (Ghosh & McSween 1998), however the Dawn mission to Vesta will be capable of making that distinction (Russell & 20 co-authors 2004).

The presence of basaltic material on the surface of Vesta was originally inferred based on a coarse spectrum across visible wavelengths (McCord et al. 1970). Basaltic melts derived from a chondritic precursor (like those presumed to be on the surface of Vesta) will contain pyroxenes, plagioclase and small amounts of olivine. Pyroxenes are spectroscopically characterized by deep and broad 1- and 2-μm absorption features. Figure 1.3 shows a visible (Bus & Binzel 2002b) and NIR (Gaffey 1997) spectrum of Vesta and a reflectance spectrum of a howardite meteorite (Pieters & Hiroi 2004). These objects clearly show basaltic absorption features at 1 and 2 μm. The depth, center and shape of these features are dictated by temperature, grain size and calcium content (Hardersen et al. 2004) and are attributable to Fe^{2+} ionic transitions within

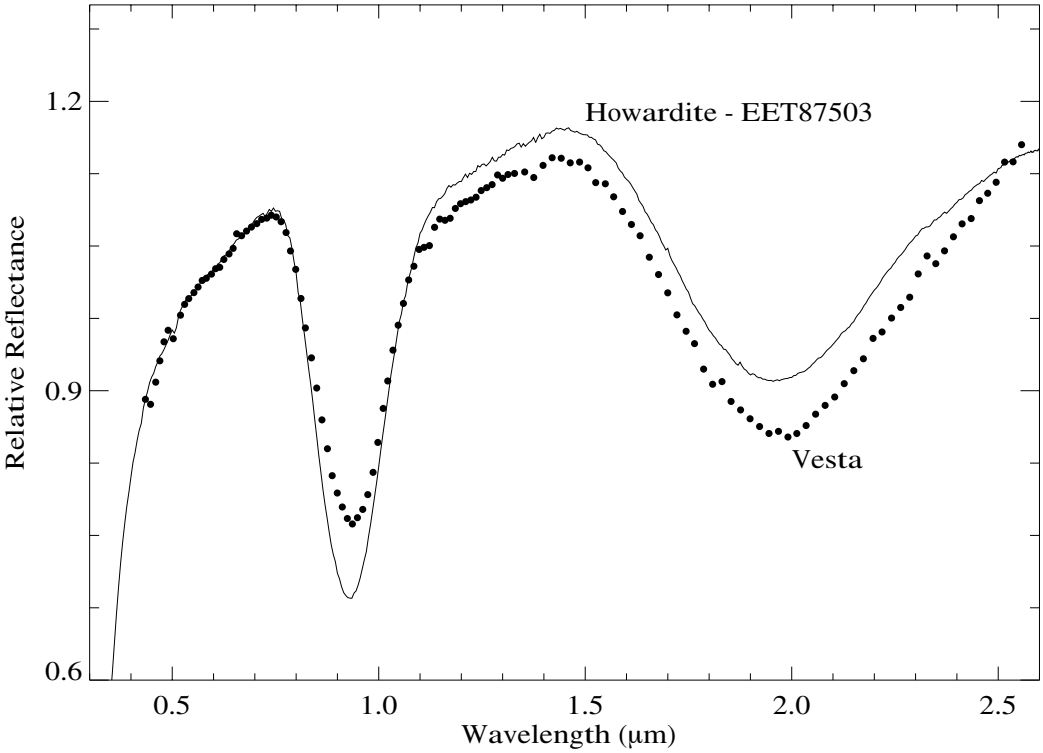

Figure 1.3 Visible to NIR spectra of basaltic material. The spectrum of Vesta (circles) combines visible (Bus & Binzel 2002b) and NIR data (Gaffey 1997). The howardite (EET87503) data were obtained at at the Brown University Reflectance Experiment Laboratory (RELAB, Pieters & Hiroi 2004) from a sample with particulate grain sizes of less than 25 μm. These objects display the characteristic 1 and 2 μm absorption bands of basaltic material. The similarity of these spectra implies that howardites originated from the surface of Vesta.

the pyroxene crystal structure of the surface basalt (Sunshine et al. 2004). Olivine and plagioclase also show Fe^{2+} absorption features around 1 μm. Asteroids with such spectral features are classified as V-types (Tholen 1984; Bus & Binzel 2002a; DeMeo et al. 2008). The similarity between the Vesta and howardite spectra is apparent and, for lack of other suitable asteroidal analogs, is a strong argument for the HED-Vesta connection (Consolmagno & Drake 1977).

Binzel & Xu (1993) showed that 20 small asteroids (sizes $\leq$ 10 km) in the dynamical proximity of Vesta also exhibited spectra with deep 1 μm absorption bands, suggesting

the presence of basaltic material on their surfaces. Over half of these 20 asteroids were objects that had previously been identified as part of the dynamically defined Vesta family (Zappala et al. 1990). Based solely on dynamical information, asteroid families had long been known to exist (Hirayama 1918), however the spectroscopic confirmation of basaltic asteroids in the Vesta family provided strong evidence for the collisional formation of asteroid families in general and specific evidence for the collisional removal of "chips off of Vesta's surface" (Binzel & Xu 1993). It is now known that these fragments (usually referred to as the Vestoids) extend from the ν_6 secular resonance at the inner edge of the Main Belt to the 3:1 mean motion resonance at 2.5 AU (Fig. 1.4). The distribution of Vestoids throughout the inner Main Belt traces a dynamical pathway from Vesta to the Earth via these major resonances, which serve as "escape hatches" from the Main Belt and can act to deliver HED meteorites to Earth (Gladman et al. 1997).

Further evidence for the formation of the Vesta family was obtained from resolved images of Vesta taken with the Hubble Space Telescope (Thomas et al. 1997). These images reveal the presence of a large (460 km in diameter) impact crater on the south pole of Vesta, which is large enough to supply all of the fragments that make up the Vesta collisional family. Binzel et al. (1997) and Gaffey (1997) argue that albedo and spectral variations across Vesta's surface are consistent with a south pole crater that excavated through its eucritic crust to a diogenetic layer, thus providing a plausible source for the HEDs. The timing of crater formation is poorly constrained, spanning nearly the full range of Solar System history from 3.5 Gya to less than 1 Gya (Marzari et al. 1996; Asphaug 1997; Bottke et al. 2005a).

The number of spectroscopically confirmed V-type asteroids has grown to nearly 100 objects (Fig. 1.4, Table A.1) as spectroscopic data sets (e.g. Xu et al. 1995; Burbine & Binzel 2002; Bus & Binzel 2002b; Lazzaro et al. 2004; Alvarez-Candal et al. 2006) have expanded to include greater numbers of asteroids. As a result the realized dynamical extent of the Vesta family has expanded over time, progressively moving

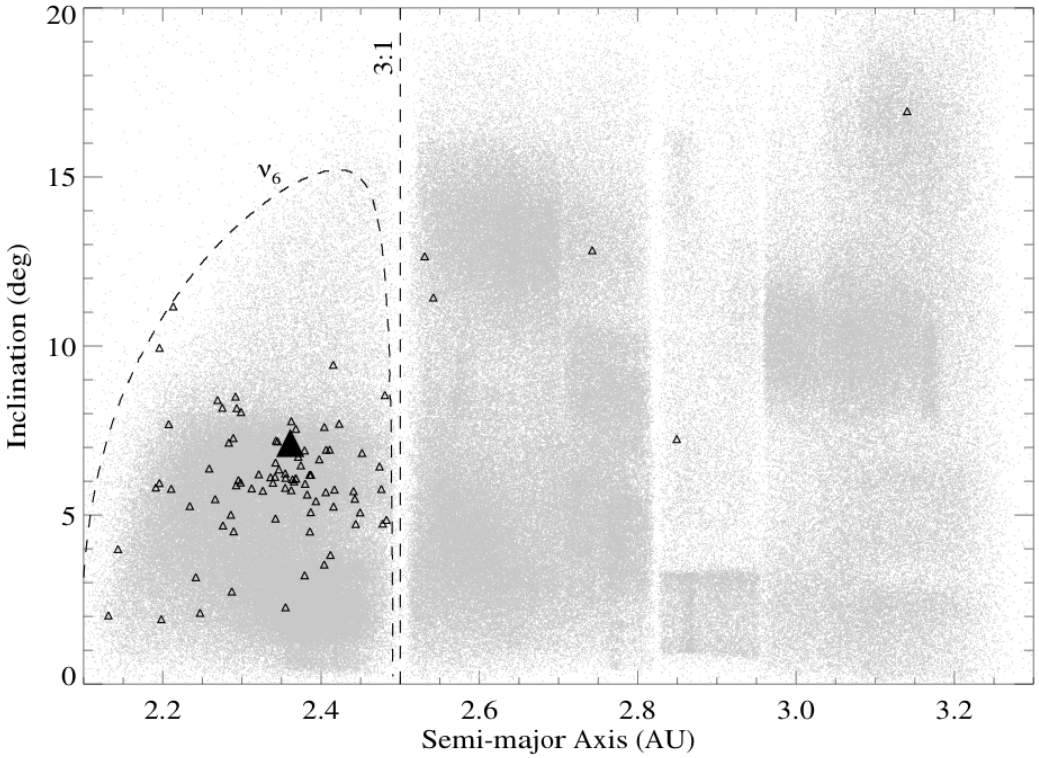

Figure 1.4 Dynamical map in osculating element space of spectroscopically confirmed V-type asteroids (open triangles), all Main Belt asteroids (gray points), and Vesta (solid triangle at 2.36 AU, 7.13°). The 3:1 mean motion resonance with Jupiter and the ν_6 secular resonance with Saturn are plotted as dashed lines. These resonances form the dynamical boundaries of the Vesta family and serve as "escape hatches" by which fragments from Vesta can be delivered to the Earth as meteorites (Gladman et al. 1997).

outwards from Vesta to incorporate newly discovered V-types. This progression has, in part, motivated theoretical investigations into the formation and evolution of asteroid families. Asphaug (1997) showed that a ~40 km impactor could remove enough of Vesta's crust to explain the observed number of Vestoids and the large south pole crater without catastrophically disrupting the parent body. Furthermore, he showed that such an impact could remove large fragments with sufficiently high ejection velocities to reproduce the currently observed collisional family. Carruba et al. (2005) showed that non-linear secular resonances and orbital migration due to the Yarkovsky effect

(drift in semi-major axis due to anisotropic thermal radiation) could explain the orbits of V-type asteroids 956 Elisa and 809 Lundia, both of which were found to lie outside of the dynamically defined Vesta family (Florczak et al. 2002). Roig et al. (2008) showed that over billions of years the Yarkovsky force could have caused the migration of 10's of small Vestoids (sizes < 3 km) across the 3:1 mean motion resonance into stable orbits in the middle Main Belt ($2.5 < a < 2.8$ AU). Finally, Nesvorný et al. (2008) showed that orbital migration due to the Yarkovsky force and resonance scattering could disperse Vestoids across most of the orbital phase space of the inner Main belt ($2.1 < a < 2.5$ AU), producing orbits well outside of the traditional boundaries of the Vesta family (Zappala et al. 1990).

1.5.4 Basaltic Crust: Non-Vestoid V-types

In the inner Main Belt ($a < 2.5$ AU) the basaltic asteroid population is dominated by fragments from Vesta's surface. The Yarkovsky effect and resonance scattering make it difficult to map the dynamical boundaries of the Vesta family (Carruba et al. 2005, 2007b; Nesvorný et al. 2008). As such, non-Vestoid basaltic asteroids have yet to be unambiguously identified in the inner Main Belt.

The dynamics and in some cases the inferred mineralogy of basaltic asteroids orbiting beyond the 3:1 mean motion resonance with Jupiter ($a > 2.5$ AU) render them unlikely to have originated from the surface of Vesta. These objects may be tracers of other differentiated parent bodies. Lazzaro et al. (2000) showed that asteroid 1459 Magnya has a visible-NIR spectrum suggestive of a basaltic surface. The current osculating orbital elements of Magnya are $a = 3.14$ AU, $e = 0.24$ and $i = 16.94°$ (Fig. 1.4). If Magnya were removed from the surface of Vesta it would have required an ejection velocity of 4.2 km/s (Zappala et al. 1996), almost an order of magnitude larger than the ejection velocities expected from the collisional formation of asteroid families (Asphaug 1997). If such ejection velocities were somehow possible then it is unlikely that Gyr-old collisional families would be observed in the Main Belt (Marzari et al.

1996, 1999). Depending on its albedo, Magnya has a size ranging from approximately 20-30 km (Delbo & 11 co-authors 2006; Tedesco et al. 2004), which is two to three times bigger than the largest members of the Vesta family (Florczak et al. 2002). For these reasons, Magnya is unlikely to have any genetic link to Vesta. This claim is supported by the mineralogical analysis of Hardersen et al. (2004) who found that the basalt on Magnya's surface is depleted in Fe-bearing pyroxene (ferrosilite) relative to Vesta.

Based on its size Magnya could be a fully differentiated body (Hevey & Sanders 2006) that has remained intact over the age of the Solar System (Bottke et al. 2005b). This contradicts the assumption that Magnya must be a collisional fragment (e.g. Lazzaro et al. 2000; Michtchenko et al. 2002). Unsuccessful searches for asteroidal fragments of crust, mantle or core in the neighborhood of Magnya (Michtchenko et al. 2002) have led these authors to conclude that Magnya is the sole remaining fragment of a collisional family that was depleted by the dynamical scattering within secular resonances.

Spectroscopic searches for basaltic asteroids in the middle and outer Main Belt have been facilitated by the identification of potentially interesting targets from the Sloan Digital Sky Survey Moving Object Catalog of photometric colors (Ivezić & 32 co-authors 2001). Following this methodology, Hammergren et al. (2006) and Binzel et al. (2007) independently discovered that 21238 (1995 WV7) is a V-type asteroid, while Roig et al. (2008) revealed the same for asteroid 40521 (1999 RL95). Both objects orbit near the outer edge of the 3:1 mean motion resonance (Fig. 1.4) and are too small to be intact differentiated bodies (their sizes are estimated at 5 and 3 km respectively). Roig et al. (2008) argue that 40521 (1999 RL95) is small enough to have migrated across the 3:1 resonance after being ejected from the surface of Vesta. This is unlikely to have been the case for 21238 (1995 WV7), thus suggesting that this object is a relic from a parent body whose other fragments have been collisionally or dynamically removed from the Main Belt.

Expansion of the Bus & Binzel (2002a) taxonomic system to infrared wavelengths resulted in the reclassification of some asteroids (DeMeo et al. 2008). Asteroid 1904 Massevitch changed from an R-type (a rare spectral type with an ambiguous mineralogical interpretation) to a V-type. Massevitch orbits in the middle Main Belt with a semi-major axis of 2.74 AU (Fig. 1.4) and has an estimated diameter of less than 20 km (Tedesco et al. 2004). It is unlikely to be a fragment from Vesta, but may be too small to be an intact differentiated body. Like asteroid 21238, Massevitch is probably a fragment from a parent body that is no longer represented by a collisional family.

Lastly, asteroid 10537 (1991 RY16) is classified in the Bus-DeMeo system (DeMeo et al. 2008) as a Vw-type (i.e. a V-type asteroid with a steep red slope). We discuss this object in greater detail in Chapter 3 and simply note at this point that 10537 has an ambiguous mineralogical interpretation, with the possibility that it is a crustal fragment from a large differentiated parent body.

1.6 Definitions

Historically, the usage of terms related to the process of differentiation, taxonomic classification, surface mineralogy and dynamical properties of asteroids has either been inconsistent or has changed over time. In the interest of clarity, we define a number of terms that will be used frequently throughout this document.

A body is termed differentiated if it segregated into a metallic core, olivine-rich mantle and a pyroxene/plagioclase-rich basaltic crust (Burbine et al. 1996). Fully differentiated bodies formed only if high degrees of silicate melting ($\gtrsim$ 50%) were achieved (Taylor 1992). Partially differentiated bodies are those which reached temperatures high enough to initiate metal-silicate differentiation (e.g. the pallasite parent body), but were either not hot enough or too small to achieve the gravitationally-segregated structure of a fully differentiated body.

V-type is a taxonomic distinction based on spectral criteria. Both visible wavelength (Tholen 1984; Bus & Binzel 2002a) and NIR wavelength (DeMeo et al. 2008) taxonomic systems exist, sometimes producing inconsistent results. When possible we will employ the most recent and complete (in terms of wavelength coverage) taxonomic system for classifying and discussing asteroid spectra. Any object with photometric colors consistent with a V-type designation is termed a V-type candidate and requires spectral data to confirm its taxonomic classification.

Basaltic asteroids are differentiated bodies or fragments of differentiated bodies with basalt on at least part of their surface. Basaltic asteroids are characterized based on interpreted mineralogy from spectroscopic data. An object with photometric colors indicative of a basaltic composition is termed a basaltic candidate. Basalt is means an olivine poor, pyroxene/plagioclase-rich melt from a differentiated parent body. The basaltic crust of such bodies (assuming Vesta-like properties) represents the upper few percent of the differentiated structure (Ruzicka et al. 1997). In this work we consider a V-type taxonomy to be directly attributable to a basaltic composition, therefore the terms V-type and basaltic are sometimes used interchangeably.

Vestoids are a dynamically-defined sub-population of V-types thought to have originated from the Vesta parent body. Both spectroscopic data and dynamical studies are required to classify an object as a Vestoid. Vestoids are typically interpreted as having a basaltic surface composition, however some asteroids with basaltic material on their surface are not Vestoids, e.g. Magnya (Lazzaro et al. 2000). An asteroid that is dynamically associated with Vesta but has not been spectroscopically observed is called a dynamical Vestoid. Approximately 80% of dynamical Vestoids are V-types (see Chapter 2).

1.7 Outstanding Questions

A number of questions emerge from the previous discussion on the asteroidal and meteoritic relics of differentiated parent bodies. We raise and initially address four main questions here with the intent of motivating subsequent chapters.

- *How many differentiated parent bodies are represented by Main Belt asteroids? Does this number agree with the meteorite record?*

  Our current understanding of the connection between differentiated asteroids and meteorites seems to suggest rough agreement between these two populations. The number of magmatic iron meteorites is in gross agreement with the number of metallic M-type asteroids (~ 100, §1.5.1). This is not to suggest that they represent the same parent bodies (the M-types are probably intact or re-accumulated cores while the irons are fragments from catastrophically disrupted bodies), but these two populations do not imply wildly different numbers of differentiated planetesimals. Furthermore, basaltic material in the Main Belt and in the meteorite collection seems to be relatively rare (excepting the Vestoids and HEDs), with only a few distinct parent bodies represented. What remains unclear is why the number of metallic cores far out weighs the apparent number of basalt-producing parent bodies (see below). On a broader level, this question has obvious relevance to understanding the extent of thermal alteration of proto-planetary bodies, an important constraint on the initial conditions of planet formation.

- *Where did differentiation occur?*

  Bottke et al. (2006) raise the interesting possibility that differentiation occurred only in the inner Solar System ($a < 2.0$ AU) where accretion times were fast enough to result in planetesimals with high initial SLR abundances. In such

a scenario all differentiated asteroids (including the M-types, Vesta, and other basaltic asteroids) formed in the inner Solar System and were later scattered into the Main Belt. These authors argue that the low probability of such a scattering event would help to explain the relative paucity of differentiated asteroids in the Main Belt. However, this scenario may be difficult to reconcile with the putative presence of multiple differentiated asteroids throughout the Main Belt (e.g. Mothé-Diniz & Carvano 2005; Nathues et al. 2005; Sunshine et al. 2004; Reed et al. 1997) as these objects seem to imply the in-situ differentiation of planetesimals.

- *Is the differentiated crust from different parent bodies mineralogically distinct? Can this be distinguished spectroscopically?*

  From the standpoint of an observer this question is important for distinguishing the number of differentiated parent bodies traced by Main Belt asteroids. Unfortunately, this question is difficult to address without physical samples from known asteroids, however some insight can be gained from meteorites. The spectroscopic similarity of all HED meteorites (including those that are not from Vesta) suggests that the answer to this question is no. Distinguishing one differentiated parent body from another may require analyses at the isotopic level (e.g. Scott et al. 2009). Future spectroscopic studies across a wide range of wavelengths (particularly in the near- and mid-IR) may provide new insights to this problem (Lim et al. 2009).

- *What explains the apparent lack of differentiated silicates (i.e. crust and mantle fragments) in the MB and in the meteorite record relative to metallic cores?*

  This is a long-standing problem that remains an open mystery (see Burbine et al. 1996). This is sometimes referred to as the "missing basalt problem" or the "great

dunite shortage" (dunite is the olivine end-member of the peridotite group and is typically associated with the mantles of differentiated bodies). The essence of this problem arises from the abundance of M-type asteroids and iron meteorites, which represent over one half ($\sim$ 100) of all meteorite parent bodies (Burbine et al. 2002). It would seem that a catastrophically disrupted differentiated body that produced these metallic fragments would have generated many more mantle (dunite) and crustal (basalt) fragments. However, these silicate remnants of differentiated bodies are conspicuously rare in our meteorite collection: the differentiated achondrites represent only 20 or so parent bodies. In addition, fragments of mantle and crust are not thought to be common amongst Main Belt asteroids (Burbine et al. 1996). This problem is further exacerbated by the fact that a number of asteroid families may represent differentiated parent bodies [e.g. Flora (Gaffey 1984), Eunomia (Reed et al. 1997; Nathues et al. 2005), Eos (Mothé-Diniz & Carvano 2005), and Thetis, Agnia and Merxia (Sunshine et al. 2004)], raising the question of why so little basaltic material from these objects remains while the Vestoids are one of the most prominent families in the Main Belt.

A number of solutions have been proposed to address how pieces of crust and mantle could be preferentially depleted relative to those from a metallic core. It is possible that the Vestoids are a relatively young family and that non-Vestoid basaltic and mantle-derived fragments have been heavily comminuted to sizes below our current observational limits (Davis et al. 1989; Burbine et al. 1996; Davis et al. 2002; Bottke et al. 2005b). A second possibility is that the alteration of asteroid surfaces by high energy photons and particles (i.e. space weathering) has erased the diagnostic spectral signatures of differentiated silicates so that this material is now masquerading in the Main Belt as S- or C-type asteroids (e.g. Wetherill & Chapman 1988). A final possibility is that pyroclastic volcanism may have ejected small blobs of molten silicates from the surfaces of young

planetesimals (Wilson & Keil 1991; Keil & Wilson 1993; Wilson & Keil 1996), leaving behind objects depleted in differentiated silicates.

The goals of this dissertation are: (1) to constrain the physical properties (e.g. sizes, number, orbital distribution) of basaltic asteroids in the Main Belt; (2) gain insight on the mineralogy of these asteroids through a comparison to basaltic achondrites here on Earth; (3) characterize the conditions in which metal-silicate differentiation occurred in the early Solar System and explore some of the physical processes that may have been involved in establishing the problem of the "missing basalt".

In Chapter 2 we present the results of a spectroscopic survey designed to target and detect asteroids whose photometric colors are similar to those of Vesta family members and thus may be considered as candidates for having a basaltic composition. From the results of this survey we compute de-biased size-frequency and orbital distributions for basaltic asteroids in the Main Belt. These results confirm that basaltic asteroids are rare and that the problem of the "missing basalt" persists. The work contained in this chapter was published in Moskovitz et al. (2008a).

In Chapter 3 we discuss the process of mineralogical characterization of basaltic asteroids based on the analysis of visible and NIR spectra. Spectral band analyses of basaltic asteroids in the inner Main Belt provides insight on the mineralogical diversity of the Vestoids and their relation to the HEDs. We also present a detailed analysis of asteroid 10537 (1991 RY16), an unusual object with an ambiguous mineralogical interpretation. This case study was published in Moskovitz et al. (2008b).

A theoretical investigation of the process of differentiation is presented in Chapter 4. The goal of this chapter is to characterize the various stages of differentiation by identifying some of the key processes involved. We show that both the formation of a metallic core and the generation of basaltic residue were fast processes that were likely to occur on planetesimals that accreted within a few Myr after CAI formation. We also investigate two phenomena that may have had a significant influence on the thermal

evolution of these planetesimals: the energetics of water-rock reactions and the migration of partial silicate melt. We finish by presenting a simple 1-D heat conduction model and the usage of that model to map out a range of parameters (namely time of accretion and size) that would lead to the differentiation of planetesimals.

Chapter 2

The Distribution of Basaltic Asteroids in the Main Belt

2.1 Introduction

The known populations of differentiated asteroids and meteorites (§1.5) suggest that basaltic material was at one time common throughout the Solar System. However, it is unclear whether there currently exists basaltic vestiges of the numerous differentiated parent bodies that once existed. To provide insight on this issue we have designed a survey to constrain the overall population and de-biased distribution of V-type basaltic asteroids in the Main Belt.

Other studies have calculated de-biased distributions of asteroid types (e.g. Gradie & Tedesco 1982; Gradie et al. 1989; Bus & Binzel 2002a), but they have been restricted to the largest and brightest asteroids and did not consider the presence of V-type asteroids beyond 2.5 AU. Our survey provides constraints on the number of basaltic asteroids up to an absolute magnitude (H) of 17.2 (absolute magnitude is a proxy for size and is defined as the magnitude of an object that is at zero phase angle, 1 AU away from the Sun and 1 AU away from the observer). This provides an increase in sensitivity of roughly 3 magnitudes compared to these previous studies and therefore probes for basaltic fragments that may represent the upper size limit to a heavily comminuted population.

Recent observational and theoretical work (Lazzaro et al. 2000; Hammergren et al. 2006; Bottke et al. 2006; Binzel et al. 2007; Nesvorný et al. 2008; Roig et al. 2008) suggests that non-Vestoid basaltic asteroids exist throughout the Main Belt, but have yet to be discovered. This survey was designed to detect such asteroids by targeting objects whose colors are similar to those of Vesta family members and thus may be considered as candidates for having a basaltic composition. Although the spectral features of basaltic material dominate in the near infrared, optical data ($0.4 - 0.95\ \mu m$) are easier to obtain for faint asteroids and can be diagnostic of such surface material. Thus, we primarily relied on optical taxonomic classification as a way of selecting and characterizing our target asteroids. The results of this survey are used to constrain the orbital and size-frequency distributions of basaltic material in the Main Belt. These distributions, in addition to an estimate for the total mass of basaltic material, suggest that Vesta was the predominant contributor to the basaltic asteroid inventory of the Main Belt, however scattered planetesimals from the inner Solar System ($a < 2.0$ AU) and other partially/fully differentiated bodies likely contributed to this inventory. We find no asteroidal evidence for a large number of previously undiscovered basaltic asteroids, which agrees with previous theories suggesting that basaltic fragments from the ~ 100 differentiated parent bodies represented in meteorite collections have been "battered to bits" (Burbine et al. 1996).

The remaining sections of this chapter are organized as follows: in §2.2 we outline the procedure of selecting target asteroids for our observational campaign. In §2.3 and §2.4 we discuss our observational procedure and data reduction techniques. In §2.5 we use our observational results to derive a size-frequency distribution of basaltic asteroids in the Main Belt. We use this result to constrain the semi-major axis distribution and the total mass of basaltic asteroids. In §2.6 we discuss and summarize these results.

2.2 Selecting Basaltic Asteroid Candidates

We selected candidate basaltic asteroids from the photometric data in the third release of the Sloan Digital Sky Survey (SDSS, York & 143 co-authors 2000) Moving Object Catalog (MOC, Ivezic et al. 2002). Our targets were chosen based upon their orbital elements and a statistically significant similarity to the *ugriz* photometric colors of the Vestoid population. The *ugriz* bands span a wavelength range from $0.35 - 0.90\ \mu m$. These five filters provide a crude spectro-photometric profile that can indicate the presence of basaltic spectral features (Fig. 2.1).

The 204,305 objects in the MOC were filtered down to ∼40,000 by removing multiple observations of single bodies, objects not matched to known asteroids in the ASTORB orbital element database (Jurić & 15 co-authors 2002; Bowell 2007), and objects with any photometric error larger than one magnitude. If this constraint on the photometric errors was more rigid, then the number of final candidates would have decreased. This would have reduced the statistical significance of our result and made it more difficult to coordinate observing runs with observable targets.

The SDSS magnitudes published in the MOC are typically denoted by *u'g'r'i'z'*. A transform (from the SDSS website, http://www.sdss.org/dr6/) is applied to these magnitudes so that solar correction in the AB system (Oke & Gunn 1983) can be performed:

$$\begin{aligned} u &= u' - 0.04 \\ g &= g' + 0.060\ (g' - r' - 0.53) \\ r &= r' + 0.035\ (r' - i' - 0.21) \\ i &= i' + 0.041\ (r' - i' - 0.21) \\ z &= z' - 0.030\ (i' - z' - 0.09) + 0.02 \end{aligned} \tag{2.1}$$

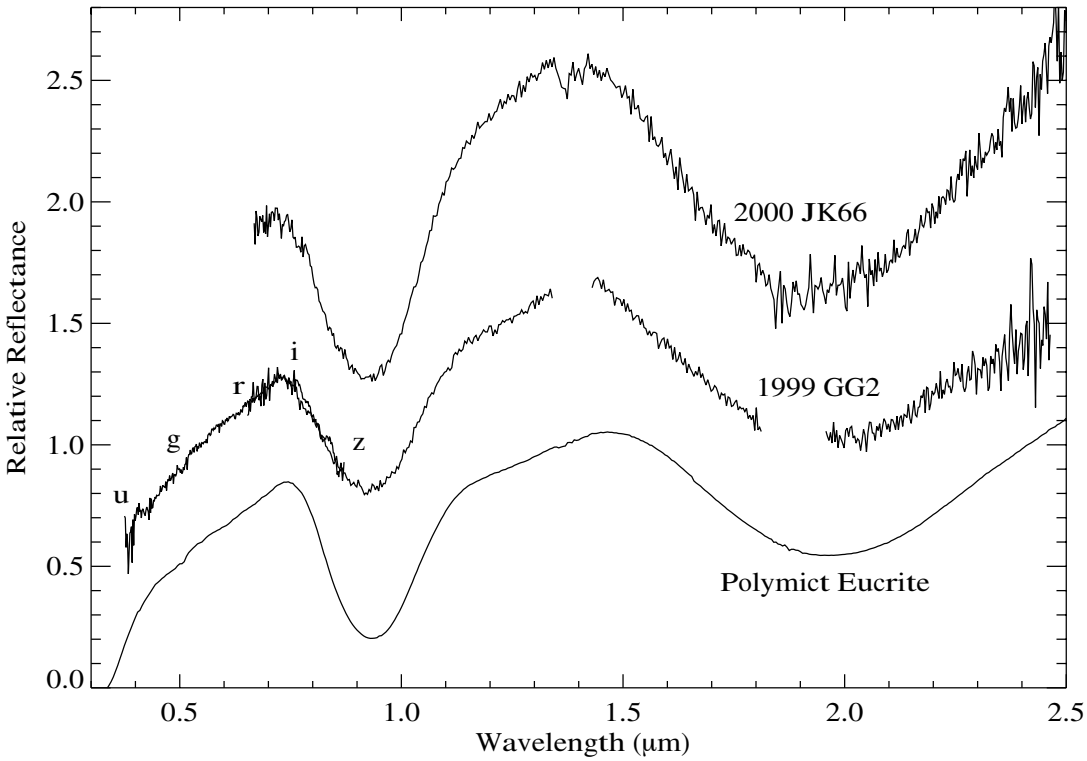

Figure 2.1 Optical (ESI on Keck II) and near-infrared (SpeX on NASA's Infrared Telescope Facility) spectra of basaltic asteroids 38070 (1999 GG2) and 33881 (2000 JK66) and a laboratory spectrum of polymict eucrite Y74450 (acquired at the NASA RELAB facility, Brown University by Takahiro Hiroi). These data clearly show the broad 1 and 2 μm absorption features that are characteristic of pyroxenes and olivine. The band centers of the SDSS *ugriz* filters are indicated on the spectrum of 38070. The spectra have been offset by increments of ± 0.5 units relative to the 1999 GG2 spectrum. Residual atmospheric absorption features around 1.4 and 2.4 μm are left in the spectrum of 2000 JK66 and are spliced from the 1992 GG2 spectrum.

Four color combinations were calculated ($u-g,\ g-r,\ r-i,\ i-z$) and solar corrected for each object in our filtered version of the MOC. The adopted solar colors were $u-g=1.43$, $g-r=0.44$, $r-i=0.11$ and $i-z=0.03$ and were subtracted from each color permutation. In addition, two principal component colors were calculated for each asteroid (Nesvorný et al. 2005):

$$PC1 \quad = \quad 0.396\,(u-g) + 0.553\,(g-r) + 0.567\,(g-i) + 0.465\,(g-z)$$

$$PC2 \quad = \quad -0.819\,(u-g) + 0.017\,(g-r) + 0.090\,(g-i) + 0.567\,(g-z) \qquad (2.2)$$

These linear combinations define a set of axes that maximize the separation between S- and C-type asteroids and are related to spectral slope and curvature respectively (Nesvorný et al. 2005).

Using a Hierarchical Clustering Method (HCM, Zappala et al. 1990) and a velocity cutoff of 70 m/s we identified 5575 dynamical Vestoids from a 2005 version of the AstDys database (http://hamilton.dm.unipi.it/cgi-bin/astdys/astibo). This cutoff does not include the 365 m/s escape velocity (Binzel & Xu 1993) from Vesta's potential well. Of these dynamical Vestoids, 1051 are included in the MOC. Certainly some fraction of these are non-V-type interlopers, however in §2.5.2 we estimate that the fraction of interlopers in the Vesta family is only $\sim 20\%$.

We fit histograms of these colors with gaussian profiles (Fig. 2.2) to define color ranges corresponding to percentile groups within the dynamical Vestoid population. These ranges were defined symmetrically relative to the fitted centroid of the profiles. For instance, the 50^{th} percentile of dynamical Vestoids in the MOC have $u-g$ colors between 0.17 and 0.35 with a most probable value of 0.26. We used the 50^{th} percentile for each of the 6 colors to statistically define the SDSS photometric properties of candidate basaltic asteroids. Table 2.1 shows the adopted range for each color. Basaltic candidates were selected as objects whose colors overlap all 6 of these ranges. Selection of targets from the 50^{th} percentile of each color range is likely to exclude non-V-type interlopers. Thus we are confident that the color ranges in Table 2.1 represent an average V-type spectral profile. This is confirmed by the success rate of our survey (§2.5).

Dynamical constraints were applied to objects that met these photometric criteria. Asteroids were excluded from the candidate list if their orbital properties overlapped the region of phase space occupied by the dynamical Vestoids. This dynamical constraint was applied to the osculating values of semi-major axis, eccentricity and

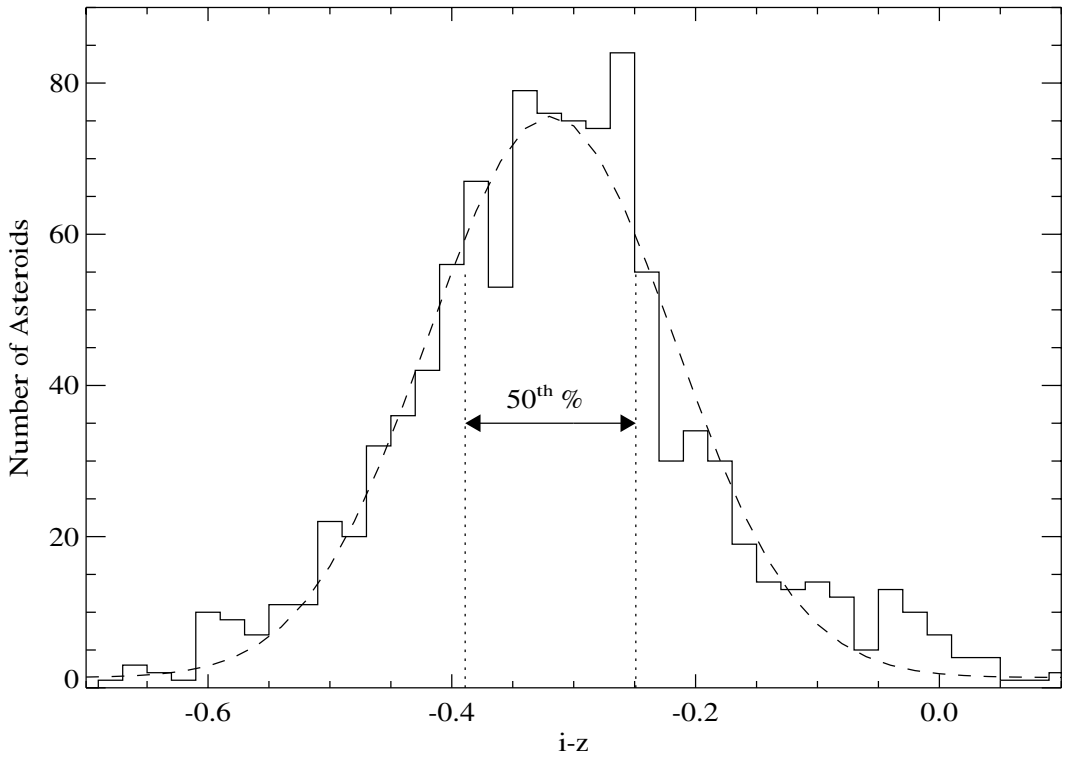

Figure 2.2 $i - z$ color histogram of the 1051 dynamical Vestoids that are included in the SDSS MOC. A gaussian fit to the distribution is shown by the dashed curve. The range of colors that correspond to the 50^{th} percentile of dynamical Vestoids (defined symmetrically relative to the center of the gaussian) is indicated.

inclination. Proper orbital elements would have been preferred but these are available for only a subset of MOC objects. The extent of phase space occupied by the 1051 dynamical Vestoids in the MOC is 2.22 - 2.48 AU in semi-major axis, 0.029 - 0.169 in eccentricities, and 4.82 - 8.26° in inclination. These photometric and dynamical constraints produced 50 targets for spectroscopic follow-up (Table 2.2, Fig. 2.4). A flow chart of the candidate selection process is shown in Figure 2.3.

Table 2.2 indicates the relative ejection velocity, Δv, required for each of the candidates to have originated from the surface of Vesta. Simplified forms of Gauss's equations can be used to express an asteroid's change of velocity in three components (tangential, radial and perpendicular to the orbital plane) relative to another body

Table 2.1 Vestoid Colors – 50^{th} Percentile

Color	Range
$u-g$	[0.170,0.350]
$g-r$	[0.201,0.281]
$r-i$	[0.061,0.121]
$i-z$	[-0.389,-0.249]
PC1	[0.360,0.520]
PC2	[-0.258,-0.078]

(Equations 4, 5 and 6 in Zappala et al. 1996). The net relative ejection velocity, Δv, is calculated by adopting these authors' simulated values for the true anomaly and argument of perihelion of the Vesta family at the time of its collisional formation (see their Fig. 12) and then adding the three components in quadrature. The 365 m/s escape velocity from Vesta (Binzel & Xu 1993) is not taken into account for these calculations. With the exception of two objects [28517 (2000 DD7) and 156914 (2003

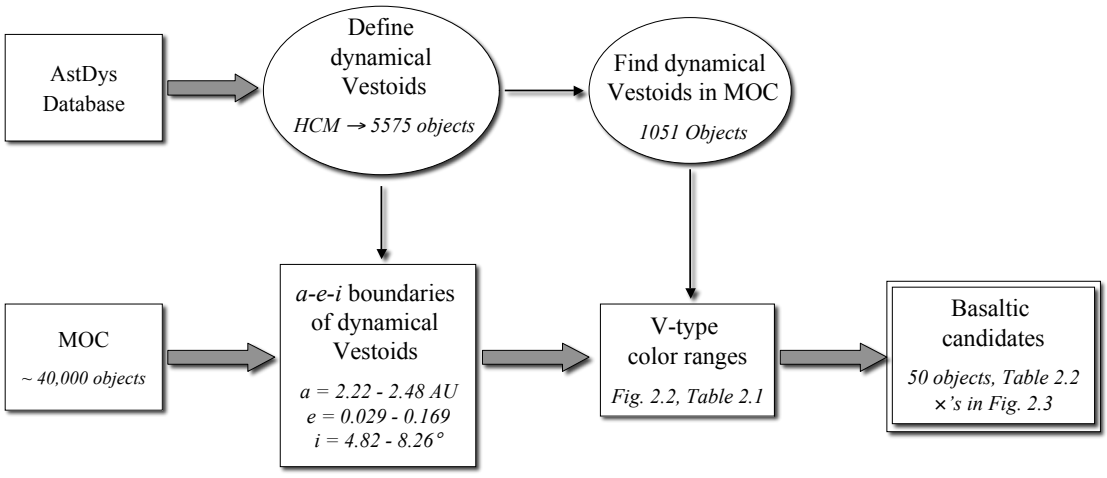

Figure 2.3 Flow chart for selecting basaltic candidates.

Table 2.2 Non-Vestoid Basaltic Candidates

Number	Designation	a (AU)	e	sin(i)	Δv (km/s)	RG06?	H06?	B07?
156914	2003 FB31	2.37	0.10	0.14	0.3			
28517	**2000 DD7**	2.29	0.09	0.14	0.4	✓	✓	✓
124343	2001 QF117	2.22	0.11	0.12	0.7		✓	
112257	2002 LC13	2.22	0.10	0.11	0.7		✓	
54668	2000 WO85	2.44	0.11	0.10	0.7		✓	
10544	1992 DA9	2.23	0.11	0.13	0.8	✓	✓	
7558	**Yurlov**	2.29	0.11	0.09	0.9		✓	
74894	1999 TB119	2.22	0.12	0.14	0.9		✓	
67416	2000 QW64	2.17	0.08	0.10	1.0		✓	
65507	4151 P-L	2.22	0.12	0.11	1.0	✓	✓	✓
60669	**2000 GE4**	2.21	0.13	0.12	1.0	✓	✓	✓
24941	**1997 JM14**	2.48	0.12	0.09	1.0		✓	
55804	1994 PD13	2.29	0.13	0.15	1.1			
2823	**van der Laan**	2.41	0.06	0.08	1.1	✓	✓	✓
56570	**2000 JA21**	2.38	0.10	0.07	1.2	✓	✓	✓
98278	2000 SE212	2.16	0.06	0.10	1.3		✓	✓
55998	1998 SQ135	2.19	0.10	0.08	1.3	✓	✓	
46690	**1997 AN23**	2.24	0.10	0.07	1.3	✓	✓	
-	2002 RS123	2.37	0.16	0.14	1.4	✓	✓	✓
6081	Cloutis	2.49	0.16	0.12	1.4	✓	✓	
110544	2001 TX96	2.68	0.06	0.17	1.6			
10537	**1991 RY16**	2.85	0.10	0.11	1.6	✓	✓	
122656	2000 RV93	2.75	0.13	0.09	1.7		✓	
44114	1998 HN21	2.18	0.02	0.10	1.7		✓	
8805	1981 UM11	2.34	0.12	0.05	1.7	✓	✓	✓
-	2002 TF149	2.77	0.02	0.10	1.9		✓	
109387	2001 QL168	2.59	0.13	0.20	2.0		✓	
86493	2000 DD17	2.14	0.09	0.05	2.0			
158606	2002 XS80	2.26	0.17	0.07	2.1			

Table 2.2 continued

Number	Designation	a (AU)	e	sin(i)	Δv (km/s)	RG06?	H06?	B07?
38070	**1999 GG2**	2.14	0.13	0.06	2.1			
-	2001 QA244	2.73	0.18	0.17	2.2			
93322	2000 SA221	2.74	0.10	0.21	2.2		✓	
84036	2002 PF50	2.33	0.15	0.04	2.2	✓	✓	
55092	2001 QO123	2.15	0.13	0.05	2.2		✓	
69634	1998 FH68	2.38	0.16	0.05	2.3		✓	
41910	2000 WS141	2.26	0.20	0.13	2.3	✓	✓	
40521	**1999 RL95**	2.53	0.05	0.22	2.3	✓	✓	
152169	2003 AV27	2.25	0.10	0.02	2.4			
107008	2000 YM112	2.35	0.18	0.05	2.4		✓	
-	2003 SG55	3.01	0.13	0.20	2.5		✓	
50802	2000 FH27	2.91	0.09	0.03	2.5		✓	
140706	2001 UV79	2.61	0.03	0.02	2.6		✓	
55550	2001 XW70	2.55	0.14	0.23	2.6		✓	
172731	2004 BY120	2.74	0.14	0.23	2.8			
129632	1998 HV36	2.53	0.24	0.12	3.0			
84021	2002 PC41	2.68	0.09	0.25	3.0		✓	
33881	**2000 JK66**	2.21	0.24	0.18	3.3	✓	✓	
86627	2000 EJ126	2.42	0.24	0.04	3.5			
-	2001 GQ5	2.20	0.26	0.15	3.6			
111515	2001 YC91	3.16	0.16	0.28	3.9		✓	

The table columns are: asteroid number and designation, semi-major axis, eccentricity, sine of inclination, ejection velocity (Δv) required to have originated from Vesta (Zappala et al. 1996) and the last three columns indicate whether the asteroid was identified as a V-type candidate by Roig & Gil-Hutton (2006, RG06), Hammergren et al. (2006, H06) or Binzel et al. (2007, B07). The candidates are sorted by their Δv values. Spectroscopic data have been obtained for candidates listed in bold-face (Table 2.3, Fig. 2.5). The orbital elements of Vesta are: $a = 2.36$ AU, $e = 0.09$ and $\sin(i) = 0.12$.

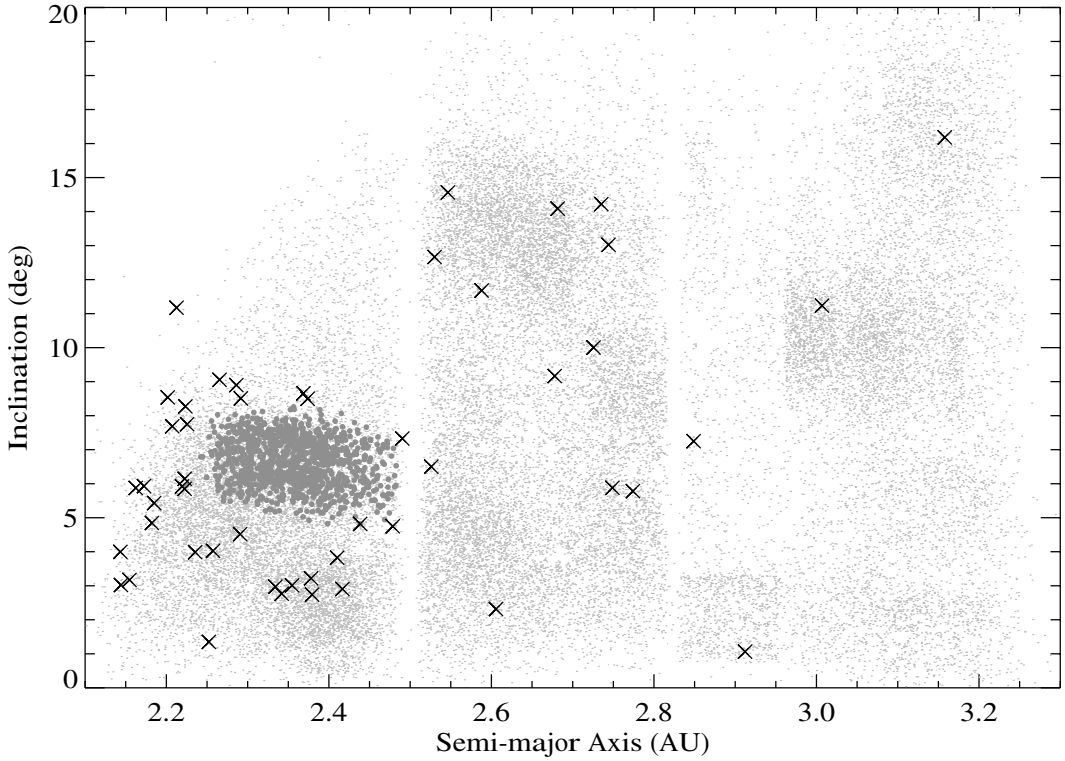

Figure 2.4 Osculating orbital elements of Vestoids (grey circles), MOC objects (small dots) and basaltic candidates ($\times$). The apparent overlap of some candidates with the Vestoids is due to projection along the unplotted eccentricity axis.

FB31)] all of the ejection velocities are greater than the ~ 0.6 km/s that is expected for multi-kilometer Vestoid fragments (Asphaug 1997).

It should be noted that calculating Δv for a pair of asteroids can be a useful metric for quantifying dynamical proximity, however dynamical effects such as Yarkovsky drift and resonance scattering can produce values of Δv for members of the same family that are much larger than the sub-km/s velocities expected from HCM family definitions (e.g. Zappala et al. 1995, 1996) and from SPH simulations of family forming impacts (e.g. Asphaug 1997; Nesvorný et al. 2006). For instance, Nesvorný et al. (2008) show that Vestoids with $\Delta v > 2$ km/s are likely and Roig et al. (2008) suggest that asteroid 40521 (1999 RL95) is a fragment from Vesta's surface even though its $\Delta v = 2.3$

km/s. Part of this problem is rooted in the HCM technique: only objects that "stand out" from the background population of asteroids can be identified as members of a collisional family. In reality the dynamical boundaries of collisional families are not so clearly defined and certainly extend into the background population and even other families.

For these reasons it is likely that our HCM-defined dynamical boundaries do not encompass the full extent of the Vestoid family, a presumption that is supported by the presence of basaltic candidates near these boundaries (Fig. 2.4). However, the inclusion of these objects as candidates does not dramatically affect our analysis or conclusions. Using a larger cutoff velocity (> 70 m/s) to expand the dynamical boundaries would connect all of the asteroids in the inner Main Belt ($a < 2.5$ AU) and would therefore neglect the possibility of selecting basaltic asteroids from other Vesta-like differentiated parent bodies. The use of a "small" cutoff velocity (i.e. one that does not encompass the entire Vestoid population) is conservative in the sense that it makes the amount of supposedly non-Vestoid basaltic asteroids larger and thus contributes to raising the upper limit for the total mass of basaltic asteroids (§2.5.2).

Other studies have employed similar color-selection techniques for identifying V-type candidates in the MOC (Roig & Gil-Hutton 2006; Hammergren et al. 2006; Binzel et al. 2007). Roig & Gil-Hutton (2006) used two principal components and $i - z$ colors to place photometric constraints on the MOC, generating over 250 non-Vestoid basaltic candidates. Sixteen of our 50 candidates are included in the Roig & Gil-Hutton (2006) list (Table 2.2). The lack of overlap is due to the different selection techniques: Roig & Gil-Hutton (2006) used only three colors to select candidates, but applied more stringent criteria on the acceptable photometric error bars. Our technique used 6 colors but applied more relaxed constraints on the photometric errors. Hammergren et al. (2006) selected V-type candidates based on $i - z$ colors which are diagnostic of the 1 μm basaltic absorption feature (Fig. 2.1), and Binzel et al. (2007) developed a system to translate the photometric measurements of MOC objects into taxonomic

classifications based on additional spectroscopic data (Bus & Binzel 2002a). The last three columns in Table 2.2 indicate whether our candidates were also identified as V-type candidates by these other groups.

It is unclear whether one of these methods is more effective at taxonomic prediction than the others. Our method and the Roig & Gil-Hutton (2006) technique produce similar results: 11 of 12 Roig & Gil-Hutton (2006) candidates and 10 out of 11 of our targets are spectroscopically confirmed V-types (this work, Roig et al. (2008); Roig & Gil-Hutton (2006); Lazzaro et al. (2004); Bus & Binzel (2002a)). The significant overlap between our candidates and those selected by Hammergren et al. (2006) suggest that these two methods are roughly equivalent. Binzel et al. (2007) and Masi et al. (2008, submitted to A&A) show that their technique is $\sim 80\%$ effective at predicting taxonomic type.

2.3 Observations

Spectra of 9 basaltic candidates have been obtained.[1] Table 2.3 contains a summary of the observational circumstances for each target asteroid. In addition, the candidates 40521 (1999 RL95) and 2823 (van der Laan) were observed as part of complementary projects performed by other groups (Binzel et al. 2001; Roig et al. 2008).

We used the Supernova Integral Field Spectrograph (SNIFS, Lantz & 14 co-authors 2004) on the University of Hawaii 2.2 meter telescope to obtain visible-wavelength spectra ($0.4 - 95\ \mu m$) of asteroids brighter than $V \sim 18.5$ magnitude. The SNIFS 6" $\times$ 6" field of view is divided into 0.4" $\times$ 0.4" spaxels (spectral pixels), which are each generated by one lens in a 225 element multi-lenslet array. The light from each spaxel is fiber-fed to a dichroic mirror that splits the light into red and blue channels. The two channels pass through separate grisms and are imaged on two 2k $\times$ 4k blue- and red-

[1] A number of asteroids that fall just outside of the 50^{th} percentile color ranges (not listed in Table 2.2) and asteroids that are part of the Roig & Gil-Hutton (2006) candidate list have also been observed. The taxonomic results of these observations can be found at www.ifa.hawaii.edu/$\sim$nmosko/Home/astobs.html

Table 2.3 Observation Summary

Object	UT Date	Inst.	Mag.	t_{exp} (s)	Analog	Type
7558 (Yurlov)	Oct. 1, 2006	ESI	16.1	1800	Avg.	V
10537 (1991 RY16)	Oct. 1, 2006	ESI	17.9	2700	Avg.	V?
	Jan. 18, 2007	SNIFS	18.3	3600	SA93-101	V?
24941 (1997 JM14)	Oct. 1, 2006	ESI	19.0	900	Avg.	V
28517 (2000 DD7)	Mar. 10, 2007	ESI	16.5	900	Avg.	V
33881 (2000 JK66)	Nov. 23, 2007	SpeX	16.6	2880	HD9562	V
38070 (1999 GG2)	Aug. 23, 2006	ESI	17.8	2700	Avg.	V
	Oct. 05, 2006	SpeX	16.9	1920	HD377	V
46690 (1997 AN23)	Mar. 10, 2007	ESI	18.7	2700	Avg.	S
56570 (2000 JA21)	Jan. 4, 2006	ESI	19.0	2700	Avg.	V
60669 (2000 GE4)	Jun. 18, 2007	SNIFS	17.8	4500	BS5534	V
2823 (van der Laan)[a]	Nov. 22, 2005	SpeX	16.4	480	SA93-101	V
40521 (1999 RL95)[b]	Apr. 30, 2006	GMOS	18.1	3000	SA107-871	V

The columns in this table are: object number and designation, UT date of observation, the instrument used, magnitude of the target from the JPL HORIZONS system, net exposure time in seconds, the solar analog that was used for calibration in the reduction process (see §2.4, Avg. indicates that the average of all solar analogs for a given night were used) and the taxonomic designation that we assigned to the spectra based upon the criteria outlined by Bus & Binzel (2002a).

[a]SMASS Database (http://smass.mit.edu/minus.html), IRTF

[b]Roig et al. (2008), Gemini South

optimized CCDs. The approximate spectral resolution ($R \equiv \lambda/\Delta\lambda$) of this instrument is 1000 at $0.43\ \mu m$ and 1300 at $0.76\ \mu m$. Bias frames, dome flats and internal arc lamp spectra are automatically obtained as part of the standard SNIFS observing routine.

The Echellette Spectrograph and Imager (ESI) on Keck II (Sheinis et al. 2002) was used to obtain optical spectra ($0.38 - 0.90\ \mu m$) of objects that were too faint to observe with SNIFS. ESI was operated in the low resolution ($R \sim 1000$) prism mode and with a wide slit of 6". We found that this width resulted in greater consistency between multiple spectra of the same asteroid. To minimize the effect of atmospheric dispersion the orientation of the slit was set close to the parallactic angle at the midpoint of the observation. Bias frames and dome flat field images were taken at the beginning and end of each night. Wavelength calibration was achieved by taking spectra of internal Hg, Cu, and Xe arc lamps at the beginning and end of each night. The dispersion for ESI was found to be very stable so that one set of arc line images could have been used to calibrate all of our data.

Near-infrared (NIR) observations were performed with SpeX (Rayner et al. 2003) on NASA's Infrared Telescope Facility (IRTF). The telescope was operated in a standard ABBA nod pattern and SpeX was configured in its low resolution (R=250) prism mode with a 0.8" slit for wavelength coverage from 0.8 - 2.5 μm. Internal flat fields and arc line spectra were obtained immediately after each target asteroid. The IDL-based SpeXtool package (Cushing et al. 2004) was used for data processing.

All targets were observed at an air mass of less than 1.3 and as near as possible to their meridian crossings. Bright field stars were used to guide the telescopes at non-sidereal rates so that the target asteroid remained centered on the slit for ESI and on the lenslet array for SNIFS. For the optical instruments we employed a maximum exposure per image of 900 seconds. For SpeX, exposure times were limited to 120 seconds. The number of exposures was selected in an attempt to obtain a consistent $S/N \sim 100$ for all asteroids.

A solar analog star was observed to calibrate each asteroid spectrum (i.e. solar correction, compensating for instrument response and removal of atmospheric absorption features, see §2.4). Analogs were observed closely in time, altitude and azimuth to the asteroid. Each one-dimensional asteroid spectrum was divided by that of an analog during the reduction process. For ESI we followed the procedure of Bus & Binzel (2002a) and divided each asteroid spectrum by the average of all analogs for a given night. The spectra of each asteroid observed with SNIFS and SpeX were calibrated using spectra of a single solar analog. Specific analogs were selected as those which minimized residual atmospheric features in the calibrated spectra of a given asteroid. We found that this prescription produced the most consistent results, which may be related to the use of brighter rather than well established solar analogs for these two instruments. The specific analog that was used for the calibration of each asteroid is given in Table 2.3.

2.4 Data Reduction

Although the reduction of asteroid spectral data varies from one instrument to the next, a number of key steps are common to all optical reductions. We outline non-standard steps here because we are not aware of an earlier comprehensive description of these processes. For further details on spectral processing of our optical data see Willman et al. (2008).

Raw two-dimensional spectral images have a number of superimposed components that must be removed to isolate one-dimensional asteroid reflectance spectra. Pixel-to-pixel variations on a CCD must be corrected by dividing data images with a normalized flat field image of a uniformly illuminated source. The normalization of this flat field must take into account the sensitivity variations on the CCD as function of position *and* as a function of wavelength. Some CCDs display optical fringing at red wavelengths (the ESI CCD shows fringing effects at the few percent level around

0.9 μm), which can be corrected by dividing the data images with a master fringe frame. The fringe pattern that affects data images is produced by parallel light rays originating at infinity, thus it can not be reproduced with dome flats. A normalized exposure of the twilight sky can be used to reproduce fringe patterns. The extraction of the 1D spectrum from the 2D image is performed by defining and subtracting an average background from the asteroid data. This effectively removes any atmospheric emission features. To correct for atmospheric absorption the 1D asteroid spectrum is divided by a solar analog spectrum. Division by the analog also removes the superimposed solar contribution in the measured reflectance.

For SNIFS, one-dimensional spectra from the red and blue channels are produced within a few minutes of data acquisition. These spectra are bias level-calibrated, flat field-corrected, cosmic ray-cleaned and have an assigned wavelength solution. We have developed a series of custom IDL scripts to perform the remainder of the data reduction. These scripts normalize the spectra at 0.55 μm, combine multiple exposures of a single object, join the red and blue channel data, divide the asteroid by a solar analog and finally re-bin the data to increase S/N. Around 0.5 μm, the sensitivity of the SNIFS red and blue channels drops, thus causing significant degradation of signal-to-noise. For cosmetic purposes the data in this region was removed.

Spectral images from ESI have a rotated dispersion axis relative to the x-axis of the CCD and significant spectral line curvature along the spatial direction. We corrected for these two effects by rotating the 2D images by 6.4° clock-wise and then straightening the curvature by applying a transform map produced from arc line images. The *identify, reidentify, fitcoords* and *transform* IRAF (Tody 1986) routines were used to perform this straightening. Once all of the spectral images were straightened the reduction proceeded following standard protocols. Dispersion solutions were determined based upon 28 different arc lines distributed throughout the wavelength range of the instrument. After dividing the asteroid spectrum by the solar analog we further divided it by a scaled model of the atmospheric absorption

features that are present beyond $0.85\ \mu m$ (Willman et al. 2008). This procedure is a fine tuning to the final asteroid spectrum and effectively minimizes residual absorption features.

Reduced optical spectra of the observed candidates are presented in Fig. 2.5. On the night of 18 June 2007, the blue channel spectrograph on SNIFS was inoperable, thus only the red channel data are presented for asteroid 60669 (2000 GE4). A spectrum of Vestoid 6093 Makoto is included in Fig. 2.5 for reference; this asteroid is not one of our basaltic candidates. Makoto was observed on 27 October, 2006 with the SNIFS instrument for a net exposure time of 2700 seconds. Only NIR observations were obtained for candidate 33881 (2000 JK66). The SpeX spectrum of this target is shown in Fig. 2.1 and clearly shows the deep 1- and 2-micron absorption bands that are indicative of a basaltic surface composition.

Asteroid 10537 (1991 RY16) was observed with both SNIFS and ESI (Fig. 2.6), facilitating comparison between spectra from the two instruments. ESI appears to have better red sensitivity, however we have not tried to fine tune the SNIFS data with an atmospheric absorption model. The slight discrepancy between these two spectra at the red-most wavelengths is likely due to imperfect correction of atmospheric features and the difference in solar analog selection. Other than these subtle differences there is very good consistency between the SNIFS and ESI data.

A number of criteria were used to discriminate a V-type asteroid from the optical data (Bus & Binzel 2002a). These included: (1) a moderate $0.4 - 0.7\ \mu m$ slope that can include a shoulder at $\sim 0.6\ \mu m$ (Vilas et al. 2000), (2) a peak reflectance of ~ 1.2 at $0.75\ \mu m$ when normalized at the canonical 0.55 μm and (3) the blue edge of the $1\ \mu m$ absorption feature reaching a depth of 0.8 or greater at 0.9 μm.

Asteroid types A, Q and R have similar spectral features to V-types (Bus & Binzel 2002a) and could become false positives in the taxonomic classification of our targets. However, errors produced by incorrectly classifying an A, Q or R-type asteroid have little bearing on our conclusions since it is likely that A- and R-types are also derived

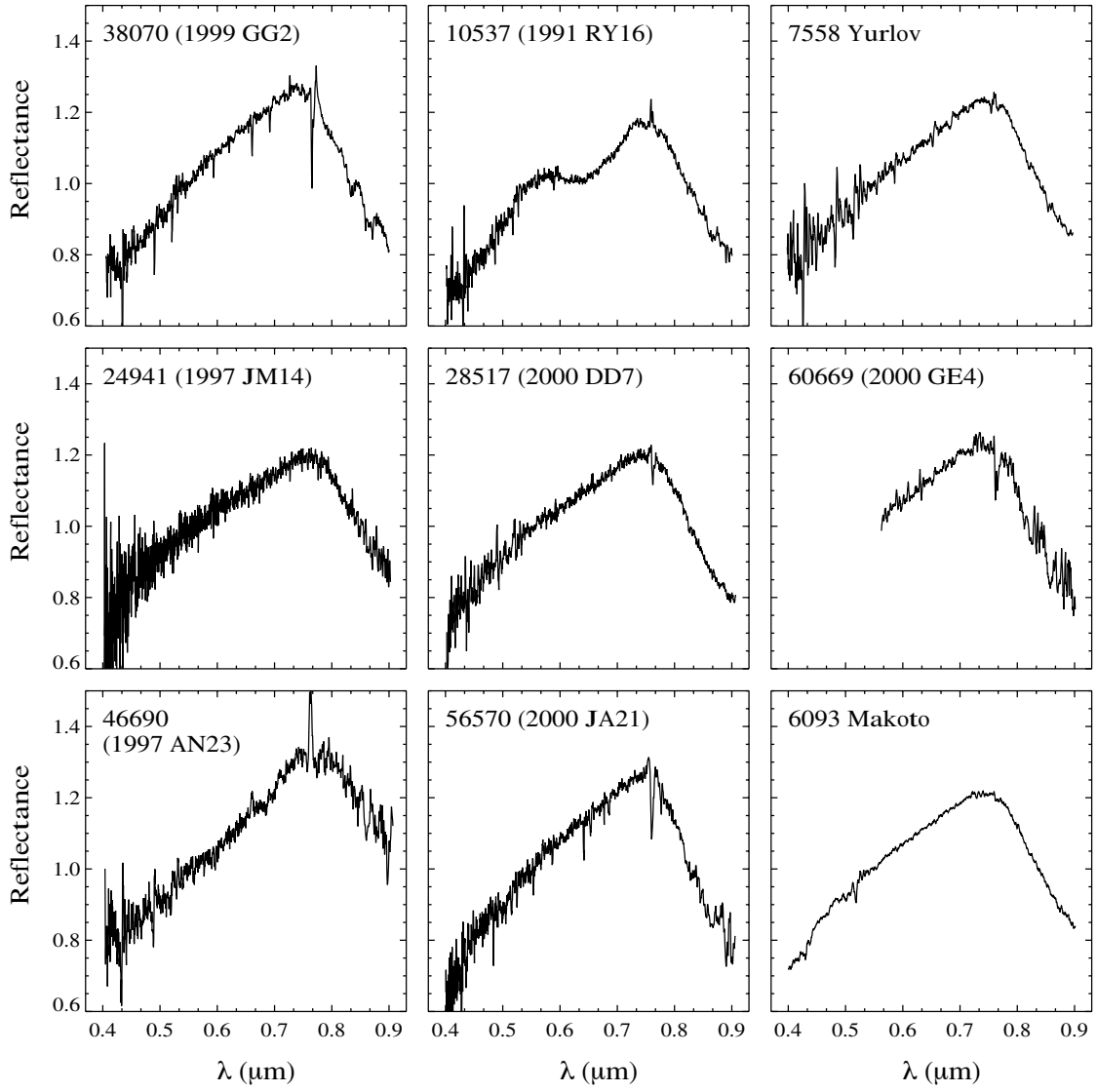

Figure 2.5 Visible wavelength spectra of basaltic asteroids. Each spectrum has been normalized at 0.55 μm. Due to instrumental problems, only the red channel data from SNIFS is shown for asteroid 60669 (2000 GE4). A spectrum of Vestoid 6093 Makoto is included for reference (obtained with SNIFS on 26 October 2006). The shallow depth of the 1 μm band in the spectrum of 1997 AN23 suggests that it is an S-type asteroid, whereas all of the others are V-types.

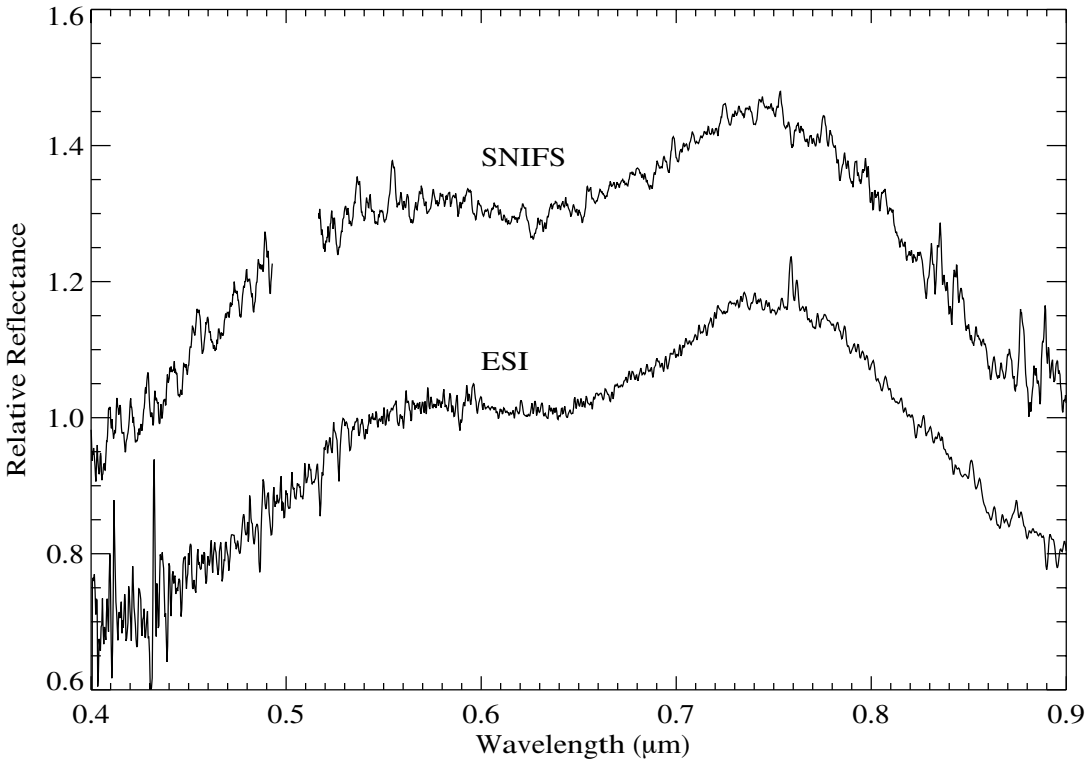

Figure 2.6 ESI and SNIFS spectra of basaltic candidate asteroid 10537 (1991 RY16). The gap in the SNIFS data corresponds to the transition region between the red and blue channels. The SNIFS data have been offset for clarity.

from differentiated parent bodies (Marchi et al. 2004; Lucey et al. 1998). Furthermore, since there are no Main Belt Q-types (they are found only amongst the NEOs) amongst the more than 2000 asteroids with assigned taxonomies it is improbable that any of our fifty Main Belt candidates are Q-type.

In some cases a taxonomic distinction can be made (Bus & Binzel 2002a). A-types tend to have steeper slopes blue-ward of $0.75\ \mu m$ and shallower $1.0\ \mu m$ absorption features. At optical wavelengths Q-types are typically distinguished from the V-class by a smaller peak reflectance (~ 1.1) and a shallower $1.0\ \mu m$ absorption feature. R-type asteroids have very similar spectral features to those of the V-class, however these asteroids are exceedingly rare. It would be unlikely that we discover one of these as

part of our observational program. A distinction between R- and V-types can be made based on a shallower $1\ \mu m$ absorption feature for R-types.

S-complex asteroids are the most common contaminant in our list of candidates. This is attributable to a few factors. By number, they are the second most abundant asteroid type in the Main Belt. In addition, the difference between S and V-class asteroids can be obscured by the relatively low signal-to-noise of the MOC measurements and the statistical method by which we have selected these targets. Fortunately S-types are easy to spectroscopically distinguish from V-types. For an S-type, the typical slope blue-ward of $0.75\ \mu m$ is less steep and the $1\ \mu m$ absorption feature is shallower (~ 0.9).

The spectral classifications of our observed basaltic candidates are listed in Table 2.3. The truncated spectrum of 60669 (2000 GE4) was sufficient to determine its taxonomic class. The spectrum of 24941 (1997 JM14) is a limiting case for a V-type asteroid, if the relative reflectance at 0.9 μm were any larger then it would be classified as an S-type. The one candidate that turned out to be an S-type was 46690 (1997 AN23). Even with the low S/N of its spectrum it is clear that the 1 μm absorption feature is not as deep as that of a typical V-type. As discussed in §2.6.1 there is some uncertainty about whether 10537 (1991 RY16) is a basaltic asteroid, but we consider the observation of this target a successful confirmation of a V-type because of the depth of its 1 μm band.

2.5 Size and Orbital Distribution of Basaltic Asteroids

Using the results and construct of our survey we develop a simple methodology to determine de-biased number distributions of basaltic asteroids that are not part of the dynamical Vestoid population. We calculate a differential size-frequency distribution, $N(H)$, where H is absolute magnitude, and a semi-major axis distribution, $N(a; H)$. We use $N(H)$ to place estimates on the mass of basaltic material represented by our

survey. These calculations are performed by correcting our candidate distributions for biases inherent to the selection process and the SDSS catalog. The underlying assumption for these calculations is that the 11 basaltic candidates that have been observed are taxonomically representative of the other 39, which in turn are representative of the underlying population of basaltic asteroids in the Main Belt.

2.5.1 Size-Frequency Distribution

We begin by equating the expected number of basaltic asteroids in our survey to the number represented by the observations:

$$N(H)\ P_s\ C(H) = (1 - F)\ n(H), \tag{2.3}$$

where $N(H)$ is the de-biased, differential number distribution as a function of absolute magnitude for basaltic asteroids outside of the dynamical Vestoid population. This is the quantity for which we want to solve. P_s is the probability that an asteroid with basaltic surface material would be selected as a candidate based on its photometric properties. $C(H)$ accounts for the completeness and efficiency of the SDSS MOC. Completeness and efficiency are two separate properties. Completeness is the fraction of all asteroids detected by a given survey whereas efficiency is the fraction of observationally accessible asteroids that were detected. The MOC is not 100% complete for any value of H because it did not have full sky coverage. However, for objects brighter than $H = 14.5$ it is 100% efficient, because it detected all of the objects that were accessible to the survey up to that limiting magnitude. F is the false-positive rate of our survey. Since ten of eleven basaltic candidates have been spectroscopically classified as V-type asteroids (Table 2.3) the false positive rate of basaltic detection, $F = 0.09$. As stated in §2.2 this value may be elevated due to uncertainties in defining the boundaries of the dynamical Vestoid population. For instance, the inner Main Belt ($a < 2.5$ AU) candidates may be characterized by one value of F that reflects

the scattering of Vestoids to large values of Δv while another value characterizes the candidates beyond 2.5 AU. Without additional observations of middle and outer belt candidates we adopt a single value of F for the entire Main Belt and therefore produce an upper limit to the basaltic material represented by the survey. The final parameter in Eq. 2.3, $n(H)$, is the differential number distribution of our 50 basaltic candidates.

P_s is calculated as the fraction of the 1051 dynamical Vestoids in the MOC that would be selected as candidates based on their photometric colors (this inherently assumes that these dynamical Vestoids are composed of basaltic material). We find that $P_s = 0.085$, a low value that is due to our stringent constraints across 6 different colors and the relatively large errors on the SDSS photometry.

$C(H)$ is derived by comparing the SDSS MOC to the ASTORB database of all known asteroids. The ratio of the differential absolute magnitude distributions of these two databases gives the product of the efficiency and completeness of the MOC relative to ASTORB. However ASTORB is not 100% complete past $H \sim 14.8$. We extrapolate the number of asteroids for $H > 14.8$ with a function of the form $\kappa 10^{\alpha H}$ where κ and α are constants (Jedicke et al. 2002). Fitting the ASTORB distribution between $H = 12.9$ and $H = 14.8$ gives the de-biased number of asteroids as a function of absolute magnitude:

$$N_{all}(H) = (5.9 \times 10^{-4}) \cdot 10^{0.5H}. \tag{2.4}$$

We limit the extrapolation of this function to a narrow range beyond $H = 14.8$. The single slope approximation will slightly overestimate the population of basaltic asteroids because the slope of the distribution is known to decrease at larger H (Jedicke et al. 2002).

Our 50 basaltic candidates span a range of absolute magnitudes from 12.9 to 17.2. We focus our calculations on the number of basaltic asteroids within this range. Figure 2.7 plots the number distributions of the MOC and ASTORB between $H = 12.9$ and 17.2. The fit to the ASTORB data (Eq. 2.4) is indicated by the dashed line. The ratio

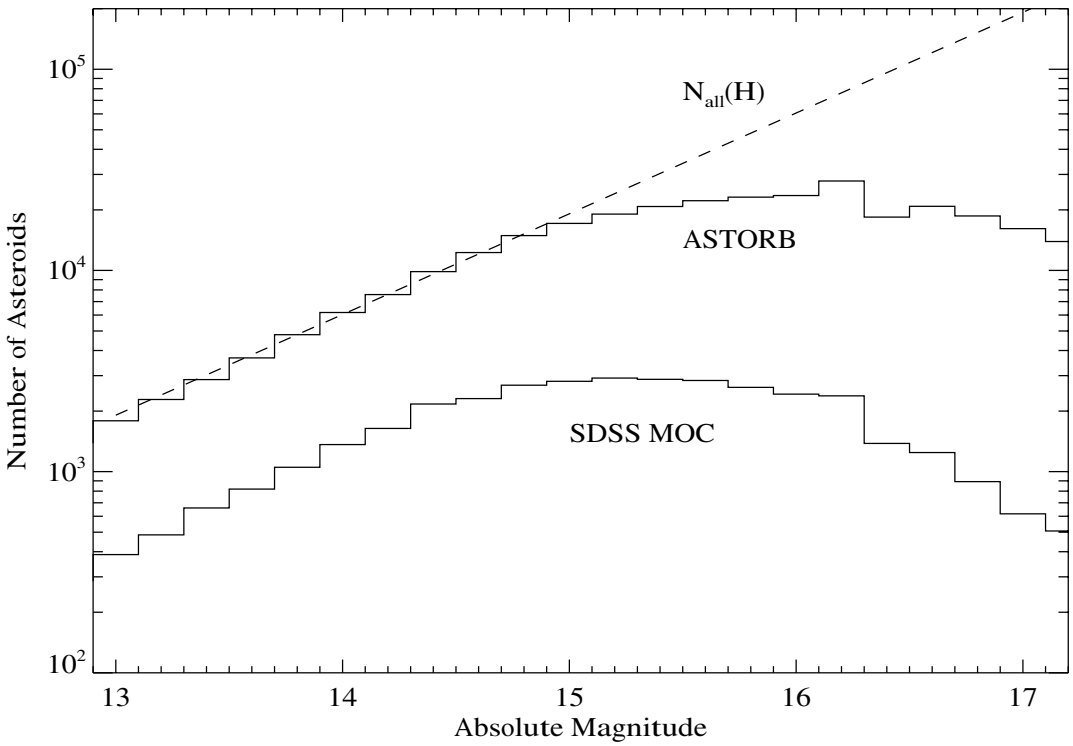

Figure 2.7 Differential size-frequency distributions for the SDSS MOC and the ASTORB database. The x-axis has been limited to the range of absolute magnitudes represented by our basaltic candidates. The extrapolation of Eq. 2.4 is indicated by the dashed line. The ratio of the SDSS MOC distribution to $N_{all}(H)$ gives the completeness and efficiency of the SDSS as a function of H.

of the MOC distribution to $N_{all}(H)$ yields $C(H)$. We find that the combined efficiency and completeness of the MOC is approximately 22% out to $H = 14.5$ and then drops off sharply to less than 1% at $H = 16.5$.

We solve Eq. 2.3 for $N(H)$ and place upper and lower 90% confidence levels on the calculated values (diamonds in Fig. 2.8). The upper limits are equal to the means of the Poisson distributions for which there is a 90% chance of observing at least $n(H)+1$ candidates within a given bin, the lower limits are equal to the means for which there is a 90% chance of observing at most $n(H) - 1$ candidates. Only upper limits can be

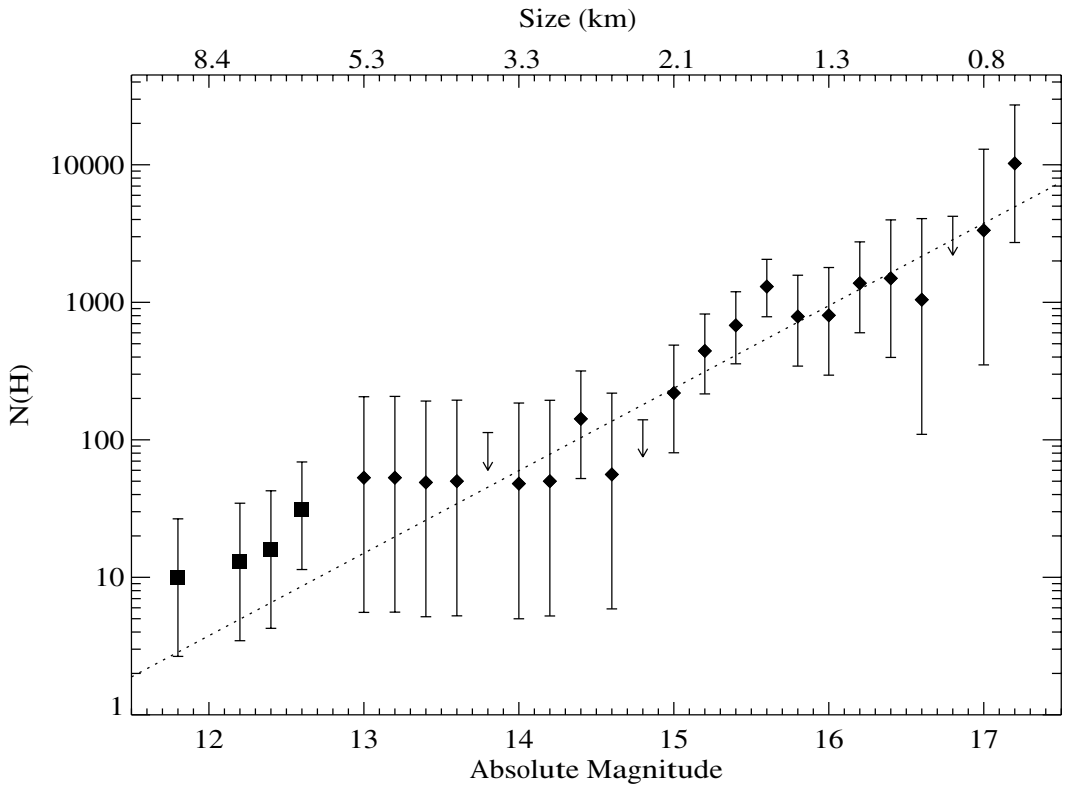

Figure 2.8 De-biased differential number distribution for basaltic asteroids in the Main Belt, excluding those within the dynamical Vestoid population. Sizes are calculated from Equation 2.5, assuming a typical albedo for V-type asteroids of 0.4. Diamonds represent the calculated points from our SDSS analysis. Squares represent the de-biased number of non-Vestoid basaltic asteroids represented by the SMASS (Bus & Binzel 2002a) and S^3OS^2 surveys (Lazzaro et al. 2004). 90% Poissonian confidence levels are plotted as upper and lower limits for each point. Certain H-bins are empty because they contained no candidates. Upper limits are indicated by arrows for these bins. This distribution is well represented by a single function of the form $\kappa 10^{\alpha H}$ (dotted line).

calculated for the H-bins with no candidates. The apparent flattening of $N(H)$ between $H = 13$ and 15 is likely a consequence of low number statistics.

A single function of the form $\kappa 10^{\alpha H}$ was fit to the $N(H)$ distribution by chi-squared minimization (Fig. 2.8). Extrapolation of this fit suggests that there are no basaltic asteroids with $H < 11$ outside of the dynamical Vestoid population; a result that is confirmed (with the exception of Magnya) by spectroscopic surveys which are close to

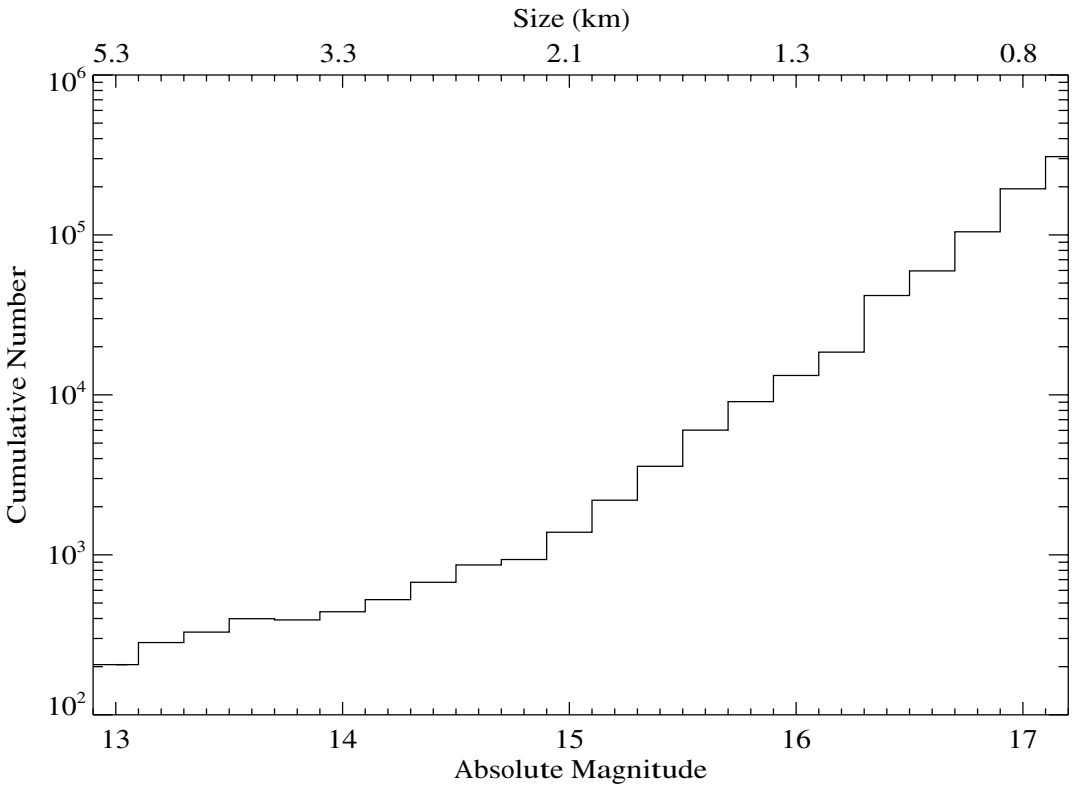

Figure 2.9 De-biased cumulative number distribution for basaltic asteroids in the Main Belt. Sizes are calculated from Equation 2.5, assuming a typical albedo for V-type asteroids of 0.4. The value for each bin represents an upper limit to the number of asteroids within the respective absolute magnitude range, thus producing a liberal approximation to the cumulative number.

100% complete at $H = 10$ and drop to a completeness of $\sim 30\%$ at $H = 11$ (e.g. Bus & Binzel 2002a; Lazzaro et al. 2004). Combining our calculated $N(H)$ distribution with the findings of these spectroscopic surveys (squares in Fig. 2.8) suggests that the overall distribution of basaltic asteroids outside of the dynamical Vestoid population is heavily weighted towards small bodies < 5 km in size ($H > 13$). The implications of this result are discussed in §2.6.

$N(H)$ is used to calculate an upper limit to the cumulative number distribution of basaltic asteroids (Fig. 2.9). To place an upper limit on the amount of basaltic material represented by our survey, we set the cumulative number of asteroids within a given

absolute magnitude range equal to the 90% Poissonian upper limit. In §2.5.3 the debiased cumulative number of basaltic asteroids is used to normalize the semi-major axis distributions.

2.5.2 Masses of Basaltic Material

We estimate an upper limit to the mass of basaltic material represented in our survey by using the $N(H)$ result. The diameter of an asteroid, D, with an assumed geometric albedo, p, is given by (Bowell et al. 1989):

$$D = \frac{1347\ km}{\sqrt{p}} 10^{-0.2H}. \tag{2.5}$$

Assuming constant density, ρ in units of kg/m^3, and a spherical body we write Eq. 2.5 in terms of mass:

$$M(H) = (1.28 \times 10^{18}\ kg) \frac{\rho}{p^{3/2}} 10^{-0.6H}. \tag{2.6}$$

Thus the total mass represented by our survey is given by:

$$M_{sur} = \int_{12.9}^{17.2} M(H)\ N(H)\ dH = (1.5 \times 10^{22}\ kg) \int_{12.9}^{17.2} N(H)\ 10^{-0.6H}\ dH, \tag{2.7}$$

where the integral is taken over the range of H represented by our candidates, ρ is set to 3000 kg/m^3 (slightly less than the bulk density of Vesta which presumably includes a metallic core, Viateau & Rapaport 2001; Baer & Chesley 2008), and p is assumed to be 0.4, a value that is approximately Vesta's albedo (Tedesco et al. 2004). We solve this integral by integrating over the $N(H)$ upper limits and obtain $M_{sur} = 5.9 \times 10^{16}$ kg. The use of the $N(H)$ upper limits produces a liberal approximation to the total mass represented by our survey. We emphasize that this mass represents the amount of basaltic material within a limited range of absolute magnitude. Based on the results of spectroscopic surveys (e.g. Bus & Binzel 2002a; Lazzaro et al. 2004) we expect there to be few undiscovered basaltic asteroids with $H < 12.9$, thus the lower H-limit to our

calculation is not expected to significantly impact the mass result. Beyond the upper H-limit there may be enough basaltic material to increase M_{sur} by a factor of a few depending on the number distribution at large H.

To place M_{sur} in perspective, we place an upper limit on the mass of basaltic material represented by the dynamical Vestoids (M_{Vest}) and conservatively estimate the mass of basaltic material excavated from the surface of Vesta based on the size of its largest crater (M_{ex}). As we show in §2.6 this upper limit to the total mass of basaltic material in the Main Belt (M_{sur} + M_{Vest}) is still much less than that expected from the volume of Vesta's largest crater (M_{ex}). Figure 2.10 depicts the regions in orbital element space that are used to calculate M_{sur} (light grey region) and M_{Vest} (dark grey region).

We calculate the net mass of basaltic material in our list of 5575 dynamical Vestoids (M_{Vest}) by de-biasing this population and removing non-V-type interlopers. Table 2.4 lists interlopers in the Vestoid dynamical space that are spectroscopically confirmed to be non-V-type and have $H < 13$. Objects fainter than this typically do not have an assigned taxonomy, thus we assume that the fraction of interlopers for $H > 13$ is $\sim 20\%$, the same as the percentage of interlopers for $H < 13$. The absolute magnitude distribution for dynamical Vestoids with non-V-type interlopers removed is shown in Fig. 2.11.

Our list of dynamical Vestoids is derived from the AstDys database which is complete to an absolute magnitude of $H = 14.8$. We extrapolate the number of basaltic dynamical Vestoids for $H > 14.8$ using the same methodology as in §2.5.1. The fit to the dynamical Vestoid distribution from $13.4 < H < 14.8$ is shown as the dashed line in Fig. 2.11. The total basaltic mass in the dynamical Vestoid population, M_{Vest}, is calculated with Eq. 2.7 by replacing $N(H)$ with the differential number distribution of dynamical Vestoids, $N_V(H)$, which is a combination of the interloper-corrected number of objects for $N_V(H < 14.8)$ and the fitted number of objects for $N_V(H > 14.8)$. The limits of

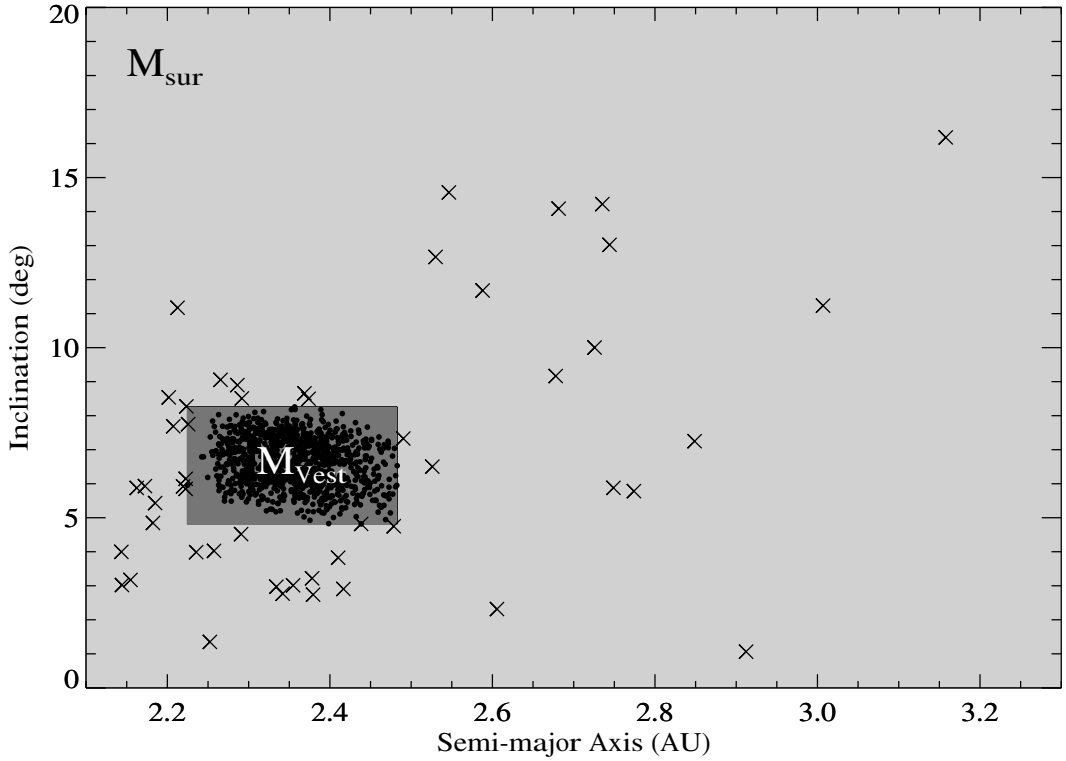

Figure 2.10 Dynamical regions corresponding to the calculated masses M_{sur} (light grey) and M_{Vest} (dark grey). The $\times$'s are the 50 basaltic candidates, the filled circles are the dynamical Vestoids. M_{sur} is the debiased mass of V-type asteroids outside of the dynamical Vestoid population and is calculated based on the results of our survey. M_{Vest} is the debiased mass of V-type asteroids within the dynamical Vestoid population taking into account the fraction of non-V-type interlopers.

integration are changed to 11.9 and 18.0 so that all known dynamical Vestoids are included. The result is $M_{Vest} = 4.8 \times 10^{16}$ kg.

A few issues may have slightly affected the calculation of M_{Vest}. First, a single-slope fit to the dynamical Vestoid distribution (dashed line in Fig. 2.11) likely produced an overestimate because de-biased absolute magnitude distributions are expected to turnover at large H (Jedicke et al. 2002). Second, the use of a more recent version of the AstDys database would produce a dynamical Vestoid family with more members (Nesvorný et al. 2008; Roig et al. 2008) and thus could slightly

Table 2.4 Interlopers in Vestoid Dynamical Space

Object	H	Type	Reference
63 (Ausonia)	7.25	S	(a)
556 (Phyllis)	9.23	S	(a)
1145 (Robelmonte)	11.05	TDS	(b)
2098 (Zyskin)	11.92	TX	(b)
2086 (Newell)	11.99	Xc	(a)
2346 (Lilio)	12.04	C	(a)
3376 (Armandhammer)	12.33	Sq	(a)
3865 (1988 AY4)	12.42	Xc	(a)
4510 (Shawna)	12.69	S	(b)
2024 (McLaughlin)	12.73	S	(b)
1781 (van Biesbroeck)	12.75	XS	(b)
5111 (Jacliff)	12.78	R	(a)
4845 (Tsubetsu)	12.81	X	(a)
1697 (Koskenniemi)	12.93	TX	(b)
5600 (1991 UY)	12.94	S	(c)

(a) Bus & Binzel (2002a)

(b) Xu et al. (1995), uncertain classifications are listed in order of taxonomic likelihood

(c) Lazzaro et al. (2004)

increase the completeness limit of this population. However, the additional dynamical Vestoids in an updated database would have $H > 14.8$ and therefore it is unlikely that they would greatly influence the mass estimate which is based on a reasonable extrapolation for the number of objects at values of $H > 14.8$. Lastly, M_{Vest} may be slightly overestimated due to unidentified interlopers in the dynamical Vestoid orbital space. All of these issues are expected to produce minor effects and as a whole are expected to increase the upper limit on M_{Vest}.

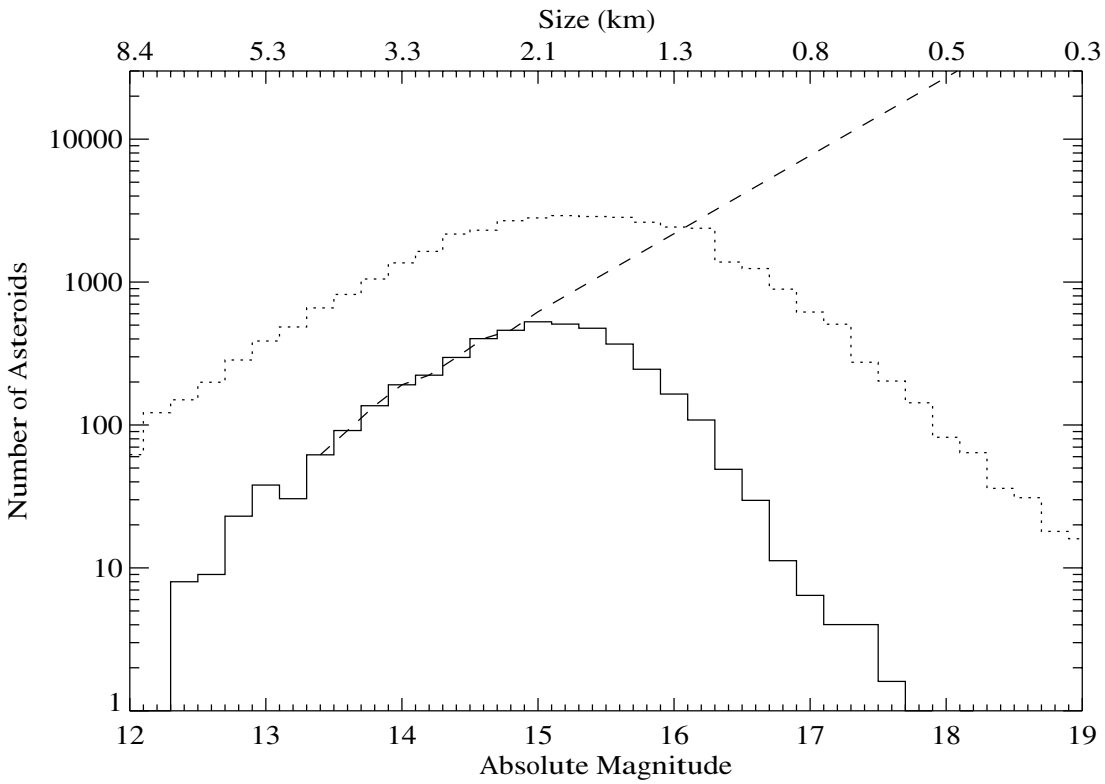

Figure 2.11 Number distribution of dynamically defined Vestoids (solid). Sizes are calculated from Equation 2.5, assuming a typical albedo for V-type asteroids of 0.4. The fit to the distribution for $13.4 < H < 14.8$ is indicated by the dashed line. The dotted curve is the SDSS MOC distribution of all asteroids within the catalog. Note the increased deficiency of small bodies ($H > 16$) in the Vestoid family relative to the MOC.

The volume of Vesta's largest crater is estimated to be 10^6 km^3 (Thomas et al. 1997) and Vesta's mean density is 3.3 g/cm^3 (Viateau & Rapaport 2001). This volume of material was excavated anywhere from 1 - 3.5 Gyr ago (Bottke et al. 2005a; Marzari et al. 1996) and since then has been depleted by collisional grinding and the scattering of fragments out of the asteroid belt. Such depletion involves a complicated interplay of processes whose efficacy is dependent on the size distribution of ejected fragments. Detailed collisional and dynamical models are necessary to address this process. Nesvorný et al. (2008) show that $\sim 10\%$ of Vestoids would dynamically escape the

asteroid belt over a time scale of 2 Gyr. Based on the results of Bottke et al. (2005b) we estimate that 50% is a reasonable estimate for the collisional depletion of the observable Vestoid family (sizes > 1 km) over a lifetime of 3.5 Gyr. Thus we expect the combined collisional and dynamical depletion of the excavated crater material to be approximately 60%. Accounting for this depletion, we calculate the remaining mass of excavated basaltic material, $M_{ex} = 1.3 \times 10^{18}$ kg.

It is unlikely that a significant fraction of M_{ex} is non-basaltic. The excavation depth, based on the size of Vesta's largest crater, was approximately 13 km (Thomas et al. 1997), which is less than or comparable to calculations for the thickness of Vesta's basaltic crust (Keil 2002) and is comparable to the size of the largest basaltic Vestoids, 1929 Kollaa (Kelley et al. 2003) and 2045 Peking (Bus & Binzel 2002a). We postpone further discussion of these calculated masses, M_{sur}, M_{ex} and M_{Vest}, until §2.6.

2.5.3 Semi-major Axis Distribution

To calculate the semi-major axis distribution of basaltic asteroids we apply the same methodology as that used to derive the absolute magnitude distribution, i.e. we simply rewrite Eq. 2.3 in terms of the independent variable a, the semi-major axis, and H:

$$N(a; H) = A(H) \, \frac{(1 - F) \, n(a)}{P_s \, C(a, H)}, \tag{2.8}$$

where $A(H)$ is a normalization factor determined from the $N(H)$ cumulative number distribution. $A(H)$ is set so that the integrated number of basaltic asteroids across all semi-major axes is in agreement with the absolute magnitude result. The upper limits to the cummulative number distribution plotted in Figure 2.9 are not used for this normalization, rather the cumulative number obtained by integrating over the calculated $N(H)$ values (diamonds in Figure 2.8) is used.

The completeness and efficiency of the MOC as a function of semi-major axis, $C(a, H)$, is also dependent on absolute magnitude. For all of the basaltic asteroids

represented by our survey:

$$C(a;\ H < 17.2) = \frac{n_{SDSS}(a;\ H < 17.2)}{N_{AST}(a;\ H < 17.2)}, \tag{2.9}$$

where n_{SDSS} is the observed semi-major axis distribution of asteroids in the SDSS MOC with H less than the specified limit and N_{AST} is the de-biased semi-major axis distribution from the ASTORB catalog. However, the latter is only complete for $H < 14.8$. We calculate $N_{AST}(a;\ H < 17.2)$ by assuming it is a scaled version of the $N_{AST}(a;\ H < 14.8)$ distribution. The scaling is performed so that the integrated number of asteroids represented by $N_{AST}(a;\ H < 17.2)$ is equal to the cumulative number predicted by $N_{all}(H)$ up to $H = 17.2$. An identical procedure is followed to calculate $C(a, H)$ for other absolute magnitude limits.

Figure 2.12 shows the de-biased semi-major axis distributions, $N(a; H)$, for three different absolute magnitude limits. 90% Poissonian confidence levels are plotted as the upper and lower limits. Some of the semi-major axis bins have zero-value due to the scarcity of candidates with $H < 15.0$ and $a > 2.5$ AU. The apparent overlap of these non-Vestoid basaltic asteroids with the region occupied by the dynamical Vestoids is a consequence of projection in inclination and eccentricity spaces.

2.6 Implications and Comparison to Other Work

We have identified 50 candidate basaltic asteroids from the SDSS MOC based on photometric and dynamical constraints. Based on observations of these basaltic candidates we have constrained the amount of basaltic material that is present outside of a region occupied by the dynamical Vestoids (defined by a-e-i orbital elements, §2.2). We have determined the de-biased distribution of this basaltic material in absolute magnitude and semi-major axis.

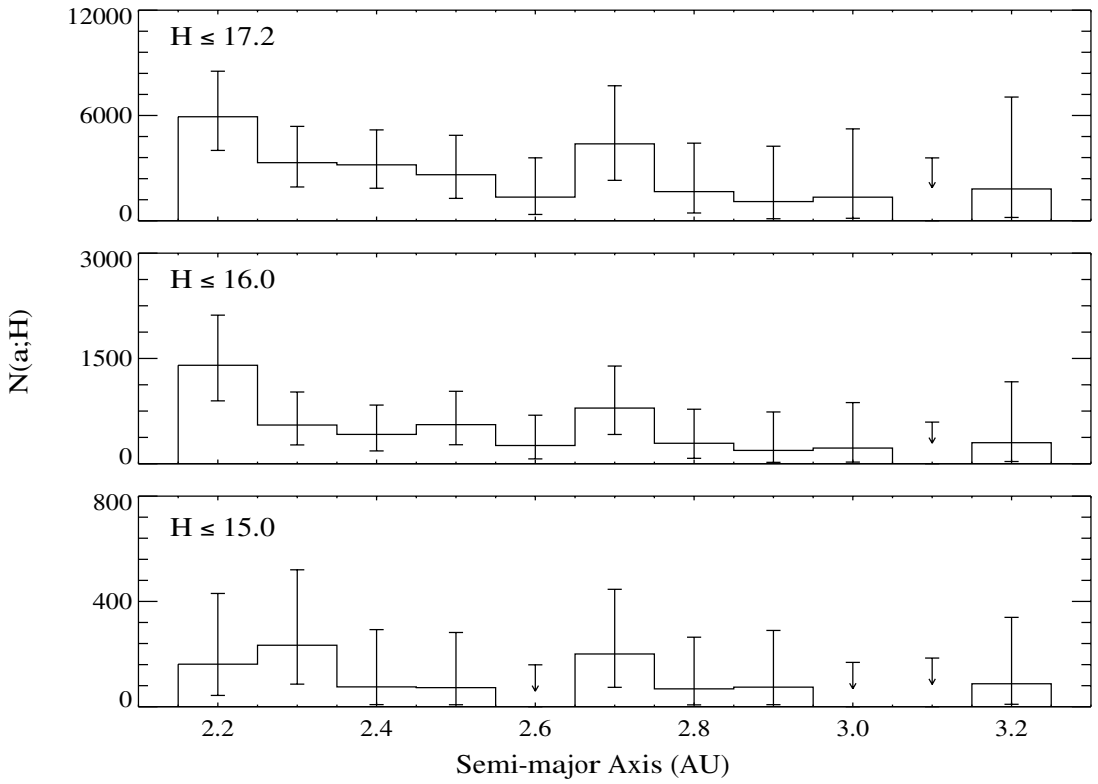

Figure 2.12 Number of basaltic asteroids as a function of semi-major axis and absolute magnitude. The integrated number of objects has been scaled to equal those represented by Fig. 2.8. Three different absolute magnitude regimes are shown. The upper and lower limits are calculated from 90% Poisson confidence levels. For bins without any candidates $N(a;H)$ becomes zero. Upper limits are indicated with arrows for these bins. Assuming a typical Vestian albedo of 0.4, the three absolute magnitude limits correspond to sizes of 0.76 km, 1.3 km and 2.0 km (from top to bottom). Dynamical simulations (Roig et al. 2008; Nesvorný et al. 2008) predict that Vestoids larger than 3 km are unlikely to cross the 3:1 resonance at 2.5 AU.

2.6.1 Basaltic Asteroids with $a > 2.5$ AU

The prospect of multiple basaltic asteroids with semi-major axes greater than 2.5 AU is particularly compelling due to the unlikelihood of numerous such objects originating from the surface of Vesta and then crossing the 3:1 mean motion resonance (Nesvorný et al. 2008; Roig et al. 2008).

Our selection process identified 12 basaltic candidates between the 3:1 and 5:2 mean motion resonances at 2.5 and 2.8 AU respectively. Six of these surround the Eunomia family (Fig. 2.4) which is one of the largest families in the Main Belt (Zappala et al. 1995) and may have derived from a partially or fully differentiated parent body. This claim is supported by a compositional gradient across the surface of Eunomia (Reed et al. 1997; Nathues et al. 2005) and a spread of surface compositions amongst members of the Eunomia family (Lazzaro & 11 co-authors 1999), both of which are consistent with a differentiated mineralogy (Gaffey et al. 2002). Presumably the basaltic crust of the Eunomia parent body was removed in the large family forming collision and/or by subsequent collisions. Asteroid 21238 (not one of our candidates) is a spectroscopically confirmed V-type that may represent some of this lost basaltic crust (Hammergren et al. 2006; Binzel et al. 2007; Carruba et al. 2007a). One of the six candidates in the vicinity of Eunomia, asteroid 40521, is a spectroscopically confirmed V-type, however there is some uncertainty about whether this object originated from the Vesta or Eunomia parent bodies (Carruba et al. 2007a; Roig et al. 2008). As compelling as these connections may be, the six candidates near Eunomia are not part of its dynamical family (D. Nesvorny, private communication, 2008). If these fragments are from Eunomia, then it seems unlikely that all six would have migrated to orbits well outside of the HCM-defined family. Therefore we suggest that these objects are not all related to Eunomia and may include fragments from Vesta that successfully jumped the 3:1 resonance without being ejected from the Main Belt.

We have identified only 4 basaltic candidates with semi-major axes greater than 2.8 AU (Fig. 2.4, Table 2.2). One of these, asteroid 10537 (1991 RY16), may be classified as a V-type because of its deep 1 μm absorption feature which is typical of this class and indicative of a pyroxene-rich and/or olivine-rich mineralogy. However it also has an unusually deep absorption feature centered at 0.63 μm that is uncommon to V-types (Fig. 2.6). These visible wavelength data have been confirmed by other observations [Duffard & Roig (2008), submitted to Planetary and Space Science]. Follow-up infrared

observations provide additional insight on the surface composition of this unusual object (Ch. 3). Another outer belt candidate is unnumbered asteroid 2003 SG55. It is possible that this object originated from the differentiated Eos parent body (Mothé-Diniz & Carvano 2005). The presence of multiple secular resonances that pass through the region surrounding 2003 SG55 (Milani & Knezevic 1990, 1992) may have provided a pathway for its orbital migration even though HCM analysis (Zappala et al. 1990) shows that it is outside of the Eos dynamical family. Future study of these outer belt basaltic candidates will have important implications for understanding the dynamical and thermal histories of these specific families.

2.6.2 Basaltic Asteroids with $a < 2.5$ AU

Defining the dynamical boundaries of the Vestoids is difficult due to effects such as Yarkovsky drift and resonance scattering (Carruba et al. 2005, 2007a). Nevertheless we have attempted to identify non-Vestoid basaltic candidates inside of 2.5 AU because neglecting to do so could exclude basaltic asteroids of non-Vestian origin. The relatively uniform distribution of basaltic candidates in this region suggests two possibilities: (1) there exists non-Vestoid basaltic asteroids in the inner belt that represent a unique differentiated parent body, or (2) Vestian fragments actually populate the full dynamical extent of the inner Main Belt. The first possibility is testable by performing mineralogical analyses (e.g. Lawrence & Lucey 2007; Gaffey et al. 1993b) on NIR spectra of basaltic candidates with large values of Δv, for example 38070 (1999 GG2) with $\Delta v = 2.1$ km/s and 33881 (2000 JK66) with $\Delta v = 3.3$ km/s. If these inner belt basaltic candidates do represent a unique differentiated parent body then they may be compositionally distinguishable from Vesta and the Vestoids (as is the case for 1459 Magnya, Hardersen et al. 2004). The second possibility can be investigated with numerical simulations. Nesvorný et al. (2008) show that the dynamical diffusion of Vestian material does in fact populate the semi-major axis extent of the inner Main Belt, but does not extend below orbital inclinations of 4°

(the proper inclination of Vesta is 6.3°). In the future, the most effective test for inner belt, non-Vestoid basaltic asteroids will be a combination of dynamical studies and mineralogical analyses.

2.6.3 Total Basaltic Asteroid Inventory

We find that the calculated size-frequency distribution of basaltic asteroids outside of the dynamical Vestoid population is heavily weighted towards small bodies. We have also shown that the mass of basaltic material outside of the dynamical Vestoid population is $M_{sur} < 5.9 \times 10^{16}$ kg. This value is comparable to the mass of basaltic material inside of the dynamical Vestoid population. Due to uncertainties in the definition of dynamical families we do not attempt to make a statement about the fraction of M_{sur} that is truly non-Vestoid in origin. We have attempted to place upper limits on M_{sur} and M_{Vest} and a conservative estimate on M_{ex}. Even so we note that $M_{sur} + M_{Vest} < M_{ex}$ by over an order of magnitude.

The size-frequency distribution ($N(H)$) and smaller total mass relative to M_{ex}, both inclusive and exclusive to the Vestoid dynamical family, are consistent with most (but not all!) basaltic asteroids deriving from the Vesta parent body. Vesta has several large craters on its surface (Thomas et al. 1997) whose collisional formation would have produced fragments of varying size. Due to ejection velocities, the Yarkovsky effect, resonance interactions and close encounters, these fragments diffused away from the Vesta parent body in orbital element space (Bottke et al. 2001; Carruba et al. 2005; Nesvorný et al. 2008). The smallest fragments experienced the fastest dynamical evolution while larger objects would take longer to separate from Vesta due to the decreased significance of the Yarkovsky force for bodies larger than 10 km (Bottke et al. 2000). Over time, small Vestoids migrated to the edge of the family at the ν_6 and 3:1 resonances. Although many of the fragments that reached these resonances were scattered into planet crossing orbits or into the Sun, some crossed over into stable orbits (Gladman et al. 1997; Roig et al. 2008; Nesvorný et al. 2008). Thus, the size-

frequency distribution of Vestoids shows a depletion of small bodies ($H > 16$) relative to the SDSS MOC distribution. This is apparent in Fig. 2.11 where the slope of the Vestoid distribution (solid curve) for $H > 16$ is steeper than that of the MOC (dotted curve). This also holds true when compared to just the subset of MOC objects that are confined to the semi-major axis range of the Vestoids ($2.2 < a < 2.5$ AU).

The abundance of small bodies (sizes < 2 km) amongst the basaltic asteroids outside of the dynamical Vestoid population (Fig. 2.11) may represent the hiding place of these "missing Vestoids". If this is true then it suggests that the shallow slope of absolute magnitude distributions at large values of H for HCM-defined collisional families (Morbidelli et al. 2003) may be attributed to the preferential loss of small bodies out of families by a process of size-dependent migration to resonances (e.g. due to the Yarkovsky effect) and subsequent scattering by those resonances.

The semi-major axis distribution indicates that the full inventory of basaltic material in the Main Belt is not consistent with an origin exclusively coupled to the formation of the large Vestian crater. With an age of 1-3.5 Gyr (Bottke et al. 2005a; Marzari et al. 1996), the primary Vesta crater was formed after the completion of planet formation. Thus, the asteroidal fragments generated in this impact evolved in a dynamical environment similar to the present day architecture of secular and mean motion resonances. In such an environment it is relatively easy for asteroids to migrate in semi-major axis because of the Yarkovsky effect, however it is more difficult to produce significant changes in inclination and eccentricity. This motivates the search for basaltic asteroids at very different i and e values than Vesta.

Our results suggest that basaltic asteroids with sizes in excess of 2 km do exist at low inclinations and beyond 2.5 AU (Fig. 2.12). Roig et al. (2008) show that it is not possible to dynamically transport many hundreds of Vestoids with diameters greater than 2 km beyond the 3:1 resonance. This is further confirmed by Nesvorný et al. (2008) whose dynamical simulations do not produce any 3 km size bodies beyond this resonance or any Vestoids with low inclination orbits ($i < 4^\circ$).

We cite three explanations for the presence of basaltic material in regions of phase space that are dynamically inaccessible to the Vestoids. One possibility is that these basaltic asteroids originated from the surface of Vesta, not from its largest crater but sometime before the Late Heavy Bombardment (LHB) more that 3.8 Gyr ago. The higher density of objects in the pre-LHB asteroid belt (Petit et al. 2002) would have made for a dynamical environment in which collisional and scattering events were greatly enhanced over present day rates. In addition, resonance sweeping during the LHB could have dispersed these asteroids' inclinations (Nesvorný et al. 2008).

A second possibility is that these objects represent scattered planetesimals from the terrestrial planet region of the Solar System (Bottke et al. 2006). In the inner Solar System solid-body accretion times would have been faster than in the Main Belt. These bodies would have accreted a higher quantity of live radioactive nuclides such as ^{26}Al and been more likely to differentiate. The amount of basaltic material that was injected into the Main Belt from the inner Solar System is currently unconstrained.

A final explanation for the presence of basaltic asteroids at low inclinations and beyond 2.5 AU is that they derived from other differentiated parent bodies that formed in the Main Belt. Although we find no asteroidal evidence for a large number of undiscovered basaltic asteroids, we cannot rule out minor contributions to the basaltic inventory from non-Vestoid differentiated bodies whose basalt has been heavily depleted due to collisions and dynamical effects (i.e. a "battered to bits" scenario, Burbine et al. 1996). It is possible that the observed distribution of basaltic asteroids in the Main Belt is derived from many different source populations including the Vestoids, inner Solar System planetesimals and a heavily depleted population of non-Vestoid differentiated bodies.

2.6.4 Comparison to Other Work

Figure 2.12 allows direct comparison to the results of Roig et al. (2008). These authors calculate size-frequency distributions for the possible number of Vestoids that have

migrated across the 3:1 resonance into dynamically stable orbits (see their Fig. 6). In their most optimistic simulations they find that on the order of 100 Vestoids with a size of 2 km or greater could cross this resonance over the maximum lifetime of the Vesta family (3.5 Gyr). Our lower and upper limits suggest that between 100 and 1850 basaltic asteroids with a size bigger than 2 km ($H < 15.0$) exist beyond 2.5 AU. The lower end of this estimate is commensurate with the Roig et al. (2008) result. However, if the basaltic asteroids in the outer belt are exclusively of Vestian origin then they would be distributed at semi-major axes near the 3:1 resonance. Our calculated distribution is in contrast to this expectation: it is roughly uniform across all $a > 2.5$ AU. This is suggestive of multiple sources of basaltic asteroids in addition to those few added by the diffusion of Vestoids across the 3:1 resonance. The very low number statistics in this region make it difficult to make more detailed inferences. Further observations are needed to provide more robust constraints on the distribution of these objects beyond the 3:1 resonance.

We also compare our calculated semi-major axis distribution to the simulation results of Nesvorný et al. (2008) and Bottke et al. (2006) (Fig. 2.13). This allows us to investigate the feasibility of two different scenarios for delivering basaltic asteroids to orbits outside of the dynamical Vestoid population. Figure 2.13 shows the normalized distribution of non-Vestoid basaltic asteroids as a function of semi-major axis. These distributions have been normalized by their maximum values (all at 2.2 AU) because limitations inherent to each work precludes the comparison of an absolute number of basaltic asteroids. We confine these distributions to the inner Main Belt ($a < 2.5$ AU) because of low number statistics for larger values of a in our analysis and the Bottke et al. (2006) simulations and the lack of any Vestoids across the 3:1 resonance in the Nesvorný et al. (2008) simulations. The distributions from the numerical simulations exclude test particles that populate the dynamical Vestoid region of orbital element space as defined in §2.2. This produces distributions that are non-Vestoid based upon our specific dynamical criteria.

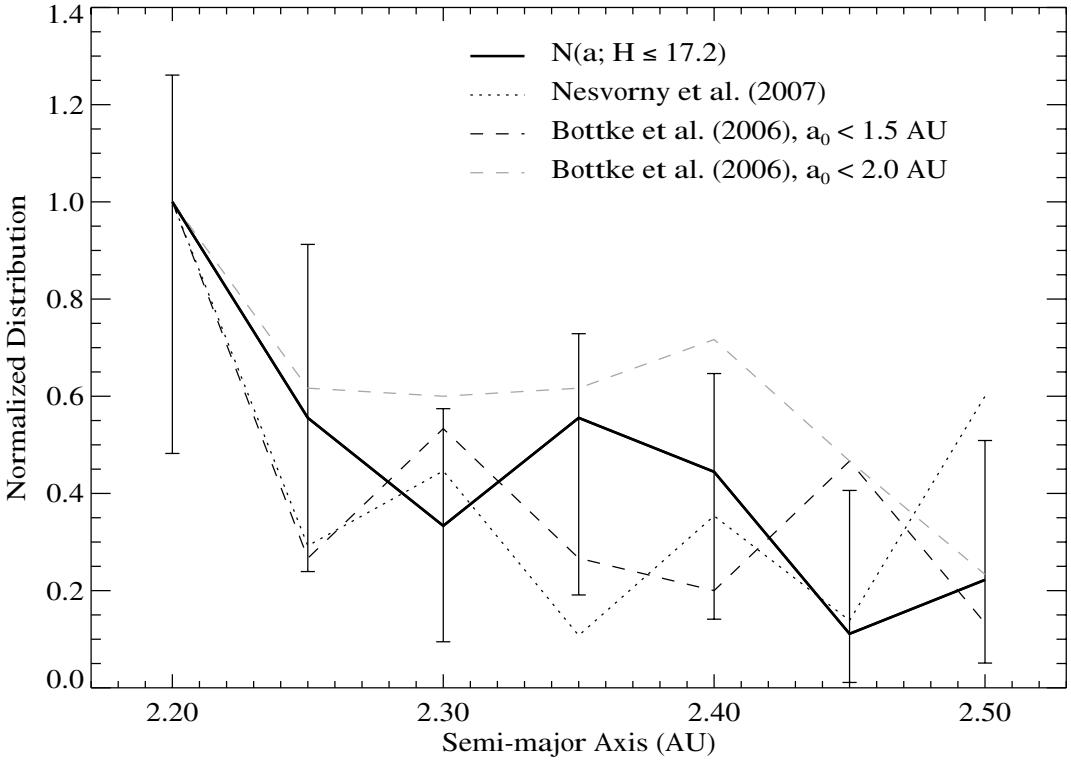

Figure 2.13 Comparison of semi-major axis distributions normalized at 2.2 AU. Our calculated distribution of basaltic asteroids is shown as the solid line with 90% Poissonian upper and lower limits. The results of two dynamical simulations are overplotted. The dotted line shows the simulated number of Vestian fragments that have evolved outside of the HCM-defined dynamical limits of this family (Nesvorný et al. 2008). The dashed lines plot the distribution of inner Solar System planetesimals scattered into the Main Belt from two different source regions, $a < 1.5$ AU (black dashed line) and $a < 2.0$ AU (grey dashed line) (Bottke et al. 2006).

The Nesvorný et al. (2008) study was designed to understand the dynamical evolution of Vesta's ejected fragments. They modeled the diffusion of Vestoids over an estimated family lifetime of 2 Gyr. If our distribution of basaltic asteroids was exclusively derived from dynamically aberrant Vestoids then we would expect it to match the Nesvorný et al. (2008) result.

The Bottke et al. (2006) study modeled the injection of planetesimal-size bodies from the inner Solar System into the Main Belt during the epoch of planet formation.

The specific source region of these planetesimals determined which are differentiated and contain basalt. Due to uncertainties in the time-scales of accretion and the initial abundance of radioactive isotopes, it is not clear where the boundary between differentiated and undifferentiated planetesimals existed. Thus we plot two distributions from the Bottke et al. (2006) results: one corresponding to all of the planetesimals that are scattered into the main belt from initial semi-major axes, a_0, less than 1.5 AU and those with $a_0 < 2.0$ AU. If our distribution was derived primarily from these scattered interlopers we would expect it to match the Bottke et al. (2006) result.

We calculate the chi-squared (χ^2) probability that these simulated distributions match our observational result. The Nesvorný et al. (2008) distribution and the Bottke et al. (2006) distribution for a planetesimal source region of $a_0 < 1.5$ AU produce χ^2 probabilities equal to 99.6% and 98.5% respectively. Within the limits of our calculations these distributions fit the data equally well. The worst fit (χ^2 probability = 73%) is the Bottke et al. (2006) distribution for a planetesimal source region of $a_0 < 2.0$ AU. The difference in probabilities from the Bottke et al. (2006) simulations suggests that the contribution of basaltic asteroids from inner Solar System planetesimals is weighted towards objects originally separated in semi-major axis from the Main Belt rather than objects that formed at semi-major axes around 2.0 AU. This is not unexpected as faster accretion times at smaller heliocentric distances would have produced a greater number of differentiated planetesimals.

This work is the first survey specifically designed to constrain the global distribution of basaltic material in the Main Belt. Future all-sky surveys such as PanSTARRS (Kaiser & 25 co-authors 2002) and LSST (Claver & 13 co-authors 2004) will greatly increase the number of known asteroids and will allow a more complete description of the basaltic asteroids. The results presented here suggest that the total amount of basaltic material in the Main Belt is very much less than expected from the ~ 100 differentiated parent bodies traced by the iron meteorites and basaltic

achondrites, a result which agrees with the suggestion that basaltic fragments have been comminuted to sizes below observational limits (e.g. Burbine et al. 1996) or that some unknown space weathering processes has obscured the spectral signature of basalt on asteroid surfaces (Wetherill & Chapman 1988). However, the inferred presence of a small amount of basaltic material throughout the Main Belt suggests that some vestige of crustal material from large differentiated bodies does exist and may represent the upper size limit of this population.

Chapter 3

Mineralogy of Basaltic Asteroids

3.1 V-type Asteroids in the Inner Main Belt

Hydrocode simulations of the collision that formed the Vesta family (Asphaug 1997) suggest that km-size fragments would have been removed with ejection velocities of no greater than 0.6 km/s. Simplified versions of Gauss's equations can be used to quantify the distance from Vesta in orbital element space that corresponds to this ejection velocity (Zappala et al. 1996). These equations are:

$$\frac{\delta a}{a} = \frac{2}{na} V_T, \tag{3.1}$$

$$\delta e = \frac{1}{na} [2 \, (cos \, f) \, V_T + (sin \, f) \, V_R], \tag{3.2}$$

$$\delta i = \frac{1}{na} \, cos(\omega + f) \, V_W, \tag{3.3}$$

where a, e and i are proper semi-major axis, eccentricity and inclination, na is the mean orbital velocity, and f and ω are the true anomaly and argument of perihelion at the time of velocity change (i.e. family formation). V_T, V_R and V_W are the components of the ejection velocity tangential to the orbit, in the radial direction and perpendicular to the orbital plane. The sum of these velocities in quadrature is the same as Δv in Chapter 2. Changes in orbital elements due to this velocity perturbation are indicated by δ. Zappala et al. (1996) calculate that $f = 90^\circ$ and $\omega + f = 30^\circ$ for the Vesta family.

With these values we can calculate the maximum extent of the Vesta collisional family in each of the three extents in parameter space by assuming that the 0.6 km/s ejection velocity is aligned exclusively along each of the corresponding velocity vectors (this is possible because δe depends only on V_R when $f = 90°$). Variation of the adopted values for f and $\omega + f$ does not have a significant effect on the calculated extent of the Vesta family. For instance, δa is unaffected by these quantities and if $\omega + f$ were set to $0°$ in order to maximize Equation 3.3 then δi would only be larger by $\sim 15\%$.

We start by defining $\delta a = a_v - a$, where a_v is the semi-major axis of Vesta. The mean Keplerian orbital velocity is given by:

$$na = \sqrt{\frac{GM_\odot}{a}}, \tag{3.4}$$

where G is the gravitational constant and $M_\odot$ is the mass of the Sun. Plugging these into Equation 3.1 yields:

$$a_v - a = \frac{2\ V_T}{(GM_\odot)^{1/2}}\ a^{3/2}. \tag{3.5}$$

Assuming $V_T = 0.6$ km/s and then solving for a gives $\delta a = 0.13$ AU, or a maximum range of semi-major axes for collisionally-produced Vestoids of $2.23 - 2.49$ AU. The maximum range of eccentricity can be calculated from Equation 3.2 if we assume that the velocity perturbation was aligned exclusively along the radial direction ($V_R = 0.6$ km/s). This yields $\delta e = 0.03$, corresponding to a maximum range of eccentricities for the Vesta family of $0.06 - 0.13$. Similarly, for inclination we obtain a range of $4.8 - 7.9°$. This region of orbital element space is enclosed by the ellipse in Figure 3.1.

When V-type asteroids with relative ejection velocities greater than 0.6 km/s were first discovered (e.g. Binzel & Xu 1993; Florczak et al. 2002) it was unclear how these objects reached such orbits. However, recent progress in the use of numerical integrators has helped to illuminate this issue. Carruba et al. (2005) showed that three-body and weak secular resonances could lead to the migration of Vestoids to orbits outside of the Vesta dynamical family. Nesvorný et al. (2008) showed that a

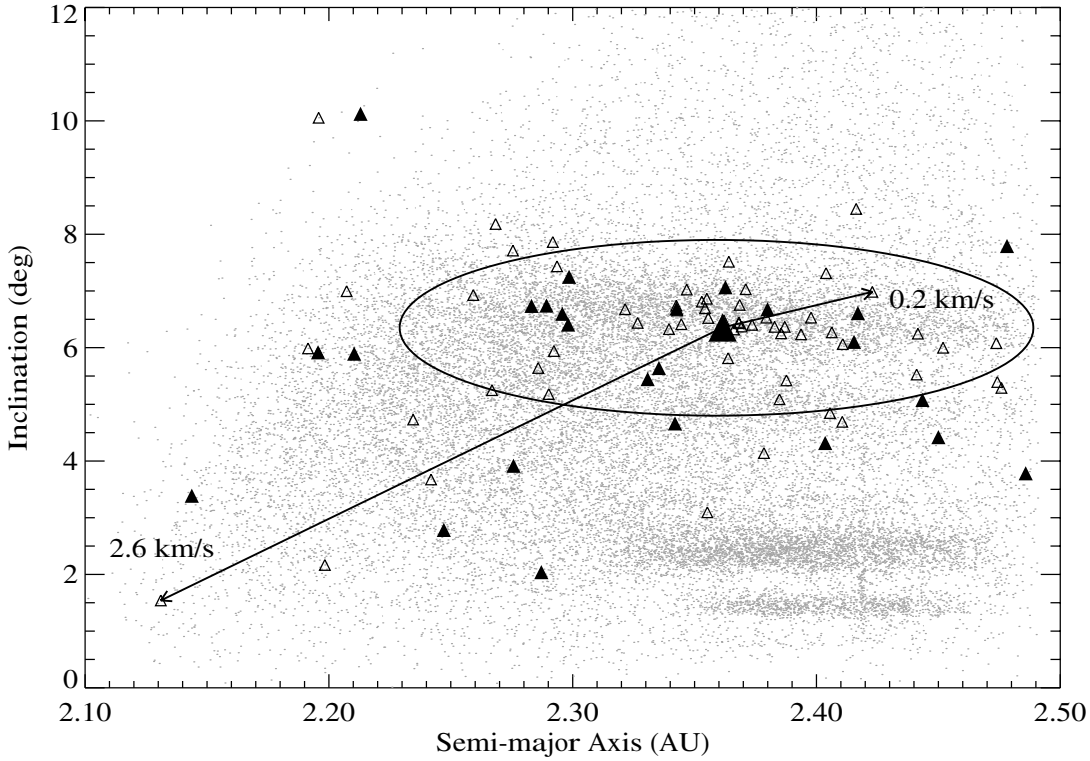

Figure 3.1 Dynamical map in proper element space of V-type asteroids in the inner Main Belt. The small filled triangles are the V-type asteroids with NIR spectra included in our study of band parameters (§3.4). The open triangles are spectroscopically confirmed V-types based solely on visible wavelength data (Table A.1). Vesta is denoted by the large filled triangle at 2.36 AU, 6.35°. The grey dots in the background are all objects from the 4th release of the SDDS MOC (Parker et al. 2008). The ellipse traces the 0.6 km/s ejection velocity relative to Vesta. The relative ejection velocities for two objects are indicated by the arrows.

combination of these resonances and the Yarkovsky effect could disperse the orbits of Vestoids to nearly the full extent of the inner Main Belt. However, these authors found that the number of V-type asteroids at low inclination ($< 6°$) could not be explained by their model of Vestoid migration. Three possibilities exist to explain this over-abundance of low-i V-types. First, these objects could be fragments of basaltic crust from a non-Vestoid differentiated body. Second, they may be from Vesta, but were removed from the surface before the Late Heavy Bombardment (LHB), before

the primary family forming collision, and were scattered to their current orbits as mean motion and secular resonances swept through the Main Belt during the LHB (Gomes 1997). Third, these objects may have been ejected from the Vesta parent body at the time of family formation and have since migrated to their current orbits by some unknown dynamical mechanism. In the first of these two possibilities, it is reasonable to suggest that V-type asteroids that are far from Vesta in orbital element space (particularly in inclination) may be spectroscopically distinct from the Vestoids, either due to a different mineralogy or space weathering effects.

A similar line of reasoning motivated Hiroi & Pieters (1998) to investigate the visible-wavelength spectral features (namely the slope and 1 μm band depth) of 20 V-type asteroids in the inner Main Belt. These authors found that Vestoids with large values of Δv tended to have steeper spectral slopes and shallower 1 μm bands than Vestoids with smaller Δv. Based on meteorite data and laboratory irradiation experiments these authors claimed that this spectroscopic trend implies a higher degree of space weathering for Vestoids at large values of Δv. However, the largest value of Δv considered by these authors was 0.65 km/s and all of the objects that were studied have now been incorporated into the Vesta dynamical family as detection completeness has increased since their study.

Duffard et al. (2004) attempted a similar investigation on the spectroscopic diversity of Vestoids based on NIR data. However, their methodology of measuring band parameters from heavily smoothed versions of very low-S/N spectra produced unexpected results, namely they found that the Band I to Band II area ratios and the Band I and Band II centers for the majority of the V-types in their sample were not in agreement with those of the HEDs (Band I and II refer to the 1 and 2 μm absorption bands common to basaltic material, see §3.2 for definitions of these parameters). Although it is known that band area ratios are highly sensitive to variations in grain size, temperature, space weathering and mineralogical diversity (Ueda et al. 2002),

band centers should be less sensitive to these affects and thus comparable between the HEDs and Vestoids.

In light of recent advances in dynamical studies (Carruba et al. 2005; Nesvorný et al. 2008) and improvements in NIR spectroscopic instrumentation (Rayner et al. 2003), we revisit the issue of the spectral diversity of basaltic asteroids by measuring the NIR spectral properties of 26 inner Main Belt V-type asteroids and one outer belt V-type. The goals of this inner belt study are threefold: (1) address the reported spectral-dynamical correlation amongst the Vestoids (Hiroi & Pieters 1998) by extending our analysis out to NIR wavelengths and by including V-types across a wider range of orbital element space; (2) address the findings of Duffard et al. (2005) to look for spectroscopic differences between V-type asteroids and HED meteorites; (3) determine if any of the V-type asteroids in the inner Main Belt have spectroscopic properties that would suggest a non-Vestoid mineralogy. We conclude this chapter (§3.6) with a discussion of the visible-NIR spectral properties of an unusual asteroid in the outer Main Belt, 10537 (1991 RY16). This object is unlikely to be related to Vesta and thus affords the opportunity to investigate a non-Vestoid differentiated mineralogy.

3.2 Tools of Mineralogical Analysis

The reflectance spectra of minerals contain absorption features that are diagnostic of properties such as composition, albedo, grain size and crystal structure. A variety of analytic tools have been proposed to infer specific mineralogical information from remote spectra. Sunshine et al. (1990) presented a method of spectral deconvolution based on the representation of absorption bands by discrete mathematical distributions. These authors find that a modified gaussian distribution of absorption strengths as a function of wavelength (derived from a power law relationship between the energies of electronic transitions and the average bond length between crystal field sites) can be used to accurately represent absorption features in pyroxene and olivine

mixtures. Numerous authors have employed this modified Gaussian model (MGM) to make statements about the surface mineralogy of a wide range of asteroid types (e.g. Vernazza et al. 2008; Mothé-Diniz et al. 2008; Sunshine et al. 2004; Hiroi et al. 1995).

Mixing model techniques involve the combination of spectra with known mineralogical origin as a means to best match observed asteroidal data. Mixture spectra can be derived from measured meteoritic reflectance data (e.g. Hiroi et al. 1993) or from spectra calculated by Hapke's radiative transfer theory (e.g. Lawrence & Lucey 2007). Successful implementation of this method requires knowledge of the grain size distribution, albedo and optical properties of the minerals on an asteroid's surface; parameters which are typically not known for telescopic targets and are free parameters in the implementation of mixing models.

Perhaps the most obvious technique for interpreting the surface mineralogy of an asteroid is via the comparison of remote data to spectral analogs from meteorite collections. Large databases of meteoritic spectra (e.g. Brown RELAB, Arizona State University's Thermal Emission Spectroscopy Library, Southwest Research Institute's Infrared Spectroscopy Laboratory) can help to establish specific links between meteorites and their parent bodies in the Main Belt. However, issues related to grain size, space weathering and selection biases inherent to the meteorite collection make it difficult to find exact matches between asteroids and meteorites (Gaffey et al. 2002).

Band analysis techniques are useful for characterizing spectral data and can be used as a starting point for deriving mineralogical information (Gaffey et al. 2002). As a characterization tool, band analyses are completely objective, requiring no knowledge or assumptions about mineralogy, and can be implemented very quickly. One goal of this chapter is to use band analysis techniques to quantify the spectral properties of HEDs and V-type asteroids to allow comparison between these two groups. For the data considered in this chapter we perform band analyses with attention to the following parameters: the minima and central wavelength of the 1

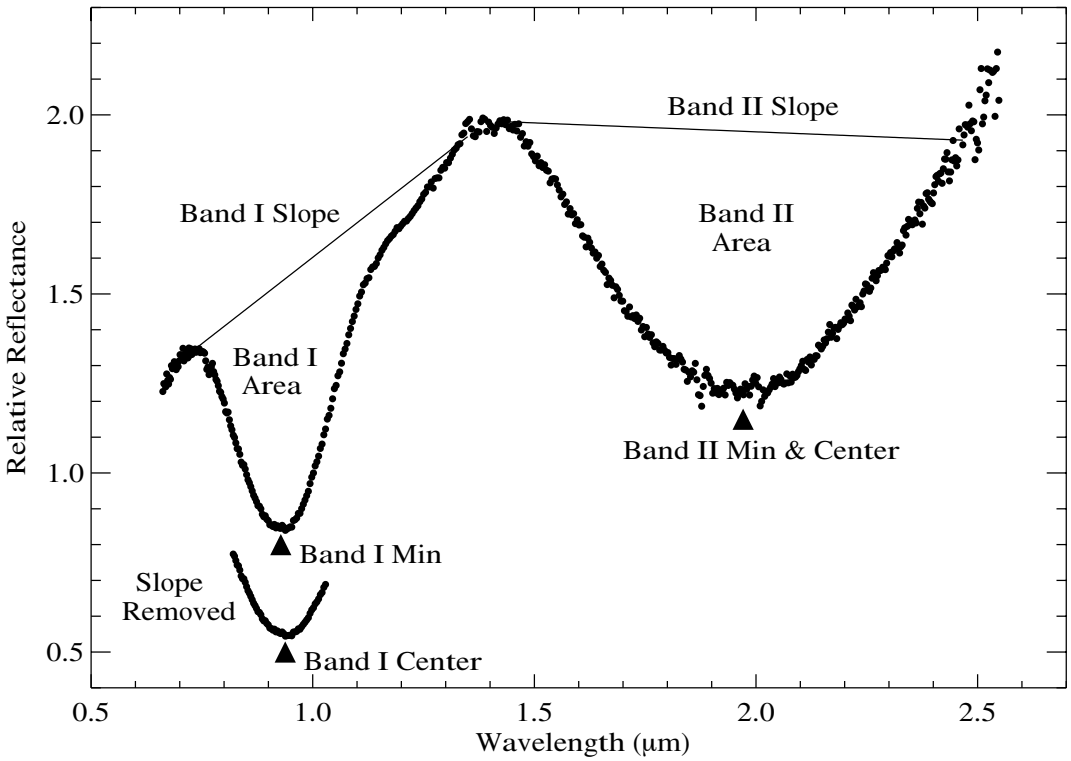

Figure 3.2 Spectrum and band parameters of V-type asteroid 5498 Gustafsson. The data have been normalized at 1.0 μm. The slope-removed data plot below the normalized spectrum. The band parameters of interest are denoted: Band I and II minima, centers, areas and slopes. This figure is adapted from Cloutis et al. (1986).

and 2 μm olivine-pyroxene absorption features (Band I and II respectively) and the ratio of areas within these two bands. One of the primary benefits of band analyses is that different asteroid and meteorite types segregate into distinct groups in band parameter phase space (Gaffey et al. 1993b). These key parameters are depicted in Figures 3.2 and 3.3.

Measurement of these parameters is dependent on several polynomial fits to actual data (Fig. 3.3). These fits include a fourth order fit to the reflectance peak at $\sim 0.7\ \mu m$, third order fits to the reflectance troughs and peak at $\sim 0.9,\ 2.0$ and $1.4\ \mu m$, and a second order fit to the red-edge of the $2\ \mu m$ band. The band minima are equal to the minima of the third order fits across each of the reflectance troughs ($0.82 - 1.03\ \mu m$ for

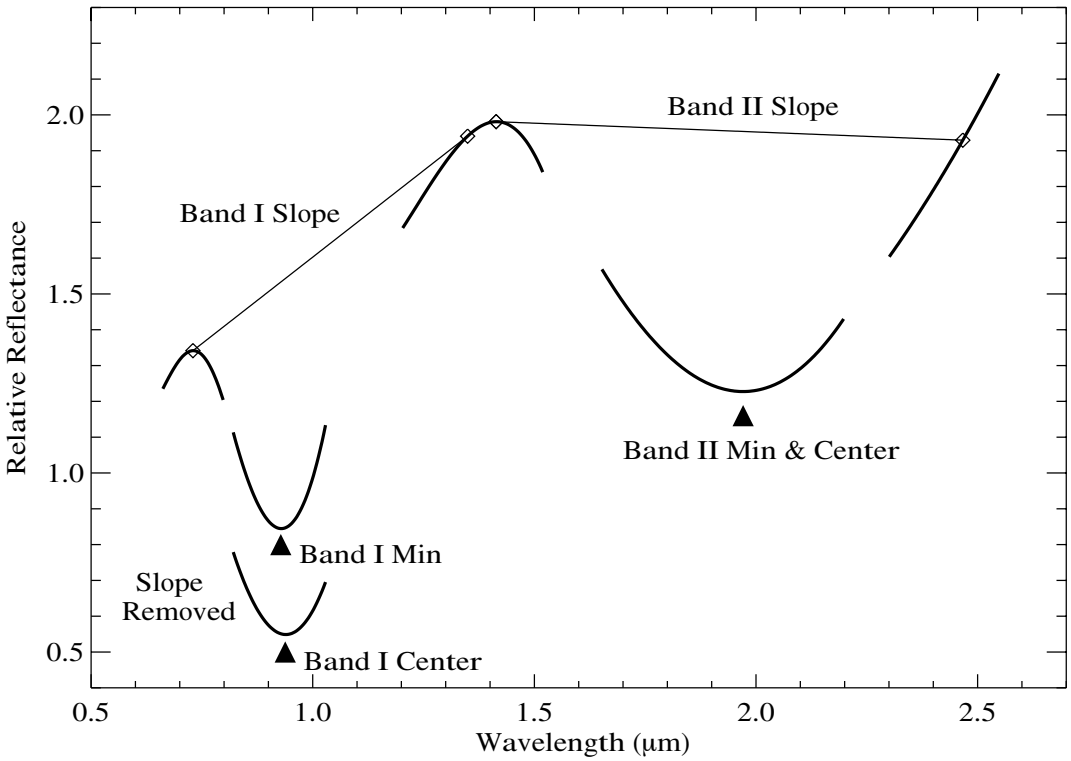

Figure 3.3 Same as Figure 3.2 with the spectrum replaced by the fitted segments. The open diamonds mark the edges and tangent points for the Band I and II slopes. Note that all band parameters are defined relative to these fitted segments, not the data.

Band I and $1.65 - 2.2\ \mu m$ for Band II). The Band I center is measured by first fitting a line (labelled Band I Slope in Figs. 3.2 and 3.3) that intersects the fitted peak at $\sim 0.7\ \mu m$ and is tangent to the reflectance peak at $\sim 1.4\ \mu m$. This continuum slope is then divided into the data and the minimum of this slope-removed band is defined as the band center. Band I centers are typically at longer wavelengths than Band I minima because of the positive Band I slope for most HEDs and V-type asteroids (§3.1). Band II centers are defined as equal to the Band II minima (without dividing out a continuum slope), because the red edge of the $2\ \mu m$ band is typically unresolved in NIR telescopic data (e.g. Fig. 3.2). We define the red edge of the $2\ \mu m$ band to be at $2.46\ \mu m$ (the reddest wavelength for which all of our data are reliable, §3.1). Band areas

are calculated as the area between the band slopes and data points. The calculation of error bars for each of these band parameters is discussed in the following section (§3.1).

We have intentionally been very explicit in our specific definitions for these band parameters because other studies have employed different methodologies. For instance, Cloutis et al. (1986) define the red edge of Band II at 2.4 μm while Gaffey et al. (2002) define it at 2.5 μm. In some studies, the band centers are defined as the wavelength at which the band areas are bisected (e.g. Binzel et al. 2009). Although these differences are subtle, they do make it difficult to compare the measurements from one study to another. We apply this methodology to all of the data considered in this chapter so that direct comparisons can be made between asteroids and meteorites.

Before we present the results of this analysis it is useful to discuss the mineralogical causes that affect each of the band parameters. As stated in §1.5.3, the 1 and 2 μm absorption bands in the spectra of igneous silicates are attributable to Fe^{2+} ionic transitions within the crystal structures of olivine and pyroxene. The variability in band centers is due to the substitution of the Fe^{2+} cation with the smaller Mg^{2+} and Ca^{2+} cations (Adams 1974; Cloutis et al. 1986). The smaller cations change the crystal structure and thus the transition energies that produce these absorption features. Amongst the HEDs, the relatively Ca- and Fe-rich eucrites have band centers at longer wavelengths than the Mg-rich and Fe-poor diogenites (Burbine et al. 2001).

Pyroxenes typically display both 1 and 2 μm absorption bands, while olivine has only a 1 μm feature (see Fig. 3 in Gaffey et al. 1993a). Thus, Band II to Band I area ratios (BAR) can be diagnostic of the relative abundance of olivine to pyroxene. In an ideal mixture of orthopyroxene (indicated subsequently as opx) and olivine, large BARs indicate opx-rich compositions and small BARs suggest olivine-rich mineralogies (Gaffey et al. 1993b). It is important to note that these trends in band parameters have been determined in ideal laboratory settings (e.g. Cloutis et al. 1986). Applications of band analysis techniques to telescopic spectra of asteroids are complicated by

differences in the space environment relative to controlled laboratory settings. Issues related to temperature, pressure, particle size distribution, space weathering and mineralogical diversity can significantly alter asteroidal reflectance spectra (Ueda et al. 2002) so that they no longer resemble meteoritic data (e.g. Vernazza et al. 2008; Burbine et al. 2009). We discuss some of these issues in §3.4 when a band analysis is performed on the spectra of V-type asteroids.

3.3 Band Analysis of HED Meteorites

To build a comparison database we perform a spectral band analysis for each of the HED meteorites that are included in the Brown RELAB spectral catalog (Pieters & Hiroi 2004). The samples that were analyzed are listed in Table A.2. We safely ignore error bars in the measurement of the meteorite band parameters: the error bars for each of the measured parameters are much smaller than the error bars for our asteroidal data (§3.4), and they become irrelevant in our statistical approach to characterizing the overall spectral properties of the HEDs.

The set of HED spectra excludes some of the data that are available in the RELAB database. We do not include samples that have been processed in laser irradiation experiments. When multiple spectra for a single sample exist we always choose data corresponding to the smallest available grain size. This approach is reasonable because the size of grains that compose the regolith of Vestoids is probably $< 25\mu m$ (Hiroi et al. 1994, 1995), which is the smallest particle size analyzed at RELAB. Our aim in analyzing these meteoritic spectra is not to perform a detailed study of spectral changes as a function of particle size, irradiation level and other variables; for such a study see Duffard et al. (2005). We perform this analysis to build a statistically significant sample of comparison data that will aid the interpretation of our asteroidal spectra.

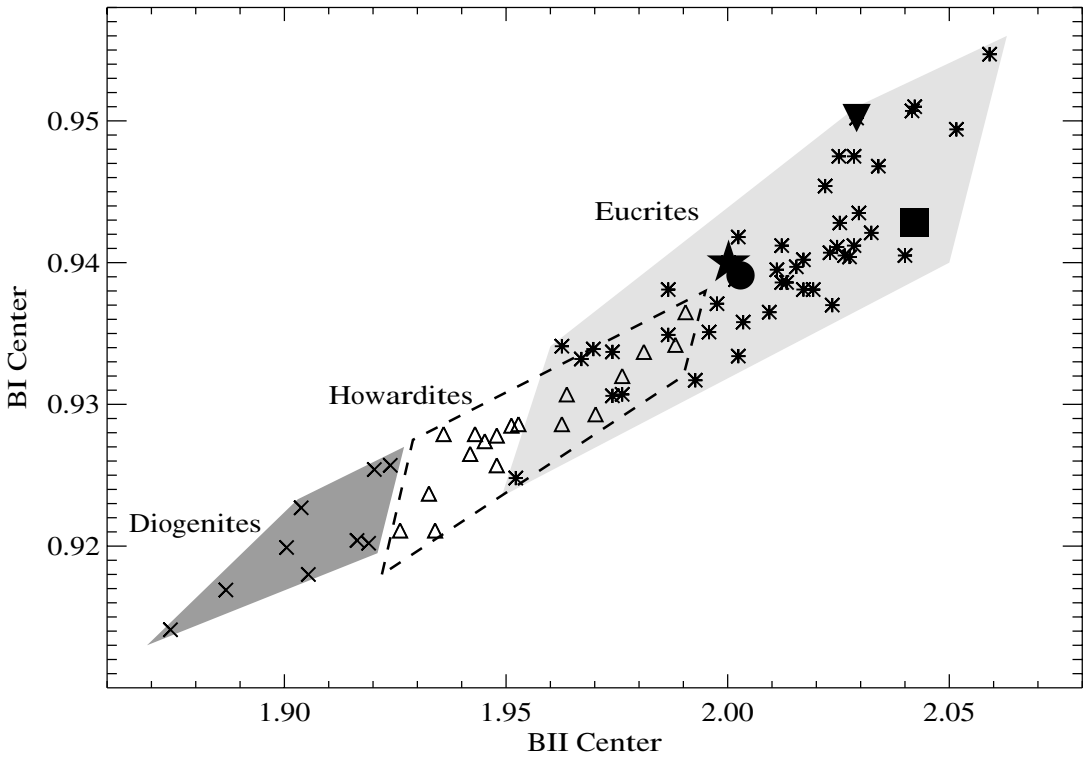

Figure 3.4 Band centers of the howardites (triangles), eucrites (asterisks) and diogenites ($\times$'s). Approximate boundaries for each of these subgroups are depicted as the dashed line, light grey and dark grey regions respectively. The eucrites and diogenites are very clearly segregated in this figure. The parameters of the four isotopically anomalous eucrites that are included in our study are denoted by the filled symbols: star (Ibitira), circle (Passamonte), upside-down triangle (NWA011), and square (PCA91007).

A plot of BI center versus BII center for the HEDs is shown in Figure 3.4. The three HED subgroups are well defined (although they do overlap) in this parameter space. The regions occupied by each subgroup have been shaded or outlined so that they can be compared to the band parameters of the V-type asteroids in §3.4. In general, eucrites tend to have band centers at longer wavelengths than the diogenites, which implies that they are more Fe-rich and have Ca/Mg abundance ratios much greater than unity. This is confirmed by chemical analyses of eucrite samples (Lodders & Fegley 1998). The diogenites have shorter wavelength band centers due to Ca/Mg abundance

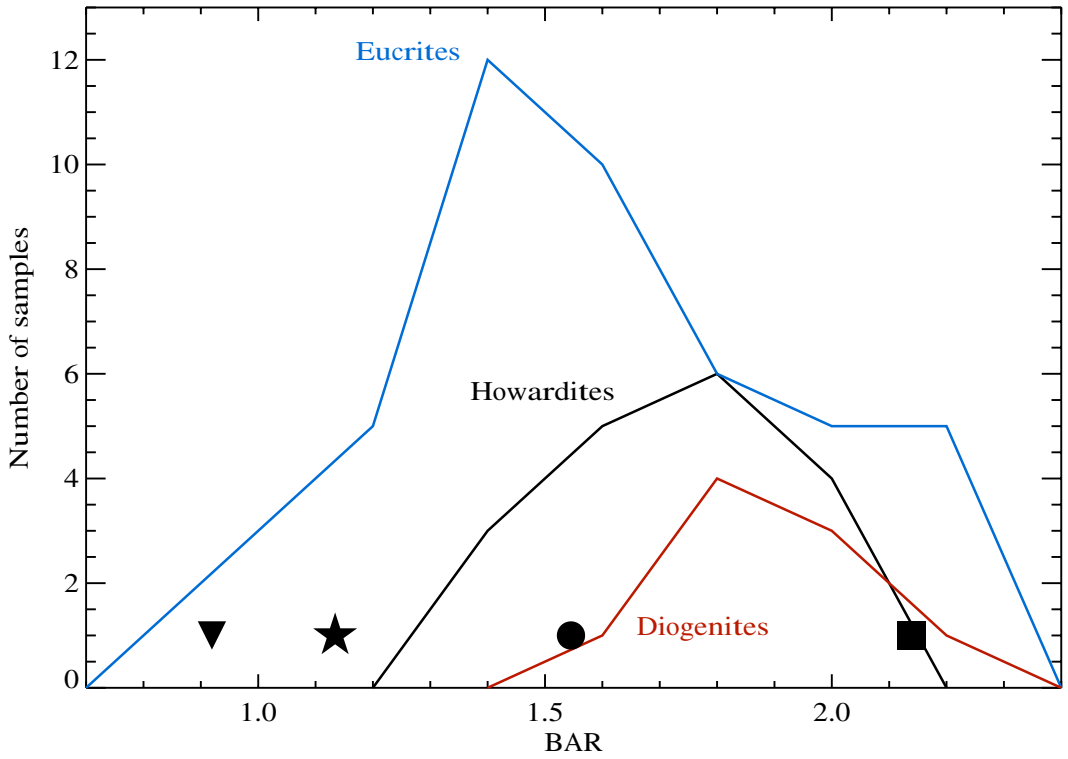

Figure 3.5 Histograms of BARs for HED meteorites with a bin size of 0.2 units. The howardites (black line), eucrites (blue line) and diogenites (red line) are not clearly segregated in this figure, though diogenites do tend towards larger BARs. As in Figure 3.4 the symbols denote the four isotopically anomalous eucrites: Ibitira (star), Passamonte (circle), NWA011 (upside-down triangle), and PCA91007 (square).

ratios much less than unity and relatively Fe-poor compositions. Unsurprisingly, the howardites (brecciated mixes of eucrites and diogenites) have band centers that are intermediate to that of the eucrites and diogenites. The compositional trend represented by the band centers is consistent with the origin of the diogenites at greater depths within the HED parent body, i.e. low-Ca diogenites crystallized and settled before high-Ca eucrites as the HED parent body cooled (Ruzicka et al. 1997).

Histograms of the BARs of the HEDs are plotted in Figure 3.5. The BARs do not clearly segregate the three subgroups, however the diogenites do trend towards larger

values. The larger relative opx abundances of the diogenites (Burbine et al. 2001) is the likely cause for their high BARs (Cloutis et al. 1986).

Of the 75 HEDs that were analyzed, four eucrites (Passamonte, Ibitira, NWA011, and PCA91007) have anomalous oxygen isotope ratios. Specifically, these meteorites all have [^{17}O/^{16}O] abundance ratios that are at least $0.03‰$ away from the mean [^{17}O/^{16}O] ratios for ordinary HEDs, which are scattered by only $\pm$ $0.016‰$ relative to their mean (Scott et al. 2009). Thus, these four eucrites are likely to have been derived from unique differentiated parent bodies. Our analysis shows that these four samples are in no way spectroscopically unique compared to other eucrites (Figs. 3.4 & 3.5). At face value this would seem to suggest that the spectroscopic properties (and by extension the mineralogy) of basaltic material from one parent body to the next is indistinguishable and that isotopic information is needed to distinguish distinct parent bodies. However, we show in §3.5 that this does not seem to be the case for V-type asteroids in the Main Belt. This may be a reflection of the small number of parent bodies (~ 150, Keil 2000) sampled by the meteorites relative to the large number of multi-km asteroids in the Main Belt ($\sim 10^6$, Burbine et al. 2002).

3.4 Band Analysis of Inner Belt V-type Asteroids

We collected NIR spectra of 26 V-type asteroids distributed throughout the inner Main Belt (Figs. 3.1 & A.1, Table 3.1). All of these observations, with the exception of the data for 4 Vesta, were performed with the SpeX instrument (Rayner et al. 2003) at NASA's IRTF. These data include our own observations, unpublished observations that were performed as part of the ongoing Small Main Belt Asteroid Spectroscopic Survey (SMASS, provided courtesy of Bobby Bus) and the spectrum of 4 Vesta from Gaffey (1997). All of the SpeX observations were made with the telescope operating in a standard ABBA nod pattern. SpeX was configured in its low resolution (R=250) prism mode with a 0.8" slit for wavelength coverage from $0.7 - 2.5\ \mu m$. Calibration and

reduction of all new observations employed the SpeXtool package (Cushing et al. 2004) and followed the protocol outlined in §2.3. The SMASS data were reduced following the procedure described in Burbine & Binzel (2002). When available, visible wavelength data from SMASS (Xu et al. 1995; Bus & Binzel 2002b) were appended to the NIR spectra to improve S/N at the blue edge of the 1 μm absorption band. Figure A.1 shows that both the 1 and 2 μm absorption bands are resolved for all 26 of the spectra and that the typical S/N is either better than or comparable to previous studies of NIR band parameters (e.g. Kelley et al. 2003; Duffard et al. 2004; Hardersen et al. 2004). The SMASS targets Kamo, Celle, Lee, Harbin and Principia were each observed at two different epochs (Table 3.1). The data from these pairs of observations were combined into composite spectra to improve S/N.

The band analysis procedure described in §3.2 was applied to each of the NIR asteroidal spectra. The results of this band analysis are summarized in Table 3.2. In order to compare these parameters to those of the HEDs, which were measured in a laboratory at ~ 300 K, a temperature correction to the band centers was required. Temperature corrections were computed following the methodology of Burbine et al. (2009). The mean surface temperature of an asteroid (T) is approximated by the equation for energy conservation:

$$T = \left[\frac{(1-A)L_0}{16\epsilon\sigma\pi r^2}\right]^{1/4}, \tag{3.6}$$

where A is the albedo, L_0 is the solar luminosity (3.827×10^{26} W), ϵ is the asteroid's infrared emissivity (assumed to be 0.9, Lim et al. 2005), σ is the Stefan-Boltzman constant and r is the asteroid's heliocentric distance. The albedo of each asteroid was assumed to be 0.3, a value that is intermediate to the range for V-type asteroids (Tedesco et al. 2004). The calculated mean surface temperature for each of the V-type asteroids is given in Table 3.2. Uncertainties in the adopted parameters (A and ϵ) do

Table 3.1 Summary of NIR Spectroscopic Observations

Object	UT Date	Heliocentric Distance (AU)	Mag.	t_{exp} (min)
4 Vesta	Feb. 18-20, 1981[a]	2.38	6.12	–
809 Lundia	Aug. 26, 2008	1.93	14.6	8
956 Elisa	Jul. 5, 2008	1.85	14.6	16
	Oct. 9, 2008	1.85	15.7	88
1929 Kollaa	Feb. 19, 2001[b]	2.21	15.3	24
2045 Peking	Jan. 14, 2002[b]	2.48	16.7	40
	Aug. 26, 2008	2.50	16.2	87
2511 Patterson	May 7, 2004[b]	2.23	16.1	32
2566 Kirghizia	May 8, 2002[b]	2.41	16.0	32
2579 Spartacus	Oct. 10, 2000[b]	2.22	16.4	28
2653 Principia	Nov. 26, 2002[b]	2.53	16.3	48
	Jul. 16, 2005[b]	2.59	15.5	28
	Apr. 19, 2008	2.29	15.3	12
2763 Jeans	Jun. 26, 2004[b]	2.24	15.7	32
	Jul. 5, 2008	1.99	14.9	16
	Aug. 26, 2008	1.92	14.9	24
2795 Lepage	Apr. 9, 2005[b]	2.26	15.9	24
2851 Harbin	Aug. 24, 2001[b]	2.42	15.6	28
	Jan. 12, 2003[b]	2.20	15.9	48
2912 Lapalma	Feb. 20, 2001[b]	2.14	15.3	32
3155 Lee	Jun. 22, 2001[b]	2.56	16.2	28
	Jul. 14, 2005[b]	2.43	15.9	28
3782 Celle	Nov. 26, 2002[b]	2.60	16.8	32
	Jun. 25, 2004[b]	2.19	15.5	28
4188 Kitezh	Aug. 14, 2001[b]	2.10	15.3	28
4215 Kamo	Nov. 11, 2002[b]	2.52	16.5	64
	Jul. 15, 2005[b]	2.51	15.6	40
	Apr. 19, 2008	2.29	15.4	12
5498 Gustafsson	Aug. 26, 2008	1.92	16.3	93
9481 Menchu	Aug. 26, 2008	2.48	17.3	40
16416 (1987 SM3)	Nov. 23, 2007	2.40	16.9	64
26886 (1994 TJ2)	Jul. 5, 2008	2.09	17.2	40
27343 (2000 CT102)	Aug. 26, 2008	1.94	16.6	48
33881 (2000 JK66)	Nov. 23, 2007	1.77	16.6	48
36412 (2000 OP49)	Nov. 23, 2007	2.12	16.9	40
38070 (1999 GG2)	Oct. 5, 2006	1.90	16.9	32
97276 (1999 XC143)	Nov. 23, 2007	2.05	16.6	56

The columns in this table are: object number and designation, UT date of observation, heliocentric distance at the time of observation, V-band magnitude of the target from the JPL HORIZONS system on the date of observation and net exposure time in minutes.
[a]Data from Gaffey (1997)
[b]Data provided courtesy of Bobby Bus

Table 3.2 Band Parameters of V-type Asteroids

Object	Heliocentric Distance (AU)	Mean Surface Temp. (K)	BI Center (μm)	ΔBII (μm)	BII Center (μm)	BAR
2000 CT102	1.94	187.7	0.925	0.020	1.935	2.78
Celle	2.39[a]	169.1	0.935	0.023	1.966	2.01
Elisa	1.85	192.2	0.931	0.019	1.963	2.70
	1.85	192.2	0.931	0.019	1.940	2.98
1999 GG2	1.90	189.6	0.940	0.019	1.989	1.85
Gustafsson	1.92	188.6	0.941	0.020	1.990	2.57
Harbin	2.31[a]	172.0	0.922	0.023	1.935	2.41
2000 JK66	1.77	196.5	0.935	0.018	1.947	2.61
Jeans	2.24	174.6	0.944	0.022	2.019	2.07
	1.99	185.3	0.940	0.020	1.994	2.31
	1.92	188.6	0.943	0.020	2.027	2.44
Kamo	2.51[a]	165.0	0.925	0.024	1.988	1.85
	2.29	172.7	0.934	0.022	1.975	2.43
Kirghizia	2.41	168.4	0.939	0.023	1.989	2.13
Kitezh	2.10	180.4	0.939	0.021	1.979	2.17
Kollaa	2.21	175.8	0.941	0.022	1.980	2.28
Lapalma	2.14	178.7	0.930	0.021	1.951	2.40
Lee	2.49[a]	165.6	0.919	0.024	1.933	2.70
Lepage	2.26	173.9	0.938	0.022	1.973	2.31
Lundia	1.93	188.1	0.937	0.020	1.954	2.62
Menchu	2.48	166.0	0.939	0.024	1.958	1.93
2000 OP49	2.12	179.5	0.941	0.021	1.986	2.10
Patterson	2.23	175.0	0.933	0.022	1.977	2.42
Peking	2.48	166.0	0.938	0.024	1.976	2.52
	2.50	165.3	0.939	0.024	1.968	2.69
Principia	2.56[a]	163.4	0.932	0.024	1.994	2.00
	2.29	172.7	0.940	0.022	2.011	2.04
1987 SM3	2.40	168.7	0.939	0.023	1.988	2.19
Spartacus	2.22	175.4	0.935	0.022	2.011	1.47
1994 TJ2	2.09	180.8	0.922	0.021	1.923	2.84
1999 XC143	2.05	182.5	0.946	0.021	2.037	2.14
Vesta	2.38	169.4	0.943	0.023	2.003	2.55

The columns in this table are: object designation, heliocentric distance at the time of observation, estimated mean surface temperature (Eqn. 3.6), BI center, temperature correction to BII center, BII center and the BII to BI area ratio (BAR). At the resolution of the spectra, the temperature correction for all of the BI centers is 0.002 μm. The band centers in this table have been temperature corrected. The maximum statistical errors (as determined from the spectrum of asteroid 2000 OP49) for these band parameters are: $\sigma_{BI} = 0.003$, $\sigma_{BII} = 0.011$ and $\sigma_{BAR} = 0.23$.
[a]Represents an average heliocentric distance from two separate observations.

not have a large affect on our resulting temperature corrections because of the small (1/4) exponent in Equation 3.6.

The temperature-dependent wavelength correction (in microns) to the BI and BII centers are given by (Burbine et al. 2009):

$$\Delta BI = (5.05 \times 10^{-3}) - (1.7 \times 10^{-5})T, \tag{3.7}$$

$$\Delta BII = (5.44 \times 10^{-2}) - (1.85 \times 10^{-4})T. \tag{3.8}$$

These equations are derived from linear fits to laboratory measured band centers for two different pyroxenes at temperatures of 293, 173 and 80 K (Moroz et al. 2000). In general these corrections are small: 0.002 μm for all of the ΔBI values (rounded to the resolution limit of the spectra) and about an order of magnitude more for ΔBII (Table 3.2). These shifts are much less than the range of measured band centers and thus do not matter greatly in our statistical approach. Nevertheless we apply the corrections to enable the best possible comparison between the meteoritic and asteroidal data sets. The temperature corrected band centers are presented in Table 3.2.

The first spectrum displayed in Figure A.1 (asteroid 2000 OP49) has the lowest wavelength-averaged signal-to-noise ratio (S/N$\sim$27) in this data set. This object's spectrum was used to estimate maximum statistical error bars for the measured asteroidal band parameters. Determining the error bars on band centers is non-trivial because the uncertainties for the observed data points are along the reflectance axis, not along the wavelength axis. To access the errors on the band centers of asteroid 2000 OP49 we ran a Monte Carlo simulation in which random noise (at the level of the measured signal-to-noise) was added to segments of the spectrum in the vicinity of the Band I and Band II minima. These segments were re-fit with a third-order polynomial and the new band centers were calculated. This process was repeated 100,000 times and the standard deviation of the measured band centers was calculated. The result of this error analysis gives $\sigma_{BI} = 0.003$ and $\sigma_{BII} = 0.011$. This procedure for estimating

errors on band centers is similar to that of Storm et al. (2007). Most of the asteroidal spectra are of much higher S/N (> 100) and thus will have band center errors that are insignificant relative to the general trends in which we are interested.

The errors for BARs are calculated by first measuring the largest and smallest possible band areas based on the S/N characteristics of a given spectrum. The maximum band areas are measured by subtracting noise at the 1-sigma level from each data point, while the minimum band areas are measured by adding noise at the 1-sigma level. For example, the BII area of 2000 OP49 with 1-sigma worth of noise subtracted from the data points is 0.608 and the BII area with 1-sigma worth of noise added is 0.516. We define the errors on the individual band areas to be one half of the difference between these maximum and minimum values. The net error on the BAR then involves the propagation of the errors from each band. Performing this analysis on the spectrum of 2000 OP49 gives a maximum error bar on the asteroidal BARs of $\sigma_{BAR} = 0.23$.

The asteroidal band centers are plotted in Figure 3.6 along with the howardite, eucrite and diogenite regions that were defined in Figure 3.4. Five asteroids (Elisa, Jeans, Kamo, Peking and Principia) were observed more than once. These individual observations are plotted, along with lines connecting those points and open circles indicating their average band centers. The maximum statistical error bars calculated from the spectrum of 2000 OP49 are indicated in this figure and are clearly much smaller than the size of the HED regions and the range of band centers displayed by the asteroids. The variability between multiple observations of individual asteroids is typically larger than the statistical errors and could be caused by compositional variation across the surface of the asteroids or could be related to uncorrected systematic effects. Vesta shows even larger variation in its band centers as a function of rotational phase (Gaffey 1997), suggesting that compositional variation is not an unreasonable explanation for the variability measured in the multiple spectra of Elisa, Jeans, Kamo, and Principia. Observations of a single asteroid through multiple

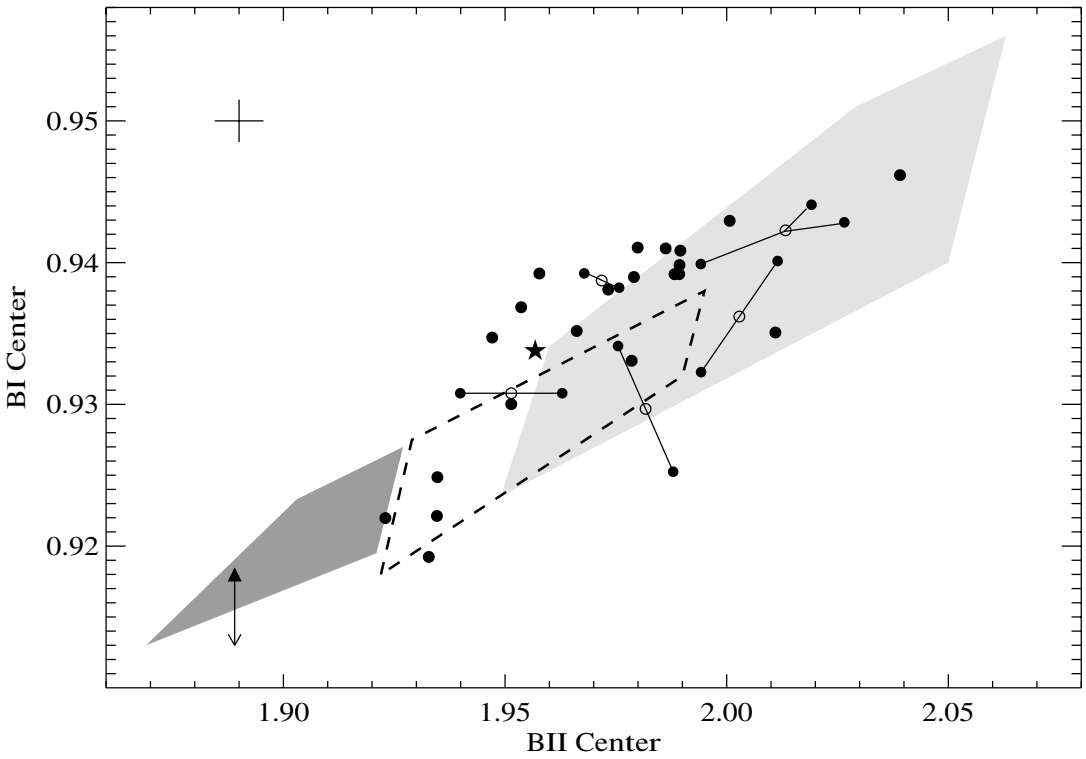

Figure 3.6 Measured band centers of V-type asteroids (solid circles). Maximal 1-sigma error bars calculated from the analysis of the spectrum of 2000 OP49 are shown in the upper left corner. The approximate boundaries for each of the HED subgroups are the same as in Figure 3.4. Multiple observations of Elisa, Jeans, Kamo, Peking and Principia are connected by the thin lines, the averages of these observations are denoted by the open circles. The temperature-corrected band centers of non-Vestoid V-type Magnya (BI center = 0.934, BII center = 1.957) is plotted as a star. The Band II center and upper limit to the Band I center for non Vestoid V-type 1995 WV7 is plotted as a triangle (lower left).

rotation periods and with multiple instruments can determine whether any systematic effects may be inherent to these SpeX data.

As previous authors have noted (Burbine et al. 2001), there appears to be a lack of diogenetic V-type asteroids in the inner Main Belt. However, we do find four objects that plot near the howardite-diogenite boundary: Harbin, Lee, 1994 TJ2 and 2000 CT102. Our measured band centers do not span the wide range of parameter space

that was claimed by Duffard et al. (2004), instead our data suggests a good correlation between the band centers of the HEDs and V-type asteroids.

We plot histograms of the asteroidal BARs in Figure 3.7. The dashed line in this figure represents all of the measured BARs that are given in Table 3.2, including the multiple observations of Elisa, Jeans, Kamo, Peking and Principia. Removing these multiple observations by averaging their respective BARs results in the histogram traced by the solid line. Again the maximum error bar calculated from the spectrum of 2000 OP49 is indicated in this figure. The range of BARs for the HEDs are over-plotted on this figure, along with the statistical mode for each of the HED subgroups. The V-type asteroids have band centers that are offset from those of the HEDs by an amount that is much greater than our maximum error bar. This discrepancy has been noted before (Duffard et al. 2005), however an explanation has yet to be found. In §3.5.1 we suggest that this may be due to either compositional differences between the HEDs and V-type asteroids or due to space weathering effects.

3.5 Spectroscopic Diversity of Inner Belt V-type Asteroids

We begin the discussion of the band analysis by considering whether any of the inner belt V-type asteroids represent distinctly non-Vestoid mineralogies. This is facilitated by first considering the spectroscopic properties of two non-Vestoid V-type asteroids in the outer Main Belt: 1459 Magnya and 21238 (1995 WV7). These are the only two non-Vestoid V-types with measured NIR spectra. From the data of Hardersen et al. (2004) we compute the band parameters of Magnya: BI center = 0.934, BII center = 1.957, and BAR = 3.758. These band centers are plotted in Figure 3.6 and are undistinguishable from the population of inner belt V-types that we have analyzed. However, the BAR of Magnya is much larger than any of the objects (asteroid or meteorite) that we have measured, thus supporting the dynamical argument that Magnya traces a non-Vestoid

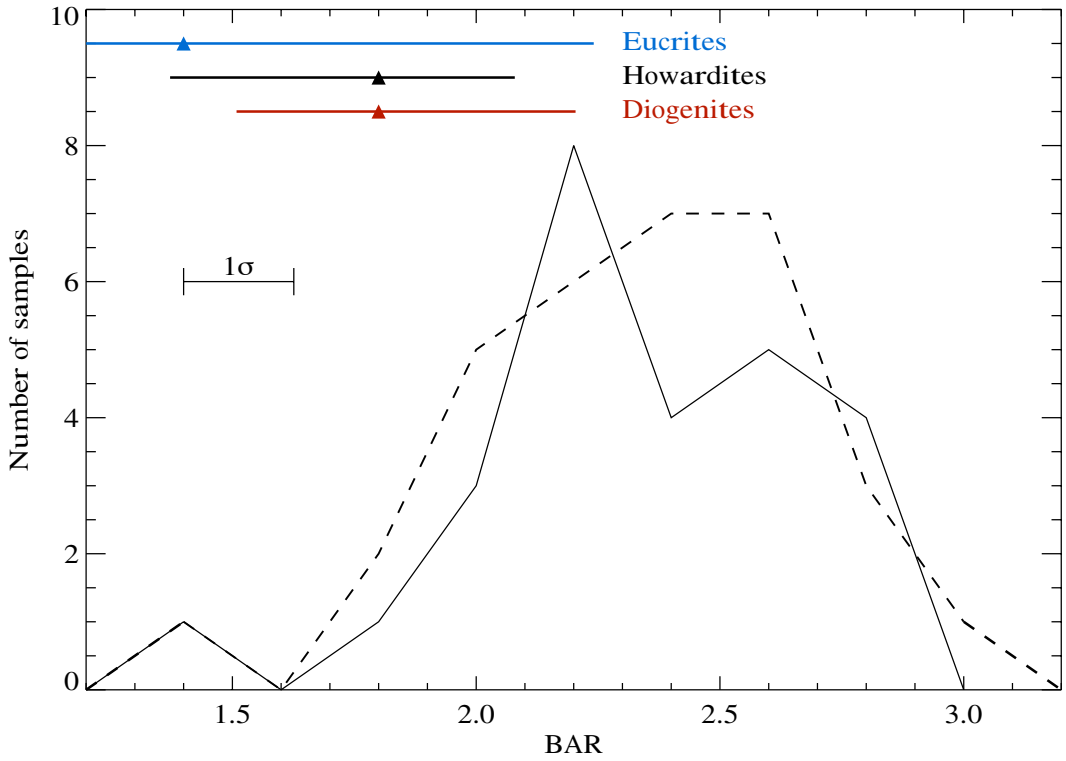

Figure 3.7 Histograms of BARs for V-type asteroids with a bin size of 0.2 units. The maximum 1-sigma error bar that was calculated from the spectrum of 2000 OP49 is indicated. The range of BARs and the statistical mode (triangles) are indicated at the top for the eucrites, howardites and diogenites. The dashed histogram includes all of the asteroid observations included in this study. The solid histogram was computed by replacing the multiple observations of asteroids Elisa, Jeans, Kamo, Peking and Principia with single sets of average band parameters. Note that the BARs of V-type asteroids are significantly higher than those of the HEDs.

differentiated parent body (Michtchenko et al. 2002). This large BAR is similar to the value obtained by Hardersen et al. (2004).

The second of the non-Vestoid V-types is asteroid 21238 (1995 WV7). Unfortunately a full ($0.5 - 2.5\ \mu m$) spectrum of this asteroid does not exist. The best available data ($0.83 - 2.46\ \mu m$) for 21238 is from the SMASS online database (http://smass.mit.edu/minus.html). From this truncated spectrum only band minima can be measured: BI minimum = 0.906, BII minimum = 1.889. Of the 26 V-type

asteroids that were analyzed, the maximum difference between the BI minimum and BI center was 0.012 μm. Assuming this as the offset between its BI minimum and center, 21238 still falls in the far lower-left corner of Figure 3.6, isolated relative to the other V-type asteroids and perhaps the sole example of a diogenetic asteroid.

The spectroscopic properties of these two non-Vestoid V-types (BAR for Magnya and inferred band centers for 21238) are unlike any of the asteroids included in our sample. Thus, the lack of any obvious spectral outliers in our set of 26 asteroids implies that they all have comparable, Vesta-like mineralogies.

It is unclear why some of the asteroids are shifted towards Band I centers that are slightly higher than those of the HEDs (Fig. 3.6). Amongst the HEDs, high Ca- and Fe-abundances push band centers to longer wavelengths (Burbine et al. 2001), however this should affect both Band I and Band II. It is possible that we have drastically underestimated the temperature corrections to the band centers (Equations 3.7 and 3.8). Another possibility may stem from the absence of visible wavelength data for some of these asteroids. This could be affecting the band analysis and pushing some objects towards longer BI centers. A final possibility is that this shift is a result of actual mineralogical differences, with V-type asteroids representing a wider range of compositions than are observed amongst the HEDs. Irrespective of the cause for this shift, we note that Figure 3.6 is a marked improvement over previous studies (e.g. Duffard et al. 2004).

We note that four objects (Harbin, Lee, 1994 TJ2 and 2000 CT102) tend to have larger BARs than the other objects in our sample and are offset towards smaller band centers from the majority of the asteroids in Figure 3.6. This apparent offset is possibly due to incomplete number statistics, with these objects representing end member mineralogies for the Vestoids.

The lack of diogenetic bodies in our sample of 26 asteroids is puzzling and remains an open mystery, one that has been previously noted in studies of V-types in the Main Belt (Burbine et al. 2001) and V-types in the NEO population (Burbine et al. 2009).

It is possible that the four asteroids near the diogenite border are mostly composed of diogenetic material with a small amount of eucritic dust contaminating their surfaces, having the effect of driving their band centers to larger values. An alternative explanation is that the removal of large km-sized fragments from diogenetic depths (~ 10s of km) within the Vesta parent body did not occur.

Lastly, we note that the asteroid Spartacus was found to have a smaller BAR (1.4661) than the rest of our sample (Fig. 3.7). This has been noted before (Burbine et al. 2001) and is thought to be related to an anomalously high olivine content relative to other Vestoids. This could be due to an origin from deep within the Vesta parent body where olivine abundances were higher than in the eucritic-diogenitic upper mantle and crust, or it could be due to an origin on another parent body. If Spartacus was removed from large depths within the Vesta parent body then we would expect other diogenetic asteroids to also be present in the Main Belt.

3.5.1 Asteroidal Versus Meteoritic BARs

A second point of discussion related to the band analysis of V-types is the large offset in BAR between the asteroids and the HEDs. It is surprising that the difference in BARs is so pronounced: the mean asteroidal BAR is 2.33 while the mean meteoritic BAR is 1.66. The origin of this offset is unclear, however effects related to terrestrial weathering of the meteorites, differences between the asteroidal and laboratory environments (e.g. temperature, grain size), instrumental systematics, compositional differences and space weathering are potential causes. We argue that only these last two possibilities are viable, with space weathering as the more likely cause.

If terrestrial weathering of the meteorites caused them to have smaller BARs, then removing found meteorites and only considering falls should reduce this offset in BAR. Of the 75 meteorite samples that were analyzed, 21 of these were observed as falls (Table A.2). Figure 3.8 shows histograms of BARs for the HED falls and V-type asteroids. After removing the found meteorites these distributions are still

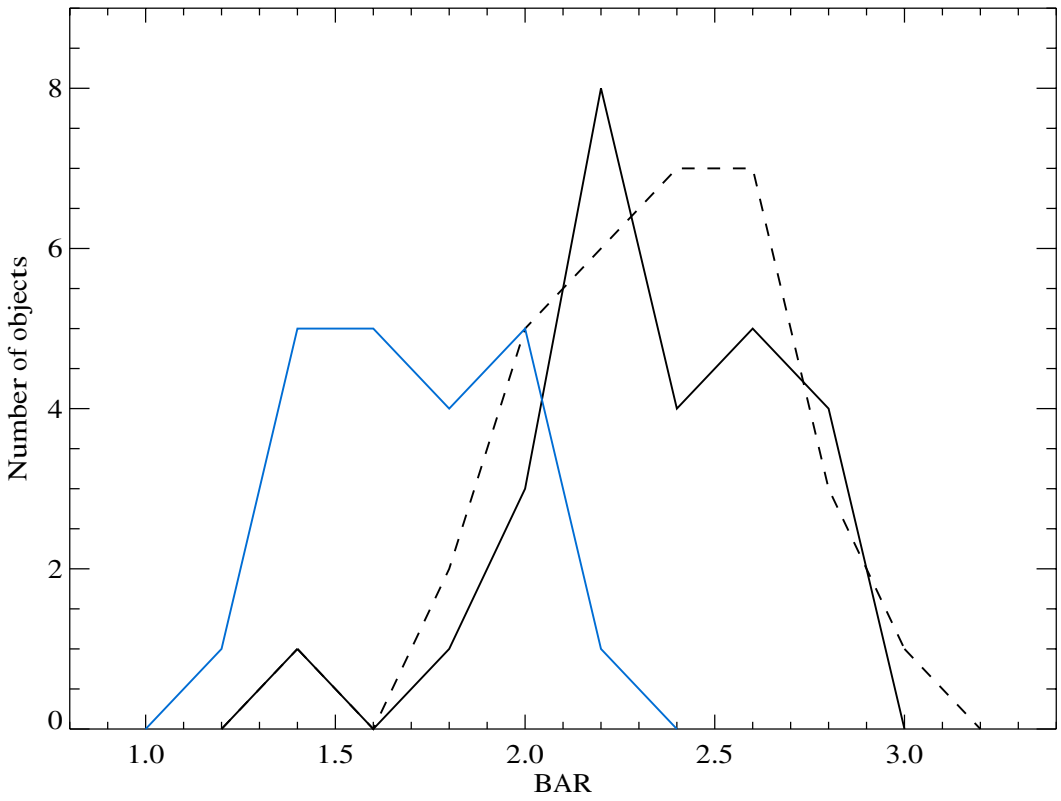

Figure 3.8 Histograms of BAR for HED falls and V-type asteroids. The dashed and solid black lines indicate the number of asteroids per bin and are the same as in Figure 3.7. The blue histogram includes only the HEDs noted as falls in Table A.2. The three HED subgroups are combined in this one histogram. The BARs of the HED falls are offset from the those of the V-type asteroids, suggesting that terrestrial weathering is not a viable cause for the discrepant BARs of these two populations.

offset by approximately the same amount: the mean BAR of HED falls is 1.67, almost identical to the mean for all HEDs (1.66). Therefore it seems unlikely that terrestrial weathering is producing the large offset in BAR.

If the asteroid's low surface temperatures were the cause of their relatively large BARs, then heliocentric distance and BAR should be directly proportional. We plot these two quantities in Figure 3.9. Although this figure shows a significant amount of scatter (which is likely due to compositional effects), there is actually an inverse relationship between BAR and heliocentric distance at a significance level of 1.9 sigma.

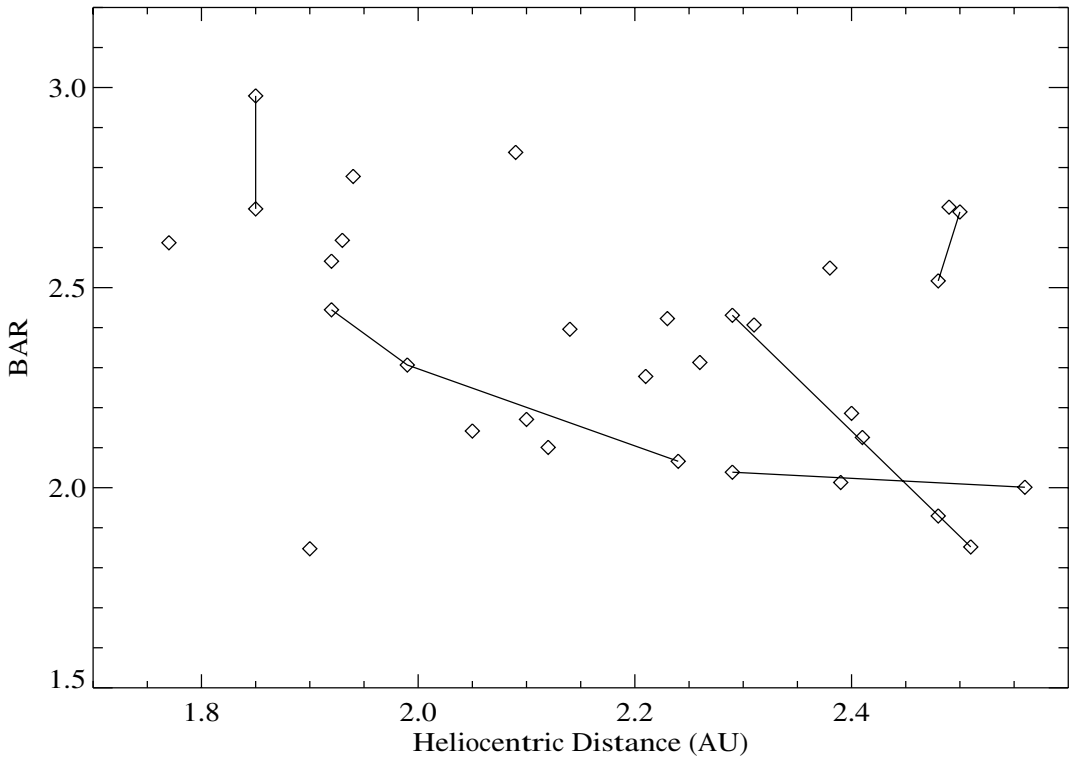

Figure 3.9 Band area ratios versus heliocentric distance at the time of observation for our full set of V-type asteroids. Multiple observations are linked together. This range of heliocentric distance corresponds to a temperature range of $\sim 160 - 200$ K. This figure shows a weak (1.9 sigma significance) inverse correlation between BAR and surface temperature.

This decrease in BAR with temperature is supported by laboratory measurements of eucritic and diogenetic samples (Hinrichs & Lucey 2002). These experiments show that with decreasing temperature the width of Band II shrinks faster than the width of Band I, thus causing BAR to drop. Therefore, the asteroidal data and these laboratory measurements suggest the opposite relationship than what would be expected if temperature were the cause of the offset between the asteroidal and meteoritic BARs.

It is unlikely that the increased thermal emission of the meteorites relative to the cold asteroids is a cause for the offset in BAR. Thermal emission from the meteorite samples causes an increase in their BII areas relative to the asteroids. This has the

effect of producing larger BARs. If this thermal emission were accounted for then the discrepancy between the meteoritic and asteroidal BARs would increase.

Grain size is also an unlikely cause for the BAR offset. Duffard et al. (2005) showed that the BARs of eucrites and diogenites increased with grain size. The particle sizes that they investigated ranged from 25 - 500 μm. They found that large grains produced BARs up to 1.9 for eucrites and a BAR of 2.04 was measured for a single diogenite. Neither of these values is high enough to overlap with the mean BAR of the V-types. Furthermore, the increase in BAR with grain size for the HEDs seems to increase quickly up 100 μm and then turns over to an almost flat distribution at larger grain sizes. If the large BARs of V-type asteroids were due to particle size, then their regoliths would have to be composed of large particles beyond the upper end of the particle size range considered by Duffard et al. (2005). This contradicts the expected small regolith grain sizes (~ 25 μm) for V-type asteroids (Hiroi et al. 1994, 1995) and the general result of polarization studies which suggest that asteroid surfaces have grains less than 300 μm in size (Clark et al. 2002).

The offset in BAR could be due to an uncorrected systematic effect inherent to the SpeX instrument or the reduction process. As shown in Figure 3.9 the variation in BAR between multiple observations of individual asteroids can, in some cases, be as large as 0.5 units in BAR. If such variation is due to uncorrected systematics then these effects may be large enough to explain the observed discrepancy between the asteroids and meteorites. However, this seems unlikely because the observations of Vesta (which were not performed with SpeX) also result in a BAR (2.55) well outside of the range displayed by the meteorites. Furthermore, reduction of SpeX data with different software packages (e.g. Kelley et al. 2003) and NIR observations of V-type asteroids with other instruments (e.g. Duffard et al. 2004) also result in large BARs. Future high-S/N observations with different NIR spectrographs will help to determine whether any systematics are affecting our results.

Compositional variation can not be ruled out as a cause for the difference between the BARs of the HEDs and the V-type asteroids. However, it seems unlikely that the composition of the HEDs would be wildly different from that of the Vestoids since these two populations are the only abundant objects with basaltic compositions in the Solar System.

Space weathering (i.e. modification of surfaces by micro-meteorite impact heating and irradiation by high energy particles) is a final possibility for explaining the large asteroidal BARs. Unfortunately little work has been done to understand the weathering of basaltic asteroids. This is partly due to claims of the "fresh" appearance of Vesta and the Vestoids (Hiroi et al. 1995; Pieters et al. 2000), an assumption that is rooted in the original finding of spectroscopic similarity between V-type asteroids and the HEDs at visible wavelengths (McCord et al. 1970; Consolmagno & Drake 1977; Binzel & Xu 1993). This dependence on visible wavelength data is problematic because it does not take into account spectroscopic information at NIR wavelengths where the most prominent and compositionally diagnostic spectral features exist.

In general, the majority of studies on the space weathering of asteroids have focused on establishing a link between the visible wavelength spectral properties of S-type asteroids and ordinary chondrite meteorites (e.g. Wetherill & Chapman 1988; Clark et al. 2002; Nesvorný et al. 2005; Willman et al. 2008). Space weathering on these bodies is thought to be analogous to that which occurs on the Moon, i.e. the production of nano-phase iron by proton bombardment and/or micro-meteorite impact results in a depression of spectral absorption features and a reddening of spectral slope (Clark et al. 2002). However, it is not clear whether these spectroscopic effects would be the same for V-type asteroids, in part because of their lower iron and olivine abundances (Burbine et al. 2001) relative to both the ordinary chondrites and typical lunar material (Lodders & Fegley 1998).

Only one series of experiments have been performed to investigate the space weathering of HED meteorites (Wasson et al. 1997, 1998). These authors use

Table 3.3 Band Parameters for Eucrite Millbillillie

Sample Info	BI Center (μm)	BI Area	BII Center (μm)	BII Area	BAR
Unaltered particulate (grain size < 75 μm)	0.942	0.151	2.025	0.234	1.553
Partially irradiated (grain size < 75 μm)	0.942	0.144	2.023	0.229	1.586
Fully irradiated (grain size > 75 μm)	0.950	0.253	1.945	0.134	0.528

laser irradiation to simulate weathering by micro-meteorite impacts. Although one eucrite (Millbillillie) and one diogenite (Johnstown) were originally included in this study, problems related to the intensity of the laser necessitated a second series of experiments in which only Millbillillie was studied. We will only discuss the results of this second set of experiments. Prior to irradiation Millbillillie was ground to particle sizes of < 75 μm. It was found that irradiation produced spherical blobs of glassy material that were similar in composition to the original sample and were typically > 75 μm in diameter. These authors divided their irradiation products into two categories (fully and partially irradiated) delineated by a cutoff in particle size at 75 μm. The fully irradiated products (> 75 μm in size) contained $\sim 95\%$ of the glassy material produced by the laser irradiation, the partially irradiated material contained the remaining 5%. We have performed our band analysis on the unaltered, partially and fully irradiated spectra (Figure 3.10) from the Wasson et al. (1998) study. The results of this band analysis are given in Table 3.3. Again the errors on these meteorite band parameters are insignificant due to the very high S/N of these laboratory data.

The spectrum of the fully irradiated material (Figure 3.10) does not resemble any of the V-type asteroids that were included in our survey (Figure A.1). Furthermore, it does not have band centers or a BAR that are comparable to any of the meteorites and asteroids that were analyzed. This suggests that the fully irradiated sample is not a

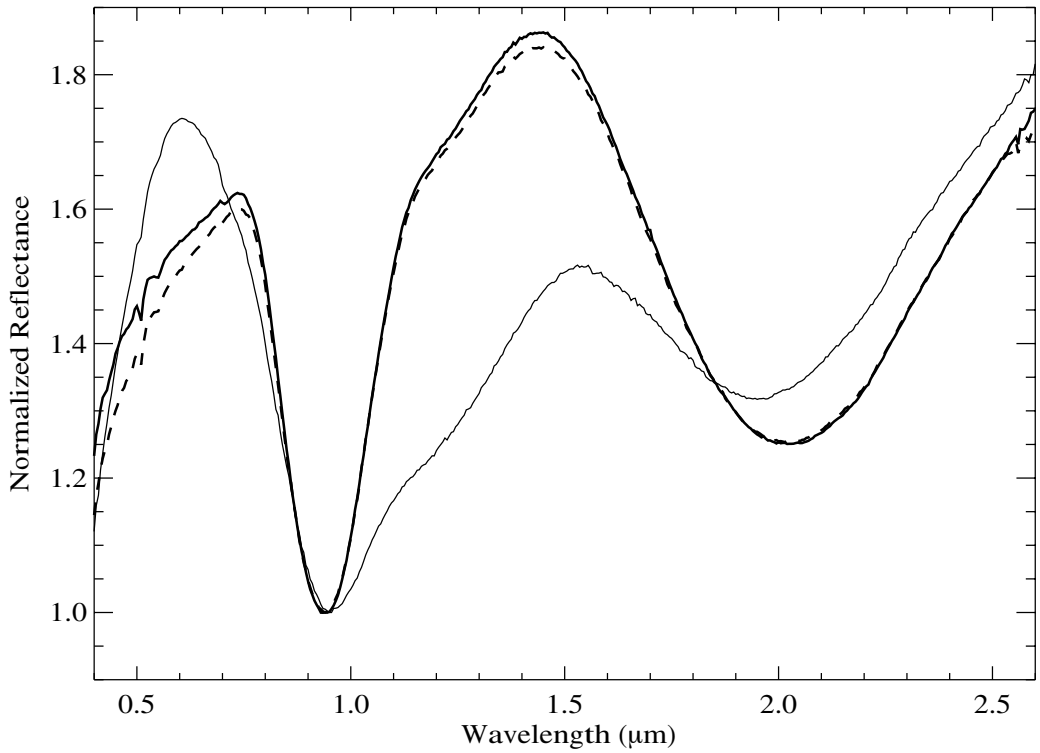

Figure 3.10 Reflectance spectra of eucrite Millbillillie from the study of Wasson et al. (1998). The spectra have been normalized by the reflectance at the wavelengths of their respective Band I centers (Table 3.3) to emphasize the change in band parameters with irradiation level. The thick black line is the unaltered particulate sample (grain size $< 75\ \mu m$). The dashed line is the partially irradiated material (grain size $< 75\ \mu m$). The thin line is the spectrum of the fully irradiated material (grain size $> 75\ \mu m$).

good analog for space weathered V-type asteroids, which is not terribly surprising due to the rather large particle sizes of this material. On the other hand the partially irradiated sample closely resembles unaltered Millbillillie material and has band centers that are typical for both the HEDs and V-type asteroids. More interesting though is that the partially irradiated sample has a BAR that is greater by $\sim 2\%$ (due to a greater decrease in the Band I area relative to Band II, see Fig. 3.10). This small fraction is far from explaining the $\sim 40\%$ offset between the BARs of the HEDs and V-type asteroids, however it does suggest the need for further study to better

understand space weathering processes on basaltic V-type asteroids. In particular, expanded irradiation and proton bombardment experiments with howardite samples (which are the best analogs to Vesta's spectrum, Pieters et al. 2006) could offer insight on the discrepancy between BARs. If the spectroscopic differences between the V-type asteroids and the HED meteorites are due to space weathering, then older, more weathered regions on Vesta's surface should have band centers similar to the HEDs, but BARs that are significantly higher. The Dawn mission (Russell & 20 co-authors 2004) will provide insight on this issue.

3.5.2 Band Parameters and Orbital Properties

Hiroi & Pieters (1998) found that V-type asteroids with values of Δv greater than 0.4 km/s tended to have visible wavelength spectra with steeper slopes and shallower 1 μm absorption bands than V-type asteroids with Δv less than 0.4 km/s. At the time, this cutoff velocity was thought to serve as an outer boundary to the Vesta dynamical family (Zappala et al. 1990). Recent hierarchical clustering method simulations (Nesvorný et al. 2008) using more complete asteroid databases (Bowell 2007) find that the Vesta family extends to values of Δv greater than 1 km/s. Thus it is not clear why Hiroi & Pieters (1998) detected a difference in spectroscopic properties for V-types that have now been incorporated into the Vesta family.

Before we revisit the spectroscopic trend suggested by Hiroi & Pieters (1998), it is worth mentioning these authors' mineralogical interpretation of their data. They propose that red slopes and shallow 1 μm absorption bands are indicative of space weathering processes on V-type asteroids. However, this claim is suspect for two reasons. First, they claim that the red slopes and shallow absorption bands of lunar basalts represent an endpoint for the weathering series of basaltic material from Vesta. As we stated earlier, it has not been experimentally established that the Vestoids would weather in the same manner as lunar material because of their lower bulk abundance of iron and olivine (Burbine et al. 2001; Lodders & Fegley 1998).

Second, this claim is based on the first series of irradiation experiments by Wasson et al. (1997), that were later discredited due to problems with the intensity of the laser. Again, further work is needed to better understand the weathering of basaltic material before the effects claimed by Hiroi & Pieters (1998) can be validated or refuted.

The analysis of Hiroi & Pieters (1998) was based on the visible wavelength spectra from Binzel & Xu (1993). The two parameters used to quantify the spectral properties of these data were "visible redness" and depth of the 1 μm absorption feature, both of which were defined relative to the reflectance peak near 0.7 μm that is characteristic of V-type asteroids. Visible redness was defined as the difference in reflectance between the peak and the reflectance at 0.55 μm. Their 1 μm band depth was defined as the difference in reflectance between the peak and the Band I minimum. Our set of asteroidal spectra does not include visible wavelength data for each asteroid, thus we are unable to measure visible redness. However, if the Vestoids have weathered surfaces with spectral slopes intermediate to the HEDs (no slope) and lunar basalt (large red slope) as Hiroi & Pieters (1998) claim, then the effect of weathering should also occur at NIR wavelengths as it does for lunar samples (Clark et al. 2002). Therefore we use Band I slope as a proxy for visible redness. Future visible wavelength observations will be used to compute visible redness for each of the asteroids in our data set so that this assumption of the equivalence between visible redness and Band I slope will not be necessary.

The Band I depths versus Band I slopes for our 26 V-type asteroids are plotted in Figure 3.11. Each asteroid in this figure is plotted as a filled circle with sizes that are proportional to the asteroid's ejection velocity relative to Vesta (Δv). The values for Δv were calculated using Equations 3.1, 3.2 and 3.3. Table 3.4 lists the band depths and Δv velocities for each of these asteroids. This figure does not display marked correlation between the three quantities Δv, Band I slope and Band I depth. In particular, V-types with large values of Δv are not preferentially distributed at large values of Band I depth and Band I slope as might be expected from the results of Hiroi

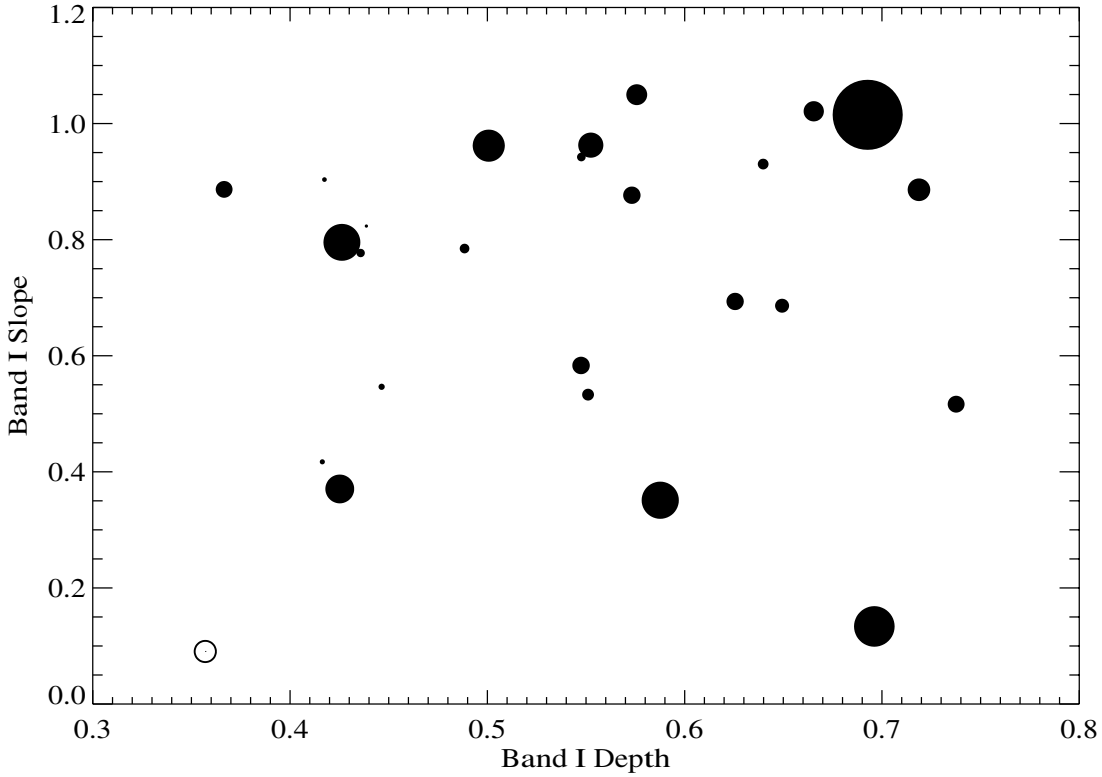

Figure 3.11 Band I depth versus Band I slope for V-type asteroids in the inner Main Belt. Each asteroid is represented by a filled circle whose size is proportional to its ejection velocity relative to Vesta (Δv). The Band I slopes are given in Table 3.2 and the Band I depths and Δv are given in Table 3.4. The asteroid with the maximum ejection velocity is 2000 JK66 (Δv = 3.3 km/s), the asteroid with the minimum is Lee (Δv = 0.15 km/s). Vesta (open circle) plots in the lower left of the figure.

& Pieters (1998). Our inability to reproduce these author's results may be related to the assumed equivalence between visible redness and Band I slope, however only three objects (Vesta, Kollaa and Lee) are shared in common between the two data sets. NIR observations of the V-type asteroids that Hiroi & Pieters (1998) categorize as "non Vesta family" objects are needed to investigate these issues.

We conclude this discussion by investigating the possibility of relationships between other band parameters and orbital properties. If the inner Main Belt contains V-type asteroids from multiple parent bodies or fragments from the surface of Vesta

Table 3.4 Band Depths and Δv for V-type Asteroids

Object	Band I Depth	a (AU)	e	i (degrees)	Δv
2000 CT102	0.665	2.331	0.144	5.45	0.954
Celle	0.446	2.415	0.108	6.10	0.292
Elisa	0.552[a]	2.298	0.158	6.41	1.185
1999 GG2	0.588	2.144	0.135	3.39	1.752
Gustaffson	0.501	2.247	0.098	2.79	1.514
Harbin	0.626	2.478	0.120	7.79	0.816
2000 JK66	0.693	2.213	0.241	10.13	3.300
Jeans	0.426[a]	2.404	0.179	4.32	1.739
Kamo	0.416[a]	2.417	0.098	6.61	0.240
Kirghizia	0.547	2.450	0.104	4.42	0.823
Kitezh	0.436	2.335	0.112	5.64	0.394
Kollaa	0.548	2.363	0.114	7.07	0.407
La Palma	0.640	2.289	0.117	6.74	0.506
Lee	0.439	2.343	0.098	6.69	0.153
Lepage	0.551	2.296	0.075	6.60	0.557
Lundia	0.576	2.283	0.145	6.74	0.984
Menchu	0.696	2.287	0.139	2.04	1.911
2000 OP49	0.719	2.276	0.111	3.92	1.066
Patterson	0.488	2.299	0.094	7.25	0.455
Peking	0.417[a]	2.380	0.090	6.68	0.219
Principia	0.649[a]	2.443	0.115	5.08	0.659
1987 SM3	0.367	2.196	0.106	5.92	0.791
Spartacus	0.738	2.210	0.081	5.89	0.795
1994 TJ2	0.573	2.342	0.123	4.66	0.819
Vesta	0.357	2.362	0.099	6.36	0.000
1999 XC143	0.425	2.486	0.142	3.78	1.357

The columns in this table are: object designation, Band I depth, proper semi-major axis, eccentricity and inclination, and the ejection velocity of the objects relative to Vesta.
[a]Represents an average band depth from multiple spectra.

that were ejected at different epochs (Nesvorný et al. 2008) then it is reasonable to suggest that there might be a correlation between spectroscopic and orbital properties, either due to a non-Vestoid parent body or a longer interval of space weathering relative to the main Vestoid population. To test this hypothesis we compute the Spearman rank probability of correlation between each of the band parameters and orbital elements of the asteroids (Table 3.5). This table shows that the probability of correlation between the band centers and inclinations is approximately 99.2%.

Table 3.5 Spearman Rank Probability of Correlation Between Band Parameters and Orbital Elements

	Semi-major Axis	Eccentricity	Inclination	Δv
BI Center	11.99	15.64	**99.20**	77.26
B1 Slope	82.86	88.20	92.26	57.00
B2 Center	25.37	67.94	**99.16**	34.98
B2 Slope	72.70	82.64	96.42	46.08
BAR	5.15	63.62	97.72	26.50

This table lists the probability (based on a Spearman rank test) that a given orbital parameter is correlated with a given band parameter. The two bold-face probabilities correspond to a correlation that is significant at a level of 2.5 sigma.

The other orbital elements show essentially no correlation ($< 90\%$) with the band parameters. This band center-inclination trend is marginally significant and will require additional spectroscopic data to determine whether it is robust.

If we assume that this band center-inclination trend is real, then we can speculate as to what it may mean for the interpretation of V-type asteroids in the inner Main Belt. We plot the band centers for each of the asteroids in Figure 3.12 with symbols that are proportional in size to the proper orbital inclination of each asteroid. Multiple observations for individual asteroids are averaged and represented by a single data point. This figure shows that the 5 lowest inclination V-types (Gustaffson, 2000 OP49, 1999 GG2, Menchu and 1999 XC143) have band centers that are near the upper edge of the asteroidal band center distribution. This finding is compelling in light of the dynamical study of Nesvorný et al. (2008). Unable to reproduce the orbits of low inclination V-types in the inner Main Belt, Nesvorný et al. (2008) conclude that these basaltic asteroids are either from a non-Vestoid parent body or are scattered remnants of a pre-LHB Vesta family. The possibility that these objects are spectroscopically distinct seems to complement this dynamical result. If this band center-inclination

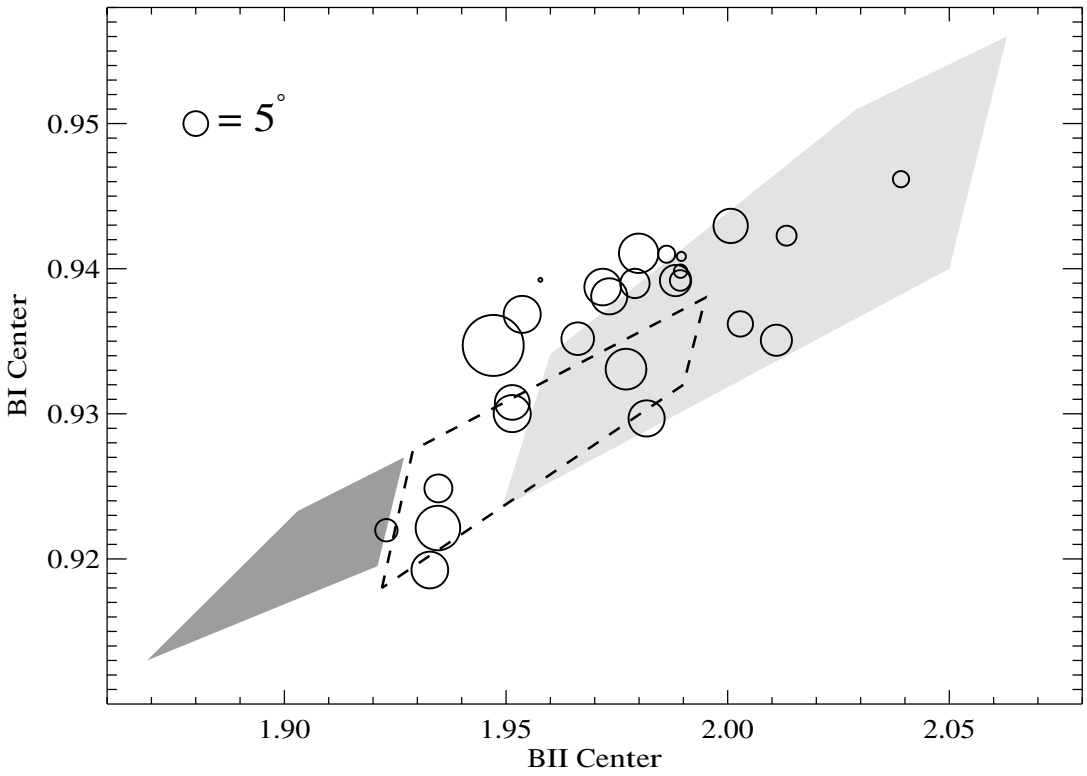

Figure 3.12 Band centers for V-type asteroids with the size of the symbols proportional to orbital inclination. Multiple observations for individual asteroids are combined into average values. The regions shaded in grey and outlined by the dashed line are the same as in Figures 3.4 and 3.6. A legend for the symbol size corresponding to 5° is shown in the upper left. Asteroids with low inclinations tend to have longer wavelength band centers.

trend is a result of two distinct populations of inner Belt V-types, then band centers at relatively long wavelengths should be a characteristic feature of other low inclination basaltic asteroids.

3.5.3 Summary of Inner Main Belt V-type Asteroids

In this section we have shown that there does not appear to be any correlation between the NIR spectral slope and orbital properties for V-types in the inner belt. This is in contrast to the visible wavelength findings of Hiroi & Pieters (1998). Future

observations at visible wavelengths for all 26 of the V-type asteroids in our sample may help to clarify this issue. With our higher S/N data we have been unable to reproduce the wide range of Vestoid band centers that was reported by Duffard et al. (2004). In particular, we find a much tighter correlation between the band centers of the V-type asteroids and the HED meteorites. We were able to confirm an offset in BAR between the HEDs and V-type asteroids (Duffard et al. 2004) and argue that this may be caused by space weathering effects. We did not find any evidence to suggest the presence of V-type asteroids with non-Vestoid mineralogies (e.g. Magnya and 1995 WV7) in the inner Main Belt. Finally, we have reported that V-type asteroids with low inclinations in the inner Main Belt may be spectroscopically distinct with a tendency towards longer wavelength band centers. This is in agreement with the dynamical results of Nesvorný et al. (2008), however additional data should be obtained to confirm or refute the significance of this finding.

3.6 Extreme Case: Outer Main Belt Asteroid 10537 (1991 RY16)

The paucity of non-Vestoid basaltic material in the Main Belt has motivated a number of recent searches (Moskovitz et al. 2008a; Roig & Gil-Hutton 2006; Hammergren et al. 2006; Binzel et al. 2007) that utilize the Sloan Digital Sky Survey Moving Object Catalog [SDSS MOC, Ivezic et al. (2002)] to identify taxonomically unclassified asteroids whose photometric colors indicate basaltic surface material. This usefulness of this technique lies in its ability to identify V-type candidates that are unlikely to have any dynamical association to Vesta. The most likely region of the Main Belt where V-type asteroids are distinctly non-Vestoid is beyond the 3:1 mean motion resonance at 2.5 AU (Nesvorný et al. 2008; Roig et al. 2008). There are currently four known V-type asteroids in this region of the Main Belt. These four objects and their Δv velocities relative to Vesta are: 1995 WV7 (1.9 km/s), Massevitch (2.6 km/s), Magnya

(4.2 km/s) and 1999 RL95 (2.6 km/s). NIR spectra of these objects offer the opportunity to investigate the specific spectral properties of non-Vestoid basaltic mineralogies (§3.5). In this section we present the optical and near-infrared (NIR) spectroscopic follow-up of another outer Main Belt V-type asteroid, 10537 (1991 RY16). This object is classified as a Vw-type in the DeMeo et al. (2008) taxonomic system, meaning that it falls within the V-taxonomic class, but has a steep red slope. The orbital elements of 10537 ($a = 2.85$ AU, $e = 0.07$ and $i = 7.25°$) place it exterior to the 3:1 resonance with a value of $\Delta v = 1.5$ km/s, suggesting that it is not a fragment from Vesta.

3.6.1 Observations

We obtained low-resolution visible spectra of 10537 on 1 October 2006 with the Echellette Spectrograph and Imager (ESI) on the Keck II telescope (Sheinis et al. 2002). Three 900-second exposures were obtained and an average of solar analog stars SA110-361, SA113-276 and SA93-101 were observed for calibration. Confirmation observations were performed on 18 January 2007 with the Supernova Integral Field Spectrograph (SNIFS) on the University of Hawaii 2.2 m telescope (Lantz & 14 co-authors 2004). Four 900-second exposures were obtained and solar analog star SA105-56 was observed for calibration. Details on the instrumental setup and reduction of ESI and SNIFS data are provided in §2.4.

On 30 January 2008 NIR follow-up observations were performed with SpeX (Rayner et al. 2003) on NASA's Infrared Telescope Facility (IRTF). Forty-one 200-second exposures were obtained. The telescope was operated in a standard ABBA nod pattern and SpeX was configured in its low resolution (R=250) prism mode with a 0.8" slit for wavelength coverage from 0.8 - 2.5 μm. Solar analogs Hyades 64 and SA 102-1081 were observed for calibration and telluric correction. The IDL-based SpeXtool package (Cushing et al. 2004) was used for data reduction.

Figure 3.13 shows that neither V-type asteroids Magnya and Vesta nor R-type asteroid 349 Dembowska (which we argue in §3.6.3 is a possible parent body for 10537)

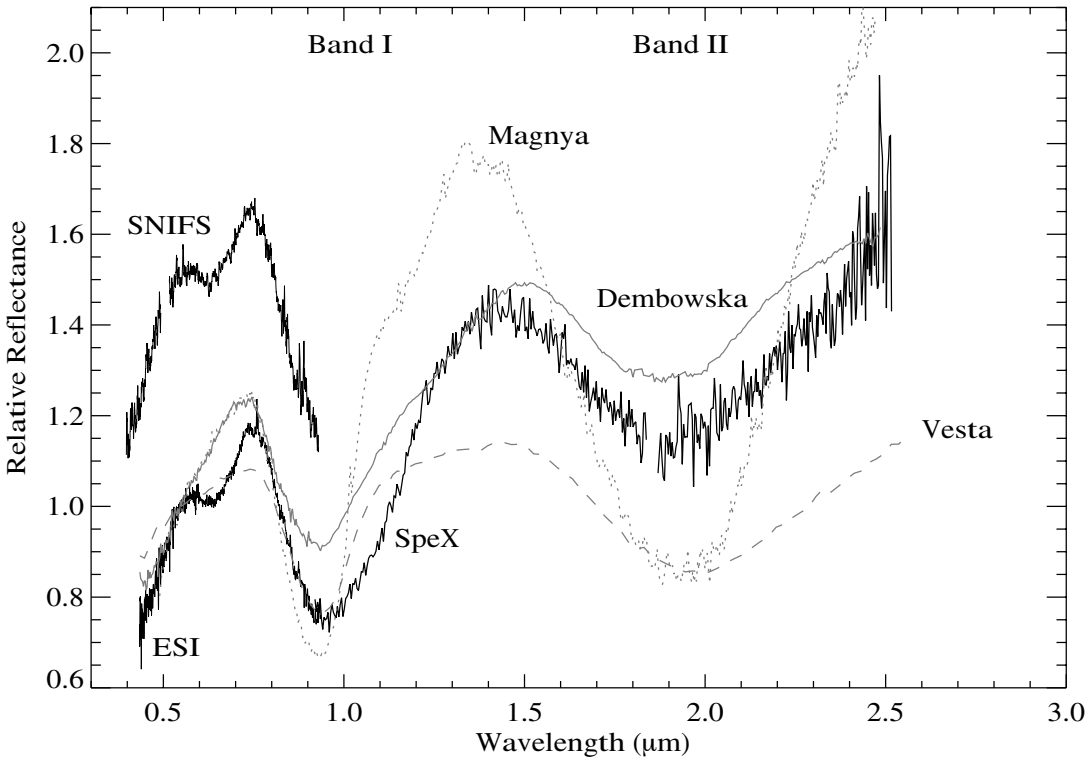

Figure 3.13 ESI, SNIFS and SpeX spectra of asteroid 10537 (solid black lines). The transition from the ESI to SpeX data occurs at $0.96\ \mu m$. The visible-wavelength spectra have been normalized at 0.55 μm and the SNIFS data have been offset for clarity. Independent observations of 10537 are in agreement with these data (Duffard & Roig 2008). The NIR data have been normalized by a scaling factor that was calculated by minimizing the chi-squared statistic between the overlap of the ESI and SpeX data ($0.75 - 0.95\ \mu m$). Spectra of V-type asteroids 1459 Magnya (Hardersen et al. 2004) and 4 Vesta (Gaffey 1997) and R-type asteroid 349 Dembowska, all normalized at 0.55 μm, are shown for comparison.

are close spectral matches to 10537. Based on a chi-squared comparison of visible-NIR spectra, we do not find any V-type asteroids in the Main Belt or near-Earth populations that are as close a spectral match to 10537 as Dembowska. Relative to V-type asteroids, the $1\ \mu m$ band of 10537 is broader and its $2\ \mu m$ band is shallower and better matched by an R-type spectrum.

3.6.2 Spectral Interpretation and Mineralogical Analysis

NIR Data

As a first order approach to characterizing the spectrum of 10537 we performed a spectral band analysis (§3.2). Without an asteroidal or meteoritic analog to the spectrum of 10537 or knowledge of its albedo, more sophisticated analyses based on Modified Gaussian (e.g. Sunshine et al. 1990) or Hapke mixing models (e.g. Lawrence & Lucey 2007) are impractical.

With a heliocentric distance of 2.44 AU at the time of NIR observation, 10537 has temperature-corrected (Equations 3.7 and 3.8) band centers of: BI center = $0.962 \pm 0.001\ \mu m$, BII center = $1.919 \pm 0.011\ \mu m$ and the band area ratio (BAR) of BII to BI = 1.337 ± 0.095 (Fig. 3.14). The error bars are determined in the same manner as in §3.1. The BAR could be smaller depending on the actual shape of the 0.63 μm absorption feature, however we estimate a lower limit to the BAR of 0.9, a value which does not significantly affect the following discussion.

The location of 10537 in Fig. 3.14 does not suggest a definitive association with any specific meteorite type: both ordinary chondrites (OCs, Marchi et al. 2005) and basaltic achondrites (BAs, Duffard et al. 2005) are known to exist in the region of the band diagram occupied by 10537. Nevertheless, useful insight can be gained from Fig. 3.14 in spite of the mineralogical ambiguity that is characteristic of this band analysis (McCoy et al. 2007).

The location of 10537 above the olivine-orthopyroxene mixing line in Figure 3.14 suggests that its surface contains a mixture of low- and high-Ca pyroxene and olivine. The BI and BII centers imply the presence of Fe-rich low-Ca pyroxenes (Adams 1974). The pronounced 1- and 2-micron bands (Fig. 3.13) suggest negligible space weathering, a property that is characteristic of Vesta and the Vestoids (Pieters et al. 2000). This ensemble of characteristics implies that 10537 may be achondritic and derived from a partially or fully differentiated parent body.

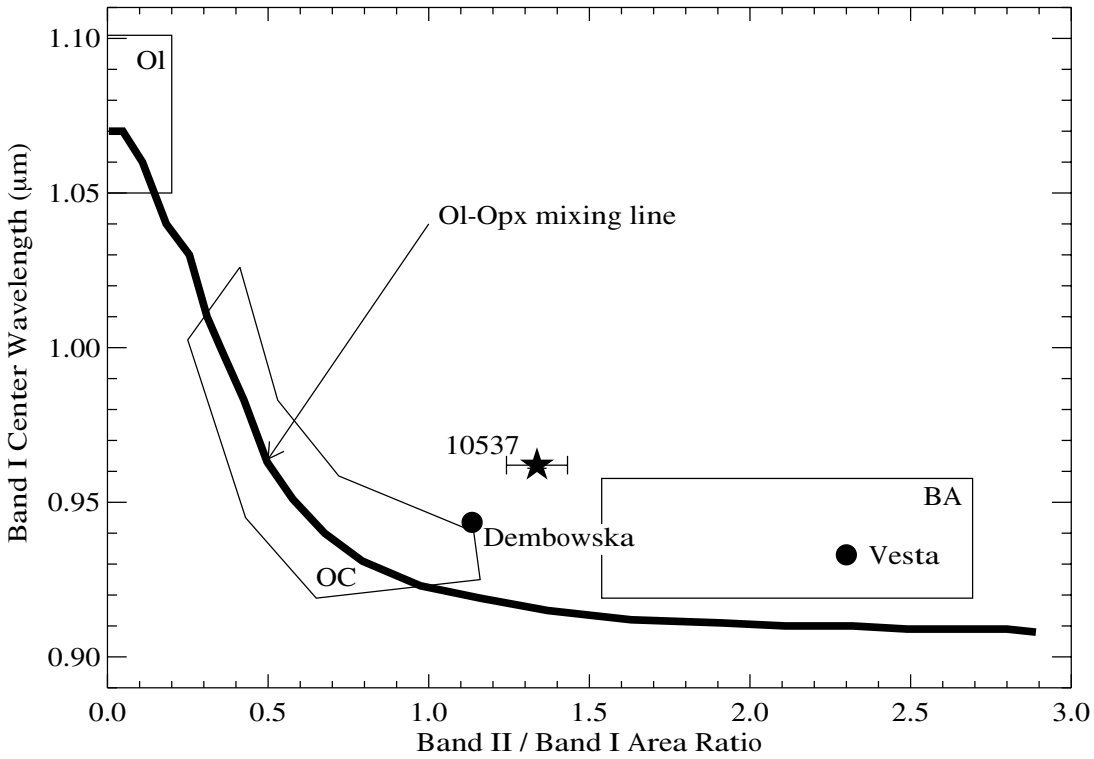

Figure 3.14 Band diagram adapted from Gaffey et al. (1993b). The bold line indicates the olivine-orthopyroxene (Ol-Opx) mixing curve which traces a range of compositions from pure olivine (upper left) to pyroxene-dominated (lower right). The regions occupied by the ordinary chondrite (OC) and basaltic achrondrite (BA) meteorites are outlined. Vestoids tend to fall within the BA region. 10537 is indicated by a star and Vesta and Dembowska by filled circles (Gaffey et al. 1993b). The errors on the Vesta and Dembowska values are comparable to the size of the symbols. Magnya plots off the figure to the right of Vesta with a BAR ~ 4 (Hardersen et al. 2004).

Visible Data

10537 displays an unusually deep absorption band at $0.63\ \mu m$ whose mineralogical interpretation is difficult because it is unprecedented amongst asteroids, rare in meteorites, and spans wavelengths that are populated with numerous solid state transitions. The eucrite meteorite Bouvante has a similar band around $0.65\ \mu m$, which may be caused by ilmenite ($FeTiO_3$) or minor elements (such as Cr) in its pyroxene crystal structure (Burbine et al. 2001). We suggest a number of other possibilities,

however future studies will be necessary to properly constrain the mineralogical cause of this feature.

One possibility is $Fe^{3+} \rightarrow Fe^{2+}$ charge transfer reactions between crystallographic sites in the pyroxene structure (Mao & Bell 1972). Ferric iron (Fe^{3+}) could have been inherited from the 10537 parent body, deposited on its surface by impacts with other bodies, or produced by shock-induced oxidation of Fe^{2+} in pyroxenes (Shestopalov et al. 2007). The 0.63 μm feature could also be attributed to the presence of other transition metal cations. Cr^{3+} is a likely candidate with other possibilities including Mn, V and Ti species (Cloutis 2002). Cr^{3+} abundances greater than 1 oxide-weight-percent in terrestrial pyroxenes are sufficient to produce large absorption features at 0.63 μm (Cloutis 2002). Silicate Cr abundances are generally less than 1% in the HED meteorites (Mittlefehldt et al. 1999). Thus it is not surprising that none of the Vestoids or HEDs display a prominent 0.63 μm band (Binzel & Xu 1993; Bus & Binzel 2002b; Lazzaro et al. 2004; Alvarez-Candal et al. 2006; Mittlefehldt et al. 1999).

Another possible source for this feature is spinel (Cloutis et al. 2004). In the NIR, spinel would increase the BAR without affecting the BI position, thus explaining why 10537 plots to the right of the Ol-Opx mixing line in Fig. 3.14. The presence of spinel, a product of metamorphic processes that is often produced in silicate melts that are rich in Al and depleted in alkali metals, would also suggest that 10537 is derived from a partially or fully differentiated parent body.

Other explanations for the 0.63 μm feature are less likely: a feature attributed to iron oxides in phyllosilicates on C-type asteroids (Vilas et al. 1993) occurs at slightly longer wavelengths ($\sim 0.7\ \mu m$), the faint iron oxide and spinel-group features observed in the spectra of S-types have band centers on either side of $0.63\ \mu m$ (Hiroi et al. 1996) and, although spin-forbidden Fe^{2+} transitions were suggested by di Martino et al. (1995) to explain a similar (but not as deep) feature in the spectrum of V-type NEA 6611 (1993 VW), these transitions occur at shorter wavelengths than 0.63 μm (Burns et al. 1973).

The prominence of this feature suggests a regolith with large grain sizes (e.g. a freshly exposed surface) or an unusually high abundance of the source mineral. It is unlikely that this feature is related to impact contamination which would have produced compositional heterogeneity across the surface, for which there is no evidence from our two visible spectra (Fig. 3.13).

3.6.3 Discussion of 10537

We have shown that 10537 is a spectroscopically unique asteroid whose composition may be suggestive of a partially or fully differentiated parent body. Its diameter is between 5 and 15 km, as determined from a plausible range of albedos (0.05-0.4) and an absolute magnitude of $H = 12.9$, and therefore is unlikely to represent an intact differentiated body (Hevey & Sanders 2006) that has remained unfragmented since the time of planet formation (Bottke et al. 2005b).

It is unlikely that 10537 is a scattered Vestoid because it orbits exterior to the 3:1 mean motion resonance (Michtchenko et al. 2002; Roig et al. 2008; Nesvorný et al. 2008). We numerically integrated the orbit of this asteroid and the four planets, Earth, Mars, Jupiter and Saturn using the N-body integration package MERCURY (Chambers 1999). Our simulations show that the orbit of 10537 is stable over 2 Gyr and presently is not in any mean-motion resonance with other planetary bodies.

10537 is not a member of any major asteroid family or near any other of our non-Vestoid basaltic candidates (Fig. 3.15). Interactions with nearby non-linear secular resonances may have aided its orbital migration away from any parent body, particularly in inclination. Two such resonances are the $g + s - g_6 - s_6$ and the $g + s - g_5 - s_7$ (Milani & Knezevic 1990, 1992). The former resonance for an eccentricity of 0.08 is shown in Fig. 3.15. Accounting for the slightly larger eccentricity of 10537 would move this resonance to higher inclinations and closer to the orbit of 10537, thus increasing its relevance to the dynamical evolution of this body.

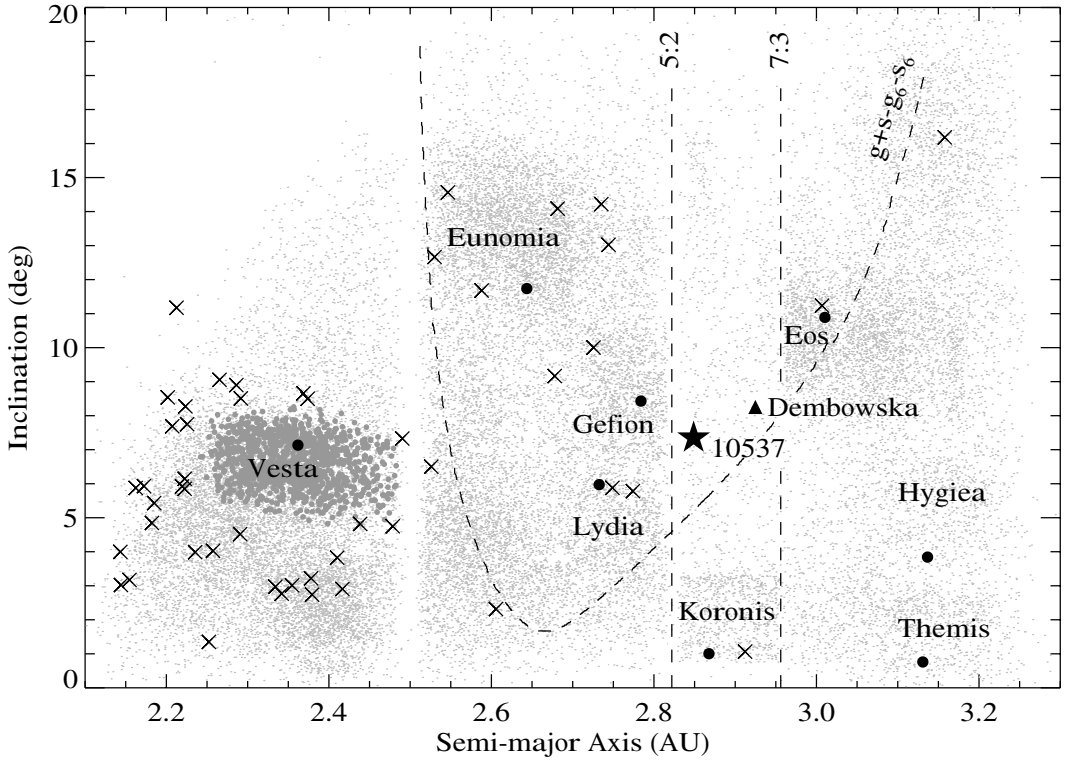

Figure 3.15 Osculating semi-major axis versus inclination for SDSS MOC asteroids (small dots), our basaltic candidates ($\times$'s), Vestoids (filled grey circles), 10537 ($\star$) and Dembowska (triangle). The major families in the vicinity of 10537 are labeled and the parent body for each are plotted as filled black circles. 10537 shows no obvious correlation with any of these major families nor is it near any other of our basaltic candidates (Moskovitz et al. 2008a). The 5:2 and 7:3 mean motion resonances with Jupiter and a nonlinear secular resonance with Saturn are shown as dashed lines.

It is likely that the Yarkovsky effect also played a role in the orbital evolution of 10537. The maximum Yarkovsky drift in semi-major axis over 4.5 Gyr for a 5-km body (a lower limit for 10537) is ~ 0.1 AU (Bottke et al. 2001). This distance rules out the possibility that 10537 originated from the Eunomia or Eos families which may be derived from partially melted or differentiated parent bodies (Nathues et al. 2005; Mothé-Diniz & Carvano 2005). Furthermore, 10537 would have had to pass through the 5:2 or 7:3 mean-motion resonance with Jupiter to reach its current orbit,

a migration that would have been slower for a 5-km body (Bottke et al. 2001) than the dynamical lifetime of an asteroid in the 7:3 resonance (Tsiganis et al. 2003).

One possible parent body for 10537 is the large (~ 140 km) Main Belt asteroid 349 Dembowska. Dembowksa is one of only four known R-type asteroids in the Main Belt (Bus & Binzel 2002a) and like 10537 has an uncertain surface mineralogy. Abell & Gaffey (2000) suggest that Dembowska has undergone some igneous processing and resembles an acapulcoite or a lodranite meteorite, differentiated achondrites that are thought to be representative of various depths within a body that experienced a few to 15% partial melting (Taylor et al. 1993). Feierberg et al. (1980) suggest that it is the cumulate mantle of a fully differentiated body. Gaffey et al. (1993b) suggest it is the residue from the silicate melt of a partially differentiated body (i.e. a partially melted body whose basaltic crust was removed). It has also been suggested that Dembowska is a space weathered ordinary chondrite (Hiroi & Sasaki 2001).

Regardless of Dembowska's interpreted mineralogy, compositional heterogeneity across its surface (Abell & Gaffey 2000) implies that a cratering event could have produced fragments like 10537. The spectral similarity between 10537 and Dembowska is consistent with this interpretation (Fig. 3.13): the difference of $\sim 10\%$ between these spectra is less than the spectral variation amongst the Vestoids. Depending on its specific mineralogical origin, the 0.63 μm feature in the spectrum of 10537 may or may not argue against a genetic relation to Dembowska. Dembowska's BAR of 1.135 and BI center of 0.9435 (Gaffey et al. 1993b) place it near 10537 in Fig. 3.14. From a purely dynamical stand point, a combination of ejection velocity (Marchi et al. 2004), interactions with secular resonances and the influence of the Yarkovsky effect suggest that 10537 could have migrated to its current orbit from the surface of Dembowska.

In spite of these similarities we note that Dembowska is merely the closest available analog to 10537 and may not be directly related in a petrogenetic sense. Under the standard paradigm of primordial clearing of the asteroid belt (Bottke et al.

2005b) most large bodies were disrupted, leaving behind representative fragments. This is a likely explanation for basaltic asteroid Magnya (Michtchenko et al. 2002) and may apply to 10537 as well.

More robust mineralogical analyses and detailed dynamical simulations will be necessary to better characterize 10537. A spectroscopic survey of asteroids in the dynamical space surrounding 10537 could reveal the presence of other similar bodies and establish or refute any connection to Dembowska. However, irrespective of whether these two asteroids are related, the spectral properties of 10537 indicate that there is more mineralogical diversity in the Main Belt than can be accounted for by traditional taxonomic definitions of asteroid families.

Chapter 4

The Thermal Evolution of Planetesimals

Following the observational investigations of the previous chapters, we now turn to a theoretical analysis of the thermal evolution of small (< 1000 km) proto-planetary bodies. Particular attention is paid to metal-silicate differentiation and the subsequent formation of basaltic material. The ultimate goal of this chapter is to provide a theoretical framework to better understand the conditions in the early Solar System that resulted in a large number of differentiated metallic cores (represented by the iron meteorites and M-type asteroids) and a relative scarcity of basaltic objects (Chapter 2). This is achieved by outlining key steps and processes that were relevant to the differentiation and partial melting of planetesimal-size bodies. Detailed numerical models are not used to investigate these issues; instead we employ the simplest treatment that can reasonably describe a given physical phenomenon. However, numerous areas in need of further investigation, either through detailed modeling or expanded laboratory experiments, are noted.

This discussion begins with an overview of the physics involved in the gravitational segregation of metal and silicates, i.e. the process of core formation (§4.1), and then moves on to the formation of basalt by the fractionation of partially molten silicate rock (§4.2). The primary aim of these two sections is to provide insight on the time scales involved in the differentiation process and how those compare to heating time scales.

The chapter continues with a series of calculations designed to illuminate two physical process that may have had an influence on the thermal histories of planetesimals, yet have not been considered in detail by previous investigators (e.g. Grimm & McSween 1989; Cohen & Coker 2000; Young et al. 2003; Hevey & Sanders 2006). The first of these (§4.3) considers the thermal consequences of melt migration by accounting for the preferential partitioning of Al in the early stages of a silicate partial melt (recall that the decay of ^{26}Al was a primary source of thermal energy in the early Solar System, Chapter 1). The second set of calculations (§4.4) considers the thermal consequences of water in the interior of planetesimals, namely the effects of exo- and endothermic energy released from chemical serpentinization reactions between liquid water and silicate rock. Both of these processes are found to dampen the peak temperatures of planetesimals and thus may have been important in limiting the number of fully differentiated bodies that formed.

This chapter concludes with the presentation of a simple 1-dimensional model of heat conduction (§4.5), which is first used as a tool to determine the lower size limit of planetesimal that could have undergone differentiation (§4.6). The output of the model is then combined with the theoretical results of the previous sections to provide a synthesis of the relevant processes, time scales and sizes associated with the differentiation of planetesimals (§4.7).

The calculations and models presented in this chapter employ a number of variables, constants and parameters. In Table 4.1 we present each of these quantities with the symbols, units and values (when relevant) that are used in the following sections. Citations for the adopted values and more detailed definitions appear in the text.

4.1 Metal-Silicate Segregation

The eutectic melting temperature in the Fe-S system is ~ 1200 K, lower by a few hundred degrees than the temperatures at which silicates begin to partially melt

Table 4.1 Symbols and Definitions

Symbol	Name and definition	Value [Units]
T	Temperature	[K]
t	Time	[s]
t_{acc}	Time of accretion	[s]
ϕ	Net melt fraction by weight	-
R	Radius of body	[m]
r	Radial variable	[m]
z	Depth	[m]
a	Grain size	[m]
μ	Viscosity	[Pa s]
$\Delta\rho$	Density contrast between solid and liquid	[kg/m^3]
$\bar{\rho}$	Mean bulk density	[kg/m^3]
V_D	Darcy velocity (Eqn. 4.5)	[m/s]
V_S	Stokes velocity (Eqn. 4.1)	[m/s]
$Q(t)$	SLR decay energy generation rate (Eqn. 4.23)	[J/kg/s]
f_{Al}	Abundance of Al in chondrites	2.62×10^{23} 1/kg
E_{Al}	^{26}Al decay energy per atom	4.0042 MeV = 6.4154×10^{-13} J
$\tau_{1/2}$	^{26}Al half life	0.74 Myr
τ_{Al}	^{26}Al mean life, = $\tau_{1/2}$ / ln(2)	1.07 Myr
τ_{mig}	Melt migration time scale (Eqn. 4.8)	[s]
C_ℓ	Concentration of ^{26}Al in the liquid phase	[1/kg]
C_s	Concentration of ^{26}Al in the solid phase	[1/kg]
C_{tot}	Total concentration of ^{26}Al, = C_ℓ + C_s	[1/kg]
D	Al Partition Coefficient	-
c_p	Specific heat at constant pressure	[J/kg/K]
k	Thermal conductivity	[W/m/K]
κ	Thermal diffusivity, = k / ($\bar{\rho} \cdot c_p$)	[m^2/s]
L_w	Latent heat of fusion for water	6 kJ/mol
L_r	Latent heat of fusion for rock	400 kJ/kg
g	Gravitational acceleration (Eqn. 4.2)	[m/s^2]
G	Gravitational constant	6.673×10^{-11} m^3/kg/s^2
$M_\odot$	Solar mass	1.989×10^{30} kg
r	Subscript indicating rock	-
s	Subscript indicating silicates	-
m	Subscript indicating metal	-
w	Subscript indicating water	-

(Yoshino et al. 2003). Thus, planetesimals may have begun to form Fe-S cores at relatively low temperatures and low silicate melt fractions. We note that Fe-Ni metal has a much higher eutectic point (~ 1800 K), thus the formation of an Fe-Ni core (like those represented by some iron meteorite groups) would have been accompanied by a higher degree of silicate melting. Nevertheless, core formation would have occurred

in one or a combination of two ways (Stevenson 1990; Taylor 1992): the gravitational settling of molten spherules of metal through a viscous silicate matrix, or by the flow of liquid metal through interconnected pore spaces between silicate grains.

The gravitational settling of metallic spherules within a partially molten planetesimal occurs at a velocity given by Stoke's law (Stevenson 1990):

$$V_S = \frac{2gd^2\Delta\rho}{9\mu_s}, \tag{4.1}$$

where g is the local gravitational acceleration, d is the size of the molten spherule, $\Delta\rho$ is the density contrast between the silicate matrix and the metallic melt and μ_s is the viscosity of the silicate matrix. Gravitational acceleration can be written in terms of bulk density ($\bar{\rho}$) and size of the planetesimal (R):

$$g = \frac{4\pi GR\bar{\rho}}{3}. \tag{4.2}$$

Thus, the characteristic time scale for gravitational settling of metallic spherules by Stoke's flow can be written using Equations 4.1 and 4.2:

$$\tau_S = \frac{R}{V_S} = \frac{27\mu_s}{8\pi d^2 G\bar{\rho}\Delta\rho}. \tag{4.3}$$

Stevenson (1990) showed that a typical size for molten spherules would have been $d \sim 1$ cm, based on plausible estimates for surface tension forces, turbulent and frictional stresses, and the coagulation of multiple metallic blobs. This is similar to the maximum value of ~ 10 cm calculated by Taylor (1992). Thus, the major uncertainty in Equation 4.3 is the viscosity of the silicate matrix (μ_s), which can vary over many orders of magnitude.

The Einstein-Roscoe relation (Eqn. 4.4) can be used to estimate the viscosity of silicates at melt fractions of greater than 50% (Renner et al. 2000), which were

probably necessary for molten globs of metal to sink and form a core (Taylor 1992):

$$\mu_s = \mu_0(1.35\phi - 0.35)^{-2.5}. \tag{4.4}$$

In this equation μ_0 is the viscosity of the silicate material at 100% melt fraction and ϕ is the melt fraction. The viscosity of fully molten silicates can vary from 0.1 Pa s (the viscosity of water at room temperature is 10^{-3} Pa s) to as much as 10,000 Pa s depending on composition, temperature and pressure (Giordano et al. 2008). If we adopt 10,000 Pa s as an upper limit to μ_0, then the maximum silicate viscosity for which this equation is valid (assuming a minimum melt fraction of 50%) is $\mu_s \sim 170,000$ Pa s. Plugging this value into Equation 4.3 along with $d = 1$ cm, $\bar{\rho} = 5500$ kg/m^3 (the mean value for a metal-silicate mixture) and $\Delta\rho = 3500$ kg/m^3 yields a maximum time scale for the sinking of metallic spherules in a silicate matrix of $\tau_S \sim 45$ kyr. This is more than an order of magnitude less than the half life of ^{26}Al. Thus if high degrees of silicate partial melting were reached within a planetesimal, then core formation by the rain out of molten metal would have proceeded quickly.

The process of core formation by the flow of molten metal through pore spaces is dependent on the relative orientation of grains within the silicate matrix (Stevenson 1990). In particular, the angle at which grain boundaries intersect (also known as the dihedral angle) can permit or prevent the flow of metallic melt. If the dihedral angle is less than 60° then melt pockets of metal will interconnect and form flow channels (Stevenson 1990). Taylor (1992) argued that porous flow necessitates large silicate melt fractions ($> 50\%$) and metal abundances ($\sim 40\%$) to overcome the high interfacial energies between molten metal and silicate gains that are associated with large dihedral angles. High pressures could also deform the silicate matrix to facilitate the flow of molten metal (Stevenson 1990).

Laboratory experiments have produced conflicting results on this issue of metal segregation by porous flow. This is in part due to a focus on high pressure regimes

that are more relevant to differentiation on bodies of terrestrial planet size. Shannon & Agee (1996) melted chondritic material at high pressures (2-20 GPa) and found that the dihedral angle did not fall below $100°$, leading to the conclusion that core formation by percolation through a silicate matrix is not feasible on bodies smaller than ~ 3000 km. Numerous other studies (see Rushmer et al. 2000; McCoy et al. 2006) have focused on melt migration at high-pressures, most of which suggest that high silicate melt fractions are necessary to facilitate core formation by pore flow. On the other hand, Yoshino et al. (2003, 2004) showed that heating of terrestrial samples at pressures of 1-3 GPa resulted in the segregation of Fe-S metal at silicate melt fractions as small as $\sim 15\%$ and Fe abundances of only 5%. At pressures of $\sim 10^{-5}$ atm and temperatures of ~ 1300 K, McSween et al. (1978) showed that Fe-S melt formed connected veins, however these veins may have formed due to the filling of the evacuated pore spaces. These experiments emphasize that a complicated interplay of temperature, pressure, metallic melt composition and silicate melt fraction may have caused core formation to proceed in different ways (e.g. melt percolation versus rain out of metal globules) on bodies of different compositions and sizes.

In light of these uncertainties it is prudent to proceed cautiously with a description of core formation by metallic melt percolation and note that further work is needed to better understand the specific conditions (if any) under which this process occurred. If core formation proceeded via the buoyant flow of liquid metal through interconnected pore spaces between silicate grains, then the velocity of melt flow can be described by Darcy's law (Taylor 1992):

$$V_D = \frac{a^2 \phi \Delta \rho g}{24 \pi \mu_m}, \tag{4.5}$$

where a is the size of the silicate grains, ϕ is the silicate melt fraction, μ_m is the viscosity of the molten metal and all other quantities are the same as in Equation 4.1. Using Equations 4.2 and 4.5 we can write a characteristic time scale for the segregation of metal from a silicate matrix by Darcy flow:

$$\tau_D = \frac{R}{V_D} = \frac{18\mu_m}{a^2\phi G\bar{\rho}\Delta\rho}. \tag{4.6}$$

To place an upper limit on this time scale we assume values of $\mu_m = 0.01$ Pa s, $a = 0.1$ mm, $\bar{\rho} = 5500$ kg/m^3 and $\Delta\rho = 3500$ kg/m^3. This viscosity is an upper limit determined from laboratory measurements of Fe and Fe-S melts at ambient pressure across a wide range of temperatures (Urakawa et al. 2001). Grain sizes of 0.1 - 1 mm are typical for chondrules, which are probably a reasonable approximation to the average grain size for metal-silicate assemblages within unmetamorphosed planetesimals (Taylor 1992). To maximize τ_d we adopt a small melt fraction of 10%, which may or may not have allowed the porous flow of metallic melt. Plugging these values into Equation 4.6 we obtain a time scale for porous flow of $\tau_D \sim 4.4$ kyr.

Interestingly, both τ_S (Eqn. 4.3) and τ_D (Eqn. 4.6) are independent of planetesimal size. The conceptual interpretation for this is that the low velocity of melt migration in small bodies (due to low gravitational acceleration) is counter-acted by the short distance over which the melt must travel to reach the center. In §4.6 we employ a one-dimensional thermal model (§4.5) to calculate a lower limit to the size of planetesimals that could have sustained high enough internal temperatures to form a metallic core.

These two descriptions of the core formation process do not account for void spaces left behind by migrating metal. This is a safe assumption as long as the ratio of metal to silicate abundance is small, thus not requiring the silicate matrix to compact down to fill these voids. For CI chondrites (which are considered a reasonable initial composition for primitive unaltered planetesimals, Lodders 2003) the combined Fe and Ni abundance is ~ 20 weight percent (Lodders & Fegley 1998). If all of this Fe and Ni were incorporated into the metal phase then Fe-Ni metal would occupy a volume fraction of less than 10%. Although the migration of 10 volume percent of metal seems like it would result in a reasonably small porosity that would not cause compacting of the matrix (many asteroids are known to have porosity in excess of 20%, Britt et al.

2002), more detailed calculations on the effects of metallic melt segregation are needed to better understand whether compaction must occur before migration can take place.

If pore flow and/or rain out are valid descriptions, then the formation of metal cores probably occurred quickly, on a time scale much faster than the decay of ^{26}Al. However, this process may have required high degrees of partial melting, which we show in the following sections were quite likely for objects that accreted within a few million years of CAI formation.

4.2 Formation of a Basaltic Crust

Numerous authors have investigated the migration of silicate partial melts and their role in the formation of basaltic crusts (Walker et al. 1978; McKenzie 1984, 1985; Taylor et al. 1993). A basaltic crust could also have formed via the fractional crystallization of a magma ocean (Mittlefehldt et al. 1999). This second theory is not considered in detail, because it is likely that a period of melt migration would have preceded the formation of a magma ocean on parent bodies that were large enough to produce multi-km basaltic asteroids and Fe-Ni cores. Furthermore, the thermal consequences of melt migration may have precluded the formation of a magma ocean (§4.3).

The migration of molten silicates will take place if there is sufficient density contrast between the melt and the surrounding solid matrix, if the melt is interconnected in a network of pore spaces between the solid grains, and if the unmelted matrix compacts to expel the melt. Typical density contrasts for silicate partial melts are relatively small ($\Delta\rho \sim$200 - 500 kg/m^3) but are sufficient for buoyant forces to facilitate migration of the melt (Walker et al. 1978). Experimental and theoretical work has shown that even at low melt fractions, molten silicates do form an interconnected network in the pore spaces between unmelted grains (McKenzie 1985).

The issue of whether a melted region becomes compacted is complicated and requires further discussion. The process of compaction involves the deformation of a silicate matrix to expel fluid melt from within its pore spaces. This process is analogous to squeezing water from a sponge. This is more complex than the description of Darcy's flow of molten metal through a rigid silicate matrix, but is necessary to account for the migration of large amounts of molten silicates.

There are a number of physical properties that control whether a melted region can compact (McKenzie 1984, 1985): these include bulk viscosity of the matrix, microscopic shear viscosity of the matrix, viscosity of the melt and permeability of the matrix to fluid flow. Making reasonable assumptions about these material properties, the size of the compacted region (δ_c) can be parameterized in terms of melt fraction, grain size and viscosity of the melt (ϕ, a and μ respectively) with the following equation (McKenzie 1985):

$$\delta_c = (10\ km)\ \phi^{3/2} \left(\frac{a}{1\ mm}\right) \left(\frac{10\ Pa\ s}{\mu}\right)^{1/2}. \tag{4.7}$$

The physical interpretation of the a and ϕ dependence in this equation is that a silicate matrix with large grain sizes and high melt fraction would easily compact across a large distance to reduce pore volume. The interpretation of the inverse μ dependence is that higher viscosity melts will be resistant to migration and thus decrease the size of the region that can be compacted.

In general, compaction-driven melt migration will occur if the thickness of the region undergoing compaction (δ_c) is smaller than the region across which melting has occurred (Taylor et al. 1993). The size of the melting zone for a planetesimal uniformly heated by radionuclide decay will be comparable to its radius (R), with the outer few kilometers experiencing the largest temperature gradient as they act to insulate the interior (Wilson et al. 2008). Thus, a useful metric to quantify whether a planetesimal has a large enough melt zone to compact is the ratio of R/δ_c. When this ratio is much greater than unity, compaction is likely to occur.

Unfortunately the four key parameters that determine whether compaction-driven melt migration occurs (R, μ, a and ϕ) can vary over many orders of magnitude, making it difficult to define generalized conditions for compaction. However, plugging representative values into Equation 4.7 for a few test cases demonstrates that compaction and melt migration likely occurred across a wide range of parameter space.

First, consider a body with a radius of 10 km, approximately the smallest planetesimal that would have reached high enough internal temperatures to differentiate (this size limit is explored further in §4.6). For a 10 km body with $\phi = 1\%$, $a = 1$ mm, and $\mu = 1$ Pa s, Equation 4.7 yields $R/\delta_c \sim 316$, suggesting that melt migration would occur easily. This ratio varies inversely with grain size, thus compaction should occur under these conditions as long as the grain size is smaller than a few cm. Furthermore, because of the weak dependence on melt viscosity, compaction would likely occur for this body down to viscosities similar to that of liquid water ($\mu \sim 1$ mPa s). However, Equation 4.7 suggests that if the melt fraction rises above 10% then the size of the compaction region would no longer be much less than that of the melt zone and melt migration may not proceed.

The physics of melt migration would have been very different for objects that reached melt fractions of greater than 50%. For small objects (~ 10 km), such large melt fractions would prevent melt migration and result in a fully molten body that could have developed a basaltic crust through the eventual fractional crystallization of its magma ocean. Melt fractions approaching 50% on larger bodies would not necessarily preclude the migration of melt. We calculate that $R/\delta_c >> 1$ for melt fractions of 50%, grain sizes of 1 mm and melt viscosities of 1 Pa s on objects that are larger than 100 km in radius. This represents a conservative lower limit to the size for which formation of a basaltic crust via silicate melt migration could occur.

These examples suggest that the limiting radius for compaction-driven melt migration is somewhere around 10 to 100 km. For bodies smaller than this, the size of the melting zone becomes comparable to that of the compaction region and the silicate

matrix does not deform to expel melt. These size limits are similar to those from calculations of buoyant melt migration within a rigid silicate matrix (Walker et al. 1978).

Based on the preceding discussion and employing the equations of Taylor et al. (1993) and McKenzie (1985), a characteristic e-folding time scale for the expulsion of molten silicates from a compacted region is derived:

$$\tau_{mig} = \frac{3000\mu}{4\pi a^2 \phi^2 (1-\phi)^2 \Delta\rho G \bar{\rho}}, \tag{4.8}$$

where $\Delta\rho$ is the density contrast between the melt and the solid silicate, $\bar{\rho}$ is the bulk density and all other parameters are the same as in Equation 4.7. This equation is valid when $R/\delta_c >> 1$, when the melt zone is comparable in size to R, and when the body is of uniform density. Like the time scales associated with core formation (Equations 4.3 and 4.6), τ_{mig} is also independent of the size of planetesimal.

In Figure 4.1 we plot τ_{mig} as a function of melt fraction (ϕ) and grain size (a) by assuming a viscosity of 10 Pa s, $\Delta\rho = 300$ kg/m^3 and $\bar{\rho} = 3300$ kg/m^3, the average density of olivine. For these specific parameters this figure shows that the melt migration time scale can be either much longer or much shorter than the ^{26}Al half life. If τ_{mig} is much shorter than the ^{26}Al half life, then this would have had significant thermal implications for silicate melts containing large quantities of ^{26}Al (see §4.3).

The least constrained parameters in Equation 4.8 are the melt viscosity (μ) and the matrix grain size (a). The viscosity of molten silicates can vary from approximately 0.001 up to 1000 Pa s and thus could shift the τ_{mig} curves in Figure 4.1 up or down by several orders of magnitude. Taylor et al. (1993) suggested that chondrules offer the best available guide to the grain sizes of unaltered planetesimals. A typical size for chondrules is ~ 0.1 mm, however grains of this size would have coarsened to serveral mm once partial melting began. This process is referred to as Ostwald ripening and acts to minimize surface energy through the growth of grains (Taylor et al. 1993).

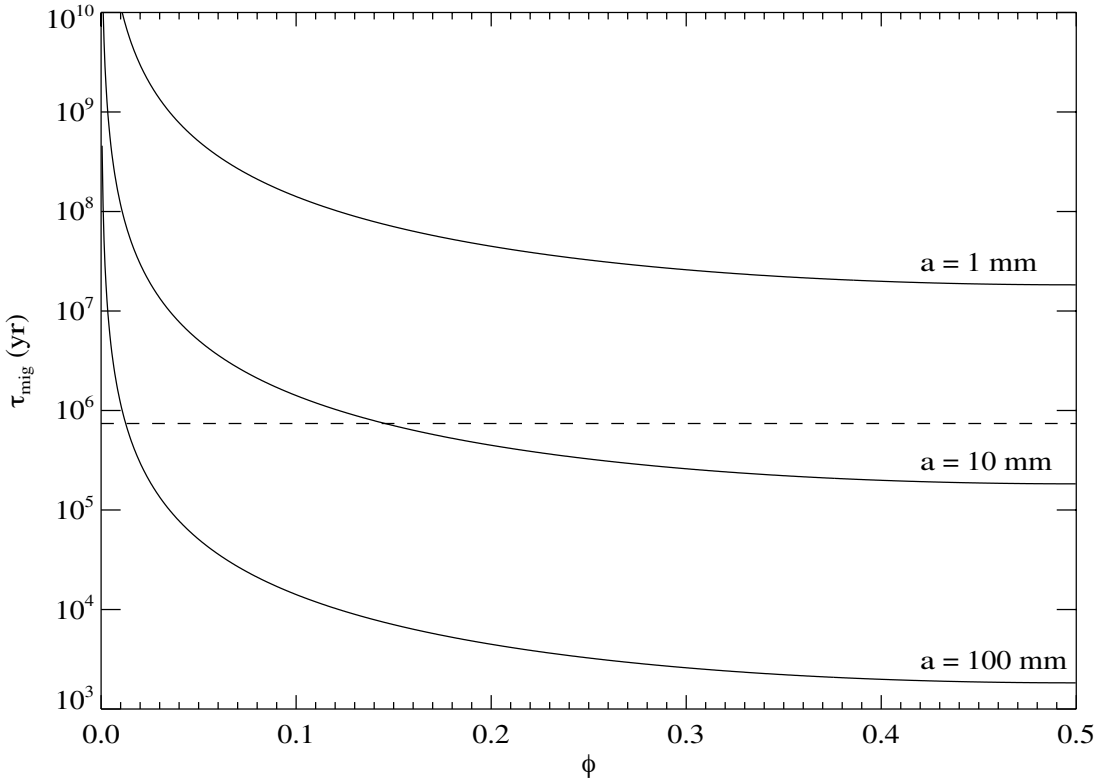

Figure 4.1 Silicate melt migration time scale (τ_{mig}) as a function of melt fraction (ϕ) and grain size (a) for a prescribed viscosity (μ) of 10 Pa s. Although variations in μ and a can have a significant influence on these curves, this figure is useful in demonstrating that in some cases migration will occur on time scales relevant to the heating of a planaetesimal, i.e. τ_{mig} can be $\lesssim$ the time scale for ^{26}Al decay (0.74 Myr, indicated by the dashed line). A magma ocean would exist for melt fractions greater than 0.5, thus rendering τ_{mig} meaningless.

Thus, sizes from approximately 0.1 mm to several cm represent a reasonable range for the grains within an unaltered planetesimal. The influence of these two parameters (μ and a) on the process of melt migration is explored in greater detail in the following section.

These calculations do not take into account any volume changes that would affect permeability and the rate of melt migration. If water were present in the interior of a planetesimal then serpentinization reactions with the silicate minerals would result in volume changes of the matrix (Cohen & Coker 2000). Around a temperature of

700 K sintering would cause a rapid increase in density and a corresponding loss of pore space (Hevey & Sanders 2006). Lastly, the production of silicate melt beginning around 1400 K would also be associated with volume changes: partial melt with a lower density than the matrix would have a larger volume. This succession of volume changes would undoubtedly lead to the formation of cracks and pore space within planetesimals, features that would facilitate the migration of melt from the interior to the surface.

The effects of convective cooling have not been included in these calculations. Convection would occur vigorously in a magma ocean (i.e. $\phi > 50\%$, Taylor et al. 1993), but it is unclear how convective motion of molten silicates at lower melt fractions within a porous matrix would affect the formation of a basaltic crust. Young et al. (2003) showed that the convection of liquid water in the interior of a porous planetesimal would occur for bodies larger than ~ 100 km in diameter. Silicate melts with viscosities several orders of magnitude larger than that of liquid water would likely increase this size limit for molten silicate convection to several hundred kilometers (Equation 28 in Young et al. 2003). Convective cooling would act to dampen the amount of melting within a given body, however the increased motion of molten material could hasten the formation of crust. More detailed modeling of the formation of basaltic crust is necessary to better understand these isssues.

4.3 The Effects of Silicate Melt Migration

Presumably for some planetesimals the silicate melt migration time scale was comparable to or less than the ^{26}Al half life (Figure 4.1). This may have had significant thermal implications because Al preferentially partitions out of solid phases and into the early stages of partial melts (Agee & Walker 1990; Miyamoto et al. 1994; Pack & Palme 2003). If these Al-enriched melts were removed from a planetesimal, then heating by the radioisotope would have been shut down.

Wilson & Keil (1991) presented a mechanism for the removal of partial melts from a planetesimal. They suggested that small amounts (~ 1000 ppm) of dissolved volatiles such as H_2O and CO_2 would have increased the buoyancy of partial melts, resulting in pyroclastic eruptions that could have ejected molten silicates from the surfaces of planetesimals smaller than ~ 100 km in radius. Objects larger than this (e.g. Vesta) had sufficient surface gravity to prevent erupted silicates from reaching escape velocities and thus could have retained their basaltic crusts. Wilson & Keil (1991) presented this argument to explain the lack of basaltic material associated with the aubrites, a meteorite group derived from a parent body that experienced high degrees of partial melting.

A zero-dimensional "box model" has been developed to investigate the thermal implications of the removal of Al-enriched partial melt from the interior of a planetesimal. This model assumes a box in which only unmelted silicates and pore space are initially present. Other materials such as water ice and metal are ignored here. In §4.4 another series of calculations are presented to investigate the thermal effects that water would have on such a system. As temperature increases due to ^{26}Al decay, partial melt is produced and then migrates out of the box on a characteristic time scale (Equation 4.8). The temperature evolution of this box is traced as a function of time. Heat loss due to conduction is not accounted for in this model because it is not necessary for simply characterizing the magnitude of the thermal effect of silicate melt migration.

The total melt fraction (ϕ), the total concentration of ^{26}Al from both the solid and liquid phases ($C_{tot} = C_\ell + C_s$) and the temperature (T) are computed as a function of time. The differential equation governing the amount of melt is:

$$\frac{d\phi}{dt} = -\frac{\phi}{\tau_{mig}} + \frac{d\Phi(T)}{dt}, \tag{4.9}$$

where τ_{mig} is given by Equation 4.8 and $\Phi(T)$ is the amount of liquid produced by the melting of the silicate matrix. This equation accounts for the amount of melt lost on the characteristic e-folding time scale for migration and the amount produced due to heating. By defining

$$\alpha = \frac{3000\mu}{4\pi a^2 G\bar{\rho}\,\Delta\rho}, \tag{4.10}$$

Equation 4.9 can be rewritten using Equation 4.8 and the chain rule for the derivative of $\Phi(T)$:

$$\frac{d\phi}{dt} = -\frac{\phi^3(1-\phi)^2}{\alpha} + \frac{\partial\Phi}{\partial T}\frac{\partial T}{\partial t}. \tag{4.11}$$

All of the physical properties of the system are included in the α-parameter. The derivative of Φ can be calculated from an empirical fit to the amount of melt produced as a function of temperature for peridotite (McKenzie & Bickle 1988):

$$\frac{\partial\Phi}{\partial T} = 3.977\times10^{-4} + 1.338\times10^{-3}\,T' + 1.409\times10^{-2}\,T'^2 \tag{4.12}$$

and

$$T' = \frac{T-1418.1}{636.2}. \tag{4.13}$$

The coefficients in these equations have been derived by calculating the solidus and liquidus temperatures of peridotite at a pressure of 1 bar (1373 and 2009 K respectively, McKenzie & Bickle 1988). This is reasonable because planetesimals smaller than 500 km in size had internal pressures of less than 1 kbar (assuming a spherical body in hydrostatic equilibrium with a mean density of 3500 kg/m^3).

The governing equation for the total concentration of ^{26}Al is:

$$\frac{dC_{tot}}{dt} = -\frac{C_\ell}{\tau_{mig}} - \frac{C_s + C_\ell}{\tau_{Al}}, \tag{4.14}$$

where C_ℓ and C_s are the concentrations of ^{26}Al in the liquid and solid phases respectively and $\tau_{Al} = \tau_{1/2}/ln(2) = 1.07$ Myr, the mean life for ^{26}Al (Goswami et al.

2005). This equation accounts for the loss of ^{26}Al due to melt migration and the loss due to decay in both the liquid and solid phases. The concentration of ^{26}Al in the liquid phase will depend on the chemical partitioning of Al into the partial melt as a function of melt fraction. It is assumed that this partitioning is an equilibrium process, i.e. the molten and solid silicates are in contact for a sufficient amount of time to reach equilibrium before the melt migrates away. This is a reasonable assumption because the time steps used in these calculations (100s to 1000s of years) are much longer than the multi-hour time scales for which Al partition coefficients have been measured in the laboratory (Agee & Walker 1990; Miyamoto et al. 1994; Pack & Palme 2003). Chemical partitioning for equilibrium melting can be described by (Best 2002):

$$C_\ell = \frac{C_{tot}}{D + \phi(1 - D)}, \tag{4.15}$$

where D is the partition coefficient for Al, defined as the ratio of the weight percent of Al in the solid to the weight percent in the liquid. Numerous investigators have measured D for a variety of silicate compositions and across a wide range of temperatures and pressures (Agee & Walker 1990; Miyamoto et al. 1994; Pack & Palme 2003). Irrespective of the experimental procedures, temperatures or pressures, D was always found to be much less than 1 (typical values ranged from 0.002 - 0.02), indicating that Al has a very strong preference towards partitioning into the liquid phase. Thus, the specific value of D does not matter greatly. We adopted a conservative value of 0.02 to minimize the amount of partitioning into the melt and thus the thermal effects of losing ^{26}Al to melt migration.

Equation 4.14 can be rewritten using Equations 4.8, 4.10 and 4.15 and by noting that $C_{tot} = C_s + C_\ell$:

$$\frac{dC_{tot}}{dt} = -\frac{\phi^2(1-\phi)^2}{\alpha(D + \phi - \phi D)}\, C_{tot} - \frac{C_{tot}}{\tau_{Al}}. \tag{4.16}$$

Finally, the evolution of temperature is governed by ^{26}Al heating and the latent heat of melting (L_r) for the silicates:

$$\frac{dT}{dt} = \frac{Q(t)}{c_p} - \frac{L_r}{c_p}\frac{d\Phi}{dt}, \tag{4.17}$$

where $Q(t)$ is the energy per unit mass per unit time released by the decay of ^{26}Al and c_p is the specific heat of the silicates at constant pressure, assumed to be 800 J/kg/K (Ghosh & McSween 1999). The latent heat of melting (L_r) is assumed to be equal to 400 kJ/kg (Ghosh & McSween 1998). $Q(t)$ can be rewritten as:

$$Q(t) = \frac{E_{Al}}{\tau_{Al}}\, C_{tot}, \tag{4.18}$$

where $E_{Al} = 4.0042$ MeV, the energy released per decay of ^{26}Al atom (Lide 2002). Thus, by employing the chain rule, Equation 4.17 becomes:

$$\frac{dT}{dt} = \frac{E_{Al}}{\tau_{Al}\, c_p}\, C_{tot} - \frac{L_r}{c_p}\frac{\partial\Phi}{\partial T}\frac{\partial T}{\partial t}. \tag{4.19}$$

Rearranging this equation by solving for dT/dt yields:

$$\frac{dT}{dt} = E_{Al}\left(\tau_{Al}\, c_p + L_r\, \tau_{Al}\, \frac{\partial\Phi}{\partial T}\right)^{-1} C_{tot}. \tag{4.20}$$

The three coupled equations for T, ϕ and C_{tot} (Eqns. 4.11, 4.16 and 4.20) are solved as a function of time using the direct finite difference method (Ozisik 1994). Initial temperature (T_0), melt fraction (ϕ_0) and ^{26}Al concentration (C_0) must be specified to solve these equations. For all simulations T_0 is set equal to 180 K, a reasonable starting temperature for a planetesimal in thermal equilibrium with the solar nebula and one that is intermediate to values chosen for other studies on the thermal evolution of planetesimals (Cohen & Coker 2000; McCord & Sotin 2005; Hevey & Sanders 2006). This initial value is not crucially important as ^{26}Al heating will quickly

increase temperatures to well outside the range of plausible starting values. At this starting temperature ϕ_0 is always equal to zero. The initial ^{26}Al concentration is determined by the amount of decay that would have occurred before a prescribed time of instantaneous accretion. The equation that is used to determine C_0 is:

$$C_0 = f_{Al} \left[\frac{^{26}Al}{^{27}Al}\right] e^{-t_{acc}/\tau_{Al}}, \tag{4.21}$$

where $f_{Al} = 2.62 \times 10^{23}$ kg^{-1} and is the number of Al atoms per kg of unaltered planetesimal (assuming a mass fraction of Al equal to 0.0113, Ghosh & McSween 1998). The ratio of ^{26}Al to ^{27}Al abundance (by number) is set to the canonical value of 5×10^{-5} (Goswami et al. 2005). t_{acc} is defined relative to the formation of CAIs (i.e. the time when ^{26}Al was introduced and began to decay).

One representative solution to Equations 4.11, 4.16 and 4.20 is shown in Figure 4.2. This simulation was run with the following parameters: $\bar{\rho} = 3300$ kg/m^3, $a = 1$ cm, $\Delta\rho = 300$ kg/m^3, $\mu = 10$ Pa s, and $t_{acc} = 1$ Myr. The top panel shows the temperature evolution and the bottom panel shows the change in melt fraction (solid line) and normalized ^{26}Al concentration (dashed line) as a function of time. Once partial melting begins Al is quickly lost from the system and subsequent heating is halted. The maximum melt fraction reached in this simulation was 22%. As the melt fraction decreases from its maximum the migration time scale increases so that $\sim 5\%$ melt is left behind by the end of the 2 Myr simulation. If thermal conduction were included in this model then heat loss would likely result in the solidification of this melt before it migrated away.

The peak temperature that is reached in this simulation is 1531 K, almost 400 K below the silicate liquidus. If melt migration were not included, then the calculated peak temperature would have been 3163 K. However, convective cooling of large silicate melt fractions, perhaps in a magma ocean, would have prevented such high

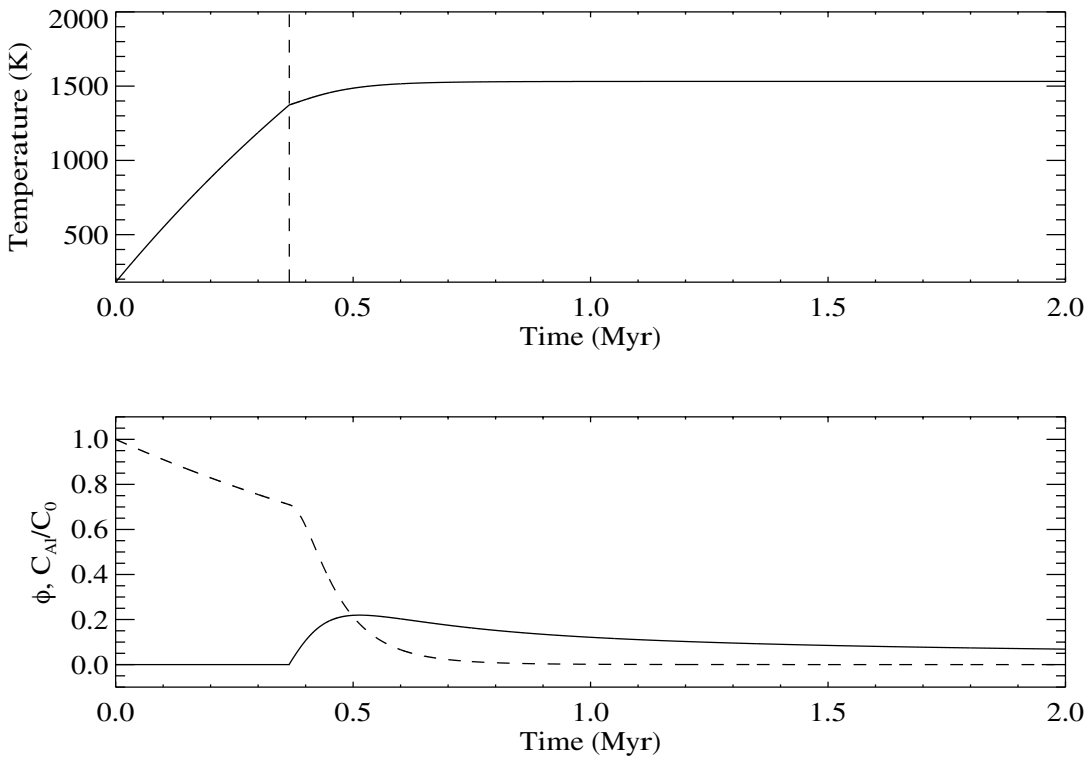

Figure 4.2 Result of melt migration simulation assuming a time of accretion of 1 Myr. The top panel shows the temperature evolution, the bottom panel shows the melt fraction (ϕ, solid line) and the normalized ^{26}Al concentration (C_{Al}/C_0, dashed line). The x-axes represent time after accretion, not the time after the formation of CAIs. The vertical dashed line in the top panel indicates the onset of partial melting ($T = 1373$ K). The total melt fraction never becomes larger than 22%. The ^{26}Al concentration initially decays with the half life of the isotope, however once partial melting begins Al is quickly lost from the system and heating essentially stops.

temperatures. Nevertheless, the migration of Al-enriched melt clearly has a significant influence on the thermal evolution of this system.

To quantify this effect, peak temperatures across a wide range of viscosities and grain sizes are computed (Figure 4.3). Each of these simulations was performed assuming instantaneous accretion at the time of CAI formation (i.e. $t_{acc} = 0$). The amount of heating is maximized by assuming no delay between the time of accretion and CAI formation, and thus minimizes the thermal effects of melt migration. Later

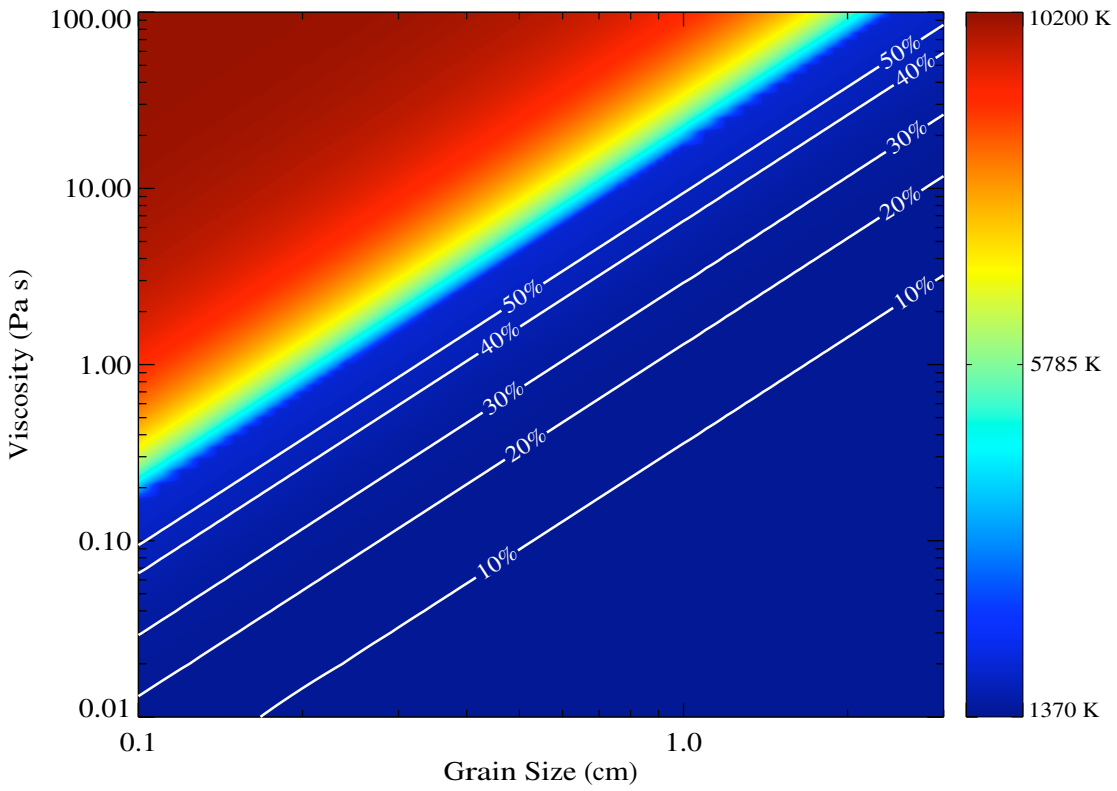

Figure 4.3 The effect of melt migration on peak temperature as a function of grain size and viscosity for systems with $t_{acc} = 0$. Without melt migration, this figure would show constant temperatures of approximately 10,200 K. The peak temperatures range from two degrees above the silicate solidus at 1373 K to just below (10,175 K) the peak temperature for a scenario with no melt migration. Temperatures corresponding to 10% intervals of partial melting (1407, 1452, 1522, 1707, and 1830 K, McKenzie & Bickle 1988) are indicated by the white contours. Combinations of viscosity and grain size that lie above the 50% melting line would result in the formation of a magma ocean.

times of accretion would result in lower overall temperatures and an even smaller range of parameter space that would produce the high degrees of partial melting necessary for differentiation.

The peak temperature for a system with no melt migration is independent of viscosity and grain size and depends only on the amount of energy released by the decay of ^{26}Al. Figure 4.3 would show a uniform temperature of 10,200 K if melt migration were not included. This is clearly an unphysical value that would not occur

in nature as conduction and convection of molten silicates would act to dampen such high temperatures.

The usefulness of Figure 4.3 is that it clearly demonstrates how the migration of Al-enriched partial melts can take a system that would otherwise reach high degrees of melting ($\gtrsim 50\%$) to one where melt fractions do not rise above 50%. More specifically, low viscosity melts ($\lesssim 0.1$ Pa s) and particle sizes greater than approximately 1 cm would prevent a body from reaching high melt fractions. Such low viscosities have been modeled (e.g. $\mu = 0.067$ Pa s by Folco et al. 2004) and measured in the laboratory (e.g. $\mu << 3$ Pa s by Knoche & Luth 1996) for chondritic melts. Thus, it is reasonable to assume that initial melts will have these low viscosities. However, as the silica content increases with melt fraction, the viscosity will increase due to polymerization of the liquid (Best 2002). This will effectively increase the migration time scale and prevent the loss of ^{26}Al. Thus the dependence of viscosity on composition would likely result in higher temperatures than indicated by Figure 4.3. More detailed calculations regarding the changing chemical composition of partial melts as a function of increasing temperature (e.g. using the MELTS software package, Ghiorso & Sack 1995) could provide additional insight on this issue.

The white contours in Figure 4.3 trace the temperatures that correspond to intervals of 10% partial melting. These temperatures, from 10 - 50% partial melting, are 1407, 1452, 1522, 1707, and 1830 K (McKenzie & Bickle 1988). Combinations of viscosity and grain size that lie above the 50% melting line would result in the formation of a magma ocean for the adopted $t_{acc} = 0$. It is useful to further quantify the conditions for the formation of a magma ocean as a function of different times of accretion. This is facilitated by combining the viscosity (μ) and grain size (a) into a single quantity, namely μ/a^2, which is the only combination of these parameters that occurs in Equations 4.10, 4.11, and 4.16. Figure 4.4 shows the combinations of μ/a^2 and t_{acc} that result in 50% partial melting (i.e. combinations of input parameters that cause the system to reach a maximum temperature of 1830 K), a limiting case for the

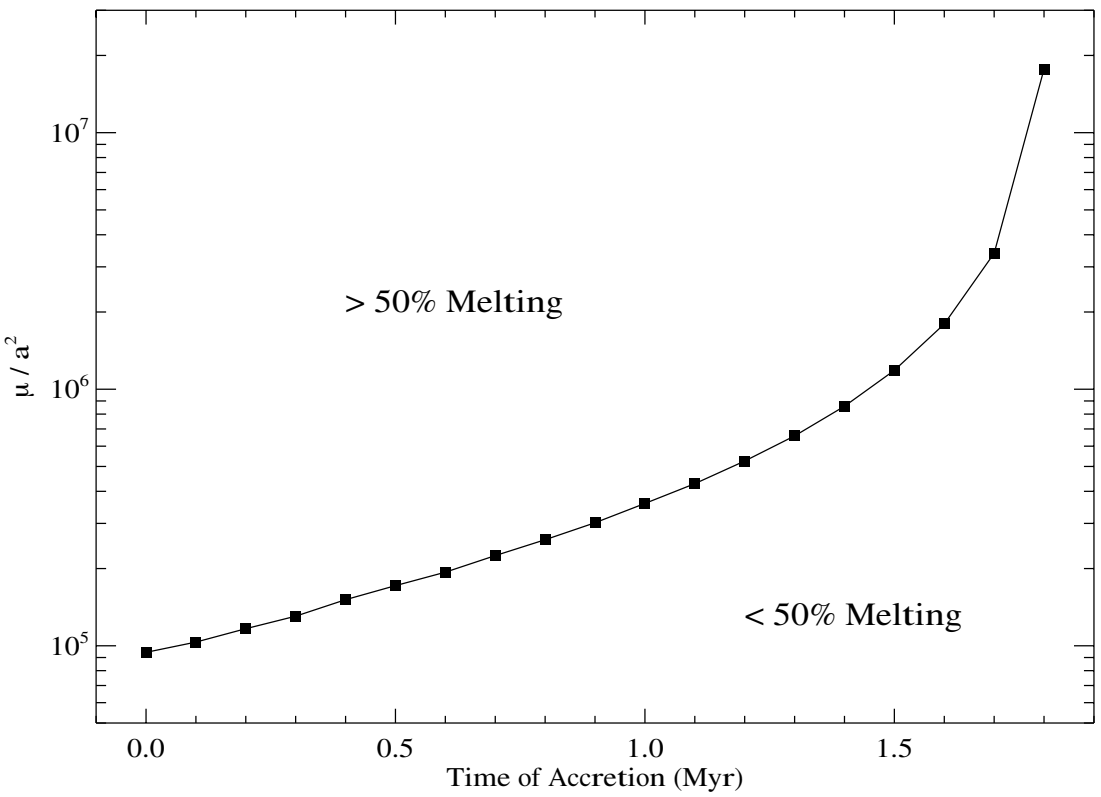

Figure 4.4 Combinations of μ/a^2 and t_{acc} that result in 50% partial melting (i.e. a maximum temperature of 1830 K). Above the set of calculated points more than 50% partial melting would occur and magma oceans would be a likely outcome. Below the calculated points less than 50% partial melting would occur and a magma ocean would be unlikely to form.

formation of a magma ocean. These calculations show that magma oceans would only occur for bodies that accreted earlier than $\sim$ 2 Myr after CAIs. For these accretion times, combinations of μ/a^2 greater than 2×10^7 (e.g. $\mu = 10$ Pa s, $a = 0.1$ mm) would always produce a magma ocean. Combinations of μ/a^2 less than 10^5 (e.g. $\mu = 1$ Pa s, $a = 1$ cm) would never result in the formation of a magma ocean due to rapid migration of Al-enriched partial melt.

A benefit of these melt migration simulations is that they provide insight on the maximum time of accretion for which silicate melting occurs. Assuming $\mu = 100$ Pa s and $a = 1$ mm, it is found that a body does not reach the silicate solidus if accretion

is later than about 2.3 Myr after CAI formation. This is a rough upper limit to the time of accretion for differentiation to occur. This result is broadly in agreement with radiometric dating of the magmatic iron meteorites, whose parent bodies accreted and differentiated within 1-2 Myr of CAI formation (Markowski et al. 2006). In addition, sophisticated thermal models that take into account the redistribution of ^{26}Al and ^{60}Fe following core and crust formation require a time of accretion within 2.85 Myr of CAI formation for the differentiation of Vesta (Ghosh & McSween 1998), a result roughly similar to our own.

Irrespective of viscosity, the simulations performed in this section suggest that grain sizes smaller than approximately 1 mm will prevent percolation and produce high melt fractions. Small grain sizes may have been a prerequisite for the formation of putative magma oceans on the parent bodies of the HEDs, angrites and iron meteorites (Taylor & Norman 1992; Righter & Drake 1997; Greenwood et al. 2005). However, if the eucrites represent the liquid expelled from a partial melt region (Consolmagno & Drake 1977; Walker et al. 1978), then larger grain sizes would have been required to facilitate melt migration.

Again irrespective of viscosity, the migration of melt occurs quickly for grain sizes larger than approximately 1 cm. This phenomenon implies a scenario in which basaltic material can be lost from a melting parent body. A planetesimal originally forms with large cm-sized grains (or such large grains form by Ostwald ripening, Taylor et al. 1993). Heating from the decay of ^{26}Al produces silicate melt at depth within the planetesimal. This melt will migrate upwards if the planetesimal's compaction region is much smaller than its melt zone. This Al-enriched melt can then be removed from the planetesimal (if it is smaller than ~ 200 km in size) via pyroclastic eruptions at the surface (Wilson & Keil 1991). These eruptions may occur following the pooling of basaltic liquid in large sills at the base of an unmelted insulating layer in the upper ~ 5 km of the planetesimal (Wilson et al. 2008). Further melting of the planetesimal's interior halts due to the loss of ^{26}Al. The residual material left behind would be

enriched in silicate phases with high melting temperatures (e.g. olivine) and Fe-Ni-S metal. The pallasite meteorites may represent such bodies (Scott 1977). Such a series of events would have precluded the formation of a basaltic crust and thus could be relevant to understanding the scarcity of basaltic objects amongst the asteroids and meteorites. However, the formation of an Fe-Ni-S core (like those represented by the iron meteorites) is problematic in this scenario due to the rapid loss of ^{26}Al at temperatures well below the Fe-Ni eutectic (Taylor 1992). Further modeling of heating due to ^{60}Fe decay in residual Al-depleted material may reveal a mechanism for completing the core formation process.

4.4 The Effects of Hydration Chemistry

The water content of planetesimals in the inner Solar System ($a < 5$ AU) is not well constrained (Abe et al. 2000; Stimpfl et al. 2005; Machida & Abe 2006). However, the presence of water may have played a significant role in the thermal evolution of planetesimals in this region. For example, water has a high specific heat relative to silicate rock and thus would increase the amount of energy needed to raise the temperature of a planetesimal. Water can also react with silicate rock in exo- and endothermic chemical reactions, which could serve as additional heat sources and sinks in the energy budget of a planetesimal. Lastly, if conditions were suitable (Young et al. 2003) water could convectively cool the interiors of planetesimals. In this section, the thermal consequences of these first two examples are investigated with another box model that was developed to trace the temperature evolution of a region within a planetesimal that contains a mixture of silicates and water ice. We track this system through multiple stages including the melting of water ice, the hydration of the surrounding silicates by the liquid water and the removal of water from the system as dehydration reactions occur.

These simulations are similar to those of several previous studies. Grimm & McSween (1989) investigated the effects of water on the thermal evolution of carbonaceous chondrite parent bodies and Cohen & Coker (2000) investigated the length of time and spatial extent of a liquid water phase on the CM meteorite parent body. Both of these studies focused on low temperature aqueous alteration processes and thus did not explore the general consequences of hydration chemistry on the overall thermal histories of planetesimals. Wilson et al. (2008) investigated the complete thermal history of the ureilite parent body including hydration, dehydration, partial silicate melting and smelting. The calculations presented here, albeit much simpler, are most similar to the Wilson et al. (2008) work. Where the calculations in this section differ is with a more detailed consideration of the chemistry of water-rock interactions. We also consider the effect of variable water volume fraction on thermal history, which was not investigated in Wilson et al. (2008).

When liquid water comes into contact with silicate rock, hydration reactions can occur. Three reactions that may have been relevant to chondritic bodies in the early Solar System are (Grimm & McSween 1989; Cohen & Coker 2000; Schulte et al. 2006):

(1) $2Mg_2SiO_4 + 3H_2O \rightarrow Mg_3Si_2O_5(OH)_4 + Mg(OH)_2$

(2) $Mg_2SiO_4 + MgSiO_3 + 2H_2O \rightarrow Mg_3Si_2O_5(OH)_4$

(3) $Fe_2SiO_4 + 5Mg_2SiO_4 + 9H_2O \rightarrow 3Mg_3Si_2O_5(OH)_4 + Mg(OH)_2 + 2Fe(OH)_2$.

where Mg_2SiO_4 is the mineral fosterite, $Mg_3Si_2O_5(OH)_4$ is serpentine, $Mg(OH)_2$ is brucite, $MgSiO_3$ is enstatite, Fe_2SiO_4 is fayalite and $Fe(OH)_2$ is iron hydroxide.

Table 4.2 lists the thermodynamic properties for each of these reactions at a pressure of 1 bar, which is a reasonable approximation for planetesimals smaller than 500 km in size. ΔH_{hyd} refers to the enthalpy of reaction that is released when water hydrates the minerals and ΔH_{dehyd} refers to the endothermic energy consumed when the reverse reaction occurs at higher temperature. The third column in this table

Table 4.2 Thermodynamic properties of hydration reactions

Reaction	ΔH_{hyd} (kJ)	ΔH_{dehyd} (kJ)	$\Delta H_{hyd}/mol\ H_2O$ (kJ/mol)	T_{rev} (K)
(1)	-81.1	+205.6	-27.0	450
(2)	-69.8	+153.7	-34.9	500
(3)	-273.3	+626.5	-30.4	400

($\Delta H_{hyd}/mol\ H_2O$) lists the energy released by hydration per mol of water consumed. The last column in this table is the temperature at which these reactions are driven in the reverse direction, i.e. the dehydration temperature T_{rev}. The dehydration temperatures were calculated by taking the ratio of the enthalpies of reaction to the entropies of reaction (McMurry & Fay 2001). Both of these quantities were calculated by summing over the enthalpies/entropies of formation for each of the reactants and products (Robie & Hemingway 1995). The differences in the heats of reaction for hydration versus dehydration are due to the difference in the enthalpies of formation for the minerals at 0° compared to T_{rev} and due to the heat of vaporization of water which must be overcome to dehydrate the minerals at temperatures above 100°C. The difference between ΔH_{hyd} and ΔH_{dehyd} shows that significantly more energy is required to drive dehydration than is released by hydration, making the overall water-rock interaction non-conservative.

Although the energy released by hydration reactions can vary over a wide range, the energy released per mole of water consumed is roughly constant (~ 30 kJ/mol). This is relevant to systems in which water is the limiting agent, i.e. when the abundance of water is sufficiently low that it is completely consumed by hydration reactions. Wilson et al. (1999) calculated that typical chondritic silicates could consume nearly 30 volume percent (~ 10 weight percent) of pore water via hydration. The amount of water in the simulations presented here is restricted to values smaller

than 30 volume percent to avoid the consequences of unreacted liquid water, namely fluid convection. Detailed numerical models (e.g. extending the work of Young et al. 2003) would be required to check whether the time scale for convective motion of liquid within a porous planetesimal was longer than the time for hydration reactions to proceed, an assumption implicit to the model presented here. Employing the assumption that all water in the system is consumed renders the specific hydration reaction irrelevant to the overall energy budget of the system. It is also assumed that any void space left behind by reacting water is perfectly compensated for by volume changes associated with hydration of the silicates. This assumption is probably accurate to within ~ 10 volume percent (Cohen & Coker 2000). Finally, it is assumed that the water escapes from the system as steam upon dehydration from the rock.

The reaction kinetics for hydration reactions at low pressures (< 1 kbar), like those that would have been present on planetesimals, are not well studied. Cohen & Coker (2000) assumed hydration reaction coefficients that were dependent on both pressure and temperature and found that the calculated conditions within their meteorite parent bodies led to very fast reaction rates. This is based on experimental work (Wegner & Ernst 1983) which shows that complete hydration of silicate rock at temperatures of a few hundred °C and a few kbar of pressure can occur on time scales of tens of days. We adopt the assumption that the reaction rates are fast, but note that further experimental work is needed to better understand the thermodynamics of hydration chemistry in conditions that are relevant to planet formation (particularly low pressures). For the box model presented here, in which heat loss due to conduction is not considered, the specific reaction rates do not matter as long as the integrations are long enough to reach a steady state.

These simulations are broken into 5 stages (Figure 4.5). The differential equations for each stage are solved using Euler's method. The first stage involves the heating of the ice-rock mixture from an initial temperature (180 K) to the melting point of water (273 K). Initially, it is assumed that the porosity of the planetesimal is completely filled

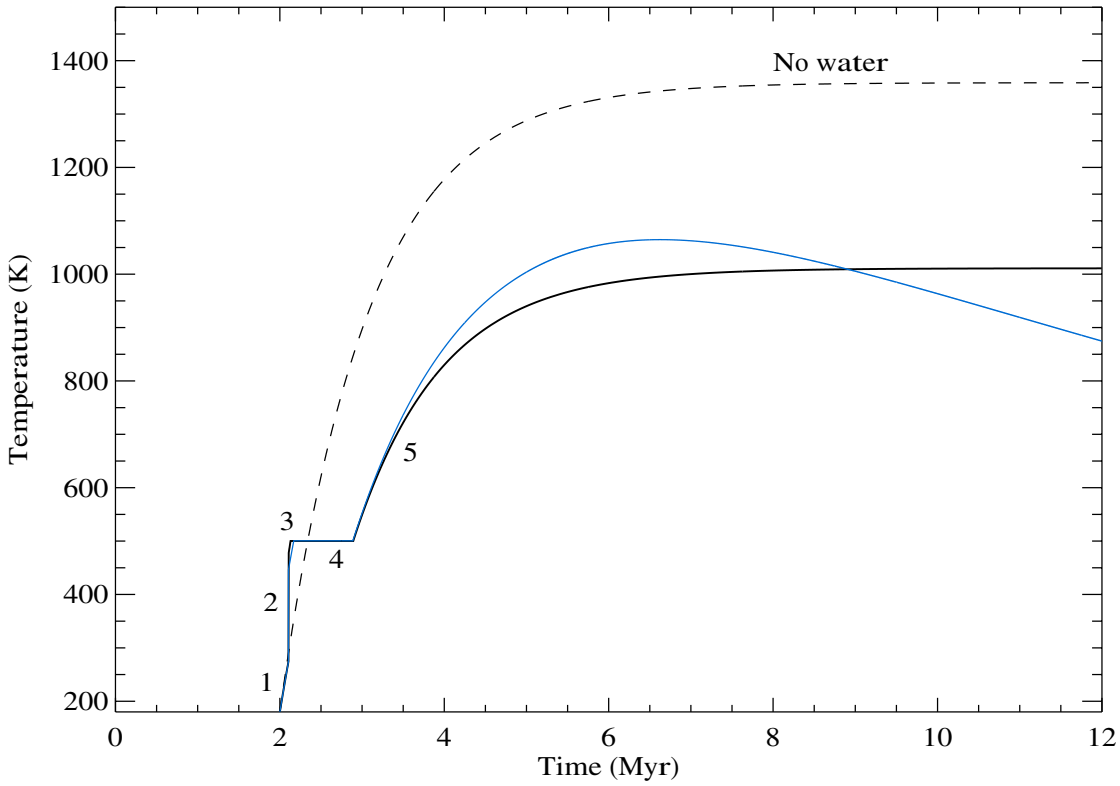

Figure 4.5 Temperatures as a function of time (relative to CAI formation) for a planetesimal with an accretion time of 2 Myr. The five stages of the thermal evolution are labeled: stage 1 is heating of the ice-rock mixture by ^{26}Al decay, stage 2 is the hydration jump, stage 3 is ^{26}Al heating of the hydrated rock, stage 4 is the dehydration plateau, and stage 5 is ^{26}Al heating of the dehydrated rock. The black curves represent the outcome of the box model for the cases of a system with no water (dashed) and 25 volume % water (solid). The blue curve is a result from the 1-dimensional thermal model (§4.5) with the addition of water and shows the temperature evolution at 50% radius within a body 100 km in diameter.

with water ice. The heating in this stage is governed solely by the decay of ^{26}Al:

$$\frac{dT}{dt} = \frac{Q(t)}{c}, \tag{4.22}$$

where the heating term in this case is given by:

$$Q(t) = \frac{V_r \; f_{Al} \; E_{Al}}{\tau_{Al}} \left[\frac{^{26}Al}{^{27}Al}\right] \; e^{-t/\tau_{Al}}. \tag{4.23}$$

V_r represents the volume fraction of rock in the system and all other quantities are the same as in the previous sections. The specific heat for this stage is represented by a weighted average over the heat capacities of the two components (Grimm & McSween 1989):

$$c = \frac{c_r\, m_r + c_w\, m_w}{m_r + m_w}, \tag{4.24}$$

where the r and w subscripts refer to rock and water ice respectively, and m represents the mass fraction of each component. c_w is set to 2108 J/kg/K and c_r is set to the standard value of 800 J/kg/K.

Stage 2 begins when the melting point of water is reached. The latent heat of fusion for water (L_w) is 6 kJ/mol at low pressure ($\sim$1 bar). As shown in Table 4.2, the exothermic energy released in hydration reactions is typically $\sim$ 30 kJ/mol of water reacted. Thus, as soon as the water ice begins to melt it reacts with the rock and starts a runaway process in which all of the ice melts and is quickly consumed. This is assumed to be an instantaneous process in which the heat of reaction (minus the heat of fusion for water) is added to the system. The thermodynamic properties of reaction (2) from Table 4.2 are used for these calculations. The magnitude of this spike in temperature due to hydration is solely dependent on the number of moles of water per unit volume in the simulation. Hydration reactions that result in the production of gases such as CO_2 and H_2 are not considered (Wilson et al. 1999; Rosenberg et al. 2001). This allows a simpler approach, however it also is likely to over-estimate the peak temperatures in the system as the internal production of large volumes of gas could lead to fracturing (Wilson et al. 1999) which would hasten the cooling process.

Stage 3 begins when all of the water is consumed and the hydrated rock again begins to heat from the decay of ^{26}Al. The temperature evolution of this stage is also governed by Equations 4.22 and 4.23, however c is now replaced by the specific heat of the silicates, $c_r = 800$ J/kg/K.

Stage 4 is referred to as the dehydration plateau. This occurs when temperatures become high enough to drive the hydration reactions backwards. It is assumed that all of the energy from ^{26}Al heating goes into fueling these reactions and does so until the rock is completely dehydrated. Due to the high temperatures at which dehydration occurs (> 400 K), the water in these reactions is released in the gas phase and is assumed to immediately exit the system. The effects of vapor pressure as gaseous water is expelled from the silicate rock are not considered. As in the hydration phase, these effects may have included the formation of fissures or even the complete disruption of the planetesimal (Wilson et al. 1999). The consequences of such processes would have been to further lower peak temperatures, thus this analysis represents a conservative approximation for the thermal effects of water.

Finally, stage 5 involves further ^{26}Al heating of the dehydrated rock until this heat source is exhausted. Figure 4.5 shows the results from one of these box model simulations (black solid curve). This model was run assuming an accretion time 2 Myr after CAI formation and a planetesimal with 10 weight percent water (~ 25 volume percent). The temperature in this system reaches approximately 1000 K at a time 10 Myr after accretion. If no water is included in this model then the peak temperature would have been about 1350 K (dashed curve).

The five stages of water-rock interaction have also been incorporated into a 1-dimensional heat conduction model (§4.5), whose results are compared (blue curve) to the 0-dimensional box model (Figure 4.5). The 1-D result represents the temperature evolution at a depth of 25 km within a planetesimal 100 km in size. The reasonable agreement between the two models suggests that the simple box model is sufficient to characterize the general thermal effects of hydration.

A series of box model simulations are run for a range of water volume fractions (0 - 0.3) and accretion times (0 - 5 Myr). The peak temperature for each combination of these variables is recorded (Figure 4.6). As expected, later accretion times and larger water volume fractions result in lower peak temperatures. For instance an

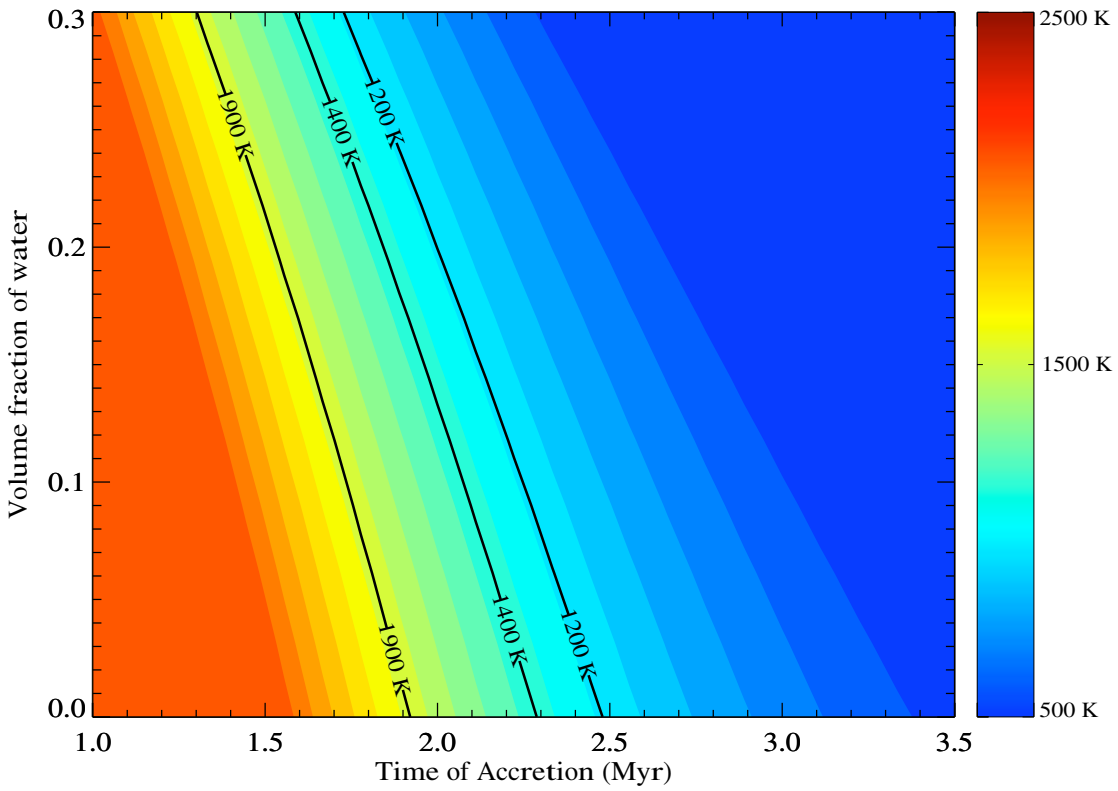

Figure 4.6 Contours of peak temperature as a function of accretion time and water volume fraction. Contours for the Fe-S eutectic (1200 K), the silicate solidus (1400 K) and the silicate liquidus (1900 K) are shown. Large water volume fractions can translate into temperature effects of several hundred Kelvin, and thus may have prevented the partial melting of bodies that accreted $\sim$ 2 Myr after the formation of CAIs.

object that accretes at 2.0 Myr with a water volume fraction of 30% would achieve peak temperatures well below the silicate solidus at 1200 K, whereas a body that accretes at the same time with no water would reach temperatures approaching the silicate liquidus at 1900 K.

Objects with accretion times earlier than $\sim$ 1 Myr were relatively unaffected by the presence of water. Such objects would have had large silicate melt fractions and, as previously noted, are likely candidates for the parent bodies of the iron meteorites. At the other extreme, objects with accretion times later than $\sim$ 4 Myr would never have

reached temperatures high enough to dehydrate. Such objects may be represented by the aqueously altered CI and CM chondrites (Krot et al. 2005b). The large swath of dark blue contours on the right side of Figure 4.6 represents systems that did not have enough remaining energy from the decay of ^{26}Al to fully dehydrate the silicate rock. These simulations suggest that water had the most significant impact on bodies that accreted around 2 Myr after CAI formation. Specifically, dehydration reactions on these bodies could have prevented temperatures from reaching the Fe-S eutectic or even the silicate liquidus. However, for such effects to occur, large water volume fractions ($> 10\%$) were required. Such abundances of water may or may not have been relevant to planetesimals in the inner Solar System (Abe et al. 2000; Stimpfl et al. 2005; Machida & Abe 2006).

In general, the results from these calculations suggest that the effects of water on planetesimals and the differentiation process were not major. However, these conclusions are tenuous due to a primary assumption in these calculations: namely the neglect of vapor phases throughout the various stages of water-rock interaction. As previously noted, build up of internal vapor pressures could have caused internal fracturing of planetesimals (Wilson et al. 1999), thus the cooling effects of water may have been grossly underestimated by neglecting this process. Modeling that combines the detailed thermodynamics presented here with a more realistic treatment of gas production and mobilization (e.g. Wilson et al. 1999) would be a useful step towards understanding the significance of water on the thermal histories of planetesimals.

4.5 One-Dimensional Thermal Model

Thus far arguments have been presented for various thermal processes without considering the conductive loss of heat. This has facilitated derivations that do not depend on temperature gradients as a function of depth within planetesimals. In this section a simple 1-dimensional thermal conduction model is developed and then used

to investigate the effect of planetesimal size on the differentiation process (§4.6) and for outlining scenarios of thermal evolution for a range of sizes and accretion times (§4.7).

The 1-dimensional equation for heat conduction in a spherically symmetric system with internal heating is (Grimm & McSween 1989):

$$\frac{\partial T}{\partial t} = \frac{1}{r^2}\frac{\partial}{\partial r}\left(r^2 \kappa \frac{\partial T}{\partial r}\right) + \frac{Q(t)}{c_p}, \tag{4.25}$$

where r is the radial coordinate, $Q(t)$ is the decay energy per unit mass per unit time for ^{26}Al and c_p is the specific heat at constant pressure. κ is the thermal diffusivity and is related to the thermal conductivity k, the density ρ and specific heat c_p:

$$\kappa = \frac{k}{\rho\, c_p}. \tag{4.26}$$

Using Equation 4.26, assuming a radially constant density, κ and c_p, and expanding Equation 4.25 gives the conduction equation for $r > 0$:

$$\frac{\partial T}{\partial t} = \frac{2k}{r\rho c_p}\frac{\partial T}{\partial r} + \frac{k}{\rho c_p}\frac{\partial^2 T}{\partial r^2} + \frac{Q(t)}{c_p}, \qquad r > 0 \tag{4.27}$$

At $r = 0$ this equation breaks down. This singularity can be remedied by deriving a separate differential equation for $r = 0$. Expanding the offending $1/r$ term in a Taylor series gives:

$$\frac{2k}{r\rho c_p}\frac{\partial T}{\partial r} \approx \left(\frac{2k}{r\rho c_p}\frac{\partial T}{\partial r}\bigg|_{r=0} + r\left(-\frac{2k}{r^2\rho c_p}\frac{\partial T}{\partial r} + \frac{2k}{r\rho c_p}\frac{\partial^2 T}{\partial r^2}\bigg|_{r=0}\right.\right. . \tag{4.28}$$

The first two terms on the right hand side of this equation cancel, leaving:

$$\frac{2k}{r\rho c_p}\frac{\partial T}{\partial r} \approx \frac{2k}{\rho c_p}\frac{\partial^2 T}{\partial r^2} \tag{4.29}$$

Plugging this into Equation 4.27, yields the conduction equation for $r = 0$:

$$\frac{\partial T}{\partial t} = \frac{3k}{\rho c_p}\frac{\partial^2 T}{\partial r^2} + \frac{Q(t)}{c_p}, \qquad r = 0 \tag{4.30}$$

Equations 4.27 and 4.30 are solved using the explicit finite difference method (Ozisik 1994) with a constant temperature prescribed for the outer boundary of the body ($r = R$). The initial temperature of the body is assumed to be constant across all radii and is equal to the prescribed boundary temperature. For each time step the heating from ^{26}Al decay is computed using the following equation:

$$Q(t) = f_{Al}\left[\frac{^{26}Al}{^{27}Al}\right]\frac{E_{Al}}{\tau_{Al}}\, e^{t/\tau_{Al}}, \tag{4.31}$$

where t is the time relative to CAI formation and all other terms are the same as in §4.3. It is important to note that the latent heats associated with silicate phase changes are not considered in this model. This has the effect of artificially increasing temperatures for small bodies and increasing the time of accretion for which melting occurs.

Solving these differential equations requires specification of the parameters k, c_p, ρ, R and t_{acc}. For all simulations a specific heat and density of 800 J/kg/K (Ghosh & McSween 1999) and 3300 kg/m^3 respectively are assumed. R and t_{acc} are the two primary variables in these calculations. The thermal conductivity of the planetesimal, k, will depend on its porosity. These calculations assume zero porosity and a thermal conductivity of 2.1 W/m/K (Turcotte & Schubert 2002). If the porosity of the planetesimal were 30% (an estimate for the upper limit to asteroidal porosity, Britt et al. 2002), then the effective thermal conductivity can be calculated as the volume-weighted average of the thermal conductivity for silicate material (2.1 W/m/K) and a value of zero conductivity for empty pore space (Grimm & McSween 1989). This calculation decreases the effective thermal conductivity to 1.47 W/m/K, which does not have a large effect on the results in the following two sections. Assuming

no porosity maximizes heat flow and thus results in a lower limit for the calculated internal temperatures.

A solution to Equations 4.27 and 4.30 is presented in Figure 4.7. This simulation was run for a body with a radius of 50 km and a time of accretion 2.2 Myr after CAI formation. The spatial and temporal resolutions of this simulation were 250 m and 800 yr respectively. These high resolutions (relative to the size of the body and the time span of the integration) assure stability of the numerical result. The initial and boundary temperatures were set to 180 K. The peak temperature achieved by this body was 1483 K at a time of 6.8 Myr after the formation of CAIs (equivalent to 4.6 Myr after its time of accretion). This result agrees very well with other thermal model calculations (e.g. Hevey & Sanders 2006).

4.6 The Sizes of Differentiated Bodies

This thermal model is used to determine a lower size limit for the differentiation of a planetesimal. In §4.1 and §4.2 it was shown that the time scales for the formation of metallic cores and basaltic crusts are independent of size, provided that temperatures remain high enough to sustain partial melting. Thus, to better characterize this temperature constraint, it is useful to define a characteristic cooling time for a spherical planetesimal.

The characteristic time scale for thermal conduction is often given by R^2/κ (Turcotte & Schubert 2002). However, this approximation is only valid for conduction into a semi-infinite half space and does not necessarily apply to an internally heated sphere. This is made apparent by comparing R^2/κ to e-folding times from the 1-dimensional numerical model. For example, consider the 100 km object modeled in Figure 4.7. From Equation 4.26 its thermal diffusivity is 7.9×10^{-7} m^2/s, which yields $R^2/\kappa = 100$ Myr. However, the numerical model shows that the peak temperature at the center of this body drops by a factor of $1/e$ in 16 Myr (this is defined as

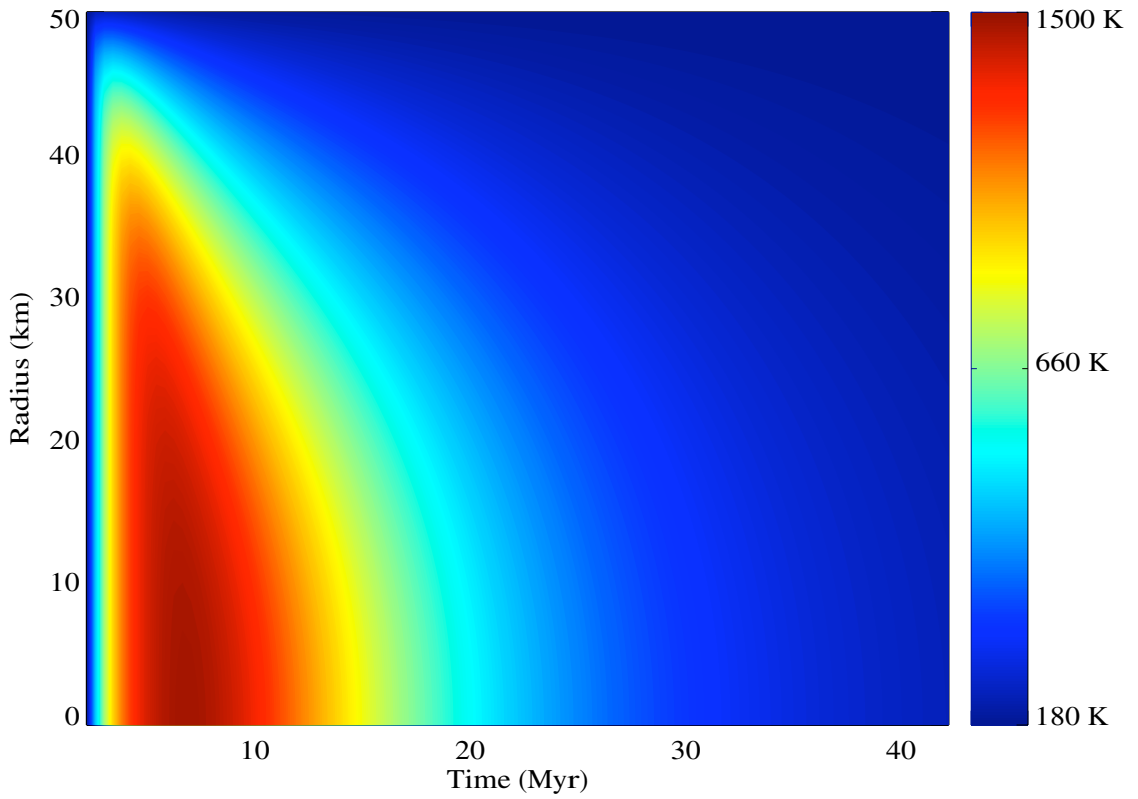

Figure 4.7 Temperature evolution of a planetesimal with a radius of 50 km. The time of accretion for this body was 2.2 Myr after CAI formation and is the starting time of the simulation. The radial temperature profiles are plotted as a function of time relative to CAI formation. The body reaches its maximum temperature 4.6 Myr after accretion ($\sim$ six ^{26}Al half lives), and then cools over a time scale of ~ 16 Myr.

the characteristic e-folding time for a given planetesimal). Analytical calculations of thermal conduction time scales (Osuga 2000) support this numerical result that characteristic times should be reduced by a factor of a few from R^2/κ for spherically symmetric systems.

E-folding time scales are numerically computed to better characterize the cooling of spherical planetesimals (Figure 4.8). This figure clearly shows that the modeled e-folding time scales (diamonds) are not well represented by the R^2/κ approximation (dashed curve). At large radii (> 20 km), the e-folding time is much longer than the time scale for the decay of the heat source ($\tau_{Al} = 1.07$ Myr). Thus the thermal

evolution of these bodies occurs on time scales well represented by a conduction model proportional to R^2/κ. At small radii (< 20 km), the numerical model produces roughly constant e-folding times that asymptotically approach τ_{Al}. These bodies require longer than R^2/κ to cool due to the influence of the internal ^{26}Al heat source. However, it is important to note that the peak temperatures of these objects do not become large. For example, a planetesimal with a radius of 1 km that accretes at 1 Myr will reach a peak temperature of 186 K, only 6 K above its starting temperature, but will then require ~ 1 Myr for that temperature to be reduced to 183.8 K (a factor of 1/e less than its peak).

The following parameterization is adopted for the cooling time of a spherical body that is internally heated with a fixed temperature at its outer boundary:

$$\tau_{cool} = 0.115 \, \frac{R^2}{\kappa}. \tag{4.32}$$

This equation represents a fit to the numerically computed e-folding times for planetesimals with radii larger than 20 km (Figure 4.8).

Comparison of the cooling time scale (τ_{cool}) to the heating time scale (τ_{Al}) is a simple way to approximate a limiting size for differentiation. Objects with $\tau_{cool} < \tau_{Al}$ would be unlikely to sustain melting temperatures, whereas objects with $\tau_{cool} > \tau_{Al}$ could differentiate. These time scales are equal for a body with a radius of ~ 15 km. Actual implementation of the numerical model suggests that bodies as small as ~ 15 km in diameter could reach the silicate solidus (1400 K) and maintain this temperature for hundreds of thousands of years. This probably would have been a sufficient interval for core formation to proceed (§4.1). Silicate fractionation by melt percolation would be unlikely to occur on this body (it would have been too small to compact), however a differentiated mantle and crust could have formed from the crystallization of a magma ocean (models of fractional crystallization on small bodies would be useful to investigate the size limit for which differentiation within a magma ocean could

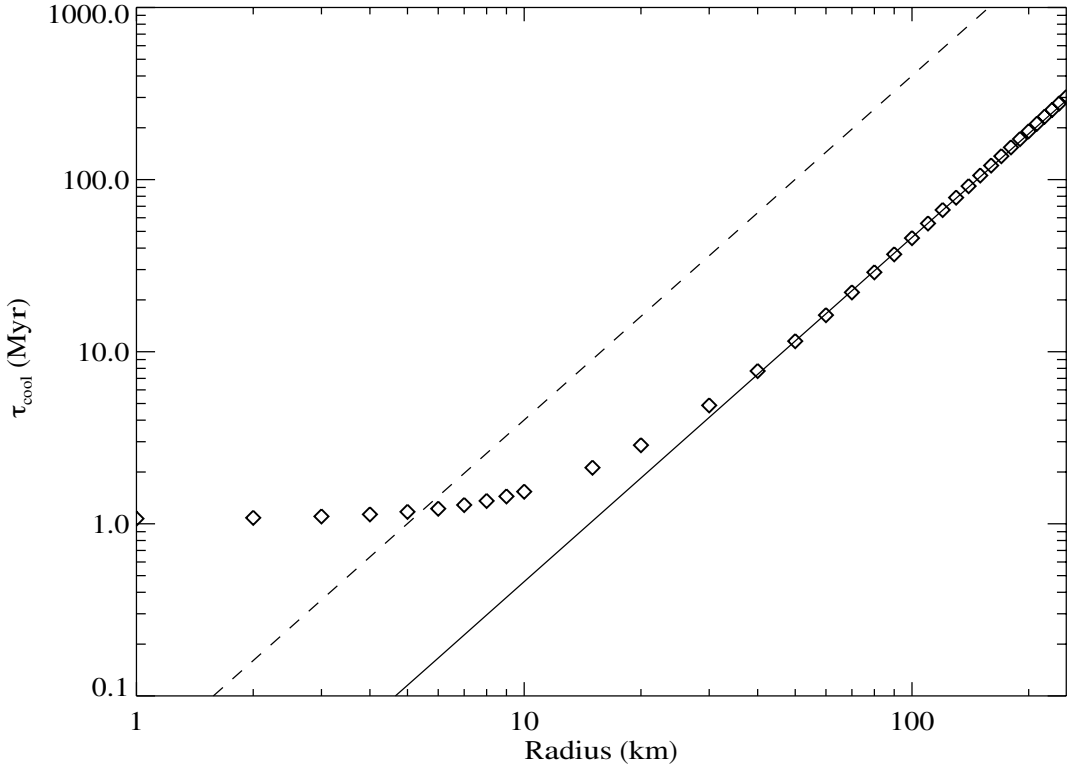

Figure 4.8 Characteristic cooling time scale as a function of planetesimal radius. The dashed line represents R^2/κ for $\kappa = 7.9 \times 10^{-7}$. The e-folding time scales from the numerical model are shown as the diamonds and are defined as the time it takes the peak temperature at the center of a planetesimal to drop by a factor of 1/e. It is clear that conduction time scales of R^2/κ do not accurately describe an internally heated sphere with a fixed boundary temperature. The functional form of the fit to the numerical e-folding times at large radii (solid curve) is given by Equation 4.32.

have occured). Therefore, the thermally-derived size limit for a differentiated body is similar to the compaction limit, i.e. objects larger than ~ 15 km in diameter could have differentiated, but only if they accreted within 1 Myr of CAI formation. This size limit increases with time of accretion so that by 1.5 Myr a body would have to be 40 km in diameter to differentiate and by 2 Myr a body would have to be 80 km in size. For accretion times beyond approximately 2.3 Myr (three ^{26}Al half lives) it is unlikely that ^{26}Al decay could fuel the differentiation process.

In the Main Belt, the asteroids Magnya and Massevitch are the only V-types (other than Vesta) that are ~ 20 km or larger in diameter. The preceding thermal calculations suggest that these bodies could represent intact differentiated planetesimals, however it is unclear whether a 20 km asteroid could escape collisional disruption over the age of the Solar System (Bottke et al. 2005b).

4.7 Thermal Evolution Scenarios

This chapter concludes with a synthesis of the previous sections and aims to provide a broad perspective on the relevant processes, time scales and sizes associated with the differentiation of planetesimals. Much of this information has been distilled into Figure 4.9. This figure has axes of radius (R) and time of accretion relative to the formation of CAIs (t_{acc}). The maximum radius in this figure (250 km) roughly corresponds to the size of Vesta. Equation 4.32 was used to calculate a second ordinate axis that indicates the equivalent τ_{cool} for each radius. The value of κ used in Equation 4.32 was 7.9×10^{-7} m^2/s, which corresponds to the default values of thermal conductivity $k = 2.1$ W/m/K, bulk density $\rho = 3300$ kg/m^3 and specific heat $c_p = 800$ J/kg/K.

The 1-dimension thermal model was run for every location in this $R-t_{acc}$ parameter space. The peak temperatures at a depth equal to 50% of the radius were recorded for each $R - t_{acc}$ pair. The three solid curves in this figure represent the objects whose peak temperatures were equal to the Fe-S eutectic (1200 K), the silicate solidus (1400 K) and the silicate liquidus (1900 K). These curves segregate this figure into two primary domains. To the right of these curves, no melting would occur. This is the region of parameter space that would produce meteorites and asteroids with low degrees of thermal metamorphism, e.g. the carbonaceous chondrites (Krot et al. 2005b) and C-type asteroids (Gaffey et al. 1993a). To the left of these curves, high

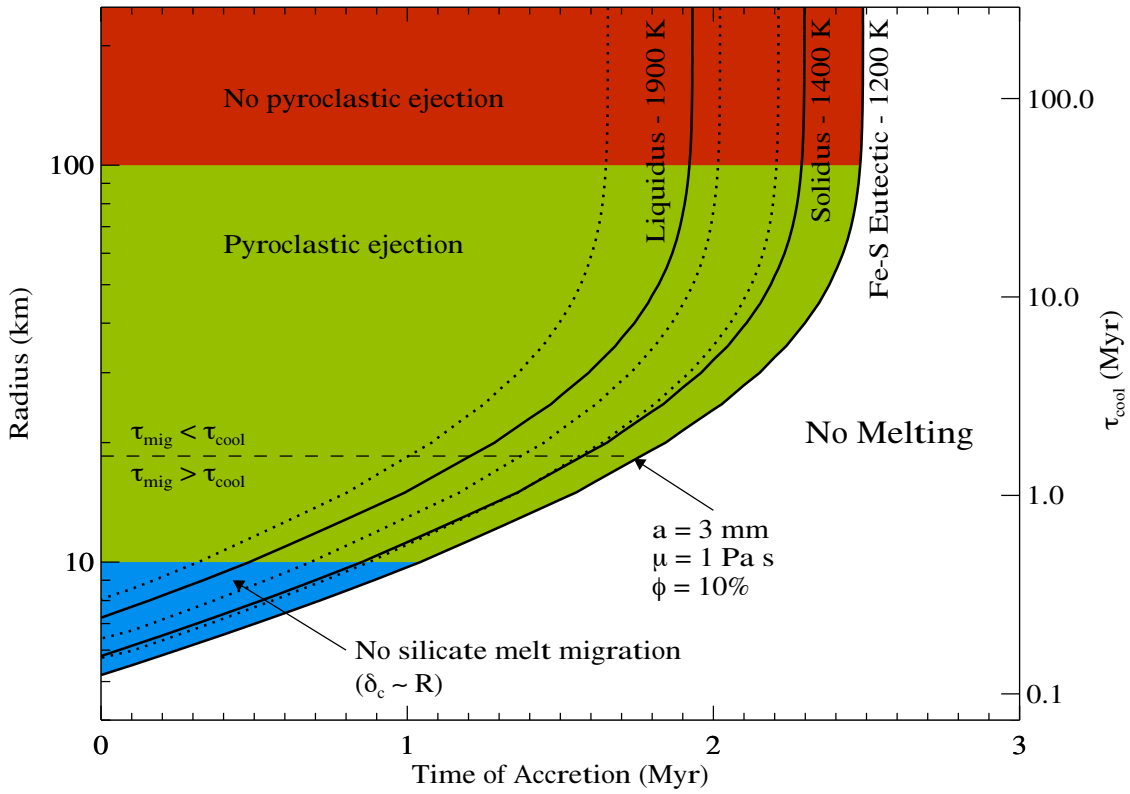

Figure 4.9 Summary of thermal evolution processes. In this radius (R) and time of accretion (t_{acc}) parameter space the curves represent contours of peak temperatures for $R-t_{acc}$ pairs. The solid curves were calculated assuming a purely silicate composition, the dotted curves represent a planetesimal with 10 weight percent water. The blue region represents bodies for which compaction-driven melt migration would not occur because the size of the compaction region (δ_c) would have been comparable to R. The green and red regions represent size constraints for pyroclastic ejection of silicate melt (Wilson & Keil 1991). The dashed line represents a particular example ($a = 3$ mm, $\mu = 1$ Pa s, $\phi = 10\%$) for which the melt migration time scale (τ_{mig}) is comparable to the conductive cooling time scale (τ_{cool}). See text for additional details regarding this figure.

degrees of melting would occur, which would likely be accompanied by the presence of a vigorously convecting magma ocean (Taylor et al. 1993; Righter & Drake 1997).

The peak temperatures at 50% radius for planetesimals with 10 weight percent water (~ 25 volume percent) were also recorded. This was achieved by incorporating the equations from §4.4 into the 1-dimensional thermal model. This incorporation

accounts for the thermal effects of water-rock interactions, specifically the heats of reaction associated with hydration and dehydration chemistry. Peak temperatures of 1200, 1400 and 1900 K for these hydrous planetesimals are plotted as the dotted lines in Figure 4.9. These curves show that the thermal effects of water-rock chemistry require slightly earlier accretion times for a planetesimal to reach the Fe-S eutectic, silicate solidus and silicate liquidus.

The colored regions in Figure 4.9 represent various constraints on the production and migration of silicate melt. The blue region represents the size (< 10 km) for which a planetesimal is too small for compaction-driven melt migration to occur, i.e. δ_c is comparable to R. These bodies would not be able to differentiate by melt migration, but could potentially achieve a differentiated structure via the fractional crystallization of a magma ocean. This region of no silicate melt migration could extend to larger radii (perhaps as high as 100 km) depending on the specific grain size and material properties of the planetesimal (§4.2).

The green and red regions represent a result from Wilson & Keil (1991). As previously stated, these authors found that dissolved volatiles in silicate melts could lead to the buoyant ascent of melt to the surface of a planetesimal. If the surface gravity of this planetesimal were sufficiently low, then pyroclastic eruptions could eject the melt at speeds greater than the escape velocity. This process would have occurred on planetesimals smaller than 100 km in radius (green region). Objects larger than this, like Vesta, would have re-accreted the erupting melt to form a basaltic surface. As shown in §4.3 the removal of ^{26}Al from the interior of the planetesimals within the green region of this figure could have dramatically altered their peak temperatures.

The last feature to discuss in Figure 4.9 is the horizontal dashed line at R=18.5 km, which derives from the melt migration calculations in §4.2. As stated in that section, it is difficult to derive generalized conditions for which melt migration would have been an important cooling mechanism. However, the consequences of migration may have been significant for plausible values of melt fraction ϕ, grain size a, melt viscosity μ

and radius R. The melt migration time scale (τ_{mig}) is equal (1.57 Myr) to the conductive cooling time scale (τ_{cool}) for a body with a radius of 18.5 km when the following assumptions are made: a grain size of 3 mm, a silicate melt viscosity of 1 Pa s and a melt fraction of 10%. With these specific material properties, the region above the dashed line in Figure 4.9 would correspond to planetesimals for which the migration of Al-enriched melt was a faster cooling mechanism than conduction. Below the dashed line, migration was slower than conduction so that the thermal consequences of melt percolation would not have been significant. Varying the assumed grain sizes and melt properties in this system can shift this horizontal line across the full range of radii in this figure so that melt migration could either become the dominant cooling mechanism for all planetesimals (achieved by assuming larger a, smaller μ and/or larger ϕ) or it could become insignificant relative to conduction (through some combination of smaller a, larger μ, smaller ϕ). If $\tau_{mig} > \tau_{cool}$ then the formation of a basaltic crust by melt percolation would not occur. Of course the other relevant time scale in this situation is the ^{26}Al half life. Irrespective of what the dominant cooling mechanism is, if a planetesimal does not cool on a time scale faster than ~ 1 Myr, then it will experience an increase in temperature.

It is important to note that the properties of a planetesimal (ϕ, a, μ) probably changed throughout its lifetime, so that cooling by conduction may have dominated when low melt fractions were present, while cooling by melt migration would have taken over with increasing melt fraction. Convection, a very effective cooling mechanism (Hevey & Sanders 2006), has not been considered in any of these calculations but is one that would have likely followed both a conductive and a melt migration stage. Planetesimals that developed a magma ocean would experience the onset of convection and a hastening of the cooling process (Taylor et al. 1993).

This dissertation concludes by placing Figure 4.9 and the calculations from this chapter into the broader context of asteroidal and meteoritic evidence for differentiation in the early Solar System. In the preceding chapters it was shown that

differentiation seemed to have been a common occurrence during the planet formation process. However, in the present-day, mantle and crustal fragments are depleted relative to the number of metallic cores represented by the iron meteorites and M-type asteroids. Reconciling this discrepancy requires the invocation of loss processes for basaltic and mantle material. Though it has been suggested that the formation of an Fe-S core may have occurred on planetesimals with low silicate melt fractions (i.e. minimal production of basalt, §4.1), the formation of Fe-Ni cores (represented by the iron meteorites) required high temperatures ($\gtrsim$1700 K) near the silicate liquidus, which would have resulted in the production of basaltic melt. This is not a viable scenario for explaining the abundance of iron meteorite parent bodies and the relative lack of heavily metamorphosed silicates. Furthermore, the processes (melt migration, hydration chemistry) explored in this chapter may have been important in limiting the number of planetesimals that reached differentiation temperatures, but they were not mechanisms that would result in the preferential loss of crust and mantle.

For lack of other options a return to the canonical explanations for the relative paucity of basaltic and mantle material in the Main Belt and amongst meteorites is necessary: collisional grinding (Burbine et al. 1996), space weathering (Wetherill & Chapman 1988), and eruptive loss of silicate magmas to space (Wilson & Keil 1991). Future observations (both spectroscopic and photometric) of small objects in the Main Belt can be used to check whether basaltic material is present on bodies that in the past have fallen below observational limits. This is an important test of whether collisional grinding (and subsequent dynamical loss due to Yarkovsky migration) is a cause for the lack of basalt in the Main Belt. A better understanding of the spectral properties of basaltic asteroids and how these properties are affected by exposure to the space environment can provide insight on whether space weathering is causing underestimates for the amount of differentiated material in the Main Belt. Finally, comprehensive models that incorporate the role of melt migration and the effects of water and other volatiles should be performed to provide further insight

on the conditions in the early Solar System that resulted in the differentiation of planetesimals.

Appendix A

Asteroid and Meteorite Data

A.1 Spectroscopically Confirmed V-type Asteroids

Table A.1 Spectroscopically Confirmed V-type Asteroids

Number	Designation	a (AU)	e	i (deg)	H (mag)	Reference
4	Vesta	2.36	0.09	7.14	3.2	(a) (b) (c) (f) (j) (k) (p)
809	Lundia	2.28	0.19	7.14	11.8	(d) (e) (h)
854	Frostia	2.37	0.17	6.09	12.1	(g)
956	Elisa	2.30	0.20	5.96	12.6	(d) (e)
1273	Helma	2.39	0.16	5.41	12.8	(f) (k) (p)
1459	Magnya	3.14	0.24	16.95	9.9	(e) (f) (h) (o)
1468	Zomba	2.20	0.27	9.95	13.6	(i)
1904	Massevitch	2.74	0.08	12.84	11.3	(j)
1906	Naef	2.37	0.13	6.47	12.7	(f) (k) (p)
1914	Hartbeespoortdam	2.41	0.15	5.68	12.4	(g)
1929	Kollaa	2.36	0.08	7.78	12.2	(b) (f) (j) (k) (p)
1933	Tinchen	2.35	0.12	6.88	12.9	(f) (k) (p)
1946	Walraven	2.29	0.24	8.17	11.9	(g)
2011	Veteraniya	2.39	0.15	6.19	12.9	(k) (p)
2045	Peking	2.38	0.06	6.91	12.2	(b) (f) (j)
2113	Ehrdni	2.47	0.10	6.44	13.2	(k) (p)
2442	Corbett	2.39	0.12	5.09	12.8	(f) (j) (p)
2468	Repin	2.33	0.16	5.72	12.4	(b)
2486	Metsahovi	2.27	0.08	8.40	12.4	(g)
2508	Alupka	2.37	0.13	6.08	13.5	(b)
2511	Patterson	2.30	0.10	8.05	12.5	(b)
2547	Hubei	2.39	0.13	6.20	14.0	(b)
2113	Ehrdni	2.47	0.10	6.44	13.2	(k) (p)

Table A.1 continued

Number	Designation	a (AU)	e	i (deg)	H (mag)	Reference
2442	Corbett	2.39	0.12	5.09	12.8	(f) (j) (p)
2468	Repin	2.33	0.16	5.72	12.4	(b)
2113	Ehrdni	2.47	0.10	6.44	13.2	(k) (p)
2442	Corbett	2.39	0.12	5.09	12.8	(f) (j) (p)
2468	Repin	2.33	0.16	5.72	12.4	(b)
2486	Metsahovi	2.27	0.08	8.40	12.4	(g)
2508	Alupka	2.37	0.13	6.08	13.5	(b)
2511	Patterson	2.30	0.10	8.05	12.5	(b)
2547	Hubei	2.39	0.13	6.20	14.0	(b)
2566	Kirghizia	2.45	0.08	5.08	12.6	(b) (j)
2579	Spartacus	2.21	0.07	5.78	13.0	(b) (f) (j)
2590	Mourao	2.34	0.12	6.13	12.7	(f) (k) (p)
2640	Hallstrom	2.40	0.09	6.65	13.0	(b)
2653	Principia	2.44	0.08	4.74	12.1	(b) (f)
2704	Julian Loewe	2.39	0.10	4.51	13.2	(b)
2763	Jeans	2.40	0.22	3.54	12.6	(b) (f)
2795	Lepage	2.30	0.03	6.04	13.2	(b)
2823	van der Laan	2.41	0.09	3.82	13.2	(l)
2851	Harbin	2.48	0.12	8.55	12.3	(b) (f) (j)
2912	Lapalma	2.29	0.07	7.28	12.7	(b) (j)
3153	Lincoln	2.42	0.13	7.70	13.3	(k) (p)
3155	Lee	2.34	0.10	7.20	12.6	(b) (j) (p)
3265	Fletcher	2.41	0.14	6.94	13.1	(b)
3268	De Sanctis	2.35	0.13	6.35	13.4	(f) (k) (p)
3307	Athabasca	2.26	0.10	6.38	13.9	(b)
3344	Modena	2.42	0.12	9.45	12.9	(l)
3494	Purple Mountain	2.35	0.13	5.84	12.7	(p)
3498	Belton	2.35	0.10	6.23	13.5	(b)
3536	Schleicher	2.34	0.05	6.56	13.8	(b)
3657	Ermolova	2.31	0.13	5.79	12.7	(f) (p)
3782	Celle	2.42	0.10	5.25	12.5	(b)
3849	Incidentia	2.48	0.05	5.77	13.1	(b) (f)
3850	Peltier	2.23	0.16	5.27	13.9	(b)
3869	Norton	2.45	0.13	4.36	13.0	(p)
3900	Knezevic	2.37	0.14	6.73	13.6	(b)
3944	Halliday	2.37	0.15	7.55	13.1	(f) (k) (p)
3968	Koptelov	2.32	0.09	6.21	12.9	(f) (k) (p)
4005	Dyagilev	2.45	0.15	6.84	12.7	(f) (p)
4038	Kristina	2.37	0.13	6.00	13.3	(k) (p)
4147	Lennon	2.36	0.08	5.74	13.0	(f) (k) (p)
4188	Kitezh	2.34	0.15	6.12	12.7	(b) (f) (j)
4215	Kamo	2.42	0.06	5.76	12.4	(b) (f) (p)
4278	Harvey	2.27	0.18	5.47	14.0	(d) (h)
4311	Zguridi	2.44	0.15	5.48	13.6	(b) (f)
4434	Nikulin	2.44	0.13	5.71	13.2	(b)
4546	Franck	2.36	0.06	6.10	13.6	(k) (p)
4796	Lewis	2.36	0.18	2.27	13.2	(b)
4900	Maymelou	2.38	0.13	5.93	13.0	(b) (f)

Table A.1 continued

Number	Designation	a (AU)	e	i (deg)	H (mag)	Reference
4977	Rauthgundis	2.29	0.11	5.88	13.7	(b)
4993	Cossard	2.37	0.06	6.94	13.0	(b)
5111	Jacliff	2.35	0.13	5.81	13.1	(j)
5240	Kwasan	2.38	0.10	5.61	12.4	(b)
5481	Kiuchi	2.34	0.06	5.96	13.0	(h)
5498	Gustafsson	2.25	0.15	2.11	14.5	(q)
6406	1992 MJ	2.28	0.18	8.17	12.5	(g)
7148	Reinholdbien	2.29	0.05	5.01	13.0	(g)
7558	Yurlov	2.29	0.10	4.52	13.4	(q)
8693	Matsuki	2.41	0.16	6.93	12.8	(g)
8761	Crane	2.24	0.09	3.16	13.9	(q)
9147	1977 DD1	2.19	0.11	5.82	13.7	(q)
9254	Shunkai	2.36	0.19	6.06	13.6	(q)
9481	Menchu	2.29	0.09	2.74	14.0	(q)
9553	Colas	2.20	0.12	1.92	14.6	(q)
10537	1991 RY16	2.85	0.07	7.25	12.9	(q)
12543	1998 QM5	2.36	0.18	7.01	13.8	(q)
12851	1998 DT9	2.13	0.12	2.03	15.1	(q)
16416	1987 SM3	2.20	0.10	5.95	13.8	(q)
21238	1995 WV7	2.54	0.11	11.44	12.9	(l) (m)
24941	1997 JM14	2.48	0.09	4.75	15.5	(q)
26886	1994 TJ2	2.34	0.16	4.90	14.7	(q)
28517	2000 DD7	2.29	0.04	8.50	13.5	(q)
33881	2000 JK66	2.21	0.29	11.17	14.4	(q)
36412	2000 OP49	2.28	0.16	4.69	14.2	(q)
38070	1999 GG2	2.14	0.22	4.00	15.4	(q)
40521	1999 RL95	2.53	0.07	12.66	14.9	(n)
50098	2000 AG98	2.35	0.17	7.18	13.2	(q)
56026	1998 VN52	2.40	0.17	7.61	14.5	(q)
56570	2000 JA21	2.38	0.13	3.22	15.4	(q)
60669	2000 GE4	2.21	0.20	7.69	15.5	(q)
97276	1999 XC143	2.48	0.18	4.86	14.5	(q)

V-type NEAs are not included in this table. Osculating orbital elements (a, e, i) and absolute magnitude (H) are from Bowell (2007). References:
(a) McCord et al. (1970); (b) Bus & Binzel (2002a); (c) Gaffey (1997); (d) Florczak et al. (2002); (e) Lazzaro et al. (2004); (f) Burbine & Binzel (2002); (g) Alvarez-Candal et al. (2006); (h) Lazzaro et al. (2000); (i) T. Burbine, private communication, 2008; (j) DeMeo et al. (2008); (k) Binzel & Xu (1993); (l) Masi et al. (2008); (m) Hammergren et al. (2006); (n) Roig et al. (2008); (o) Hardersen et al. (2004); (p) Xu et al. (1995); (q) This work.

A.2 Band Parameters of HED Meteorites

Table A.2 Band Parameters of HED Meteorites

Sample Name	Type	Particle Size (μm)	BI Center (μm)	BII Center (μm)	BAR
EET83376	Howardite	25	0.934	1.981	1.7840
EET87503	Howardite	25	0.929	1.970	1.6192
EET87513	Howardite	25	0.932	1.976	1.4692
GRO95535	Howardite	25	0.929	1.963	1.6713
GRO95574	Howardite	125	0.929	1.953	1.7572
QUE94200	Howardite	25	0.921	1.926	1.8620
QUE97001	Howardite	125	0.924	1.933	2.0792
Y7308	Howardite	25	0.927	1.942	1.6972
Y790727	Howardite	25	0.931	1.964	1.9103
Y791573	Howardite	25	0.926	1.948	1.8023
Bialystok[a]	Howardite	150	0.937	1.990	1.6414
Binda	Howardite	25	0.928	1.948	1.6933
Bununu[a]	Howardite	25	0.928	1.951	1.4740
Frankfort[a]	Howardite	25	0.927	1.945	1.7644
Kapoeta[a]	Howardite	25	0.928	1.936	1.3722
Le Teilleul[a]	Howardite	25	0.928	1.943	1.9352
Pavlovka[a]	Howardite	chip	0.921	1.934	1.9778
Petersburg	Howardite	25	0.934	1.988	1.8304
A87272	Eucrite	25	0.941	2.029	1.2244
A881819	Eucrite	25	0.931	1.976	1.5599
ALH78132	Eucrite	45	0.933	1.967	2.1383
ALH85001	Eucrite	25	0.925	1.952	1.5517
ALHA76005	Eucrite	25	0.935	1.996	1.7261
ALHA81001	Eucrite	45	0.937	2.024	2.7991
ALHA81011	Eucrite	125	0.951	2.042	1.3355
ALHA85001	Eucrite	1000	0.932	1.993	1.6795
BTN00300	Eucrite	45	0.947	2.029	0.9420
EET83251	Eucrite	1000	0.937	2.009	2.1906
EET87520	Eucrite	45	0.951	2.042	1.1116
EET87542	Eucrite	25	0.940	2.017	1.3458
EET90020	Eucrite	25	0.941	2.012	0.9865
EET92003	Eucrite	125	0.933	2.002	1.6588
EETA79005	Eucrite	25	0.934	1.974	2.0033
EETA79006	Eucrite	125	0.935	1.987	1.9342
EETA790B	Eucrite	1000	0.937	1.998	2.0071
GRO95533	Eucrite	25	0.941	2.040	1.4581
LEW85303	Eucrite	25	0.945	2.022	1.5695
LEW87004	Eucrite	25	0.934	1.963	1.7839
MAC02522	Eucrite	45	0.970	2.160	0.8309
MET01081	Eucrite	45	0.939	2.002	1.2518
PCA82501	Eucrite	125	0.943	2.025	1.9056

Table A.2 continued

Sample Name	Type	Particle Size (μm)	BI Center (μm)	BII Center (μm)	BAR
PCA82502	Eucrite	25	0.941	2.025	2.2161
PCA91006	Eucrite	125	0.942	2.002	1.3592
PCA91007	Eucrite	125	0.943	2.042	2.1384
PCA91078	Eucrite	45	0.955	2.059	1.7840
Y74450	Eucrite	25	0.934	1.970	1.3623
Y75011	Eucrite	1000	0.947	2.025	1.2378
Y791186	Eucrite	1000	0.949	2.052	1.4823
Y792510	Eucrite	25	0.942	2.032	1.3369
Y792769	Eucrite	25	0.941	2.026	1.6585
Y793591	Eucrite	25	0.939	2.011	1.8571
Y82082	Eucrite	25	0.947	2.034	1.6305
Y980318	Eucrite	75	0.940	2.016	1.4857
Bereba[a]	Eucrite	25	0.941	2.023	1.7060
Bouvante	Eucrite	25	0.943	2.030	2.2411
Cachari	Eucrite	25	0.940	2.027	1.4802
Ibitra[a]	Eucrite	25	0.940	2.000	1.1341
Jonzac[a]	Eucrite	25	0.939	2.013	1.7952
Juvinas[a]	Eucrite	25	0.936	2.003	1.6049
Millbillillie[a]	Eucrite	25	0.938	2.019	1.3609
Moore County[a]	Eucrite	25	0.938	1.987	1.3885
NWA011	Eucrite	25	0.950	2.029	0.9193
Padvarninkai[a]	Eucrite	25	0.939	2.012	1.4851
Pasamonte[a]	Eucrite	25	0.939	2.003	1.5453
Serra de Mage[a]	Eucrite	25	0.931	1.974	1.5117
Stannern[a]	Eucrite	25	0.938	2.017	1.9172
EETA79002	Diogenite	25	0.917	1.887	1.7581
LAP91900	Diogenite	1000	0.925	1.920	1.9701
Y74013	Diogenite	25	0.920	1.919	1.7630
Y75032	Diogenite	25	0.926	1.924	1.7040
Ellemeet[a]	Diogenite	25	0.920	1.901	1.9083
Johnstown[a]	Diogenite	25	0.914	1.874	1.5085
Roda[a]	Diogenite	chip	0.923	1.904	1.9880
Shalka[a]	Diogenite	chip	0.918	1.905	2.2039
Tatahouine[a]	Diogenite	chip	0.920	1.916	1.8623

Columns in this table are: name of the sample, meteorite type, mean particle size of the sample when the spectra were measured, BI and BII centers, and the ratio of BII area to BI area (BAR). Some samples were not ground into particles to measure their reflectance spectrum: these are indicated as "chip" in the particle size column.
[a] Indicates a fall rather than a find

A.3 NIR Spectra of Inner Main Belt V-types

In this section we present the NIR spectra of all inner Main Belt V-types analyzed in §3.4. The designation of the targets are shown in each panel. Some targets were observed on multiple occasions: the dates of these observations are indicated in a year, month, day format (YYMMDD) following the object designation. Observations prior to the year 2006 were either performed as part of the Small Main-Belt Asteroid Spectroscopic Survey (SMASS) or, for the spectrum of 4 Vesta, by Gaffey (1997). When available, visible wavelength SMASS spectra are appended to these data. Multiple SMASS observations of Kamo, Celle, Lee, Harbin and Principia were combined into composite spectra. All spectra have been normalized to unity at 1 μm and are all presented at the same scale.

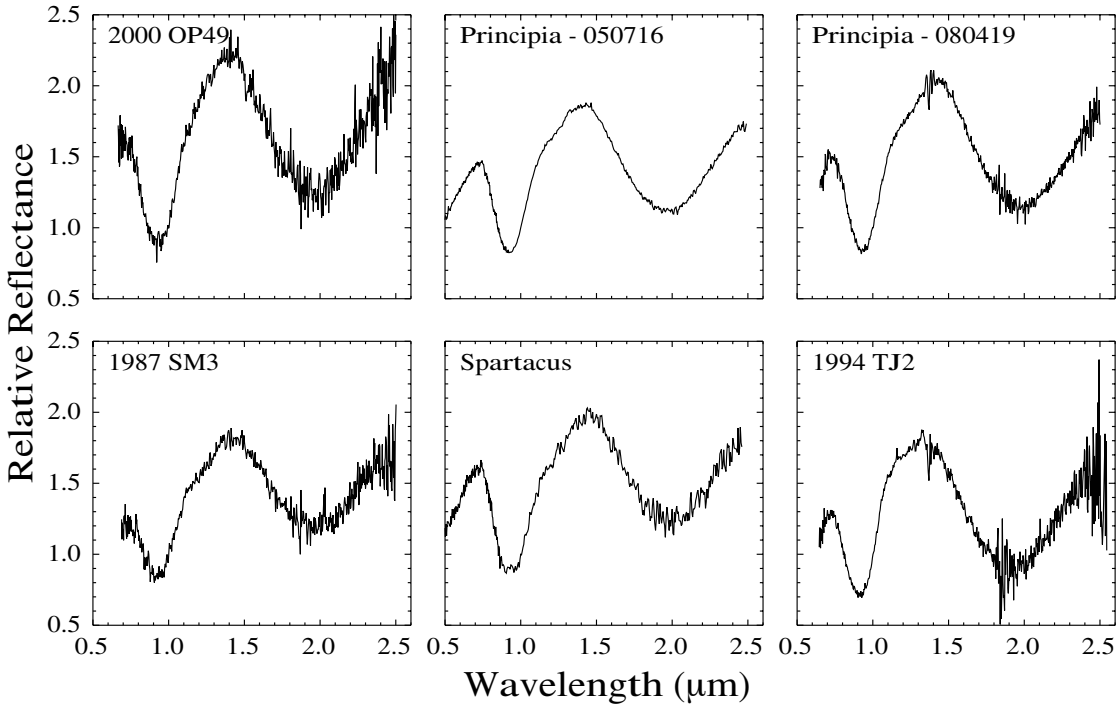

Figure A.1 NIR spectra of inner Main Belt V-types

Figure A.1 continued

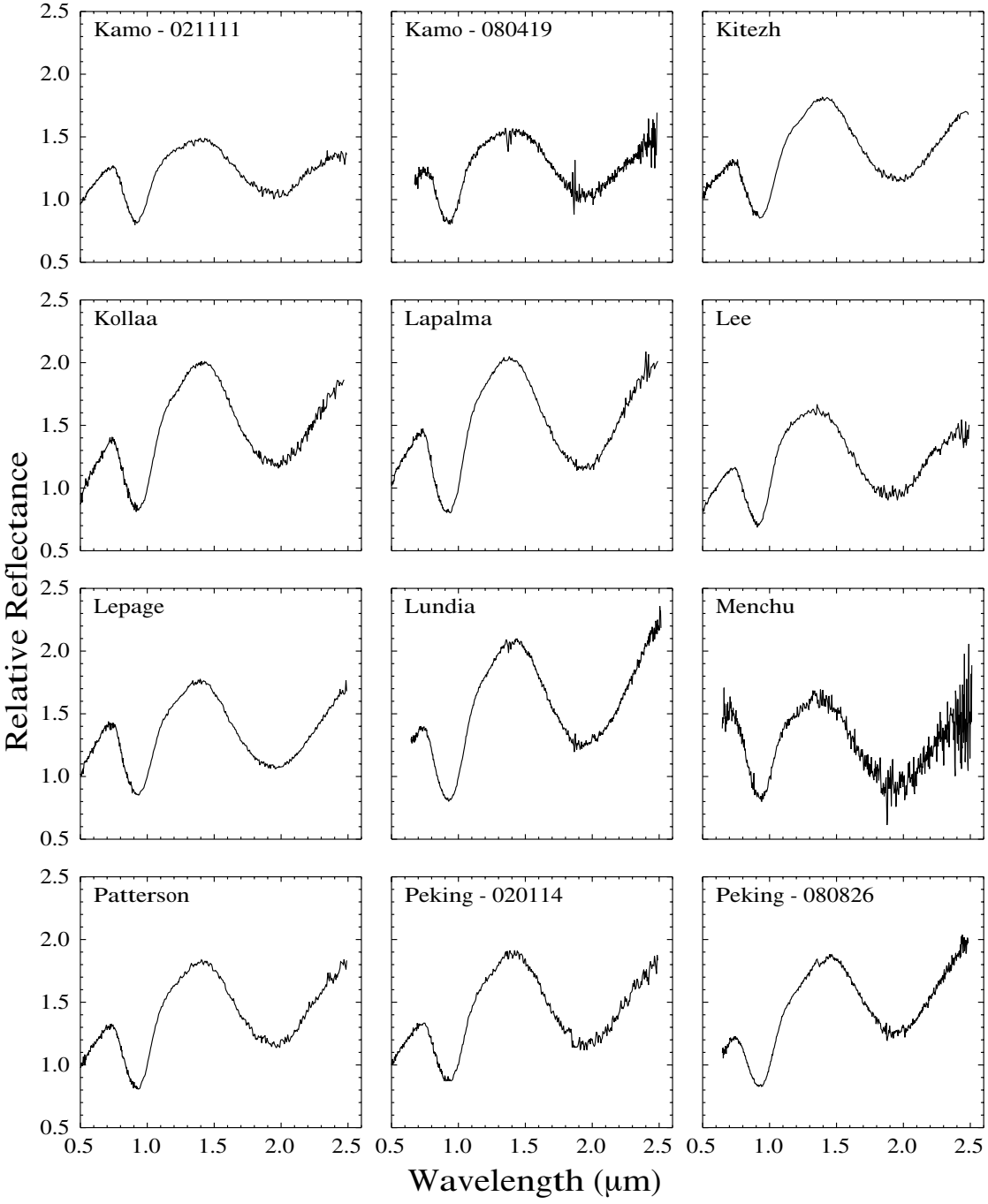

Figure A.1 continued

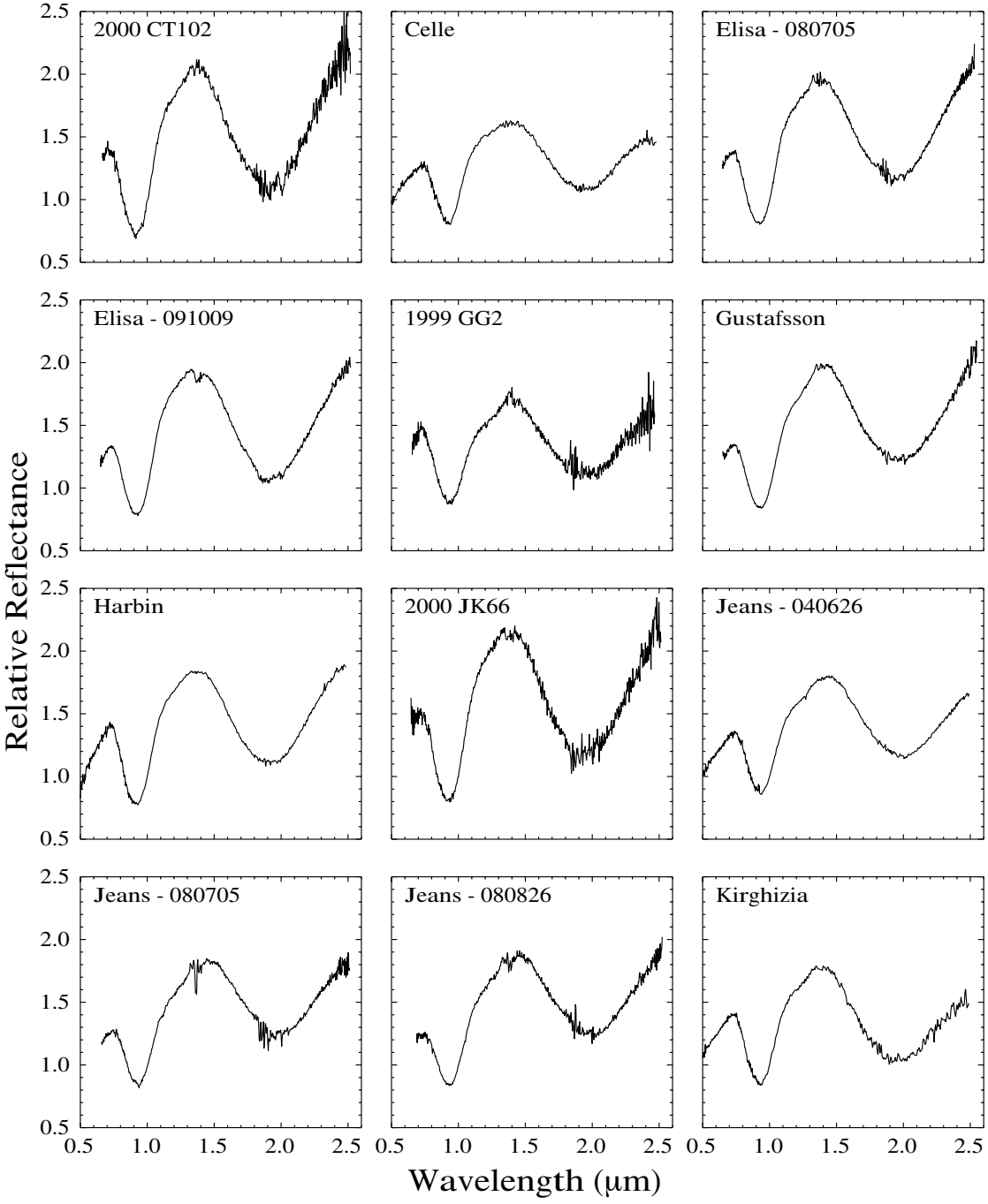

Figure A.1 continued

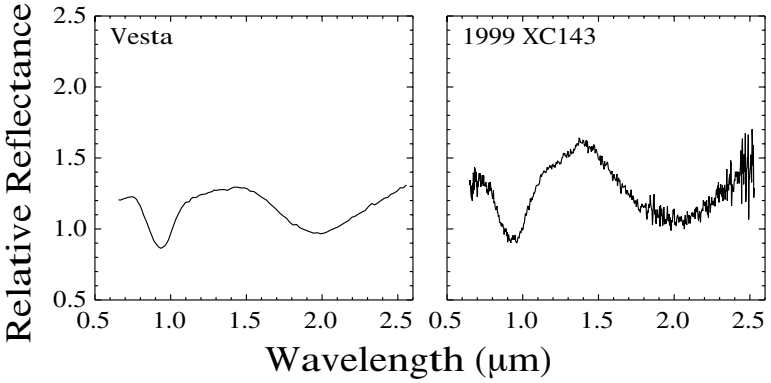

References

Abe, Y., Ohtani, E., Okuchi, T., Righter, K., & Drake, M. 2000, Water in the Early Earth (Tucson: University of Arizona Press), 413–433

Abell, P. A., & Gaffey, M. J. 2000, in Lunar and Planetary Institute Conference Abstracts, Vol. 31, Lunar and Planetary Institute Conference Abstracts, 1291

Adams, J. B. 1974, Visible and near-infrared diffuse reflectance spectra of pyroxenes as applied to remote sensing of solid objects in the solar system, Journal of Geophysical Research, 79, 4829

Agee, C. B., Li, J., Shannon, M. C., & Circone, S. 1995, Pressure-temperature phase diagram for the Allende meteorite., Journal of Geophysical Research, 100, 17725

Agee, C. B., & Walker, D. 1990, Aluminum partitioning between olivine and ultrabasic silicate liquid to 6 GPa, Contrib. Mineral Petr., 105, 243

Alvarez-Candal, A., Duffard, R., Lazzaro, D., & Michtchenko, T. 2006, The inner region of the asteroid Main Belt: a spectroscopic and dynamic analysis, Astronomy and Astrophysics, 459, 969

Anders, E., & Grevesse, N. 1989, Abundances of the elements - Meteoritic and solar, Geochimica et Cosmochimica Acta, 53, 197

Asphaug, E. 1997, Impact origin of the Vesta family, Met. Planet. Sci., 32, 965

Baer, J., & Chesley, S. R. 2008, Astrometric masses of 21 asteroids, and an integrated asteroid ephemeris, Celestial Mechanics and Dynamical Astronomy, 100, 27

Baker, J., Bizzarro, M., Wittig, N., Connelly, J., & Haack, H. 2005, Early planetesimal melting from an age of 4.5662Gyr for differentiated meteorites, Nature, 436, 1127

Belskaya, I. N., & Lagerkvist, C.-I. 1996, Physical properties of M class asteroids, Planetary and Space Science, 44, 783

Bendjoya, P., & Zappalà, V. 2002, Asteroid Family Identification, Asteroids III, 613

Best, M. G. 2002, Igneous and metamorphic petrology (Wiley-Blackwell)

Binzel, R. P., Bus, S. J., Burbine, T. H., & Rivkin, A. S. 2001, in Lunar and Planetary Institute Conference Abstracts, Vol. 32, Lunar and Planetary Institute Conference Abstracts, 1633

Binzel, R. P., Gaffey, M. J., Thomas, P. C., Zellner, B. H., Storrs, A. D., & Wells, E. N. 1997, Geologic Mapping of Vesta from 1994 Hubble Space Telescope Images, Icarus, 128, 95

Binzel, R. P., Masi, G., Foglia, S., Vernazza, P., Burbine, T. H., Thomas, C. A., Demeo, F. E., Nesvorny, D., Birlan, M., & Fulchignoni, M. 2007, in Lunar and Planetary Institute Conference Abstracts, Vol. 38, Lunar and Planetary Institute Conference Abstracts, 1851

Binzel, R. P., Rivkin, A. S., Thomas, C. A., Vernazza, P., Burbine, T. H., Demeo, F. E., Bus, S. J., Tokunaga, A. T., & Birlan, M. 2009, Spectral properties and composition of potentially hazardous Asteroid (99942) Apophis, Icarus, 200, 480

Binzel, R. P., & Xu, S. 1993, Chips off of asteroid 4 Vesta - Evidence for the parent body of basaltic achondrite meteorites, Science, 260, 186

Bottke, W. F., Durda, D. D., Nesvorný, D., Jedicke, R., Morbidelli, A., Vokrouhlický, D., & Levison, H. 2005a, The fossilized size distribution of the main asteroid belt, Icarus, 175, 111

Bottke, W. F., Durda, D. D., Nesvorný, D., Jedicke, R., Morbidelli, A., Vokrouhlický, D., & Levison, H. F. 2005b, Linking the collisional history of the main asteroid belt to its dynamical excitation and depletion, Icarus, 179, 63

Bottke, W. F., Nesvorný, D., Grimm, R. E., Morbidelli, A., & O'Brien, D. P. 2006, Iron meteorites as remnants of planetesimals formed in the terrestrial planet region, Nature, 439, 821

Bottke, W. F., Vokrouhlický, D., Broz, M., Nesvorný, D., & Morbidelli, A. 2001, Dynamical Spreading of Asteroid Families by the Yarkovsky Effect, Science, 294, 1693

Bottke, Jr., W. F., Rubincam, D. P., & Burns, J. A. 2000, Dynamical evolution of main belt meteoroids: Numerical simulations incorporating planetary perturbations and Yarkovsky thermal forces, Icarus, 145, 301

Bowell, E. 2007, Orbits of Minor Planets (Bowell+ 2009), VizieR Online Data Catalog, 1, 2001

Bowell, E., Hapke, B., Domingue, D., Lumme, K., Peltoniemi, J., & Harris, A. W. 1989, in Asteroids II, ed. R. P. Binzel, T. Gehrels, & M. S. Matthews, 524–556

Britt, D. T., Yeomans, D., Housen, K., & Consolmagno, G. 2002, Asteroid Density, Porosity, and Structure, Asteroids III, 485

Burbine, T. H., & Binzel, R. P. 2002, Small Main-Belt Asteroid Spectroscopic Survey in the Near-Infrared, Icarus, 159, 468

Burbine, T. H., Buchanan, P. C., Binzel, R. P., Bus, S. J., Hiroi, T., Hinrichs, J. L., Meibom, A., & McCoy, T. J. 2001, Vesta, Vestoids, and the howardite, eucrite,

diogenite group: Relationships and the origin of spectral differences, Met. Planet. Sci., 36, 761

Burbine, T. H., Buchanan, P. C., Dolkar, T., & Binzel, R. P. 2009, in Lunar and Planetary Institute Science Conference Abstracts, Vol. 40, Lunar and Planetary Institute Science Conference Abstracts, 1922

Burbine, T. H., McCoy, T. J., Meibom, A., Gladman, B., & Keil, K. 2002, Meteoritic Parent Bodies: Their Number and Identification, Asteroids III, 653

Burbine, T. H., Meibom, A., & Binzel, R. P. 1996, Mantle material in the main belt: Battered to bits?, Met. Planet. Sci., 31, 607

Burns, R. G., Vaughan, D. J., Abu-Eid, R. M., Witner, M., & Morawski, A. 1973, in Lunar and Planetary Science Conference, Vol. 4, Lunar and Planetary Science Conference, 983

Bus, S. J., & Binzel, R. P. 2002a, Phase II of the Small Main-Belt Asteroid Spectroscopic SurveyA Feature-Based Taxonomy, Icarus, 158, 146

—. 2002b, Phase II of the Small Main-Belt Asteroid Spectroscopic SurveyThe Observations, Icarus, 158, 106

Carruba, V., Michtchenko, T. A., & Lazzaro, D. 2007a, On the V-type asteroids outside the Vesta family. II. Is (21238) 1995 WV7 a fragment of the long-lost basaltic crust of (15) Eunomia?, Astronomy and Astrophysics, 473, 967

Carruba, V., Michtchenko, T. A., Roig, F., Ferraz-Mello, S., & Nesvorný, D. 2005, On the V-type asteroids outside the Vesta family. I. Interplay of nonlinear secular resonances and the Yarkovsky effect: the cases of 956 Elisa and 809 Lundia, Astronomy and Astrophysics, 441, 819

Carruba, V., Roig, F., Michtchenko, T. A., Ferraz-Mello, S., & Nesvorný, D. 2007b, Modeling close encounters with massive asteroids: a Markovian approach. An application to the Vesta family, Astronomy and Astrophysics, 465, 315

Cellino, A., Bus, S. J., Doressoundiram, A., & Lazzaro, D. 2002, Spectroscopic Properties of Asteroid Families, Asteroids III, 633

Chabot, N. L., & Haack, H. 2006, Evolution of Asteroidal Cores (Meteorites and the Early Solar System II), 747–771

Chambers, J. 2006, A semi-analytic model for oligarchic growth, Icarus, 180, 496

Chambers, J. E. 1999, A hybrid symplectic integrator that permits close encounters between massive bodies, Mon. Not. R. Astron. Soc., 304, 793

Chesley, S. R., Ostro, S. J., Vokrouhlický, D., Čapek, D., Giorgini, J. D., Nolan, M. C., Margot, J.-L., Hine, A. A., Benner, L. A. M., & Chamberlin, A. B. 2003, Direct Detection of the Yarkovsky Effect by Radar Ranging to Asteroid 6489 Golevka, Science, 302, 1739

Ciesla, F. J., & Cuzzi, J. N. 2006, The evolution of the water distribution in a viscous protoplanetary disk, Icarus, 181, 178

Clark, B. E., Hapke, B., Pieters, C., & Britt, D. 2002, Asteroid Space Weathering and Regolith Evolution, Asteroids III, 585

Claver, C. F., & 13 co-authors. 2004, in Society of Photo-Optical Instrumentation Engineers (SPIE) Conference Series, ed. J. M. Oschmann, Jr., Vol. 5489, 705–716

Clayton, D. D. 1980, Chemical energy in cold-cloud aggregates - The origin of meteoritic chondrules, Astrophys. J., Lett., 239, L37

Cloutis, E. A. 2002, Pyroxene reflectance spectra: Minor absorption bands and effects of elemental substitutions, Journal of Geophysical Research (Planets), 107, 5039

Cloutis, E. A., Gaffey, M. J., Jackowski, T. L., & Reed, K. L. 1986, Calibrations of phase abundance, composition, and particle size distribution for olivine-orthopyroxene mixtures from reflectance spectra, Journal of Geophysical Research, 91, 11641

Cloutis, E. A., Sunshine, J. M., & Morris, R. V. 2004, Spectral reflectance-compositional properties of spinels and chromites: Implications for planetary remote sensing and geothermometry, Met. Planet. Sci., 39, 545

Cohen, B. A., & Coker, R. F. 2000, Modeling of liquid water on CM meteorite parent bodies and implications for amino acid racemization, Icarus, 145, 369

Consolmagno, G. J., & Drake, M. J. 1977, Composition and evolution of the eucrite parent body - Evidence from rare earth elements, Geochimica et Cosmochimica Acta, 41, 1271

Cushing, M. C., Vacca, W. D., & Rayner, J. T. 2004, Spextool: A Spectral Extraction Package for SpeX, a 0.8-5.5 Micron Cross-Dispersed Spectrograph, Publications of the Astronomical Society of the Pacific, 116, 362

Davis, D. R., Durda, D. D., Marzari, F., Campo Bagatin, A., & Gil-Hutton, R. 2002, Collisional Evolution of Small-Body Populations, Asteroids III, 545

Davis, D. R., Farinella, P., & Marzari, F. 1999, The Missing Psyche Family: Collisionally Eroded or Never Formed?, Icarus, 137, 140

Davis, D. R., Weidenschilling, S. J., Farinella, P., Paolicchi, P., & Binzel, R. P. 1989, in Asteroids II, ed. R. P. Binzel, T. Gehrels, & M. S. Matthews, 805–826

Delbo, M., & 11 co-authors. 2006, MIDI observations of 1459 Magnya: First attempt of interferometric observations of asteroids with the VLTI, Icarus, 181, 618

DeMeo, F. E., Bus, S. J., Binzel, R. P., & Slivan, S. M. 2008, Bus-DeMeo Taxonomy: Extending Asteroid Taxonomy into the Near-Infrared, LPI Contributions, 1405, 8186

di Martino, M., Manara, A., & Migliorini, F. 1995, 1993 VW: an ordinary chondrite-like near-Earth asteroid., Astronomy and Astrophysics, 302, 609

Dollfus, A., Mandeville, J. C., & Duseaux, M. 1979, The nature of the M-type asteroids from optical polarimetry, Icarus, 37, 124

Drake, M. J. 1979, Geochemical evolution of the eucrite parent body - Possible nature and evolution of asteroid 4 Vesta (Tucson: University of Arizona Press), 765–782

Dreibus, G., & Wänke, H. 1980, The bulk composition of the eucrite parent asteroid and its bearing of planetary evolution., Z. Naturforsch., A, Band 35a, p. 204 - 216, 35, 204

Duffard, R., Lazzaro, D., & de León, J. 2005, Revisiting spectral parameters of silicate-bearing meteorites, Met. Planet. Sci., 40, 445

Duffard, R., Lazzaro, D., Licandro, J., de Sanctis, M. C., Capria, M. T., & Carvano, J. M. 2004, Mineralogical characterization of some basaltic asteroids in the neighborhood of (4) Vesta: first results, Icarus, 171, 120

Duffard, R. D., & Roig, F. 2008, Two New Basaltic Asteroids in the Main Belt?, LPI Contributions, 1405, 8154

Feierberg, M. A., Larson, H. P., Fink, U., & Smith, H. A. 1980, Spectroscopic evidence for two achondrite parent bodies - Asteroids 349 Dembowska and 4 Vesta, Geochimica et Cosmochimica Acta, 44, 513

Florczak, M., Lazzaro, D., & Duffard, R. 2002, Discovering New V-Type Asteroids in the Vicinity of 4 Vesta, Icarus, 159, 178

Folco, L., Bland, P. A., D'Orazio, M., Franchi, I. A., Kelley, S. P., & Rocchi, S. 2004, Extensive impact melting on the H-chondrite parent asteroid during the cataclysmic bombardment of the early solar system: Evidence from the achondritic meteorite Dar al Gani 896, Geochimica et Cosmochimica Acta, 68, 2379

Gaffey, M. J. 1984, Rotational spectral variations of asteroid (8) Flora Implications for the nature of the S-type asteroids and for the parent bodies of the ordinary chondrites, Icarus, 60, 83

—. 1997, Surface Lithologic Heterogeneity of Asteroid 4 Vesta, Icarus, 127, 130

Gaffey, M. J., Burbine, T. H., & Binzel, R. P. 1993a, Asteroid spectroscopy - Progress and perspectives, Meteoritics, 28, 161

Gaffey, M. J., Burbine, T. H., Piatek, J. L., Reed, K. L., Chaky, D. A., Bell, J. F., & Brown, R. H. 1993b, Mineralogical variations within the S-type asteroid class, Icarus, 106, 573

Gaffey, M. J., Cloutis, E. A., Kelley, M. S., & Reed, K. L. 2002, Mineralogy of Asteroids, Asteroids III, 183

Ghiorso, M. S., & Sack, R. O. 1995, Chemical mass transfer in magmatic processes. IV. A revised and internally consistent thermodynamic model for the interpolation and extrapolation of liquid-solid equilibria in magmatic systems at elevated temperatures and pressure, Computer, 119, 197

Ghosh, A., & McSween, H. Y. 1998, A Thermal Model for the Differentiation of Asteroid 4 Vesta, Based on Radiogenic Heating, Icarus, 134, 187

Ghosh, A., & McSween, Jr., H. Y. 1999, Temperature dependence of specific heat capacity and its effect on asteroid thermal models, Met. Planet. Sci., 34, 121

Giordano, D., Russell, J. K., & Dingwell, D. B. 2008, Viscosity of magmatic liquids: A model, Earth Planet. Sci. Lett., 271, 123

Gladman, B. J., Migliorini, F., Morbidelli, A., Zappala, V., Michel, P., Cellino, A., Froeschle, C., Levison, H. F., Bailey, M., & Duncan, M. 1997, Dynamical lifetimes of objects injected into asteroid belt resonances, Science, 277, 197

Gomes, R., Levison, H. F., Tsiganis, K., & Morbidelli, A. 2005, Origin of the cataclysmic Late Heavy Bombardment period of the terrestrial planets, Nature, 435, 466

Gomes, R. S. 1997, Dynamical Effects of Planetary Migration on the Primordial Asteroid Belt, Astronomical Journal, 114, 396

Goswami, J. N., Marhas, K. K., Chaussidon, M., Gounelle, M., & Meyer, B. S. 2005, in Astronomical Society of the Pacific Conference Series, Vol. 341, Chondrites and the Protoplanetary Disk, ed. A. N. Krot, E. R. D. Scott, & B. Reipurth, 485

Gradie, J., & Tedesco, E. 1982, Compositional structure of the asteroid belt, Science, 216, 1405

Gradie, J. C., Chapman, C. R., & Tedesco, E. F. 1989, in Asteroids II, ed. R. P. Binzel, T. Gehrels, & M. S. Matthews, 316–335

Greenwood, R. C., Franchi, I. A., Jambon, A., & Buchanan, P. C. 2005, Widespread magma oceans on asteroidal bodies in the early Solar System, Nature, 435, 916

Grimm, R. E., & McSween, H. Y. 1993, Heliocentric zoning of the asteroid belt by aluminum-26 heating, Science, 259, 653

Grimm, R. E., & McSween, Jr., H. Y. 1989, Water and the thermal evolution of carbonaceous chondrite parent bodies, Icarus, 82, 244

Haack, H., Rasmussen, K. L., & Warren, P. H. 1990, Effects of regolith/megaregolith insulation on the cooling histories of differentiated asteroids, Journal of Geophysical Research, 95, 5111

Hammergren, M., Gyuk, G., & Puckett, A. 2006, (21238) 1995 WV7: A New Basaltic Asteroid Outside the 3:1 Mean Motion Resonance, ArXiv Astrophysics e-prints

Hardersen, P. S., Gaffey, M. J., & Abell, P. A. 2004, Mineralogy of Asteroid 1459 Magnya and implications for its origin, Icarus, 167, 170

Harris, A. W. 1979, Asteroid rotation rates II. A theory for the collisional evolution of rotation rates, Icarus, 40, 145

Harvey, R. P., & Cassidy, W. A. 1989, A statistical comparison of Antarctic finds and modern falls - Mass frequency distributions and relative abundance by type, Meteoritics, 24, 9

Hayashi, C. 1981, Structure of the Solar Nebula, Growth and Decay of Magnetic Fields and Effects of Magnetic and Turbulent Viscosities on the Nebula, Progress of Theoretical Physics Supplement, 70, 35

Hevey, P. J., & Sanders, I. S. 2006, A model for planetesimal meltdown by 26Al and its implications for meteorite parent bodies, Met. Planet. Sci., 41, 95

Hinrichs, J. L., & Lucey, P. G. 2002, Temperature-Dependent Near-Infrared Spectral Properties of Minerals, Meteorites, and Lunar Soil, Icarus, 155, 169

Hirayama, K. 1918, Groups of asteroids probably of common origin, Astronomical Journal, 31, 185

Hiroi, T., Bell, J. F., Takeda, H., & Pieters, C. M. 1993, Modeling of S-type asteroid spectra using primitive achondrites and iron meteorites, Icarus, 102, 107

Hiroi, T., Binzel, R. P., Sunshine, J. M., Pieters, C. M., & Takeda, H. 1995, Grain sizes and mineral compositions of surface regoliths of Vesta-like asteroids., Icarus, 115, 374

Hiroi, T., & Pieters, C. M. 1998, Origin of vestoids suggested from the space weathering trend in the visible reflectance spectra of HED meteorites and lunar soils, Antarctic Meteorite Research, 11, 163

Hiroi, T., Pieters, C. M., & Takeda, H. 1994, Grain size of the surface regolith of asteroid 4 Vesta estimated from its reflectance spectrum in comparison with HED meteorites, Meteoritics, 29, 394

Hiroi, T., & Sasaki, S. 2001, Importance of space weathering simulation products in compositional modeling of asteroids: 349 Dembowska and 446 Aeternitas as examples, Met. Planet. Sci., 36, 1587

Hiroi, T., Vilas, F., & Sunshine, J. M. 1996, Discovery and Analysis of Minor Absorption Bands in S-Asteroid Visible Reflectance Spectra, Icarus, 119, 202

Ivezić, Ž., & 32 co-authors. 2001, Solar System Objects Observed in the Sloan Digital Sky Survey Commissioning Data, Astronomical Journal, 122, 2749

Ivezic, Z., Juric, M., Lupton, R. H., Tabachnik, S., & Quinn, T. 2002, in Presented at the Society of Photo-Optical Instrumentation Engineers (SPIE) Conference, Vol. 4836, Society of Photo-Optical Instrumentation Engineers (SPIE) Conference Series, ed. J. A. Tyson & S. Wolff, 98–103

Jedicke, R., Larsen, J., & Spahr, T. 2002, Observational Selection Effects in Asteroid Surveys, Asteroids III, 71

Jurić, M., & 15 co-authors. 2002, Comparison of Positions and Magnitudes of Asteroids Observed in the Sloan Digital Sky Survey with Those Predicted for Known Asteroids, Astronomical Journal, 124, 1776

Kaiser, N., & 25 co-authors. 2002, in Presented at the Society of Photo-Optical Instrumentation Engineers (SPIE) Conference, Vol. 4836, Society of Photo-Optical Instrumentation Engineers (SPIE) Conference Series, ed. J. A. Tyson & S. Wolff, 154–164

Keil, K. 2000, Thermal alteration of asteroids: evidence from meteorites, Planetary and Space Science, 48, 887

—. 2002, Geological History of Asteroid 4 Vesta: The ”Smallest Terrestrial Planet”, Asteroids III, 573

Keil, K., Stoeffler, D., Love, S. G., & Scott, E. R. D. 1997, Constraints on the role of impact heating and melting in asteroids, Met. Planet. Sci., 32, 349

Keil, K., & Wilson, L. 1993, Explosive volcanism and the compositions of cores of differentiated asteroids, Earth Planet. Sci. Lett., 117, 111

Kelley, M. S., Vilas, F., Gaffey, M. J., & Abell, P. A. 2003, Quantified mineralogical evidence for a common origin of 1929 Kollaa with 4 Vesta and the HED meteorites, Icarus, 165, 215

Kirkwood, D. 1876, On the distribution of the asteroids. (Salem, Mass., Printed at the Salem press)

Knoche, R., & Luth, R. W. 1996, Density measurements on melts at high pressure using the sink/float method: Limitations and possibilities, Chemical Geology, 128, 229

Krot, A. N., Amelin, Y., Cassen, P., & Meibom, A. 2005a, Young chondrules in CB chondrites from a giant impact in the early Solar System, Nature, 436, 989

Krot, A. N., Keil, K., Goodrich, C. A., Scott, E. R. D., & Weisberg, M. K. 2005b, Classification of Meteorites, Vol. Meteorites, Comets and Planets: Treatise on Geochemistry, Volume 1 (Oxford: Elsevier Science), 83

Lantz, B., & 14 co-authors. 2004, in Presented at the Society of Photo-Optical Instrumentation Engineers (SPIE) Conference, Vol. 5249, Society of Photo-Optical Instrumentation Engineers (SPIE) Conference Series, ed. L. Mazuray, P. J. Rogers, & R. Wartmann, 146–155

Lawrence, S. J., & Lucey, P. G. 2007, Radiative transfer mixing models of meteoritic assemblages, Journal of Geophysical Research (Planets), 112, 7005

Lazzaro, D., & 11 co-authors. 1999, The Eunomia Family: A Visible Spectroscopic Survey, Icarus, 142, 445

Lazzaro, D., Angeli, C. A., Carvano, J. M., Mothé-Diniz, T., Duffard, R., & Florczak, M. 2004, S^3OS^2: the visible spectroscopic survey of 820 asteroids, Icarus, 172, 179

Lazzaro, D., Michtchenko, T., Carvano, J. M., Binzel, R. P., Bus, S. J., Burbine, T. H., Mothé-Diniz, T., Florczak, M., Angeli, C. A., & Harris, A. W. 2000, Discovery of a Basaltic Asteroid in the Outer Main Belt, Science, 288, 2033

Lee, D. C., & Halliday, A. N. 1997, Core formation on Mars and differentiated asteroids, Nature, 388, 854

Lee, T., Papanastassiou, D. A., & Wasserburg, G. J. 1976, Demonstration of Mg-26 excess in Allende and evidence for Al-26, Geophys. Res. Lett., 3, 41

Levison, H. F., Bottke, W., Gounelle, M., Morbidelli, A., Nesvorny, D., & Tsiganis, K. 2008, in AAS/Division of Dynamical Astronomy Meeting, Vol. 39, AAS/Division of Dynamical Astronomy Meeting, 12.05

Lide, D. R. 2002, CRC Handbook of chemistry and physics : a ready-reference book of chemical and physical data (CRC Handbook of chemistry and physics : a ready-reference book of chemical and physical data, 83rd ed., by David R. Lide. Boca Raton: CRC Press, ISBN 0849304830, 2002)

Lim, L. F., Emery, J. P., & Moskovitz, N. A. 2009, in Lunar and Planetary Institute Science Conference Abstracts, Vol. 40, Lunar and Planetary Institute Science Conference Abstracts, 2204

Lim, L. F., McConnochie, T. H., Bell, J. F., & Hayward, T. L. 2005, Thermal infrared (8 13 μm) spectra of 29 asteroids: the Cornell Mid-Infrared Asteroid Spectroscopy (MIDAS) Survey, Icarus, 173, 385

Lodders, K. 2003, Solar System Abundances and Condensation Temperatures of the Elements, Astrophys. J., 591, 1220

Lodders, K., & Fegley, B. 1998, The planetary scientist's companion / Katharina Lodders, Bruce Fegley. (New York : Oxford University Press, 1998. QB601 .L84 1998)

Lowry, S. C., & 10 co-authors. 2007, Direct Detection of the Asteroidal YORP Effect, Science, 316, 272

Lucey, P. G., Keil, K., & Whitely, R. 1998, The influence of temperature on the spectra of the A-asteroids and implications for their silicate chemistry, Journal of Geophysical Research, 103, 5865

Lupishko, D. F. 2006, On the bulk density of the M-type asteroid 16 Psyche, Solar System Research, 40, 214

Lynn, W. T. 1907, The discovery of Vesta, The Observatory, 30, 103

Machida, R., & Abe, Y. 2006, in Lunar and Planetary Institute Science Conference Abstracts, Vol. 37, 37th Annual Lunar and Planetary Science Conference, ed. S. Mackwell & E. Stansbery, 1615

Magri, C., Nolan, M. C., Ostro, S. J., & Giorgini, J. D. 2007, A radar survey of main-belt asteroids: Arecibo observations of 55 objects during 1999 2003, Icarus, 186, 126

Mao, H. K., & Bell, P. M. 1972, Optical and electrical behavior of olivine and spinel (Fe2SiO4) at high pressure, Carnegie Inst. Washington Yearbook, 71, 520

Marchi, S., Brunetto, R., Magrin, S., Lazzarin, M., & Gandolfi, D. 2005, Space weathering of near-Earth and main belt silicate-rich asteroids: observations and ion irradiation experiments, Astronomy and Astrophysics, 443, 769

Marchi, S., Lazzarin, M., & Magrin, S. 2004, An R-type asteroid within near-Earth objects?, Astronomy and Astrophysics, 420, L5

Markowski, A., Quitté, G., Halliday, A. N., & Kleine, T. 2006, Tungsten isotopic compositions of iron meteorites: Chronological constraints vs. cosmogenic effects, Earth Planet. Sci. Lett., 242, 1

Marzari, F., Cellino, A., Davis, D. R., Farinella, P., Zappala, V., & Vanzani, V. 1996, Origin and evolution of the Vesta asteroid family., Astronomy and Astrophysics, 316, 248

Marzari, F., Farinella, P., & Davis, D. R. 1999, Origin, Aging, and Death of Asteroid Families, Icarus, 142, 63

Masi, G., Foglia, S., & Binzel, R. P. 2008, Search and Confirmation of V-type Asteroids Beyond 2.5 AU Using Sloan Digital Sky Survey Colors, LPI Contributions, 1405, 8065

McCord, T. B., Adams, J. B., & Johnson, T. V. 1970, Asteroid Vesta: Spectral Reflectivity and Compositional Implications, Science, 168, 1445

McCord, T. B., & Sotin, C. 2005, Ceres: Evolution and current state, Journal of Geophysical Research (Planets), 110, 5009

McCoy, T. J., Corrigan, C. M., Sunshine, J. M., Bus, S. J., & Gale, A. 2007, in Lunar and Planetary Institute Conference Abstracts, Vol. 38, Lunar and Planetary Institute Conference Abstracts, 1631

McCoy, T. J., Mittlefehldt, D. W., & Wilson, L. 2006, Asteroid Differentiation (Tucson: University of Arizona Press), 733–745

McKenzie, D. 1984, The generation and compaction of partially molten rock, J. Petrol., 5, 713

—. 1985, The extraction of magma from the crust and mantle, Earth Planet. Sci. Lett., 74, 81

McKenzie, D., & Bickle, M. J. 1988, The volume and composition of melt generated by extension of the lithosphere, J. Petrol., 29, 625

McKinnon, W. B. 2008, Could Ceres be a Refugee from the Kuiper Belt?, LPI Contributions, 1405, 8389

McMurry, J., & Fay, R. C. 2001, Chemistry (New Jersey: Prentice Hall)

McSween, Jr., H. Y., Ghosh, A., Grimm, R. E., Wilson, L., & Young, E. D. 2002, Thermal Evolution Models of Asteroids, Asteroids III, 559

McSween, Jr., H. Y., Taylor, L. A., & Lipschutz, M. E. 1978, in Lunar and Planetary Science Conference Proceedings, Vol. 9, Lunar and Planetary Science Conference Proceedings, 1437–1447

Michtchenko, T. A., Lazzaro, D., Ferraz-Mello, S., & Roig, F. 2002, Origin of the Basaltic Asteroid 1459 Magnya: A Dynamical and Mineralogical Study of the Outer Main Belt, Icarus, 158, 343

Milani, A., & Knezevic, Z. 1990, Secular perturbation theory and computation of asteroid proper elements, Celestial Mechanics and Dynamical Astronomy, 49, 347

—. 1992, Asteroid proper elements and secular resonances, Icarus, 98, 211

Mittlefehldt, D., McCoy, T., Goodrich, C., & Kracher, A. 1999, Non-chondritic meteorites from asteroidal bodies, Planetary Materials, 4.01

Mittlefehldt, D. W. 1979, in Lunar and Planetary Science Conference Proceedings, Vol. 10, Lunar and Planetary Science Conference Proceedings, ed. N. W. Hinners, 1975–1993

Miyamoto, M., Mikouchi, T., & McKay, G. A. 1994, in Lunar and Planetary Inst. Technical Report, Vol. 25, Lunar and Planetary Institute Science Conference Abstracts, 923–924

Morbidelli, A., Bottke, Jr., W. F., Froeschlé, C., & Michel, P. 2002, Origin and Evolution of Near-Earth Objects, Asteroids III, 409

Morbidelli, A., Nesvorný, D., Bottke, W. F., Michel, P., Vokrouhlický, D., & Tanga, P. 2003, The shallow magnitude distribution of asteroid families, Icarus, 162, 328

Moroz, L., Schade, U., & Wäsch, R. 2000, Reflectance Spectra of Olivine-Orthopyroxene-Bearing Assemblages at Decreased Temperatures: Implications for Remote Sensing of Asteroids, Icarus, 147, 79

Moskovitz, N. A., Jedicke, R., Gaidos, E., Willman, M., Nesvorný, D., Fevig, R., & Ivezić, Ž. 2008a, The distribution of basaltic asteroids in the Main Belt, Icarus, 198, 77

Moskovitz, N. A., Lawrence, S., Jedicke, R., Willman, M., Haghighipour, N., Bus, S. J., & Gaidos, E. 2008b, A Spectroscopically Unique Main-Belt Asteroid: 10537 (1991 RY16), Astrophys. J., Lett., 682, L57

Mothé-Diniz, T., & Carvano, J. M. 2005, 221 Eos: a remnant of a partially differentiated parent body?, Astronomy and Astrophysics, 442, 727

Mothé-Diniz, T., Carvano, J. M., Bus, S. J., Duffard, R., & Burbine, T. H. 2008, Mineralogical analysis of the Eos family from near-infrared spectra, Icarus, 195, 277

Nathues, A., Mottola, S., Kaasalainen, M., & Neukum, G. 2005, Spectral study of the Eunomia asteroid family. I. Eunomia, Icarus, 175, 452

Nesvorný, D., Enke, B. L., Bottke, W. F., Durda, D. D., Asphaug, E., & Richardson, D. C. 2006, Karin cluster formation by asteroid impact, Icarus, 183, 296

Nesvorný, D., Jedicke, R., Whiteley, R. J., & Ivezić, Ž. 2005, Evidence for asteroid space weathering from the Sloan Digital Sky Survey, Icarus, 173, 132

Nesvorný, D., Roig, F., Gladman, B., Lazzaro, D., Carruba, V., & Mothé-Diniz, T. 2008, Fugitives from the Vesta family, Icarus, 193, 85

Nesvorný, D., Vokrouhlický, D., Morbidelli, A., & Bottke, W. F. 2009, Asteroidal source of L chondrite meteorites, Icarus, 200, 698

Oke, J. B., & Gunn, J. E. 1983, Secondary standard stars for absolute spectrophotometry, Astrophys. J., 266, 713

Ostro, S. J., Hudson, R. S., Nolan, M. C., Margot, J.-L., Scheeres, D. J., Campbell, D. B., Magri, C., Giorgini, J. D., & Yeomans, D. K. 2000, Radar Observations of Asteroid 216 Kleopatra, Science, 288, 836

Osuga, T. 2000, Characteristic time required to achieve uniform temperature in thermal conduction of N-dimensional sphere heated from surface, Japan Journal of Applied Physics, 39, 6111

Ozisik, M. N. 1994, Finite difference methods in heat transfer (CRC Press)

Pack, A., & Palme, H. 2003, Partitioning of Ca and Al between forsterite and silicate melt in dynamic systems with implications for the origin of Ca, Al-rich forsterites in primitive meteorites, Met. Planet. Sci., 38, 1263

Parker, A., Ivezić, Ž., Jurić, M., Lupton, R., Sekora, M. D., & Kowalski, A. 2008, The size distributions of asteroid families in the SDSS Moving Object Catalog 4, Icarus, 198, 138

Petit, J.-M., Chambers, J., Franklin, F., & Nagasawa, M. 2002, Primordial Excitation and Depletion of the Main Belt, Asteroids III, 711

Pieters, C. M., Binzel, R. P., Bogard, D., Hiroi, T., Mittlefehldt, D. W., Nyquist, L., Rivkin, A., & Takeda, H. 2006, in IAU Symposium, Vol. 229, Asteroids, Comets, Meteors, ed. L. Daniela, M. Sylvio Ferraz, & F. J. Angel, 273–288

Pieters, C. M., & Hiroi, T. 2004, in Lunar and Planetary Inst. Technical Report, Vol. 35, Lunar and Planetary Institute Science Conference Abstracts, ed. S. Mackwell & E. Stansbery, 1720

Pieters, C. M., Taylor, L. A., Noble, S. K., Keller, L. P., Hapke, B., Morris, R. V., Allen, C. C., McKay, D. S., & Wentworth, S. 2000, Space weathering on airless bodies: Resolving a mystery with lunar samples, Met. Planet. Sci., 35, 1101

Raymond, S. N., Quinn, T., & Lunine, J. I. 2004, Making other earths: dynamical simulations of terrestrial planet formation and water delivery, Icarus, 168, 1

Rayner, J. T., Toomey, D. W., Onaka, P. M., Denault, A. J., Stahlberger, W. E., Vacca, W. D., Cushing, M. C., & Wang, S. 2003, SpeX: A Medium-Resolution 0.8-5.5 Micron Spectrograph and Imager for the NASA Infrared Telescope Facility, Publications of the Astronomical Society of the Pacific, 115, 362

Reed, K. L., Gaffey, M. J., & Lebofsky, L. A. 1997, Shape and Albedo Variations of Asteroid 15 Eunomia, Icarus, 125, 446

Renner, J., Evans, B., & Hirth, G. 2000, On the rheologically critical melt fraction, Earth Planet. Sci. Lett., 181, 585

Righter, K., & Drake, M. J. 1997, A magma ocean on Vesta: Core formation and petrogenesis of eucrites and diogenites, Met. Planet. Sci., 32, 929

Rivkin, A. S., Howell, E. S., Lebofsky, L. A., Clark, B. E., & Britt, D. T. 2000, The nature of M-class asteroids from 3-micron observations, Icarus, 145, 351

Robie, R. A., & Hemingway, B. S. 1995, Thermodynamic properties of minerals and related substances at 298.15 K and 1 bar (10^5 Pascals) pressure and at higher temperatures, U.S. Geol. Survey Bull., vol. 2131, p. 461-461 (1995)., 2131, 461

Roig, F., & Gil-Hutton, R. 2006, Selecting candidate V-type asteroids from the analysis of the Sloan Digital Sky Survey colors, Icarus, 183, 411

Roig, F., Nesvorný, D., Gil-Hutton, R., & Lazzaro, D. 2008, V-type asteroids in the middle main belt, Icarus, 194, 125

Rosenberg, N. D., Browning, L., & Bourcier, W. L. 2001, Modeling aqueous alteration of CM carbonaceous chondrites, Met. Planet. Sci., 36, 239

Rushmer, T., Minarik, W. G., & Taylor, G. J. 2000, Physical Processes of Core Formation (Tucson: University of Arizona Press), 227–243

Russell, C. T., & 20 co-authors. 2004, Dawn: A journey in space and time, Planetary and Space Science, 52, 465

Ruzicka, A., Snyder, G. A., & Taylor, L. A. 1997, Vesta as the HED Parent Body: Implications for the Size of a Core and for Large-Scale Differentiation, Met. Planet. Sci., 32, 825

Safronov, V. S. 1969, Evoliutsiia doplanetnogo oblaka. (LOC)

Schulte, M., Blake, D., Hoehler, T., & McCollom, T. 2006, Serpentinization and Its Implications for Life on the Early Earth and Mars, Astrobiology, 6, 364

Scott, E. R. D. 1977, Formation of olivine-metal textures in pallasite meteorites, Geochimica et Cosmochimica Acta, 41, 693

Scott, E. R. D., Greenwood, R. C., Franchi, I. A., & Sanders, I. S. 2009, in Lunar and Planetary Inst. Technical Report, Vol. 40, Lunar and Planetary Institute Science Conference Abstracts, 2263

Scott, E. R. D., & Wasson, J. T. 1975, Classification and properties of iron meteorites, Reviews of Geophysics and Space Physics, 13, 527

Shannon, M. C., & Agee, C. B. 1996, High pressure constraints on percolative core formation, Geophys. Res. Lett., 23, 2717

Sheinis, A. I., Bolte, M., Epps, H. W., Kibrick, R. I., Miller, J. S., Radovan, M. V., Bigelow, B. C., & Sutin, B. M. 2002, ESI, a New Keck Observatory Echellette Spectrograph and Imager, Publications of the Astronomical Society of the Pacific, 114, 851

Shestopalov, D. I., McFadden, L. A., & Golubeva, L. F. 2007, Exploration of faint absorption bands in the reflectance spectra of the asteroids by method of optimal smoothing: Vestoids, Icarus, 187, 469

Sonett, C. P., & Colburn, D. S. 1968, Electrical Heating of Meteorite Parent Bodies and Planets by Dynamo Induction from a Pre-main Sequence T Tauri "Solar Wind", Nature, 219, 924

Stevenson, D. J. 1990, Fluid dynamics of core formation. (Oxford), 231–249

Stimpfl, M., Drake, M. J., Deymier, P., & Lauretta, D. 2005, Origin of planetary water by adsorption in the accretion disk, Geochimica et Cosmochimica Acta Supplement, 69, 748

Storm, S., Bus, S. J., & Binzel, R. P. 2007, in Bulletin of the American Astronomical Society, Vol. 38, Bulletin of the American Astronomical Society, 448

Sunshine, J. M., Bus, S. J., McCoy, T. J., Burbine, T. H., Corrigan, C. M., & Binzel, R. P. 2004, High-calcium pyroxene as an indicator of igneous differentiation in asteroids and meteorites, Met. Planet. Sci., 39, 1343

Sunshine, J. M., Pieters, C. M., & Pratt, S. F. 1990, Deconvolution of mineral absorption bands - An improved approach, Journal of Geophysical Research, 95, 6955

Tachibana, S., & Huss, G. R. 2003, The Initial Abundance of ^{60}Fe in the Solar System, Astrophys. J., Lett., 588, L41

Tachibana, S., Huss, G. R., Kita, N. T., Shimoda, G., & Morishita, Y. 2006, ^{60}Fe in Chondrites: Debris from a Nearby Supernova in the Early Solar System?, Astrophys. J., Lett., 639, L87

Taylor, G. J. 1992, Core formation in asteroids, Journal of Geophysical Research, 97, 14717

Taylor, G. J., Keil, K., McCoy, T., Haack, H., & Scott, E. R. D. 1993, Asteroid differentiation - Pyroclastic volcanism to magma oceans, Meteoritics, 28, 34

Taylor, G. J., & Norman, M. D. 1992, in Physics and Chemistry of Magma Oceans from 1 Bar to 4 Mbar, ed. C. B. Agee & J. Longhi, 58

Tedesco, E. F., Noah, P. V., Noah, M., & Price, S. D. 2004, IRAS Minor Planet Survey V6.0, NASA Planetary Data System, IRAS-A-FPA-3-RDR-IMPS-V6.0, 12

Tholen, D. J. 1984, PhD thesis, AA(Arizona Univ., Tucson.)

Thomas, P. C., Binzel, R. P., Gaffey, M. J., Storrs, A. D., Wells, E. N., & Zellner, B. H. 1997, Impact excavation on asteroid 4 Vesta: Hubble Space Telescope results, Science, 277, 1492

Tody, D. 1986, in Presented at the Society of Photo-Optical Instrumentation Engineers (SPIE) Conference, Vol. 627, Society of Photo-Optical Instrumentation Engineers (SPIE) Conference Series, ed. D. L. Crawford, 733

Tsiganis, K., Varvoglis, H., & Morbidelli, A. 2003, Short-lived asteroids in the 7/3 Kirkwood gap and their relationship to the Koronis and Eos families, Icarus, 166, 131

Turcotte, D. L., & Schubert, G. 2002, Geodynamics - 2nd Edition (Cambridge University Press)

Ueda, Y., Hiroi, T., Pieters, C. M., & Miyamoto, M. 2002, in Lunar and Planetary Inst. Technical Report, Vol. 33, Lunar and Planetary Institute Science Conference Abstracts, 2023

Urakawa, S., Terasaki, H., Funakoshi, K., Kato, T., & Suzuki, A. 2001, Radiographic Study on the Viscosity of the Fe-FeS Melts at the Pressure of 5 to 7 GPa, American Mineralogist, 86, 578

Urey, H. C. 1955, The Cosmic Abundances of Potassium, Uranium, and Thorium and the Heat Balances of the Earth, the Moon, and Mars, Proceedings of the National Academy of Science, 41, 127

Vernazza, P., Binzel, R. P., Thomas, C. A., Demeo, F. E., Bus, S. J., Rivkin, A. S., & Tokunaga, A. T. 2008, Compositional differences between meteorites and near-Earth asteroids, Nature, 454, 858

Viateau, B., & Rapaport, M. 2001, Mass and density of asteroids (4) Vesta and (11) Parthenope, Astronomy and Astrophysics, 370, 602

Vilas, F., Cochran, A. L., & Jarvis, K. S. 2000, Vesta and the Vestoids: A New Rock Group?, Icarus, 147, 119

Vilas, F., Larson, S. M., Hatch, E. C., & Jarvis, K. S. 1993, CCD Reflectance Spectra of Selected Asteroids. II. Low-Albedo Asteroid Spectra and Data Extraction Techniques, Icarus, 105, 67

Vokrouhlický, D., & Nesvorný, D. 2008, Pairs of Asteroids Probably of a Common Origin, Astronomical Journal, 136, 280

Walker, D., Stolper, E. M., & Hays, J. F. 1978, A numerical treatment of melt/solid segregation - Size of the eucrite parent body and stability of the terrestrial low-velocity zone, Journal of Geophysical Research, 83, 6005

Wasson, J. T., Pieters, C. M., Fisenko, A. V., Semjonova, L. F., Moroz, L. V., & Warren, P. H. 1997, in Lunar and Planetary Inst. Technical Report, Vol. 28, Lunar and Planetary Institute Science Conference Abstracts, 1505

Wasson, J. T., Pieters, C. M., Fisenko, A. V., Semjonova, L. F., & Warren, P. H. 1998, in Lunar and Planetary Inst. Technical Report, Vol. 29, Lunar and Planetary Institute Science Conference Abstracts, 1940

Wegner, W. W., & Ernst, W. G. 1983, Experimentally determined hydration and dehydration reaction reats in the system MgO-SiO_2-H_2O, American Journal of Science, 238, 151

Wetherill, G. W. 1980, Formation of the terrestrial planets, Ann. Rev. Astron. Astrophys., 18, 77

Wetherill, G. W., & Chapman, C. R. 1988, Asteroids and meteorites (Meteorites and the Early Solar System), 35–67

Willman, M., Jedicke, R., Nesvorný, D., Moskovitz, N., Ivezić, Ž., & Fevig, R. 2008, Redetermination of the space weathering rate using spectra of Iannini asteroid family members, Icarus, 195, 663

Wilson, L., Goodrich, C. A., & Van Orman, J. A. 2008, Thermal evolution and physics of melt extraction on the ureilite parent body, Geochimica et Cosmochimica Acta, 72, 6154

Wilson, L., & Keil, K. 1991, Consequences of explosive eruptions on small solar system bodies - The case of the missing basalts on the aubrite parent body, Earth Planet. Sci. Lett., 104, 505

—. 1996, Clast sizes of ejecta from explosive eruptions on asteroids: implications for the fate of the basaltic products of differentiation, Earth Planet. Sci. Lett., 140, 191

Wilson, L., Keil, K., Browning, L. B., Krot, A. N., & Bourcier, W. 1999, Early aqueous alteration, explosive disruption, and re-processing of asteroids, Met. Planet. Sci., 34, 541

Wisdom, J. 1985, Meteorites may follow a chaotic route to earth, Nature, 315, 731

Wood, J. A., & Pellas, P. 1991, in The Sun in Time, ed. C. P. Sonett, M. S. Giampapa, & M. S. Matthews, 740–760

Xu, S., Binzel, R. P., Burbine, T. H., & Bus, S. J. 1995, Small main-belt asteroid spectroscopic survey: Initial results, Icarus, 115, 1

Yamaguchi, A., Misawa, K., Haramura, H., Kojima, H., Clayton, R. N., Mayeda, T. K., & Ebihara, M. 2001, Northwest Africa 011, a New Basaltic Meteorite, Meteoritics, 36, 228

Yang, J., & Goldstein, J. I. 2006, Metallographic cooling rates of the IIIAB iron meteorites, Geochimica et Cosmochimica Acta, 70, 3197

Yang, J., Goldstein, J. I., & Scott, E. R. D. 2007, Iron meteorite evidence for early formation and catastrophic disruption of protoplanets, Nature, 446, 888

York, D. G., & 143 co-authors. 2000, The Sloan Digital Sky Survey: Technical Summary, Astronomical Journal, 120, 1579

Yoshino, T., Walter, M. J., & Katsura, T. 2003, Core formation in planetesimals triggered by permeable flow, Nature, 422, 154

—. 2004, Connectivity of molten Fe alloy in peridotite based on in situ electrical conductivity measurements: implications for core formation in terrestrial planets, Earth Planet. Sci. Lett., 222, 625

Young, E. D., Zhang, K. K., & Schubert, G. 2003, Conditions for pore water convection within carbonaceous chondrite parent bodies - implications for planetesimal size and heat production, Earth Planet. Sci. Lett., 213, 249

Zappala, V., Bendjoya, P., Cellino, A., Farinella, P., & Froeschle, C. 1995, Asteroid families: Search of a 12,487-asteroid sample using two different clustering techniques., Icarus, 116, 291

Zappala, V., Cellino, A., dell'Oro, A., Migliorini, F., & Paolicchi, P. 1996, Reconstructing the Original Ejection Velocity Fields of Asteroid Families, Icarus, 124, 156

Zappala, V., Cellino, A., Farinella, P., & Knezevic, Z. 1990, Asteroid families. I - Identification by hierarchical clustering and reliability assessment, Astronomical Journal, 100, 2030